Computer modeling and experimental work on the astrobiological implications of the martian subsurface ionising radiation environment

A thesis submitted submitted to University College London
for the Degree of Doctor of Philosophy

Lewis R. Dartnell

April 2008

Centre for Mathematics & Physics in the Life Sciences and Experimental Biology (CoMPLEX)
University College London
Wolfson House
4 Stephenson Way
London NW1 2HE

I, Lewis R. Dartnell, confirm that the work presented in this thesis is my own. Where information has been derived from other sources, I confirm that this has been indicated in the thesis.

Abstract

Any microbial life extant in the top meters of the martian subsurface is likely to be held dormant for long periods of time by the current permafrost conditions. In this potential habitable zone, a major environmental hazard is the ionising radiation field generated by the flux of exogenous energetic particles: solar energetic protons and galactic cosmic rays. The research reported here constitutes the first multidisciplinary approach to assessing the astrobiological impact of this radiation on Mars.

A sophisticated computer model has been constructed *de novo* to characterise this complex subsurface ionising radiation field and explore the influence of variation in crucial parameters such as atmospheric density, surface composition, and primary radiation spectra. Microbiological work has been conducted to isolate novel cold-tolerant bacterial strains from the Dry Valleys environment of Antarctica, an analogue site to the martian surface, and determine their phylogenetic diversity and survival under high-dose gamma-ray exposure frozen at -79°C, a temperature characteristic of the martian mid-latitude permafrost.

Original results are presented pertinent to microbial survival time, persistence of organic biomarkers, and calibration of the optically stimulated luminescence dating technique, as a function of depth. The model predicts a population of radiation resistant cells to survive in martian permafrost soil for 450,000 years at 2 m depth, the proposed drill length of the ExoMars rover. The Antarctic culturing studies identified representatives of four bacterial genera. The novel isolate *Brevundimonas* sp. MV.7 is found to show 99% 16S sequence similarity to cells discovered in NASA spacecraft assembly clean rooms, with the experimental irradiation determining this strain to suffer 10^{-6} population inactivation after a radiation dose of 7.5 kGy in martian permafrost conditions. Integrating the modelling and experimental irradiation, this research finds a contaminant population of such cells deposited just beneath the martian surface would survive the ambient cosmic radiation field for 117,000 years.

Acknowledgments

First and foremost, I would like to thank my supervisors Prof. Andrew Coates and Prof. John Ward. Thank you for agreeing to take me on for this diverse research project, and for all your expert guidance and encouragement along the way. Laurent Desorgher has also been utterly gracious in offering his time and help, and talk me through the finer aspects of particle physics and Geant4 programming. Without their efforts this project would not have gotten off the ground.

Many other people have been enormously helpful over the last four years, especially Trevor for all things computational, and Steph, Emma, Steve, Sam and Will in the lab.

Just as appreciated are those who have enticed me away from the computer or lab bench – lunches, coffees, cakes and pints with the assorted posse of Wolfson House and Darwin. Trev, Chris, Alex, Alé, Charlotte, Cathy, Edd, Ana, Ian, AJ, Eric, Andrew, Chloe, Claire, Ian: cheers!

Vicky, you have been a continued bedrock of support and comfort. Thank you for bouncing me out of my down-swings. And finally, of course, thank you to mum and dad, and Beccy for putting up with my long periods of self-absorption and familial neglect...

Contents

1 Introduction **15**

1.1 Martian environment 16

1.1.1 Water 16

1.1.2 Atmospheric loss 16

1.1.3 Crustal Magnetic anomalies 19

1.1.4 Astrobiological potential 19

1.1.5 Ultra-violet radiation 20

1.1.6 Terrestrial analogue site 20

1.1.7 Deep life 21

1.2 Cosmic Ionising Radiation 22

1.3 Radiobiology 25

1.4 Modelling approaches 27

1.4.1 Boltzmann equation 27

1.4.2 Monte Carlo 29

1.5 Previous modelling work 30

1.5.1 Improvements of this model 31

1.6 Optically Stimulated Luminescence dating 32

1.7 Analysis of environmental microbial diversity 32

1.8 Aims of this research 33

1.9 Thesis outline 34

2 Geant4 Method **36**

2.1 Major class categories . . . 37

2.2 G4RunManager . . . 38

2.3 DetectorConstructor . . . 39

2.3.1 Geometry . . . 39

2.3.2 Materials . . . 40

2.4 PhysicsList . . . 40

2.4.1 Particles . . . 41

2.4.2 Physics Processes . . . 41

2.4.3 Simulation of particle interactions . . . 41

2.4.4 Cuts . . . 43

2.4.5 Magnetic fields . . . 43

2.5 PrimaryGeneratorAction . . . 45

2.5.1 General Particle Source . . . 45

2.6 Sensitive Detectors and Hits . . . 46

2.7 User Interface . . . 46

2.8 Visualisation . . . 47

2.9 Optional User Actions . . . 48

2.10 General . . . 48

2.10.1 Geant4 types . . . 48

2.10.2 Geant4 units . . . 49

2.10.3 Randomisation . . . 49

2.11 Chapter summary . . . 49

3 Model Development **51**

3.1 Development . . . 51

3.2 Model Geometry and composition . . . 52

3.2.1 Atmosphere composition . . . 53

3.2.2 Surface composition . . . 53

3.2.3 Geometry . . . 54

3.3 Visualisation . . . 62

3.4 Physics models . . . 62

3.4.1 Class structure . . . 64

3.4.2 Hadronic physics . . . 64

3.4.3 Cut in range . . . 66

3.4.4 Resolution of physics bug . . . 66

3.5 Particle Source . . . 69

3.5.1 SEP and GCR primary spectra models . . . 69

3.5.2 Primary source geometry . . . 70

3.5.3 Fluence normalisation . . . 71

3.6 Event detection and data capture . . . 72

3.6.1 First configuration . . . 72

3.6.2 Second configuration . . . 73

3.6.3 Biologically-weighted doses . . . 73

3.7 Magnetic field . . . 74

3.7.1 Calculation of gyroradii . . . 75

3.8 Randomisation . . . 78

3.9 Distributed computing . . . 78

3.10 Post-processing . . . 79

3.10.1 Proton-only approximation . . . 81

3.11 Chapter summary . . . 82

4 Experimental method 83

4.1 Sterilization conditions . . . 83

4.2 Sampling of Antarctic soils . . . 83

4.3 Solutions and Media . . . 84

4.3.1 X-gal (5-bromo-4-chloro-3-indoyl-βD-galactopyranoside) . . . 84

4.3.2 Ampicillin . . . 84

4.3.3 Phosphate Buffer Solution (PBS) . . . 84

4.3.4 Culture media . . . 84

4.4 Cultivation of microbes from Antarctic samples . . . 85

4.5 Identification of isolated strains . . . 86

4.5.1 DNA extraction . . . 86

4.5.2 Agarose gel electrophoresis . . . 87

4.5.3 PCR amplification of 16S gene . . . 87

4.5.4 PCR product cleaning and extraction . . . 88

4.5.5 DNA ligation . . . 88

4.5.6 Transformation . . . 88

4.5.7 Purification of Transformed plasmids . . . 89

4.5.8 DNA sequencing . . . 89

4.5.9 Analysis of Sequence Data . . . 89

4.6 Irradiation experiments . . . 90

4.6.1 Irradiation vessels . . . 90

4.6.2 Preparation of cell samples . . . 91

4.6.3 Irradiation procedure . . . 91

4.7 Chapter summary . . . 100

5 Results: Model validation **101**

5.1 Resolution of primary spectrum error . . . 101

5.2 Charged particle propagation within crustal fields . . . 104

5.3 Comparison of surface particle energy spectra . . . 105

5.3.1 PLANETOCOSMICS . . . 105

5.3.2 MarsGRAM . . . 106

5.3.3 Surface neutron environment . . . 107

5.3.4 Mars Odyssey . . . 108

5.4 Comparison of particle fluence . . . 109

5.4.1 Particle traversal per unit area . . . 109

5.5 Proton-weighting approximation . . . 110

5.6 Chapter summary . . . 111

6 Modelling Results **112**

6.1 Particle energy spectra and fluences . . . 112

6.2 Microbial survival . . . 117

6.3 Dose deposited in regolith . . . 119

6.3.1 Surface properties . . . 119

6.3.2 Solar activity . . . 121

6.3.3 Topographic elevation . . . 122

6.3.4 Diminishing atmospheric pressure over geological time . . . 123

6.4 Chapter summary . . . 125

7 Microbiology & irradiation results **126**

7.1 Culturing from Antarctic Dry Valley . . . 126

7.2 Growth of *D. radiodurans* . . . 131

7.3 Identification of isolated strains . . . 131

7.4 Gamma irradiation . . . 133

7.5 Chapter summary . . . 142

8 Discussion **143**

8.1 Modeled microbial survival . . . 144

8.2 Modeled dose deposition in regolith . . . 146

8.2.1 Preservation of astrobiological markers . . . 146

8.2.2 OSL dating . . . 148

8.3 Model comparison for dose deposited in regolith . . . 148

8.4 Data comparison of both model configurations . . . 152

8.5 Experimental irradiation . . . 157

8.5.1 *E. coli* survival . . . 157

8.5.2 Enhanced radioresistance at -79°C . . . 158

8.6 Conclusions . . . 163

8.7 Further Work . . . 165

8.8 Research Summary . . . 167

Bibliography **169**

9 Appendices **186**

9.1 Appendix I: Antarctic isolates 16S rRNA sequences . . . 186

9.2 Appendix II: Irradiation survival data . . . 193

9.3 Appendix III: Publications . . . 199

List of Figures

1.1 Map of the martian globe 17

1.2 Map of soil water content 18

1.3 Map of crustal magnetic anomalies 18

1.4 SEP and GCR primary spectra 23

1.5 Secondary cascade 24

1.6 Free radical reactions 26

1.7 Formalism of Boltzmann transport equation 28

2.1 Class category structure of Geant4 37

2.2 Particle interaction processes in Geant4 43

2.3 Magnetic deflection of a charged particle 44

3.1 Maps of martian surface pressure and temperature 57

3.2 Altitude profiles of martian atmospheric pressure, density and temperature . . . 59

3.3 Altitude-density profiles of calculated primordial atmospheres 61

3.4 Visualisation of the martian radiation model 63

3.5 Geant4 classes and energy ranges used in physics modelling 65

3.6 Anomalous flux-depth profile indicating physics bug 67

3.7 Gradient in GCR flux through solar system 70

3.8 Particle propagation through simulated magnetic anomalies 76

3.9 Post-processing pipeline for model data 79

3.10 Recreation of GCR proton spectrum 80

3.11 Recreating complete GCR flux 81

4.1 Cranfield University gamma irradiation facility 92

4.2 Scale diagram of experimental design for first radiation exposure 96

4.3 Box and whisker plot of *D. radiodurans* cell counts 97

4.4 Scale diagram of experimental design for first radiation exposure 99

5.1 Comparison of SPENVIS and CREME-96 primary spectra 102

5.2 Refitting of modelled primary spectra 103

5.3 Comparison of refitted data 104

5.4 Surface fluence maps beneath crustal anomalies 104

5.5 Comparison of results against PLANETOCOSMICS 106

5.6 Comparison of results against MarsGRAM 107

5.7 Comparison of results against Clowdsley *et al.* (2000) 108

5.8 Comparison of results against Mars Odyssey data 109

5.9 Verification of proton-only approximation 110

6.1 Particle energy spectra on the martian surface 113

6.2 Depth profiles of proton and HZE spectra 114

6.3 Particle energy spectra at 1 m depth 115

6.4 Flux-depth profiles 115

6.5 Contributions to surface particle spectra 116

6.6 Depth profile of radiation dose 117

6.7 Dose profiles in different surface scenarios 120

6.8 Dose profiles over solar activity cycle 121

6.9 Dose contributions as a function of proton primary energy 122

6.10 Dose profiles at different topographic elevations 123

6.11 Dose profiles under increasing atmospheric depth 124

7.1 Colony photographs of novel isolates 130

7.2 Colony photograph of *D. radiodurans* 131

7.3 Phylogenetic tree of novel isolates and major bacterial clades 135

7.4 Phylogenetic trees of novel isolates and related strains 136

7.5 Gamma-ray survival curve of *E. coli* 138

7.6 Gamma-ray survival curve of *D. radiodurans* 138

7.7 Gamma-ray survival curve of *Brevundimonas* sp. MV.7 139

7.8 Gamma-ray survival curve of *Rhodococcus* sp. MV.10 139

7.9 Gamma-ray survival curve of *Pseudomonas* sp. MV.27 140

7.10 Combined survival curves of all irradiated strains 140

8.1 Comparison of dose profile results against previous studies 149

8.2 Comparison of particle source geometries in free space 150

8.3 Comparison of dose results against Mileikowsky *et al.* (2000) 151

8.4 Discrepancy between the two model configurations 154

8.5 The mean biological weighting factor applied 156

8.6 Comparison of irradiation survival results against previous studies 159

8.7 Irradiation survival as a function of temperature 162

List of Tables

3.1 Cuts in range selected for electromagnetic particles 66

3.2 Physics bug test runs 68

3.3 Biological weighting factors for dose deposition 73

3.4 Q-L relationships 74

4.1 PCR primer pair 87

4.2 Sample exposure doses for first irradiation 95

4.3 Comparison between *D. radiodurans* cell counts 98

4.4 Sample exposure doses for second irradiation 99

5.1 Comparison of results against Cucinotta *et al.* (2002) 109

6.1 Calculated microbial survival times 118

7.1 Colony growth over 15 days incubation 127

7.2 List of isolated microbial strains 129

7.3 16S rRNA identification of novel isolates 132

7.4 Psychrotolerant relatives of novel isolates 134

7.5 Freeze-thaw survival rates 137

7.6 Summary of irradiation survival characteristics 141

8.1 Comparison of dose rates against previous studies 153

List of Abbreviations

AU	Astronomical Unit
CDZ	Czapek-Dox (growth medium)
CREME	Cosmic Ray Effects on MicroElectronics
DH	Dry Homogenous (surface model)
DNA	DeoxyriboNucleic Acid
ESA	European Space Agency
GCR	Galactic Cosmic Rays
Geant4	GEometry ANd Tracking 4
HZE	High-Z High-Energy
HZETRN	HZE TRaNsport
LB	Luria Bertani (growth medium)
LET	Linear Energy Transfer
MC	Monte Carlo
MCD	Mars Climate Database
MV	Miers Valley
NASA	National Aeronautics and Space Administration
NB	Nutrient Broth (growth medium)
OD	Optical Density
OSL	Optically-Stimulated Luminescence
PBS	Phosphate Buffer Solution
PCR	Polymerase Chain Reaction
PI	Pure Ice (surface model)
RBE	Relative Biological Effectiveness
rDNA	ribosomal DNA
RNA	RiboNucleic Acid
rRNA	ribosomal RNA
SEP	Solar Energetic Particles
SPENVIS	SPace ENVironment Information System
UV	Ultra-Violet
WH	Wet Heterogeneous (surface model)

Chapter 1

Introduction

The central tenet behind the research programme reported here is that the planet Mars has at some point in its history provided environmental conditions suitable for the emergence of life, and that signs of this biology may remain in the near subsurface to be detected by our lander probes. In this first chapter, the lines of evidence supporting this argument are laid out, providing the context and background information for the rest of the thesis and introducing the methodologies employed here.

Current understanding on Mars, in terms of its environmental conditions both primordial and present, will be reviewed first. This will cover aspects of the atmosphere and distribution of liquid water over planetary time; the major hazards that martian life would have to endure, including water availability ultra-violet radiation and chemically oxidising conditions; and terrestrial analogue sites to the martian environment and the extremophile organisms that survive in them.

This research programme has focussed on the limitation to the persistence of organisms, and evidence of their existence, posed by the ionising radiation environment generated in the martian near subsurface by the constant flux of cosmic rays. The composition of the space radiation environment is described, as well as the interactions of such high energy particles with shielding material, the biological damage inflicted by ionising radiation and the response of different organisms. Certain aspects of the martian radiation environment have been studied in the past, and the computer modelling methodologies and results are reviewed here. In addition to estimating microbial survival times, determining the rate of radiation dose deposition in the martian subsurface is necessary for calibration of the optically stimulate luminescence technique for dating sediments.

Alongside modelling of the martian radiation environment, experimental work was conducted on the microbial diversity present in the Antarctic Dry Valleys, an analogue site of the martian surface. The history of the molecular biology technique employed here is described.

1.1 Martian environment

1.1.1 Water

The martian surface is today a cold barren desert. Even during summer in the mid-latitudes the ground temperature lies between 230 K and 180 K [43]. This coupled with an average atmospheric pressure of only 600 Pa at the reference datum altitude means that the current regime lies beneath the triple-point of water and so surface water is unstable as a liquid over much of the martian surface and seasonal cycle [142].

There is extensive large-scale geomorphological evidence, however, for the primordial planet being warmer and wetter [186, 214], including extensive valley networks, great floods channels, pooling in crater lakes, and estuarine deposition fans [120, 147]. Some researchers have also argued that the northern basin held a large ancient ocean; Head *et al.*(1999) [105], for example, recently claimed that the Mars Orbiter Laser Altimeter (MOLA) altitude map shows the northern basin to be particularly flat and smooth enough, with an encircling geological contact "shoreline" as evidence of a large ancient ocean. Such claims are currently the subject of intense debate, however [143, 184].

Much of the original martian volatile inventory is believed to remain locked in the subsurface as a permafrost shell [50, 28, 120]. Water ice has been inferred to lie very close to the martian surface, especially at high latitudes in the southern highlands and northern basin, by the characteristic modification of backscattering cosmic radiation by hydrogen [82, 156, 40]. High levels of hydrogen in an irradiated target efficiently moderate secondary neutrons, causing a decrease at epithermal energies and an enhancement of thermal neutrons. Neutron capture by the hydrogen nucleus produces a gamma photon of 2.2 MeV, and so presents a second signature of hydrogen content. Both of these indicators have been detected in the martian surface by instruments aboard Mars Odyssey: neutron moderation by the Neutron Spectrometer (NS) [82] and High Energy Neutron Detector (HEND) [156], and a 2.2 MeV spike in the gamma emission spectrum by the Gamma Ray Spectrometer (GRS) [40]. Data summation over a longer data gathering phase has allowed a more reliable global mapping of water abundance, finding a "moist" spot just 10°N of the equator and an estimation of the depth to the top of the cryosphere on the order of tens of centimetres [157].

More recently, NASA's Mars Exploration Rover *Opportunity* found unmistakable signs of the chemical action of standing surface liquid water, proof of a sea once having covered Meridiani Planum [213] (location marked as (5) on map in Figure 1.1 on the following page). Images from Mars Global Surveyor have identified recent gullies within the walls of high latitude impact craters [144], which even appear to have been modified between successive observations [145], suggesting that liquid water has flowed on the martian surface within the past decade.

Figure 1.1 displays a map of the martian globe, showing the landing sites of a number of probes and other sites of interest, discussed elsewhere in this thesis. Figure 1.2 shows the measured epithermal neutron flux indicating the distribution of soil water content [157].

1.1.2 Atmospheric loss

The persistence of liquid water on the primordial martian surface requires a higher atmospheric pressure and more effective greenhouse effect than at present; a warmer wetter Mars [195, 185,

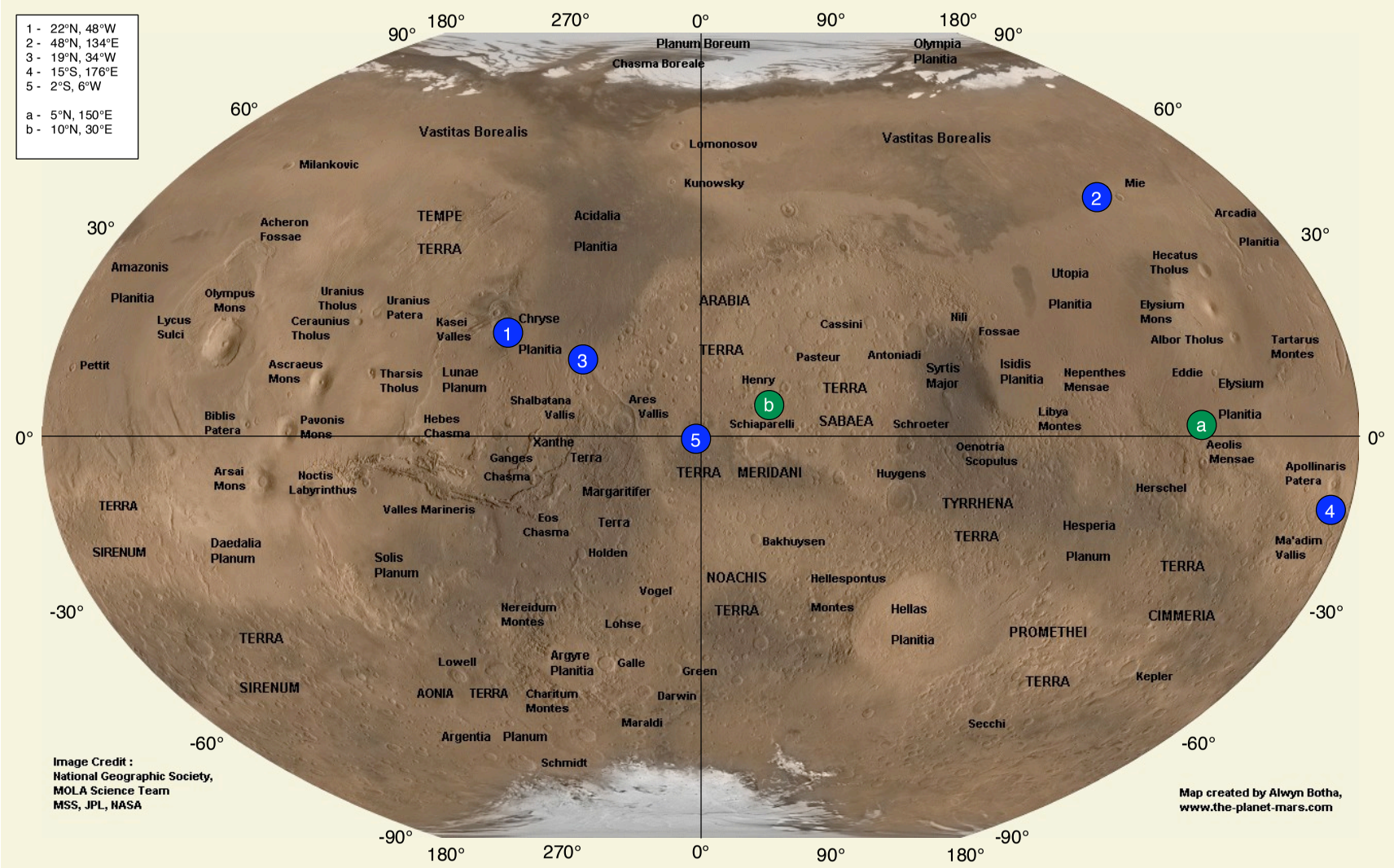

Figure 1.1: Map of the martian globe, annotated by the author with numbered blue labels to mark the landing sites of several probes and lettered green labels to indicate other locations of interest on the martian surface discussed within this thesis. (1) Viking 1; (2) Viking 2; (3) Pathfinder; (4) Spirit; (5) Opportunity. (a) "Frozen sea" at Elysium [162]; (b) Midlatitude location with presumed high ice content [157]

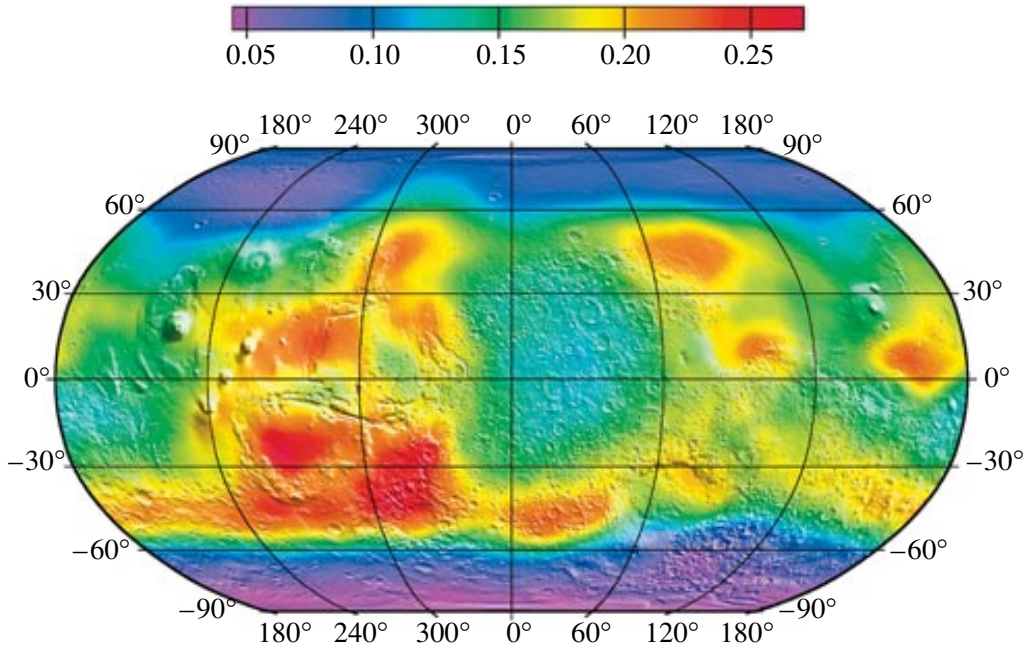

Figure 1.2: Distribution of backscattered epithermal neutron flux. Colour-coding indicates counts/sec from the High Energy Neutron Detector aboard Mars Odyssey (purple; low → red; high), where a decrease in epithermal neutron flux is interpreted as a high proportion of soil water content, seen to exist around the poles as well as certain mid-latitude regions [157].

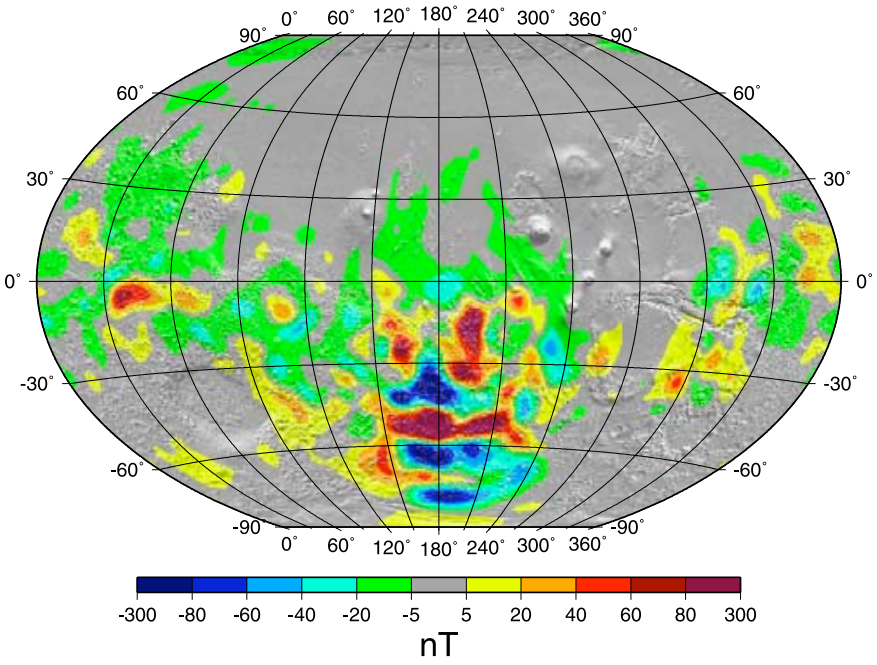

Figure 1.3: Map of the modelled radial components of the martian crustal magnetic anomalies at ∼370 km altitude [16], showing the most intense anomalies in the ancient southern highlands.

186]. The implication is that a thick primordial atmospheric column has since been eroded away through processes such as pick-up-ion sputtering, hydrodynamic removal, impact erosion and chemical reactions with the crust, as reviewed recently in Jakosky *et al.* 2001 [119]. The bias of heavy nitrogen over lighter isotopes in the crustal rock implies that over 90% of the primordial atmosphere could have escaped the planet by impact erosion and other causes, rather than having reacted with surface minerals to form carbonates, for example [92, 41].

1.1.3 Crustal Magnetic anomalies

The terrestrial geomagnetic field protects our atmosphere from sputtering by the solar wind, but Mars has no such global shielding. Crustal magnetic anomalies detected by Mars Global Surveyor indicate that Mars did once have a global dipole [1]. This is believed to have failed very early in the planet's history, around 4 billion years ago (Gya), and so would have exerted little influence on the evolution of the atmosphere [2]. The most intense anomalies exist in the Southern highlands, around Terra Sirenum and Cimmeria, and deflect the solar wind to create an asymmetric bow shock as the planet rotates [62] and generate auroral emissions [35]. Thousand-kilometer long east-west lineations apparently present in the anomalies of the southern highlands have been offered as evidence of primordial plate tectonics, analogously to sea-floor spreading zones on Earth [56]. Such claims have been questioned, however, due to the lack of evidence of pole reversals [103] or symmetry, as well as doubts that the anomalies are even linear [13]. Other crustal anomalies do record evidence of paleomagnetic pole reversals. The positions of the core field poles were estimated from the location and polarity of ten large isolated anomalies, and opposite polarity poles were found to cluster tightly together [14, 18, 17].

Numerous models of the crustal anomalies have been developed. Purucker *et al.* (2000) [189] describes an equivalent source model based on a uniformly distributed array of vertical dipoles; Arkani-Hamed has developed a 50-degree spherical harmonic model (SHM) [13], an improved 50-degree SHM [15], and a 62-degree SHM [16]; and Cain *et al.* 2003 [42] describes a 90-degree SHM.

1.1.4 Astrobiological potential

The elemental abundances of the martian regolith are similar to the Earth's crust, with concentrations of some of the biogenic elements actually being higher on Mars (such as calcium and phosphorus) [29]. Although nitrogen abundance is now low in the martian surface, this may not have been limiting in the primordial environment and there seems to be no elemental constraints on Mars developing life with the same "chemical code" as the terrestrial biosphere [29]. Similar to the primordial terrestrial situation, a significant amount of organic molecules, precursors to the biochemistry that developed on Earth, is expected to have been delivered by comet and meteorite fall onto a warmer wetter primordial Mars [87].

The combined presence of energy sources such as sunlight or geothermal heat flow, liquid water, and organic molecules early in the planet's history supports the possibility of a martian genesis of life. The subsequent collapse of the martian environment, with decreasing atmospheric pressure and increasing desiccation and UV irradiance, may have driven surface life to extinction, with chemoautotrophic psychrophiles retreating to deep groundwater or beneath ice

cover [201]. Of all the challenges facing modern Mars life, the lack of free water is probably the most restrictive, as other hazards, such as radiation, UV, and temperature are all tolerated by terrestrial organisms [47]. The extremes of survival exhibited by terrestrial organisms has been discussed within the context of the martian environment by Nealson (1997) [165] and reviewed more recently by Horneck (2000) [109].

Thin films of liquid water are present around grain boundaries in water ice down to -20°C, far below the bulk freezing point, and so microbial life may survive metabolically-active, at least periodically, in the martian polar regions [118]. Microbes may remain on the surface in cryptoendolith niches, communities contained within the more clement micro-environment and UV protection of rock fissures (analogous to those found in the Antarctic Dry Valleys, as described in Section 1.1.6) [54, 55], preserved in permafrost water ice [201], or active as chemosynthetic ecosystems in deep aquifers [39].

In addition to temperature and liquid water stability, another critical hazard for near-surface life today is ultra-violet radiation.

1.1.5 Ultra-violet radiation

Mars has a much higher surface solar ultra-violet (UV) flux than Earth due to lower total atmospheric pressure and lack of significant ozone layer or other UV absorbers [53]. Solar UV readily photolyses biomolecules such as amino acids and DNA, inhibits chlorophyll [219, 53], and rapidly deactivates unshielded cells [55] so that a bacterial cell lying exposed on the martian surface would be inactivated within minutes [200]. The similarity between current Mars fluxes and Archean Earth fluxes (DNA-weighted irradiances) suggests that UV flux may not itself be a limitation to the survival of life on the martian surface [55], and sufficiently-shielded phototrophic habitable zones may remain within shocked rocks [55] or beneath polar ice [57]. The combination of this irradiation with the very cold temperatures and lack of liquid water renders the martian surface extremely inhospitable, however.

Furthermore, the long-term UV flux is believed to have created an oxidising layer in the martian topsoil, hypothesised to explain the failure of the Viking landers (see Figure 1.1) to detect any organic material down to parts per billion levels [234], not even that expected from meteoritic in-fall [87]. UV penetrates only millimetres into regolith [55], but wind-mixing can distribute oxidants within the loose topsoil (estimated to be about a meter deep at Meridiani Planum [210]) and so present a serious biological hazard beyond the penetration of UV.

The combination of very low water availability, high UV flux, oxidation hazard and scarcity of organic molecules renders the martian top surface extremely inhospitable [47]. The depth of the oxidising layer is difficult to constrain but is probably not substantially greater than one meter [236]. The problem of oxidation can be minimised by searching at the bottom of a recent impact crater or boulders in the ejecta blanket, or the putative Cerberus pack-ice [162].

1.1.6 Terrestrial analogue site

The climate of Antarctica is very arid, and the continent contains the most extreme cold-desert regions on Earth [110]. The so-called Dry Valleys cover an area of roughly 5,000 km^2 in Southern

Victoria Land, at altitudes above 1000 m, and exhibit extensive areas of rock and soil completely devoid of snow or ice. Water delivery by precipitation is exceedingly low and falls solely as snow, with any exposed ice quickly subliming away into the desiccating katabatic (downslope) winds descending off the high Antarctic plateau. Air temperature ranges between -15°C and 0°C in the summer months, dropping down to -40°C in the winter, and transient summer meltwater is frequently the sole source of moisture. This environment is also exposed to enhanced levels of UVB radiation through the ozone hole that results from stratospheric ozone depletion each spring [81]. In many respects then, the Antarctic Dry Valleys are a meaningful analogue of the environmental conditions prevalent on modern Mars, and thus a valuable research site for microbial survival [110, 233].

No plant or animal life is visible within the Dry Valleys, and microbiological culturing studies have found some soils to be effectively sterile [110]. The principle habitable zone is within a narrow region under the surface of rocks, with both rock fissures and pore spaces colonised by cryptoendolithic microorganisms. The ecosystems are comprised of photosynthetic cyanobacteria and lichens as well as heterotrophic bacteria [93]. The endolithic niche provides several features to create a more clement internal microenvironment, including trapping of moisture and warmth, and filtering out harmful UV wavelengths whilst transmitting photosynthetically active radiation [93, 53].

The work reported here involves culturing novel bacterial isolates from surface samples of the Miers Valley and assessing their survival characteristics, as explained in more detail in Section 4.2 on page 83.

1.1.7 Deep life

A great amount of water is believed to remain on Mars, probably soaked down into the sponge-like regolith, thought to be highly porous and brecciated to an appreciable depth from the heavy bombardment [212, 50]. On Mars, the depth necessary for the ambient temperature to rise high enough for liquid water is calculated to be around 3.7 km at the equator, increasing to 6–7 km in mid-latitudes, but these estimates are dependent on estimated parameters such as the geothermal gradient and freezing point depression from salt concentration [107]. There exists the possibility, therefore, that chemosynthetic martian life remains alive to this day far underground, where the internal heat of the planet melts the underside of the permafrost shell into a liquid water aquifer [39], and has been proposed as the source of the recently-detected atmospheric methane [90, 137]. Such a habitat would be analogous to the deep hot biosphere known on Earth, with bacteria discovered within a bore hole at 5.3 km depth in the crust [217]. Life may also survive in small refugial habitats nearer the surface around local geothermal hotspots, such as the Tharsis or Elysium volcanic regions [39].

However, gaining access to such a deep environment on Mars is technologically challenging. One proposed technique is an electrically heated probe that penetrates by melting through rock [146], whereas drilling a 5–10 km bore-hole on Mars would require substantial drilling equipment, and almost certainly human supervision [51]. The maximum depth obtainable by near-future robotic probes will be on the order of only meters. ESA's ExoMars rover, currently planned for launch in 2013, has been designed with a 2 m drill bit [222].

In this accessible region any microbes will likely be dormant, cryopreserved by the current freezing conditions, and so metabolically inactive and unable to repair cellular degradation as

it occurs. Thus the primary environmental hazard to cells and remnant biological molecules protected from UV or oxidation is the accumulation of radiation damage from exogenous ionising particles, described in the next section. Unlike Earth, the current martian surface is unprotected from cosmic particle radiation by a global dipole magnetic field or sufficient atmospheric shielding.

1.2 Cosmic Ionising Radiation

The cosmic rays of the space radiation environment beyond low Earth orbit, such as that incident on Mars, are dominated by galactic cosmic rays and solar particle events [216, 75, 164, provide good reviews]. Solar particle events, such as flares and coronal mass ejections, accelerate protons up to energies of typically around several hundred MeV. The flux of these solar energetic protons (SEP) is thus sporadic in nature, and dependent on the 11-year solar activity cycle, one half of the 22-year Hale cycle and due to the periodic reversal of the sun's magnetic field [172]. The peak flux of galactic cosmic ray (GCR) particles, at around 500 MeV/nucleon, is about four orders of magnitude lower than SEP but the power law tail of the spectra extends up to 10^{20} eV at extremely low fluxes. The GCR spectrum is composed of 85% protons, 14% alpha (helium nuclei), and a small fraction of heavy ions (fully ionised atomic nuclei) and electrons, and is thought to be mainly accelerated by Type II supernovae. GCR below about 1 GeV/nucleon are modulated by the heliosphere [133] so their flux is anticorrelated with the solar activity cycle. Localised shorter-term decreases in the GCR flux, called Forbush decreases, occur when plasma clouds emitted by the sun during coronal mass ejections shield the lower energy cosmic rays [172].

The dipolar terrestrial magnetic field also influences the flux of cosmic rays, with charged particles deflected and denied access to particular latitudes if their magnetic rigidity, the ratio of particle momentum to charge, is less than the necessary cut-off rigidity [216]. Mars no longer possesses a global dipolar magnetic field, and the influence of the crustal anomalies (described in Section 1.1.3 on page 19) on the cosmic radiation is addressed in this research.

Figure 1.4 plots the GCR primaries energy spectra for hydrogen to iron ions under solar minimum conditions, and solar maximum for hydrogen and helium, 10 MeV/nuc – 1 TeV/nuc as given by the CREME-96 model (see Section 3.5.1 on page 69 for further details). The four energy sections used in this research when simulating the GCR spectra are also shown. The annual mean SEP flux at martian orbit provided by SPENVIS (see Section 3.5.1) for 10 MeV – 200 MeV is shown in blue. Solar particle events produce a harder spectrum than this mean shown, with an enhancement in flux at energies up to several GeV, but these are short-lived and rare.

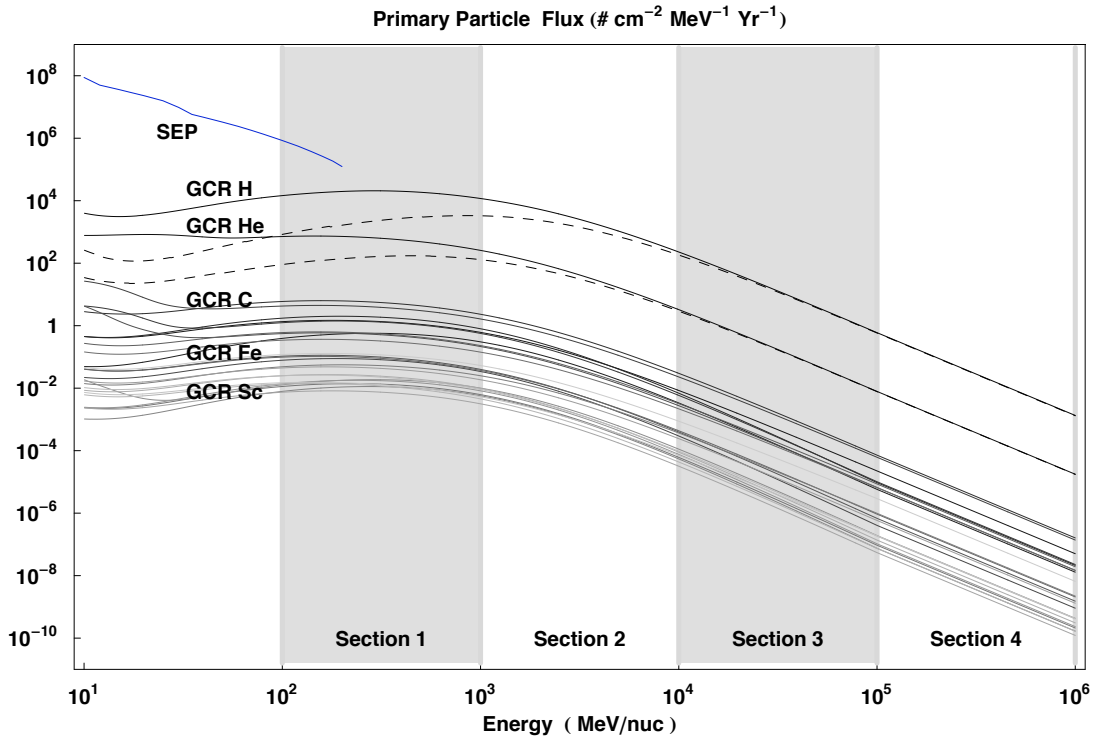

Figure 1.4: Primary energy spectra for GCR ions (H – Fe) at solar minimum (solid lines) and also solar maximum (dashed lines) for H and He, provided by CREME-96 model (see Section 3.5.1 on page 69 for further details). The annual mean SEP flux at martian orbit provided by SPENVIS is displayed in blue. The four energy sections used in this research when simulating the GCR spectra are also shown.

Thus, SEP and GCR primaries represent two complementary populations of ionising particles; high flux but relatively low energy and much lower flux but extending up to very high energy levels, respectively.

The energetic GCR produce extensive showers of secondary particles in the terrestrial atmospheric column, as shown in Figure 1.5. When a GCR strikes an atmospheric nucleus energetic secondary mesons (pions and kaons), gammas, nucleons and nuclear fragments are produced, which then decay or interact with other nuclei. Secondary mesons decay over a short time-scale to produce muons, gamma rays and electrons. Thus the air shower is composed of a central "hard component" core of nuclear fragments within a spreading "soft component" cone of the electromagnetic cascade [75]. The flux of secondaries builds with increasing shielding depth until the Pfotzer maximum, after which the average particle energy is below the threshold for new particle production and the cascade steadily decays. On Earth, this Pfotzer maximum occurs at an altitude of around 15 km; roughly the cruising altitude of Concorde.

In radiological research, the amount of shielding is often given in units of column density, g/cm^2, representing the total integrated mass of shielding in front of a unit area (which can be simply converted into units of true distance by dividing by mean density). Beneath the ~1,000 g/cm^2 terrestrial atmospheric shielding depth GCR produce a dose rate of around 0.3-1 mGy/year at sea level [33]. With an atmospheric shielding depth of only 16 g/cm^2 [205], similarly-structured cascades will occur in the top meters of the martian regolith.

High velocity charged particles, other than electrons, lose energy in matter primarily through ionisation and atomic excitation. The mean rate of energy loss (commonly taking units of MeV

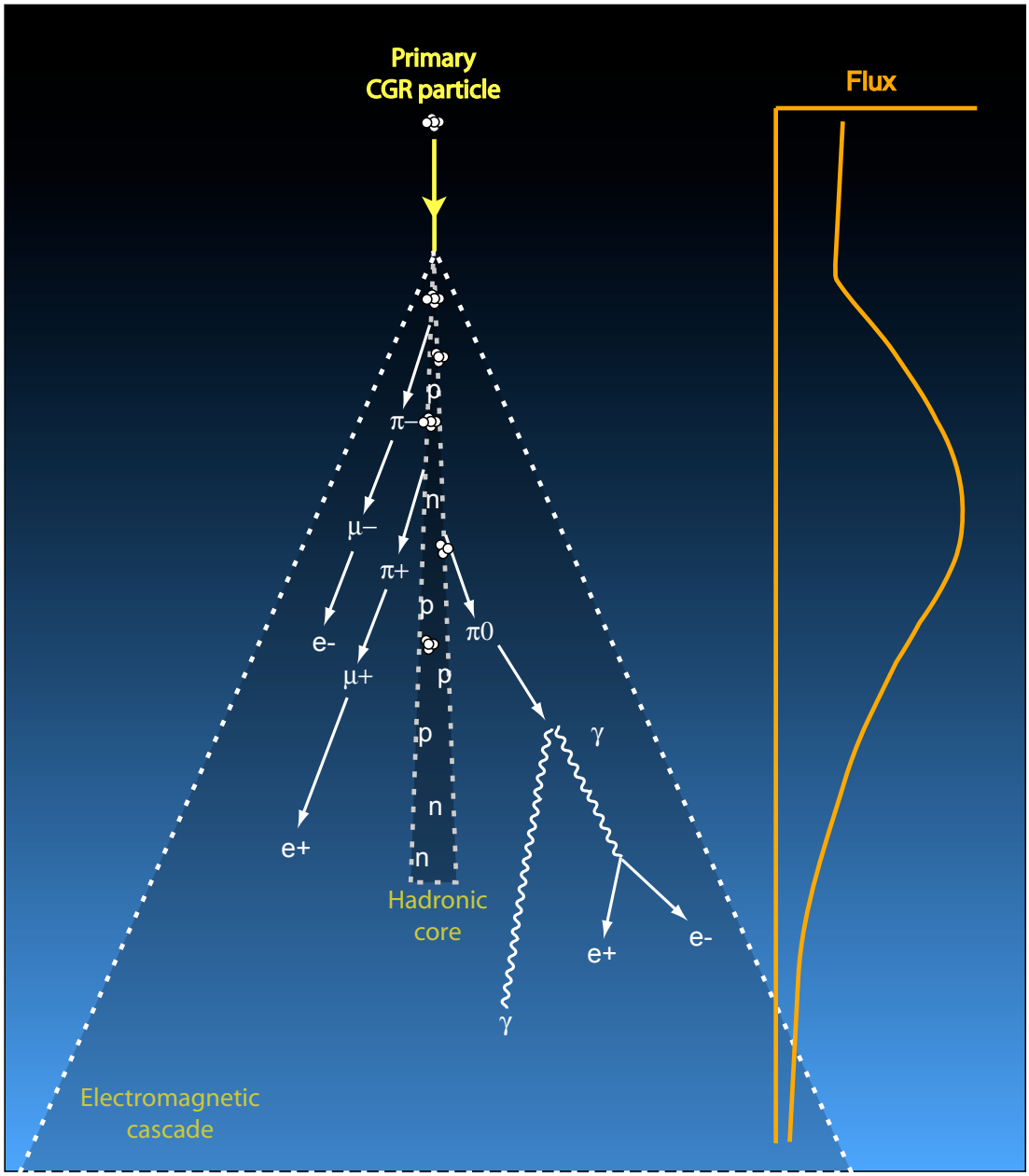

Figure 1.5: Air shower: schematic representation of the cascade of secondary particles generated in the terrestrial atmosphere by an energetic GCR primary. Shown are the central hadronic core and spreading cone of electromagnetic radiation, as well as the particle flux building to the Pfotzer maximum before absorption dominates. Diagram produced by the author.

$g^{-1}cm^2$ or keV μm^{-1}), referred to as the particle's stopping power, S, is given by the Blethe-Bloch equation. In its full form the Blethe-Bloch equation contains many terms including the mean atomic number and mass of the shielding material, the mean excitation energy and the maximum kinetic energy which can be imparted to a free electron, as well as relativistic corrections if necessary [76]. The major determinants of a HZE particle's energy loss, however, are its charge and velocity [133]:

$$S = \frac{dE}{dx} \alpha \frac{Z^2}{\beta^2} \tag{1.1}$$

where Z is the atomic number of the projectile nucleus (which corresponds to the total charge for a fully-ionised GCR HZE particle) and β is the ratio of the particle velocity to the speed of light, v/c [133]. Thus, the stopping power of a cosmic ray HZE increases non-linearly with charge; a GCR iron ion (Z=26) loses energy to the target material 676 times more rapidly than a proton, and consequently cannot penetrate shielding as far. The rate of energy loss is also much greater for slower ions, and this is observed as a sharp increase in ionisation at the end of a particle track [121].

No ionising radiation detector has yet been landed on the martian surface, although the martian radiation environment experiment (MARIE) aboard Mars Odyssey was designed to detect both GCR and SEP particles in martian orbit [235]. Radiation detectors may fly on up-coming lander missions: the Radiation Assessment Detector has been proposed for NASA's Mars Science Laboratory (scheduled launch 2009) [104] and the GEORAD package for ESA's ExoMars (scheduled launch 2013) to detect solar proton and neutron backscatter flux (an indirect measure of GCR) [10]. Until these return observational data, computer modelling will be crucial in determining the martian radiation environment both on the ground and beneath.

1.3 Radiobiology

The ionising radiation field produced by SEP and GCR is harmful to life [166] through both direct and indirect mechanisms. Direct damage occurs when deposited energy excites electrons within biomolecules, leading to ionisation or radiolysis. However, radiation primarily interacts with water as it comprises 40–70% of cells and 20% of bacterial spores. This causes radiolysis and the production of hydrated free electrons, e^-_{aq}, and highly-reactive species with unpaired electrons, free radicals, such as $H^{\cdot}$ and $^{\cdot}OH$, or their recombination products such as hydrogen peroxide [129]. Figure 1.6 summarises the major reaction pathways of water molecules either lysed or ionised by radiation [33].

Biopolymers, such as DNA, RNA, or proteins, can therefore be damaged not only by direct energy absorption, but also the indirect effect of radiochemistry and free radical diffusion [33]. Cell death from irradiation is believed to be primarily due to DNA damage, and under gamma irradiation, roughly 80% of DNA damage is caused indirectly by irradiation-induced diffusible reactive oxygen species [95]. Of these direct radiation hits, 61% of the ionisations take place in the deoxyribose phosphate backbone, with the remaining 39% distributed among the four nucleotide bases [188]. The degree of hydration of living systems (i.e. metabolically active cells comapred to desiccated bacterial spores) plays an important role in the extent of damage from

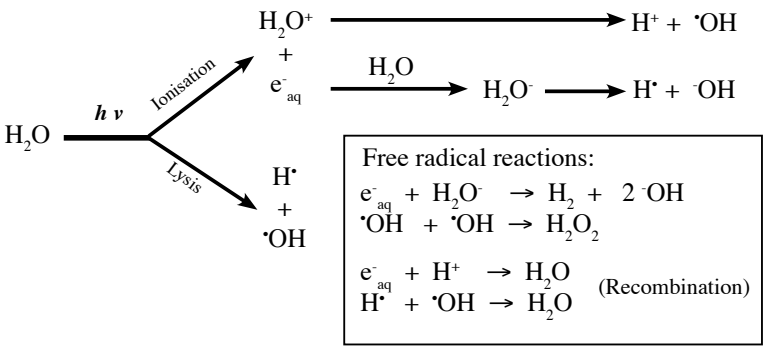

Figure 1.6: The major reaction pathways of water molecules lysed or ionised by radiation, showing generation of hydrated electrons, free radicals, and recombination products such as hydrogen peroxide. These diffusible species constitute the indirect mechanism of radiation damage. Diagram produced by the author, collating information contained within Baumstart-Khan and Facius (2001) [33].

indirect effects. Low temperatures can increase resistance against ionising radiation due to the reduced diffusion of radicals [33].

The amount of energy deposited by ionising radiation in the target material per unit mass is termed the dose, measured in J/kg, or Grays (Gy). Different ionising radiation particles are not equally hazardous to cells. Gamma radiation is weakly ionising, and on scales larger than micrometres the energy of a given dose is deposited uniformly throughout the target. The protons and high-charge/high-energy (HZE) ions of the hadronic cascade, however, are highly ionising, and HZE particles lose over 90% of their energy to ionisation of the target material in a dense track [136]. Such a pattern of dose deposition is measured as a high value of linear energy transfer (LET), defined as the energy deposited per unit track length, taking units keV/μm [124]. HZE flux is therefore particularly damaging to cellular macromolecules and can cause clusters of nearby breaks and double-strand breaks in DNA strands and are therefore particularly detrimental to cellular survival [112, 128]. The original formulation of physical absorbed dose does not take into account the dependence of biological effect on the distribution of energy deposition, and various methodologies have arisen to describe the enhanced deleterious effect of HZE particles. This study uses weighting by the relative biological effectiveness (RBE), defined as the dose of a reference radiation (usually gamma or X-rays) required to produce the same biological effect as a dose of the test radiation [122].

Bacteria such as *Escherichia coli* are rapidly inactivated by less than a hundred Gy of gamma radiation. The mesophilic, non-sporulating, gram-negative bacterium *Deinococcus radiodurans* is the most radioresistant species known, and gamma-irradiated populations can survive 5 kGy without measurable loss of viability despite massive DNA fragmentation [61], and 1% survival is still found after 10 kGy. A gamma ray dose of 6 kGy induces approximately 200 DNA double strand breaks, over 3,000 single strand breaks, and greater than 1,000 sites of base damage per *D. radiodurans* genome [30]. This remarkable resilience is believed to be mainly due to more efficient enzymatic DNA repair and recovery mechanisms [32].

A passive resistance to radiation is exhibited by the spores of the soil bacterium *Bacillus subtilis*. During environmental stress bacilli produce dormant desiccated spores [167]. These show no detectable metabolism, but the DNA is stabilised by attached proteins, and the entire spore encased in a thick envelope, giving excellent protection against desiccation, oxidising agents

and ionising radiation [203, 167]. The survival curves of such spores under assault of UV, HZE, vacuum, and even exposure to the environment of outer space have been tested [226, 108].

A further source of ionising radiation on planetary surfaces is endogenous, produced by radionuclide isotopes in rocks or mineral grains. On Earth, the major natural decay series are those of thorium (Th-232), neptunium (Np-237), and uranium-radium (U-238) and uranium-actinium (U-235) [33]. The most intense natural radiation environment on the surface of Earth is reported to be that of the monazite sand beaches in Brazil (due to their high thorium and uranium content), with a local dose rate of 400 mGy/year. Since no naturally-occurring environment produces exposures even approaching the resistance levels of organisms such as *D. radiodurans* the evolution of such extreme radiation resistance is hard to explain, except as a consequence of adaptation to tolerate desiccation-induced double strand breaks [61]. An alternative hypothesis has been proposed by Pavlov *et al.* (2006) [182], who use this observation to argue that such radioresistant life evolved on Mars and was subsequently transferred to Earth by way of martian meteorites.

1.4 Modelling approaches

Existing models that treat the propagation of energetic particle radiation through shielding material operate either by numerical solution of the Boltzmann transport equation or explicit simulation of particle interactions using a Monte Carlo (MC) code.

1.4.1 Boltzmann equation

The time independent Boltzmann equation treats particle transport as a conservation equation in phase space of three positional coordinates in Euclidean space, particle kinetic energy and direction of motion [231]. In essence, the Boltzmann transport equation treats a small volume of shielding material with particle radiation passing through it, termed a flux tube. For each j particle of interest it is calculated how many are lost within the flux tube, through absorption or particle interaction that replaces particle j with particle *k,* for example, and how many are created within the flux tube, for example by generation of j from k by particle interaction. Thus, the flux of particle j out of the end of the flux tube can be calculated from the flux of particle j into the flux tube, and knowledge of the probabilities of various particle interactions occurring in-between. This is repeated for all particles of interest and the complete thickness of the shielding mass. The Boltzmann transport equation can be summarised in a word equation as:

$$\begin{array}{c}\text{Flux of}\\ \text{particle } j \text{ out}\\ \text{of tube}\end{array} = \begin{array}{c}\text{Flux of}\\ \text{particle } j \text{ in}\\ \text{to tube}\end{array} + \begin{array}{c}\text{Summation of}\\ \text{all processes}\\ \text{creating}\\ \text{particle } j\end{array} - \begin{array}{c}\text{Summation of}\\ \text{all processes}\\ \text{removing}\\ \text{particle } j\end{array}$$

A spherical region of space is considered, centered at position vector $\vec{x}$ and with radius δ, and filled with matter described by the appropriate cross-sections for the atomic and nuclear interactions that modify the incoming particle flux. As illustrated in Figure 1.7 below, the number of particles of type j leaving the sphere through the surface element $\delta^2 d\vec{\Omega}$ is given as $\phi_j(\vec{x} + \delta\vec{\Omega}, \vec{\Omega}, E)\delta^2 d\vec{\Omega}$, where $\phi_j(\vec{x}, \vec{\Omega}, E)$ is the particle flux density.

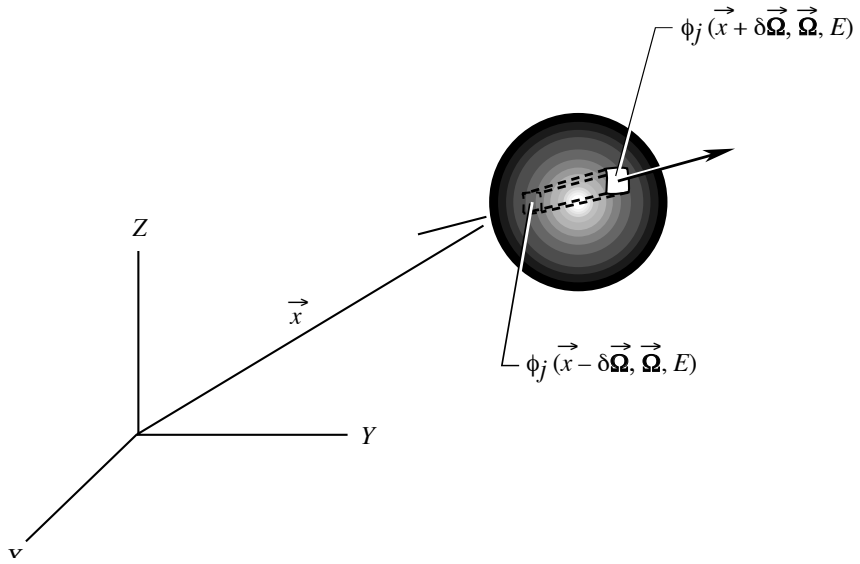

Figure 1.7: Particle transport through a flux tube linking opposite surface elements on a sphere of radius δ in Euclidean space.

The number of particles leaving the sphere would equal the number entering through the opposite surface element, $\phi_j(\vec{x}-\delta\vec{\Omega},\vec{\Omega},E)\delta^2 d\vec{\Omega}$, if this flux tube through the center of the sphere were in vacuum and no particle interactions or decay occurred. The propagating particles interact with matter, however, and both gain and loss processes act to modify the number of particles of type j exiting the sphere of interest. More particles of type j are produced by nuclear interactions of particles of other types, and particles of type j are removed by atomic and nuclear interactions. Thus, the number of particles of type j leaving the sphere is calculated by the number entering, plus those created and minus those removed by physical interactions within the sphere, as follows:

$$\begin{aligned}\phi_j(\vec{x}+\delta\vec{\Omega},\vec{\Omega},E)\delta^2 d\vec{\Omega} &= \phi_j(\vec{x}-\delta\vec{\Omega},\vec{\Omega},E)\delta^2 d\vec{\Omega} \\ &+ \delta^2 d\vec{\Omega}\int_{-\delta}^{\delta} dl \sum_k \int \sigma_{jk}(\vec{\Omega},\vec{\Omega}',E,E')\phi_k(\vec{x}+l\vec{\Omega},\vec{\Omega}',E)d\vec{\Omega}'dE' \\ &- \delta^2 d\vec{\Omega}\int_{-\delta}^{\delta} dl\sigma_j(E)\phi_j(\vec{x}+l\vec{\Omega},\vec{\Omega},E)\end{aligned}$$

where $\sigma_j(E)$ and $\sigma_{jk}(\vec{\Omega},\vec{\Omega}',E,E')$ are the macroscopic interaction cross sections for the material comprising the sphere. The latter term represents all processes whereby particles of type k moving in direction $\vec{\Omega}'$ with energy E' collide at $\vec{x}$ and undergo a nuclear reaction to produce a particle of type j moving in direction $\vec{\Omega}$ with energy E , and so is an inclusive cross section. The second term on the right hand side of this balance equation gives the source of secondary particles integrated over $2\delta(\delta^2 d\vec{\Omega})$, i.e. the total volume of the flux tube inside the sphere, and the third term gives the j particle losses due to nuclear reactions throughout the same volume. On a macroscopic scale, propagating ions lose energy continuously through Coulombic interactions with electrons in the target material and so the above equation can be simplified with a continuous slowing-down approximation. Other convenient simplifications,

including neglecting angular dependence of secondary creation and treating the forward-peaked distribution of nuclear fragments as a strict straight-ahead approximation, and neglecting the production of certain secondaries (namely mesons), allow the Boltzmann transport equation to be solved efficiently with numerical integration algorithms. The Boltzmann transport method most widely used by the space community is the HZETRN computer code, developed by NASA Langley Research Center [231].

1.4.2 Monte Carlo

Monte Carlo (MC) simulation is a fundamentally different approach to modelling particle propagation from the analytical or numerical solution of Boltzmann transport equations. An MC algorithm simulates the nondeterministic process of particle propagation by individually treating every particle; following its trajectory through matter in discrete steps and performing physical processes upon it in a probabilistic manner, dependent on interaction cross-sections. A particle in the cascade is followed and physical interactions applied until it eventually disappears by escaping the geometric boundaries of the system, comes to rest due to energy losses from ionization and excitation of atomic electrons or otherwise ceases to propagate due to absorption, or, in the case of pions and muons, decays. The probabilities of different physical interactions occurring within each step (themselves functions of incident particle type and energy and target particle type), the particle interaction cross-sections, can be taken from the same experimental databases as those used to determine the relevant gain and loss parameters in the Boltzmann equation approach.

Owing to the huge number of repeated calculations that must be performed for every primary particle, and all secondaries created in the resultant cascade, MC simulations are computationally expensive. They are, however, able to reproduce many features of the radiation environment created by GCR more faithfully than Boltzmann transport codes, such as 3D particle scattering, even with approximate two-dimensional treatments applied to the standard straight-ahead approximation (e.g., [159]). For example, the analytic code HZETRN shows good performance, but is not capable of providing the complete information of the emerging secondaries, which are required for precise analysis of radiation dose effects [139]. MC codes are, however, also limited in their accuracy by uncertainties in nuclear reaction cross-sections and secondary production, especially at high energy.

MC codes have been available for decades now, steadily improving their representation of interaction processes, particle types and applicable energy ranges [139]. Two commonly-used codes are HETC (High-Energy Transport Code) [220] and the Fortran-based FLUKA (FLUctuating KAscade) [11].

The physics modelling package selected for this research is Geant4 (GEometry ANd Tracking) [4, 5], as the toolkit has now been ported into C++ from the earlier Fortran-based code GEANT3, is widely-used by the high energy physics and space communities, and is very well supported by the user community (http://geant4-hn.slac.stanford.edu:5090/Geant4-HyperNews/index). The Geant4 code has been well-validated against experimentally-derived data for both its hadronic processing [34] and electromagnetic physics modelling [8], as is summarised in Amako *et al.* (2006) [7]. This particle physics toolkit has been employed in several general-purpose space radiation applications, including: MULASSIS (MUlti-LAyered Shielding SImulation Software) [139, 197], which is also integrated into the popular web-based

European Space Agency particle spectra database SPENVIS; GRAS (Geant4 Radiation Analysis for Space) [198]; MarsGRAM [126, 127]; ATMOCOSMICS [72] and MAGNETOCOSMICS (http://reat.space.qinetiq.com/ septimess/magcos) and their development into PLANETOCOSMICS [71]. PLANETOCOSMICS is able to model both hadronic and electromagnetic interactions of cosmic rays in the atmosphere and surface of Earth, Mars and Mercury, as well as propagation through planetary magnetic fields, and is freely available for download (http://cosray.unibe.ch/~laurent/_planetocosmics).

A discussion on how the model developed here represents an important improvement upon this previous work is provided in Section 1.5.1.

1.5 Previous modelling work

Molina-Cuberos *et al.* (2001) [159] have used a transport code solving the Boltzmann equation in the one-dimensional "straight ahead" approximation to model the propagation of GCR protons, neutrons, and muons through both the ancient and current martian atmospheric column. Spectral data is only presented for the surface flux, but the model finds that the thin current atmosphere does not significantly shield the surface, with most of the energy transferred to the ground by protons and neutrons.

Simonsen and Nealy (1991) [207] also employ a one-dimensional Boltzmann code to model the propagation of SEP and GCR particles through the atmosphere as well as the martian regolith. The objective was to calculate radiation levels for long-duration astronauts in a surface habitat protected by regolith-derived shielding. Consequently, human skin doses were calculated, not microbial survival, and only for regolith depths of up to around 80 g/cm^2. A similar study by the same group [206] has been used to calculate cosmic radiation doses and hence microbial survival within small bodies such as asteroids and comets [48]. This study by Clark *et al.* (1999) [48] calculates inactivation of bacteria inside an asteroid within 7.5 million years at 1 m depth and only 1.5 million years at 10 cm depth. Other reports describe investigations into the use of martian regolith for radiation shielding for human missions [130, 69].

Saganti *et al.* (2004) [196] performed a more in-depth analysis with respect to doses experienced by astronauts on the martian surface using the HZETRN code to solve the one-dimensional Boltzmann equation. Landscape elevation imposes variation on the attenuating thickness of atmosphere, and maps of proton and heavy ion flux, as well as skin dose equivalent, were drawn for the martian globe. De Angelis *et al.* (2004) [12] report the release of the Mars Radiation Environment Model. This model represents an advance upon the aforementioned study [196] by the inclusion of volatiles, such as water ice, in the martian subsurface when mapping the effect of topology on the martian radiation environment, but again only producing results for the surface.

Smith *et al.* (2004) [208] report on a Monte Carlo study on the influence of the atmosphere of terrestrial planets on the transmission of energetic photon radiation (X-rays and gamma-rays), produced by parent star flares, supernovae, or gamma-ray bursters. They found that thick atmospheres ($\geq$100 g/cm^2) effectively block X-rays and even gamma-rays, but nearly all of the incident energy is reprocessed into diffuse UV emission, including in the biologically-effective wavelength range.

Pavlov *et al.* (2002) [181] address the question of the martian subsurface radiation dose in the interests of astrobiology, simulating cosmic ray propagation with their own Boltzmann transport code. This study modelled the SEP and GCR flux through the current martian atmosphere and regolith, as well as the endogenous radiation input from rock radionuclide decay. The biologically-weighted dose rate was found to peak at 0.2 Gy/year at a depth of 25 g/cm^2, before decreasingly gradually to a level of 5×10^{-4} Gy/year at a depth of around 700 g/cm^2. They report that at no point does the flux exceed that which can be survived by metabolically active radioresistant terrestrial bacteria such as *D. radiodurans*. Spores, such as *B. subtilis*, or cells forced into dormancy by liquid water limitation, however, are sterilised over 30 thousand years in the top 20 g/cm^2 of soil, mostly by SEP, within 2 million years at depths down to 700 g/cm^2 by GCR, and around 40 million years at the deepest layers where background radiation becomes dominant. Furthermore, any complex organic biosignature is obliterated within 25 million years in the top 200 g/cm^2 of regolith. However, slow neutron transport below 10 MeV was not modelled, secondary pions, electrons and gammas were not included, and the HZE contribution was modelled only as helium, oxygen and iron nuclei. Overall, Pavlov *et al.* (2002) state an estimated accuracy to within 30%.

Also relevant is the work of Mileikowsky *et al.* (2000) [154], who tested the plausibility of the theory of panspermia, the transfer of life between planets within meteorites. They employed the HZETRN code to calculate the long-term accumultion of radiation doses from GCR within different depths of martian regolith and estimated survival time of populations of *B. subtilis* spores and *D. radiodurans* cells. They report a dose rate of 19.4 cGy/year with 0 g/cm^2 shielding thickness, building to a maximum of 24.9 cGy/year with 30 g/cm^2 shielding, and a million-fold death rate of *D. radiodurans* after 1.1 million years at this dose rate. Although this model was designed for small meteorites in interplanetary space, and so does not include the martian atmosphere or hemi-spherical shielding of the surface flux by the planet, their results [154] have been used as input data for radiobiological studies on the martian subsurface, such as by Kminek and Bada (2006) [135].

1.5.1 Improvements of this model

The radiation model developed here advances upon the above studies, and the space radiation models listed in Section 1.4, in a number of significant features. It is the only model to be designed specifically for addressing features of astrobiological interest of the martian radiation environment, not only upon the surface but also to 20 m depth of the subsurface. The model was designed from the outset to be rapidly reconfigurable, allowing simple modification of the subsurface characteristics and atmospheric profile properties. The physics models used here (developed in ATMOCOSMICS [72]) allow full treatment of all secondaries generated, including mesons and slow neutrons, in a complete three-dimensional simulation environment and including the crucial back-scattering component of surface flux.

Specifically, the research reported here is the first detailed description of the radiation environment of the martian subsurface, in terms of both particle energy spectra and biologically-relevant doses as a function of depth underground, the first treatment of variations in the subsurface composition, with the water component being the most crucial, and the first detailed assessment of the effect of changing atmospheric depth over geological time. Furthermore, this modelling approach has also been applied to the optically stimulated luminescence technique

for dating martian sediments as well as the persistence times of organic molecules and other biomarkers.

1.6 Optically Stimulated Luminescence dating

Another important application for modelling the martian radiation environment is in calculating the rate of dose accumulation by the rock itself. Optically Stimulated Luminescence (OSL) dating is a technique able to provide accurate, and absolute, measurements of the period since sediments were last exposed to sunlight (i.e. their time of deposition) [73]. The energy deposited by ionising radiation in suitable minerals, such as quartz and feldspar, creates free electrons trapped within the crystal lattice. Subsequently stimulating the exposed samples with light releases the stored energy as luminescence, a signal that is proportional to the radiation dose absorbed since burial [73]. Thus certain minerals act as a natural dosimeter, and the accumulated dose can be read by an instrument suitable for inclusion in a martian lander [151]. The absolute age of the sediment is given as the ratio of total absorbed radiation dose, Gy, to the local dose accumulation rate, Gy/year. Using this to date formation of a sediment layer assumes that the grains had been sufficiently exposed to light, thus resetting the dosimetry "clock", at the time of deposition; an assumption likely to be true for the aeolian-dominated deposition and high UV-flux of modern Mars [152].

Using the luminescence signal to accurately date the sediment requires knowledge of both the dose accumulation rate in the local environment and the OSL properties of the mineral. The significant exclusion of SEP and GCR from the Earth's surface by the geomagnetic field and dense terrestrial atmosphere means that the major source of ionising radiation is from decay of radionuclides in the surrounding rock itself. On the martian surface, however, ionisation from SEP and GCR cascades will dominate, and calculating the dose accumulation rate as a function of depth, under different scenarios, and its variability over time, is vital in calibrating this potentially crucial dating technique [73].

1.7 Analysis of environmental microbial diversity

It has been known for some time that there is a great disparity in the enumeration of microbial abundance in environmental samples between direct methods (such as microscopic counting studies) and indirect methods relying on cultivation of organisms and subsequent counting of colony forming units (CFU). It has been estimated that only 0.0001 - 15% of bacteria observable in nature can be cultivated *in vitro* using standard techniques; a phenomenon that has come to be known as the "great plate count anomaly" [9]. Reasons for this silent majority include known species that have entered a non-culturable state and unknown species that have never before been cultivated due to the lack of appropriate methods.

Advances in molecular techniques through the 1980s allowed microbial communities to be examined without the prior requirement of culturing [179, 111]. The bacterial 16S small subunit (SSU) ribosomal RNA (rRNA) molecule is a key element of the protein-synthesising machinery and so is functionally homologous and highly conserved between distantly-related organisms. It has a length of around 1,500 nucleotides and so the rRNA molecule, or its gene, contains

sufficient information for reliable phylogenetic analysis after cloning and sequencing of the gene from whole DNA extracts [173].

The first comprehensive phylogenetic study of life on Earth was made using 16S rRNA sequences, and discovered that the prokaryotes are in fact composed of two phylogenetically distinct groups of organisms, the eubacteria and the archaebacteria [91]. Without the limitations of culture-based methods, such molecular phylogenetic surveys have discovered a great diversity of new microbial groups, many of which are widespread and abundant in the environment. Sequencing of 16S rRNA has thus added greatly to our understanding of the extent of extant microbial diversity [68, provides a good review]. More recently, this molecular technique has been used for bacterial detection and identification in a clinical or pathogen diagnostic setting [180] or in assaying the bacterial contamination of spacecraft assembly clean rooms [158].

Although the extraction and analysis of SSU rDNA sequences allows for the phylogenetic reconstruction of environmental microorganisms to be performed without the need for cultivation, this approach is not necessary for the present work. Radiation survival work must necessarily be performed on culturable species, and so molecular phylogeny of rRNA genes will be used in this study for the identification of pure isolates from Antarctica. After extraction and amplification of rDNA sequences from bacterial colonies, the genes are sequenced and then matched against those already stored on a sequence database, using the BLAST (NCBI) tool, for example, to find the closest relative.

1.8 Aims of this research

This project is directed towards the greater understanding of the martian cosmic radiation environment, both on the surface and in the near-subsurface, and the potential biological effects of this ionising radiation field. Cosmic rays are one of the most severe hazards in the martian near-subsurface to the survival of native martian organisms, or persistence of signatures of their prior existence, and it is exactly this top few meters of soil that the forth-coming lander probes will be able to access with drills.

The first aim of this research is to construct a sophisticated Monte Carlo model of the cosmic ionising radiation environment in the martian subsurface. This model will represent an improvement on previous studies, which have on the whole employed Boltzmann transport codes and been focussed on the question of the radiobiological risk posed to human astronauts on the surface rather than survival of microbial life. The model will be designed to allow simple adjustment of important parameters, characteristics of the atmosphere (such as temporal variations in density) and composition of the subsurface (such as density and crucially also the water content, due to its significant effect on the neutron spectrum). The model will also be reconfigured to produce different data sets, from the particle energy spectra and fluence at different depths, to the biologically-weighted dose experienced by subsurface microbes, to the physically-absorbed dose deposited in the rock more appropriate to assessing persistence of organic biosignatures and calibration of optically stimulated luminescence dating.

The second major thread of this research is experimental. Cultivation studies will be performed on soil samples from the Antarctic Dry Valleys to determine diversity of native bacterial species. Once isolated, these novel isolates will be subjected to 16S ribosomal DNA extraction and sequencing in order to identify their closest relative and thus classify the isolates within genera,

or possibly even species. Once cultured, several strains will be selected for experimental irradiations, using a cobalt-60 gamma-ray source, under conditions approximating that of the martian near-subsurface in order to assess probable survival times in the cosmic radiation field.

The research conducted here thus represents an integrated programme of both theoretical modelling and experimental laboratory work into the persistence of microbial life in the martian radiation field. The model will for the first time accurately determine many aspects of the ionising particle flux, under different environmental parameters, and provide information for the design and execution of realistic experimental irradiations.

1.9 Thesis outline

The nature of this research programme is inherently multi-disciplinary. Computer modelling is employed to characterise the martian subsurface ionising radiation environment, in terms of microbial survival, persistence of organic biosignatures and calibration of optically stimulated luminescence dating, and experimental work is conducted to assess microbial diversity in the Antarctic Dry Valleys and determine radiation resistance of several of these novel isolates under martian surface temperatures. The chapters of this thesis present the development and results from this research.

The following chapter describes the operation of the high energy particle physics package used in this research, Geant4. Geant4 provides only a framework for building radiation models, and the required programme structure and mandatory user-defined classes must be understood. Chapter 3 progresses from this introduction, and describes the details of the Geant4 model developed here to calculate the martian ionising radiation environment, including the high energy particle physics models selected, and the data sources used for the cosmic radiation environment and parameters for the martian atmosphere and subsurface.

Chapter 4 describes the microbiological laboratory work conducted here, involving culturing novel cold-tolerant bacterial strains from the Antarctic Dry Valleys and characterising their phylogenetic diversity through molecular biology techniques. Several of these novel isolates and two model bacteria were selected for gamma-ray exposure experiments to determine their survival under martian radiation and permafrost temperature conditions, with these experiments designed using the results from the above computer models.

Chapter 5 is the first results chapter, detailing the extensive efforts to validate and verify the correct functioning of the new martian radiation model against previously-published studies. Chapter 6 presents all the novel results unique to two different configurations of this model, including particle energy spectra and fluxes as a function of depth, the biologically-weighted radiation doses used to assess microbial survival, and the dose deposited in the subsurface appropriate for estimating organic biosignature persistence times and calibrating optically stimulated luminescence dating.

Chapter 7 provides the results generated by the experimental component of this research. This includes the investigation into the culturable microbial diversity of a Dry Valley, identification of the novel isolates using gene sequencing, and determining the phylogenetic relationship between these strains and others previously detected in similar harsh low-temperature environments.

Also presented are the findings of the irradiation experiments on three of these novel isolates and two model microbial organisms.

The final Section, Chapter 8, discusses the implications of both the modelling and experimental results, and places them within the context of previous studies. These two parallel research programmes are woven together to inform the interpretation of both sets of discoveries, and draw conclusions on the likely survival times of microbial life in the martian near subsurface.

Chapter 2

Geant4 Method

As explained in the Introduction, the space radiation environment is diverse, both in terms of particle types and the energy range they cover. Highly energetic particles, particularly the HZE ions of the GCR, interact with shielding material in a very complex manner, generating extensive cascades of secondary radiation to create a radiation field that changes in particle composition and energy throughout the irradiated volume. Different modeling approaches to describe this cosmic radiation field exist, but the one selected for this research is Geant4, a sophisticated toolkit for simulating high energy particle physics within which a specific model must be designed and coded. This chapter deals with the method of application development and general structure of any Geant4 particle transport model, overviewing all of the mandatory and user-defined classes that must be understood and employed to build a simulation to the developer's requirements. The following chapter will deal with the specifics of the martian radiation model constructed within this coding framework, and justification of the parameters selected for the model not directly related to the programming, such as aspects of the primary radiation spectra, atmosphere, and surface composition.

Geant4 is a toolkit for the simulation of the passage of particles through matter. Its areas of application include high energy nuclear and accelerator physics, as well as studies in medical and space science [4, 5]. Geant4 represents a substantial advancement on the previous FORTRAN-based code GEANT3, and is an object-orientated particle physics toolkit written in the C++ programming language. The object-orientated programming methodology allows a system to be treated as a hierarchy of modular objects that interact with each other in a prescribed manner. For example, within the object-orientated framework of Geant4, the objects G4Electron and G4Positron inherit certain shared particle properties from the base class G4Lepton, and particle interaction processes can be attached to them.

The model of the martian cosmic ionising radiation environment was constructed within this framework, principally due to the accessibility of its modular design of C++ classes and the on-

line support provided by the user community (http://geant4-hn.slac.stanford.edu:5090/Geant4-HyperNews/index).

The Geant4 toolkit, along with accessory databases, can be downloaded from the website http://www.cern.ch/geant4/. Available support documents include the Introduction to Geant4 [96], Installation Guide [58] and Physics Reference Manual [228]. Additional details on the specific design and functionality of the Geant4 classes are contained within the User's Guide for Toolkit Developers [232], and a complete list of all Geant4 classes is provided by the Software Reference Manual [6]. Further details on aspects introduced in this methods chapter can be found in these documents; the User's Guide for Toolkit Developers [232] and Software Reference Manual [6] in particular.

The logical structure of the classes available within the Geant4 toolkit is depicted in Figure 2.1 below.

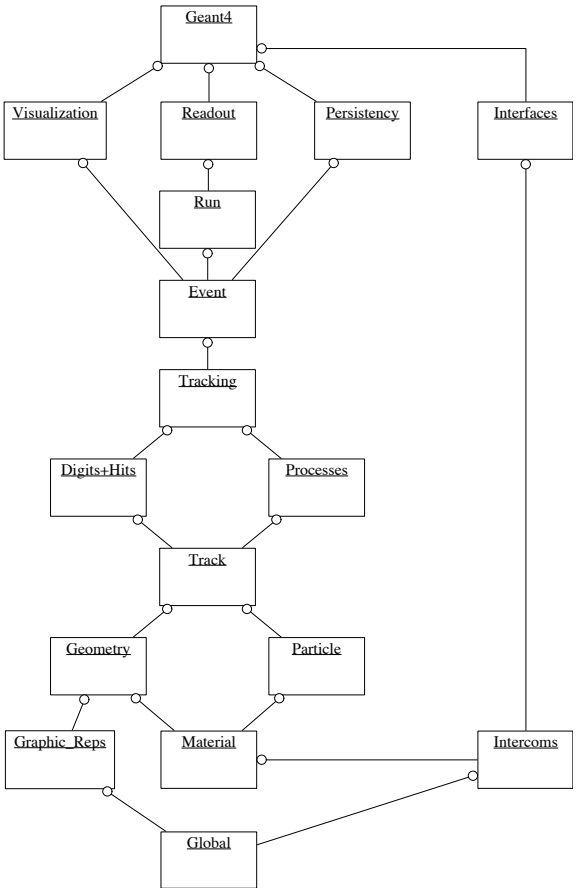

Figure 2.1: Diagram of the Geant4 class category structure [96]. Class categories are represented as boxes, with the "uses" dependency indicated by line links.

2.1 Major class categories

The function of the different class categories can be briefly described as follows.

- Run and Event
  A Geant4 *run* is the complete execution of a model, beginning with the initialisation of all

necessary classes and parameter specification, and ending with the deletion of terminated processes from memory. During a run, a sequence of *events* such as generation of primary particles and the interactions or decays of particles to create secondaries occur. The main role of events are to provide particles to the tracking management. Geant4 was designed as a "state machine" with a run manager to control the progression through different states of the life cycle of a Geant4 run, such as initialisation, idle, event processing, and quit or abort. The event loop is begun with the function *beamOn(G4int n_events)*.

- Tracking
  This is a collection of classes dealing with the propagation of particles and the factors that limit their step such as appropriate physical processes.

- Geometry and Magnetic field
  The geometry classes manage the specification of the physical arrangement of a detector within the *World* volume, and the computation of distances and volumes intersected within this space. Volumes can also be designated with a magnetic and/or electric, or user-defined, field, and the designated field managers control the propagation of particles accordingly. The object-orientated design of Geant4 means that different numerical algorithms or field specifications can be substituted very simply, without impacting any other component of the model.

- Particle and Material Definition
  These two class categories manage the specification of particles and their attributes, and the definition of material composition, respectively.

- Physics
  This category handles the physical interactions and processes associated with particle transport through matter.

- Hits and Digitisation
  Any specified interaction of a propagating particle within a volume designated as a *sensitive detector* generates a *hit*, with these classes handling the detection and cataloguing of such occurrences. The digitisation classes manage the processing of the set of hits generated by each event.

- Visualisation
  The production of graphical displays of volumes, trajectories and hits is managed by the Geant4 visualisation classes through their interfacing with underlying libraries and drivers.

- Interfaces
  A category of classes that allow the specification of an interactive command system or graphical user interface (GUI), as well as managing the interaction of Geant4 with external software such as database management systems.

2.2 G4RunManager

The first task that must be completed within a new Geant4 model is creating an instance of the G4RunManager class. This is a managemental class, responsible for the initialisation of all further procedures, including methods of the obligatory classes and any user-included classes,

and controls the overall flow of the programme as well as handling the event loops within each run. Using these additional classes, the run manager must be given all the necessary information for building and running the simulation. In general, these include: how the model geometry should be constructed; a description of all the particles and physical processes to be simulated; how the primary particle(s) of each event should be generated; any user-defined additions to this basic functionality, including the creation of sensitive detectors able to export relevant data from the simulation. These first three functions of any Geant4 simulation make-up the mandatory class objects that must be initialised: DetectorConstruction, PhysicsList and PrimaryGeneratorAction. DetectorConstruction and PhysicsList are user initialisation classes, and PrimaryGeneratorAction is a user action class. Each is derived from an abstract base class provided by Geant4, such as G4UserDetectorConstruction. There is no default behaviour provided for these classes, and so the application developer must carefully define options appropriate to the specific model requirements. G4RunManager checks the correct initialisation of these three mandatory classes when the *initialize()* function is invoked at the beginning of a run.

Geant4 provides additional optional user action classes which can be initialised and operated at will by the application developer. These include G4UserRunAction, G4UserEventAction, G4UserStackingAction, G4UserTrackingAction, and G4UserSteppingAction, which proscribe the behaviour of the model at different stages of the run loop and are dealt with in more detail in Section 2.9 on page 48. Another manager class created by the run manager is the user interface manager, G4UImanager, which allows the user to issue commands to the Geant4 model between events.

2.3 DetectorConstructor

2.3.1 Geometry

A detector geometry in Geant4 is composed of a number of volumes, organised in an hierarchical fashion. The largest volume is termed the "World volume", and most contain, with some margin, all other volumes in the detector geometry. Subsequent volumes must be created and positioned inside the World volume, or other previously-defined volumes. A smaller volume contained within a larger is called the "daughter volume"; the larger containing volume the "mother volume". The coordinate system used to specify the location of placement of a daughter volume is that of the mother volume.

A volume is created within the detector geometry in a series of steps. Firstly, a logical volume is defined. This definition includes: the geometrical properties of the object (i.e. an instance of G4Box, G4Sphere, G4Torus, G4Polyhedra, etc); the dimensions of the volume; the physical characteristics of the object, including the material it is composed of; and whether the object has magnetic field associated with it or contains any sensitive detector elements. This logical volume is then realised within the detector geometry by assigning it as a physical volume with specified placement coordinates and rotational orientation within a pre-existing physical volume. Thus instances of the same logical volume can be placed in many different locations within the detector geometry, each with a unique orientation, but all with identical size and composition. Only one volume may be placed within the detector geometry without a specified

parent physical volume, and that is the World volume. This unique case can obviously not be contained within another, and it must be created as a G4PVPlacement with a null mother pointer, with no rotation, and positioned at the origin of the global coordinate system. Complex detector set-ups can also be imported directly into Geant4 from Computer Aided Design (CAD) software.

2.3.2 Materials

There exists a hierarchy of composition of substances in the natural world. Materials are mixtures of compounds, compounds are made of elements, and elements contain several isotopes. The same hierarchy is maintained within Geant4. The G4Element class is used to create instances of elements, and creates a table as a static data member to store the properties of created instances. G4Element describes properties on an atomic scale: atomic number, nucleon number, atomic mass, and shell energy.

The G4Material class describes the macroscopic features of substances, including the user-defined density, state (solid, liquid, gas), temperature, density, and pressure, as well as calculated properties, such mean free path of a propagating particle. An instance of G4Material sits at the top of the matter definition hierarchy, and is visible to other classes within Geant4. Thus, the material specification of a volume is used by the geometry, particle tracking, and physics simulation routines during the running of a Geant4 model.

Description of desired materials is simple with Geant4. Firstly, the list of necessary elements are defined and named, each an instance of G4Element with specified atomic number, nucleon number, and so on. Compounds are then described as instances of G4Material with a given density, temperature, and so on, and the composition of different elements listed. For example, the water molecule would be defined as a compound of the pre-defined G4Elements hydrogen and oxygen, combined in the atomic ratio 2:1. More complex compounds, such as plastic polymers, can be easily specified as a mixture of elements with given fractional mass. G4Material can also be used recursively to simply build-up more and more complex substance compositions. For example, the G4Material "air" can be defined as a mixture of other G4Materials; nitrogen, oxygen, water vapour, carbon dioxide, and so on, with stated fractional masses of composition. Alongside these constructor functions, the G4Material class also contains methods designed to aid model design and error-checking, such as the member function *GetMaterialTable(),* which outputs details of the complete list of defined materials.

2.4 PhysicsList

The functions of this mandatory user initialisation class are three-fold: to define all particles, describe all physical processes to which they are to be subject, and finally to specify the range threshold for simulating electromagnetic particles. These are achieved with the three mandatory virtual methods of any class derived from G4VUserPhysicsList: *ConstructParticles(), ConstructProcesses() and SetCuts().*

2.4.1 Particles

Other than to elucidate the operation of the Geant4 toolkit, this chapter will not expand on details of the standard model of physics, whereby the "particle zoo" is categorised into bosons, fermions, leptons, hadrons, mesons and baryons. For normal applications, the user would not be required to define the properties of different particles as Geant4 defines over 100 varieties of elementary particle and nucleus by default. Each particle is represented by its own Geant4 class, derived in turn as an instance of G4ParticleDefinition. These particles are organised within Geant4 into six main categories: lepton, meson, baryon, boson, shortlived, and ion. The shortlived category contains particles which decay effectively immediately, and so are not tracked through the detector geometry and are implemented only for their involvement in physics processes. These include gluons and quarks, as well as certain excited mesons and baryons.

Unlike the G4Element class, which users can define (in terms of atomic and nucleon number, for example) to their will within the model code, most of the properties of G4ParticleDefinition are set-as "read-only" and cannot be redefined by the user without recoding and rebuilding of the physics libraries. Thus, for example, the class G4Electron cannot have its attributes of mass, charge or spin modified.

The application developer must register each particle type required in a simulation. It is important to remember that not only must primary particles be defined, but also any other particles that may appear within the model as secondaries generated by the defined physics processes.

2.4.2 Physics Processes

Physics processes define how a particle type interacts with matter as it propagates. There are several major categories of process a particle can be defined to undertake within Geant4, including electromagnetic, hadronic, decay, and transportation. Defining which processes a particle is allowed to undertake is achieved by registering them to a G4ProcessManager object which is itself attached to the G4ParticleDefiniton class unique to the specific particle. This manager class also stores the order in which certain processes are to be invoked, as well as whether the process is appropriate to the particle at rest, along a track step, or at the post step point.

Similarly to the requirement to register all particles needed for a simulation with the *ConstructParticle()* method, *ConstructProcesses()* must be invoked within the PhysicsList source code to register all necessary processes. For example, the electromagnetic physics of photoelectric effect, Compton scattering and gamma conversion (pair production) should be attached as discrete processes to the ProcessManager for gamma.

2.4.3 Simulation of particle interactions

Every process defined within Geant4 contains two groups of methods crucial to particle tracking: GetPhysicalInteractionLength (GPIL) and DoIt. Every process a particle can undertake occurs

with a certain probability, which is based on the process's cross-section. The interaction cross-section is dependent on the properties of the material being traversed and sometimes on the particle's energy, and thus the interaction length must be calculated from information regarding both the particle track and the physical volume it is propagating through. For each step, the GPILs of all relevant processes are calculated, and the shortest resultant length determines the physical process which will terminate the current step. If the shortest of these calculated physical interaction lengths is greater than the geometric distance to an approaching volume boundary the tracking manager terminates the current step at the boundary and then pushes the particle into the next volume. The GPIL method therefore serves to limit the step size of a particle track far from any volume boundaries and at the end of this step, where the process is determined to occur, the DoIt method of the selected process is invoked. DoIt implements the details of the process, and updates the particle's energy, momentum, direction and position. This probability-based reiterative process is the basis of the Monte Carlo (MC) methodology, as outlined in Chapter 1, Section 1.4.2 on page 29.

Many interactions also produce secondary particles, and these are created as new tracks and sent to the Geant4 tracking manager to continue their propagation. A track can be created either by the primary generator (i.e. the initial particle of any simulation) or a physical process, and is treated by Geant4 until it either exits the World volume or is killed. Particle tracks can be killed by an interaction (e.g. neutron capture), when they have come to rest and are stable (e.g. the deceleration of a heavy ion), or by a user's action (e.g. the culling of neutrinos in the martian model, as explained in Section 3.4.3 on page 66). Geant4 also provides the capability for creating user-defined processes which can then be attached to any particle of interest.

All physics processes within Geant4 are derived from the base class G4VProcess, which contains methods to handle many different interactions and decay processes. Geant4 divides processes into three categories: those which occur when a particle is at rest (e.g. radioactive decay, e^+/e^- annihilation), during transportation along a track step (continuous processes such as ionisation or bremsstrahlung) or at the post step point (i.e. a discrete process, which includes most of the interactions). Several continuous processes can therefore occur simultaneously along the track step, but only one can form the PostStep or AtRest action and thus different applicable processes must compete based on their cross-section.

Geant4 contains classes to handle the great variety of physical interactions, including photon processes (such as Compton scattering and pair-production), electron/positron processes (such as Bremsstrahlung and annihilation), hadron processes (such as ionisation neutron capture), and scattering of particles. A set of low energy electromagnetic processes are also available with Geant4 to cover the energy region down to 250 eV [228].

Several methods are included to model the interaction of an energetic nucleon or nucleus striking a target nucleus, such as the binary intranuclear cascade (BIC), including the pre-equilibrium evaporation, break-up or fission processes of the remaining nucleus. Energetic electron (delta-ray) production is handled, as are meson and muon decay and other processes such as neutron capture. The purpose of this section is not to provide an exhaustive discussion of all physical processes handled by Geant4, but a brief over-view of the diversity of methods the toolkit provides which were used in the construction of the martian radiation model, as summarized in Figure 2.2.

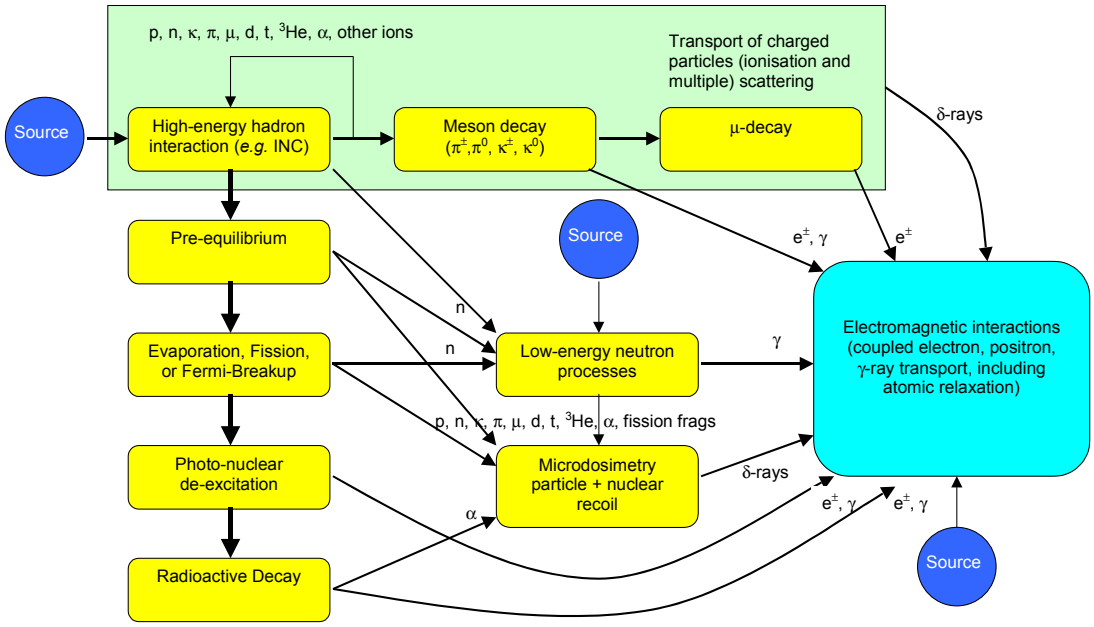

Figure 2.2: A simplified schematic of the particle interaction processes handled by the Geant4 physics models. High energy nucleon-nucleus or nucleus-nucleus collisions are simulated with intranuclear cascades (INC), producing further nuclear fragments or nucleons as well as secondaries which decay through the pathway of mesons, muons and electromagnetic particles. The pre-equilibrium decay of the recoiling nucleus is simulated through various evaporation, break-up and de-excitation processes back to a stable nucleus. Low energy neutron processes, such as capture, are handled, as are electromagnetic interactions such as pair production. Other processes shown here include ionisation and delta-ray generation. Any of these particles can also be specified as a primary source. Diagram produced by *Qinetiq*.

2.4.4 Cuts

Once all materials, particles and physics processes have been constructed, the application developer needs to specify a threshold below which some electromagnetic processes will produce no secondary. The Geant4 Application Developers' Guide states that this requirement is to avoid infrared divergence [232]. Thus, the *SetCuts()* method must be invoked to specify production thresholds for gamma, electron and positron. This is defined within the PhysicsList code as a distance, or range cut-off, but is internally converted to an energy cut-off for each defined material within DetectorConstructor. The application developer has the option of resorting to *SetCutsWithDefault()*, which sets to 1.0 mm, appropriate for many particle detector configurations, or alternatively, if greater control over the simulation parameters is desired, different range cuts can be specified for each of the three particles (gamma, electron and positron) and also for each geometrical region.

2.4.5 Magnetic fields

Geant4 is also able to simulate the curved trajectory taken by a charged particle propagating through a region containing a magnetic or electric field. Magnetic fields can be attributed to the World volume, and are thus said to be global. Field managers can also be associated with

any daughter volumes, in which case this local field over-rides the specification of the global. For the purposes of the martian radiation model, only magnetic fields are of interest.

Figure 2.3 shows how a charged particle, such as a proton, with a velocity in the plane perpendicular to a magnetic field is deflected into a circular trajectory by the Lorentz force, the radius of which is termed the *gyroradius* or *cyclotron radius.* If the particle has a component of its velocity vector along the B-field, it will spiral along the field line [132]. Calculation of the gyroradius is demonstrated in Section 3.7.1 on page 75.

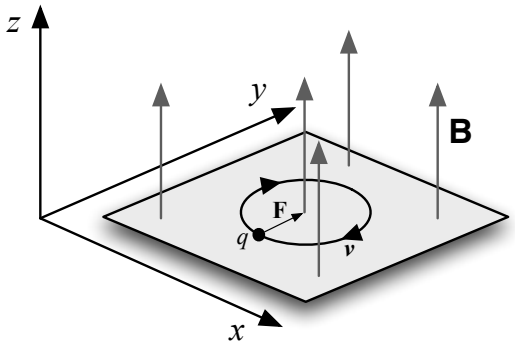

Figure 2.3: A charged particle, q, (such as a proton) moving with velocity **v** in the plane perpendicular to a magnetic field, **B**, will experience a Lorentz force, **F**, perpendicular to its instantaneous velocity vector and so be deflected into a circular trajectory, the radius of which is termed the *gyroradius* or *cyclotron radius.* If the particle has a component of its velocity vector along the B-field, it will spiral along the field line [132]. Diagram produced by the author.

Within Geant4, at each step point during propagation the vector of the local magnetic field is queried and used to calculate the Lorentz force exerted on the charged particle. The equations of motion for such a particle are a set of ordinary differential equations, which Geant4 generally solves numerically by integration using a Runge-Kutta method. Within a uniform field, an analytical solution can be found. The selected method is used to calculate the particle's propagation in a field, and this curved path is broken up into linear chord segments. The chord segments are chosen so as to closely approximate the true curved path, and are used by Geant4 to interrogate the geometry as to whether the particle crosses a volume boundary.

For accurate simulation, these chord segments must be chosen so that they do not deviate significantly from the true curved trajectory. Within a region with an intense magnetic field, a propagating particle may be forced to take many, much smaller, transport steps than would otherwise be required by the interaction distance calculated from the region's material properties. There is an obvious trade-off, therefore, between trajectory accuracy and processing time required, and the user must optimise this to their own needs. A further consideration is that when propagating near the boundaries of other volumes, a particle following the true curved trajectory may hit the object and interact whereas the linear approximation misses, and thus a physical event is neglected in the simulation.

Several parameters can be set by the user to adjust the accuracy of the integration and interrogation of the model geometry. The user has control over the maximum difference between the calculated chord approximation and the curved path, the minimum and maximum error in the particle's final position, and the error in whether the approximate track misses or intersects with a volume. The use of different integration algorithms is also advisable, depending on how closely the magnetic field can be locally approximated to be uniform, or how smooth

the field lines are. By default, Geant4 uses a classical fourth-order Runge-Kutta stepper. If the field is calculated from a field map, and particularly if it is not very smooth, a lower order stepper should be used. These options include G4SimpleHeum (third-order), G4ImplicitEuler or G4SimpleRunge (second-order), or G4ExplicitEuler (first-order). A first-order stepper is recommended only for very rough fields.

Geant4 provides default values for the tracking parameters, but good improvements can be made by optimizing them for a particular simulation. For example, the Geant4 defaults have been selected by the consortium for a particle accelerator detector scenario, and so the parameters are selected to provide fine-scale tracking over short distances. In a planetary context, such as modeling charged particle propagation through the geomagnetic dipole, processing time improvements of over two-orders of magnitude over the default settings can be made by relaxing the accuracy to larger scales [Geant4 Users' forum, 27 June 2005, Timothy Chambers].

2.5 PrimaryGeneratorAction

The final mandatory user class that must be derived is an action class for handling the generation of primary particles during a simulation run. The application developer must specify within this class how a primary event should be generated. For example, G4ParticleGun is the simplest means, and generates primary particles emanating from a single point within the World volume. The user is able to specify the particle to be created, its energy, the position vector of the generation point, and the momentum vector of the released particle (i.e. the direction of the beam-line within the detector geometry). The G4ParticleGun class does not itself provide any randomisation or distribution functionality, and in order to vary primary particle parameters, such as origination position, propagation direction or energy, the user must build-in logical structures to re-specify the desired parameter based on the event number, for example.

2.5.1 General Particle Source

The Geant4 toolkit was originally developed by a consortium of researchers based at CERN to simulate high energy physics in particle accelerators. As such, there was only the requirement for a relatively simple method of generating primary particles; essentially monoenergetic and focussed in a narrow beam. The space community, however, had a demand for simulations with easy specification of the primary energy spectrum, position distribution and velocity distribution. To meet this need, the General Particle Source (GPS) module was developed by Qinetiq (http://reat.space.qinetiq.com/gps).

Extending functionality beyond the basic point source provided by Geant4, GPS can be used to define a great variety of particle sources. Primaries can be generated from a planar surface, such as a rectangle or square, or the surface of a three-dimensional shape, or even its entire volume. For example, a natural formulation for simulating the cosmic ray flux impingement on a spacecraft would be to position the object inside a spherical shell with the inner surface acting as a particle source.

A variety of standard angular distributions, such as cosine-law which reproduces the isotropic angular flux of GCR and SEP radiation, can be chosen, or there is the option to specify a user-defined distribution by entering a histogram. Several distributions in energy are also provided,

including the option to simply describe a linear, exponential or power-law distribution, or enter a user-defined histogram. For these more complicated particle source specifications, it is most convenient to create different macros containing the lines of code for GPS set-up.

2.6 Sensitive Detectors and Hits

The method for using Geant4 to not only simulate high energy particle propagation, but also capture pertinent information and output data from the model is through sensitive detectors (SDs). Logical volumes within the model geometry are specified to act as sensitive detectors within DetectorConstructor. The principle function of a SD class is to generate hit objects from any particle that performs a step within, in to, or out of the assigned volume. A hit is a snapshot of a particle track inside a SD, and contains various information that may be of interest to the application developer, such as the position and time of the triggering step, the energy and momentum of the particle, the energy deposition along the step, as well as geometrical information of the sensitive detector triggered. Hits generated during an event are temporarily stored in an Hits Collection (HC), which can then be sent to external data analysis software before the HC is wiped at the start of a new event.

Geant4 provides an abstract base class, G4VSensitiveDetector, which is used to create a user class with three mandatory methods: *Initialize()*, *ProcessHits()*, and *EndOfEvent()*. *Initialize()* sets up appropriate hits collections to store information as it is generated during an event. The *ProcessHits()* method is called every time a hit is generated by a step, and thus a C++ logical structure can be used to decide which hits are of interest and what information on them to store. This method is treated in detail in the next chapter on development of the martian radiation model. *EndOfEvent()* deals with the treatment of a hits collection once it has been filled during an event, such as printing data tables to the screen, drawing hits to the visualisation channel, or post-processing it using Geant4's Digitization module.

2.7 User Interface

A Geant4 model can be designed to be operated in one of four modes. The first, and by far the most basic method, is to construct a programme in a purely "hard-coded" batch mode. This involves pre-programming a simulation with all the parameters and behaviour that are required (by specifying a "batch" of jobs to be processed within the PrimaryGeneratorAction, for example), compiling the source code to an executable, and then simply letting the programme run autonomously. Once initiated, no control can be exerted over the running of the simulation, and any desired changes to the run must be affected by re-coding the programme, re-compiling the source, and then running from scratch again. The limitations presented by such a mode of operation are obvious.

Alternatively, the programme can be largely hard-coded, but have the capability to read-in an external macro file containing commands. This is a slightly more advanced programming paradigm, as it requires the construction of public class functions to over-write hard-coded default parameter settings with those contained within the macro file. The advantage of such a model set-up, however, is that the programme itself does not need to be recoded and recompiled

in order to rerun the simulation with modified input parameters or operating behaviour. The macro file need only be up-dated with the new settings, and the pre-compiled simulation run again.

A more sophisticated approach is to employ other Geant4 classes, of the "intercom" category, to act as command interpreters and allow interactive involvement of the user. In this operating mode, a very generic simulation can be designed and compiled, with the user having the option of modifying any desirable aspect of the model set-up, such as details of the detector geometry, primary particle flux, or simulation visualisation, within the running programme by entering command lines from the keyboard. The easiest such set-up would be to create a structure of menu options, with the user able to select commands to modify appropriate parameter values between events. The most complex solution would be the construction of a complete graphical user interface (GUI) employing Operating System-style buttons or pull-down menus. Providing such an all-inclusive model mode would be very labour-intensive during the coding and bug-checking stage of programme development, and thus probably only be appropriate for a Geant4 package designed for release to be used by a wide community. For a model being written to simulate a more specific scenario for the use of a few researchers, a batch mode with macro-input capability is almost certainly adequate. This is the strategy adopted for the martian radiation model.

2.8 Visualisation

The Geant4 package needs to be used with a variety of different visualisation software, and so does not provide any one built-in visualiser but defines an abstract interface and drivers that can be used with any number of external graphics applications. Visualisation drivers that can be set-up with Geant4 include OpenGL, OpenInventor, DAWN and VRML. Some visualisation options require the building of additional libraries or setting of different environmental variables. Realisation of a visualisation driver is achieved by constructing a visualisation manager class, inheriting from the base class G4VisManager, which is instantiated and initialised in the *main()* function of the Geant4 code. Since different applications of the same model may be better-suited by different visualisation drivers, and the initialisation of some drivers is mutually exclusive, it is best to code the instantiation and initialisation of each driver in a macro, which can be called from within the *main()* function as required.

There are three main components of a Geant4 visualisation. The "scene" is a set of raw 3D data generated for the purpose of visualisation. The "scene handler" processes the data in a scene for later visualisation, incorporating the camera view-point settings or drawing style (wireframe, lit surfaces), for example. The "viewer" generates images based on the scene data processed by the scene handler. Orientation and scaling of the model, camera position and viewing direction, and panning and zooming can all be controlled with this system. Since the production of a single image can necessitate several lines of commands, it is also preferable to codify different common viewing options within separate macros that can be called upon through the user interface.

Within Geant4, various objects can be prepared for visualisation. The most useful, in terms of aiding geometry design and error-checking, is to be able to visualise the three-dimensional lay-out of the detector construction, and confirm the arrangement, relative positions, possible

overlapping, and so on, of the physical volumes. During the scene handler specification, certain volumes can be selected to be excluded from visualisation to enable "peer-through".

The trajectories of particles can also be stored as visualisable lines, and also be arbitrarily colour-coded on the basis of any required particle attributes. The Geant4 default is to colour neutral particles green, positively-charged species blue, and negative particles red. More sophisticated schemes are possible, however, and individual particles can be assigned unique colours to aid in the interpretation of complex visualised sets of particle tracks.

The depiction of particle hits within a visualised simulation is also a common tool. The location of a particular interaction, such as energy deposition, can be symbolised in a graphic with a colour-coded dot. Also possible is the highlighting of the entire physical volume that contains the coordinates of the hit.

An example of the visualisation output from the martian radiation model is provided in Figure 3.4 on page 63.

2.9 Optional User Actions

Alongside the user classes that must be initiated (DetectorConstruction, PhysicsLists and PrimaryGeneratorAction), Geant4 provides a further five optional user classes that can be used to gain control of the simulation at various stages. Two of these allow the user to invoke methods at the beginning or end of a *run* or each *event*. Typical uses of these might be to initialise data storage structures for information generated by the simulation, and to process and output it afterwards. The user can also exert control over the Geant4 stacking manager, which handles the order of processing particle tracks, or even to kill selected particles by deleting their track from the stacking manager. Control can also be taken over aspects of the tracking and stepping of particles.

2.10 General

2.10.1 Geant4 types

Geant4 provides an enormous collection of classes, types, structures and constants that are globally accessible throughout the package by the inclusion of a single header file, globals.hh. Even objects that are already commonly available within standard C++ libraries, such as basic numeric types, vectors or arrays, are provided as Geant4 versions so as to ensure portability of any Geant4 model to other platforms. All Geant4 nomenclature follows a homogenous prefixed style, including, for example, G4int, G4bool, G4String, and G4VHit. Other types are defined by corresponding classes of the Computing Library for High Energy Physics (CLHEP) distribution, including G4ThreeVector and G4RotationMatrix.

2.10.2 Geant4 units

The system of units used internally by Geant4 is that of CLHEP, i.e.: distance (mm), time (ns), energy (MeV), charge (eplus), temperature (kelvin), amount of substance (mole), angle (radian), solid angle (steradian). All other units can be defined from these fundamental ones, as follows, for example:

```
meter = m = 1000*mm
m3 = m*m*m
```

Users are free to use whichever units they prefer, provided they have been previously defined. Although values given to Geant4 without units, either hard-coded in the source code or entered by the user through the command interface, are implicitly assumed to be in the internal system, this lazy practice is strongly discouraged to avoid any potential confusion. The complete list of basic units used by Geant4, and those derived from these fundamental units, such as degree, joule, coulomb, is given in *SystemOfUnits.h*. The physical constants defined by the Geant4 system, such as the speed of light, Planck constant, electron mass, and so on, are given in the header file *PhysicalConstants.h*.

2.10.3 Randomisation

Randomisation within Geant4 is provided by the HEPRandom module distributed within CLHEP. A variety of classes implement different randomisation engines and random distributions. A random generator consists of a distribution associated with an engine, and can implement the algorithm to produce pseudo-random numbers. Several different HEPRandom engines are available within the Geant4 toolkit: HepJamesRandom (the default), DRand48Engine, RandEngine, RanluxEngine and RanecuEngine. The internal state of the RanecuEngine is represented simply by two numbers of numerical type *long*, whereas all the other engines have a much more complex representation. This is significant because saving the internal status of a random generator and restoring it later allows a simulation run to be reproduced identically from a given stage. RanecuEngine is thus the most suitable for this operation, and its internal status can be fetched and reset very easily with the *getSeeds()* and *setSeeds()* methods respectively.

2.11 Chapter summary

- Geant4 is a C++ object-orientated toolkit for simulating high energy particle physics, including deflection within magnetic fields, within which specific simulations can be constructed. Geant4 is well-suited for the martian radiation model.

- Three classes are mandatory for the application developer to define: DetectorConstruction, PhysicsList, and PrimaryGenerator, which define the geometry and composition of the model, the particles and physical processes to be modeled, and the source of primary particles, respectively.
- The most important optional user action classes define the sensitive detectors to extract relevant data from the model, handle visualisation, and provide command interfaces.

Chapter 3

Model Development

As explained in the previous chapter, Geant4 provides a framework for high energy particle physics simulation, but within this toolkit a specific model must be designed and constructed. This chapter describes the development of the martian ionising radiation model within the Geant4 class structure. Details are given on the selection of appropriate parameters for the geometry and composition of the model atmosphere and subsurface, the primary radiation source, particle physics modeling and the post-processing of simulated data.

3.1 Development

The Geant4-based model was in a process of continual development, improvement, and adaptation for over a year and a half, between March 2005 and November 2006. The model was developed in a series of small incremental steps, being verified and checked at each stage of development. Every time a new improvement was planned and was about to be implemented, a copy of the most current version was made before modifications began. Each of these developmental versions was safely archived for possible future referral, for a number of reasons. Firstly, if insurmountable difficulties are encountered progressing onwards and coding new capabilities it is often best to be able to return to the predecessor version and try again. Furthermore, in the case of accidental deletion or disruption of code it is paramount to have original saved versions, and when bug-hunting new code it is advantageous to be able to compare between parental and descendent versions to help tracking down, isolating and correcting errors. Finally, different results are more naturally produced by different configurations of the primary model, and so variants were stored for future use. A detailed history file documenting the versions was kept, describing exactly the capabilities and incremental improvements of each model, and which parent they descended from. This enabled rapid identification of the appropriate version when required.

The martian model was built up from the basis of a generic pedagogic example provided within the standard Geant4 distribution. "Novice Example 01" consists solely of the three obligatory Geant4 user classes outlined in Chapter 2: DetectorConstruction, PrimaryGeneratorAction and PhysicsList. It was adopted as the starting point for development on the basis of its simplicity and potential to serve as a skeleton for further complexification. The geometrical set-up of this simplistic model consists of an experimental hall 1 m by 1 m by 3 m in length, containing a tracker tube with calorimeter blocks. A few materials, such as aluminium and lead, are also defined in DetectorConstruction. The PrimaryGenerator produces particles from a point source, which traverse along the center line of the cuboid hall. The sole particle to be defined within the PhysicsList is the fictitious *geantino*. This effectively functions as a test particle within Geant4 as it has no charge, does not participate in any physical interactions or decay pathways, and whose only prescribed behaviour is transportation.

The final martian radiation model was built from this starting point, through an incremental sequence of modifications and importing and adapting of code from other teaching examples and open-source Geant4 software, as outlined in more detail below.

3.2 Model Geometry and composition

The first of the three obligatory classes within the Geant4 framework is the DetectorConstructor. As explained in greater detail in the previous chapter, this file describes both the geometrical layout of the model and the composition of objects within it. Magnetic fields are attached to logical volumes by the DetectorConstructor class, but also require other user-defined classes and so development of this functionality is described in full in Section 3.7 on page 74.

The geometrical set-up for the martian radiation simulation is essentially a bipartite column. The top section of this cuboid represents the atmospheric column on Mars, and the lower section the martian subsurface. Two configurations of the martian subsurface model were developed to address different aspects of the radiation environment. The first configuration contains micron-thick water layers embedded at regular depths in the subsurface to extract data on particle energy spectra and biologically-relevant radiation doses; the second configuration employs minimal layering and outputs dose deposition within the subsurface bulk itself.

In the interests of future versatility, the dimensions of the World volume are not themselves stated explicitly within DetectorConstructor, but are calculated at compile-time from the specified dimensions of the component daughter volumes, atmosphere and regolith. This reduces the likelihood of run-time errors and crashes due to inconsistency of the specified dimensions and overlap of volumes. The z-position (i.e. altitude within the columnar design) of the subcomponent volumes is calculated on-the-fly from specified dimensions for the same reason. This means that the code is much more adaptable, with only the desired changes made to regolith or atmosphere dimensions required, and the absolute positions and dimensions of the encompassing World volume automatically calculated accordingly.

Geant4 allows the precise definition of material composition, in terms of atomic content, by the sequential specification of named components. Thus, the complete list of compounds within the martian atmosphere and surface above trace levels are defined from the relative elemental contributions. Mixtures of these compounds are subsequently described by a list of the components and their relative contribution by mass.

3.2.1 Atmosphere composition

The atmosphere of the current martian atmosphere is taken from the Mars Climate Database (see Section 3.2.3.2 for a full description). The atmospheric column is assumed to be homogenous with respect to composition as a function of altitude, 95.5% CO_2 and with traces of N_2 (2.7%), Ar (1.6%), O_2(0.13%), CO (0.07%) and H_2O (0.03%), and constant over planetary history.

3.2.2 Surface composition

The composition of martian surface soil and rock was taken from Wänke *et al.* (2001) [225], who report data for both martian soil (several independent measurements plus a calculated average) and calculated soil-free rock, as determined by the Alpha Proton X-ray Spectrometer (APXS) instrument aboard the Sojourner rover, part of the Mars Pathfinder mission (location marked as (3) on map in Figure 1.1 on page 17). Sojourner measured the composition of 9 rocks and soil in 7 locations around the Pathfinder landing site in the mouth of Ares Vallis (19.28°N, 33.52°W). Although distant from the locations of the martian landers, this average soil composition agreed well (due to global wind-mixing). The percentages given do not sum exactly to 100%, so in the Geant4 material definition the slight deficit was attributed to SiO_2, by far the dominant constituent of the surface rock and dust.

At compile-time, Geant4 converts these material definitions into the relative elemental composition, as propagating radiation particles are blind to mineralogical details or material structure and interact only with the Coulomb fields and nuclei of atoms within the material. Thus, describing the composition of the martian dusty surface with distinct wind-mixed mineral grains, or rock pore spaces laden with permafrost ice, reduces to the simple specification of percentage mass of water, silica, ferric oxide, and so on, and the corresponding bulk density.

Three different models of the martian subsurface were built to represent various possible locations for microbial life. These are: "Dry Homogenous" (DH), "Pure Ice" (PI), and "Wet Heterogeneous" (WH).

3.2.2.1 Dry Homogenous

The Dry Homogenous (DH) surface model is set to the material composition of the calculated mean martian soil [225]. The bulk density of the martian wind-drifted fines was determined to be 1.10 ± 0.15 g/cm^3 by the Viking 1 lander at Chryse Planitia [49] (location marked as (1) on map in Figure 1.1 on page 17). A density of 3 g/cm^3 is reported to be more appropriate for martian meteorites and rock [154]. The simple homogenous slab of surface material modeled in "Dry Homogeneous" was set to an intermediate density of 2.81 g/cm^3; the arithmetic mean of a 2 m depth of 1.1 g/cm^3 loose soil atop an 18 m column of 3 g/cm^3 compacted regolith. Thus, the "Dry Homogenous" scenario is a uniform block of arid regolith with the dry topsoil composition given above and set to a density of 2.81 g/cm^3.

3.2.2.2 Pure Ice

The Pure Ice (PI) scenario was constructed to emulate certain water-ice environments on the martian surface, such the northern polar cap, within high-latitude impact craters or putatively beneath a thin coating of dust on the plains of Elysium [162] (location marked as (a) on map in Figure 1.1 on page 17). For comparison of generated data, the Pure Ice scenario is also valuable as representing the opposing extremity to Dry Homogenous: a solid block of water ice to contrast against the homogenous column of dry martian soil. The material composition of the PI model is simply specified as the solid state of the compound H_2O, with a density of 1 g/cm^3.

3.2.2.3 Wet Heterogeneous

The more sophisticated composition model, Wet Heterogeneous (WH), attempts to recreate the layered structure of the martian subsurface. As explained in Chapter 1, both neutron and gamma spectroscopy data confirm the existence of greater amounts of hydrogen in the near subsurface at high latitudes, as well as certain regions nearer the equator, and is assumed to be due to permafrost water [82, 156, 40]. Mitrofanov *et al.* (2004) [157] report that the moistest low-latitude region is within Arrabia Terra, centered on coordinates 10°N and 30°E (location marked as (b) on map in Figure 1.1 on page 17). They constructed both a single homogeneous layer and a two-layered (top layer relatively dry, lower layer containing the bulk of the detected water) model of the martian subsurface. Fitting their measured neutron back-scatter data, they found that the region within Arrabia Terra is best represented by a top dry layer of 2% water by mass, roughly 29 g/cm^2 deep, overlying a wet layer with around 16% water by mass. WH combines these soil layering moisture parameters with the dichotomy between wind-blown un-compacted surface dust and denser underlying regolith. The WH model is thus stratified into a 25 cm layer of 1.1 g/cm^3 topsoil, 2% water by weight; a 75 cm deep layer of 1.1 g/cm^3 topsoil with 16% water, and the bottom 19 m as 3 g/cm^3 regolith with 16% water.

3.2.3 Geometry

The two major geometric volumes within the model, the atmosphere and regolith columns, require a layered structure of subdivision, but for different reasons. Horizontal layering is required to recreate the density and temperature profile of the atmosphere. In the first configuration of the model, the regolith is also finely layered so as to embed micron-thick water slices at regular depths to emulate cells in the subsurface and extract information on particle fluence, energy, and deposited dose as a function of depth underground.

Geant4 provides two methods for simplifying the construction of repeated volumes and saving computer memory which could be suitable for generating layering within the atmosphere and regolith parent volumes. Using the G4PVReplica class would be one natural solution, as it automates the construction and positioning of repeated objects (i.e. simplifying the calculation of the placement coordinates). The axis of segmentation is defined, along with the number of desired segments (and any rotational variation of the repeated volumes along the axis), and the specified volume is automatically subdivided accordingly. The problem with such an approach is that this produces identical instances of the same logical volume, and so does not allow for the

modification of dimensions or composition of the volume. Thus G4PVReplica was discounted as a useful method for generating layering within either the atmosphere (which demands layers of differing thickness, see below) or subsurface (which requires a changing composition with depth).

An alternative class provided by Geant4 is G4PVParameterised, which allows the repeating of a volume with certain attributes parameterised by copy number. For example, the shape, size, position, rotation, material, event reporting or visualisation attributes of each volume in the series can be related to its number in the series. Thus the thickness and position of the individual atmospheric slabs could be linked to their copy number during generation by G4PVParameterised. Writing the source code to correctly specify the desired set-up, and allow quick changes, was found to be too unwieldy using G4PVParameterised, however, and a simpler solution was found for atmosphere and surface layering. This solution is explained in detail in the Atmosphere Section 3.2.3.1, below.

Both the atmosphere and surface regions are created as a hierarchical structure of two levels. Using the atmosphere as the exemplar, a container physical volume (i.e. *Atmosphere_phys*) is created with the dimensions of the complete atmospheric column, but with composition set to vacuum, and is positioned appropriately at the top of the World volume. The second level of organisation is that of layering within the atmosphere (i.e. *AtmosLayer_phys*), with each successive slab created with the desired thickness and gas composition, pressure and temperature.

This two-level hierarchical design was selected for two reasons. Firstly, positioning the atmospheric layers within a container volume simplifies calculation of the correct position of each layer along the z-axis (altitude), since daughter volumes use the local coordinate system of their immediate parent volume, not the World volume. Thus, if for example the regolith region is decreased in thickness, the altitude mid-position of Atmosphere_phys is recalculated, but no change is necessary in the defined locations of the atmosphere layers because they are defined relative to their parent column. Secondly, in the case of simulating particle propagation through the crustal magnetic anomalies, the field manager can be assigned to the atmospheric column as a whole and thence inherited by all the atmospheric layer daughter volumes.

3.2.3.1 Atmosphere

In order to exert the required control over generation of a succession of atmosphere layers, certain sections of source code defining the construction of volumes were placed within a logical *for* loop, stepping through the variable *AtmosLayerNum* from 1 to the total number of desired atmosphere layers. Within this loop are placed statements to:

- Define the shape of the current layer, allowing specification of the thickness of each G4Box.
- Specify the G4Material "martianAir" with the desired gaseous composition, density, pressure and temperature.
- Construct the layer logical volume with the predefined thickness and composition, and with desired visual attributes.
- Instantiate this logical volume as a physical volume positioned at the desired altitude above the martian surface.

Thus, this construction allowed precise control over the thickness and composition of each new logical volume, with the position vector of each resultant physical volume offset to produce an ordered array of volumes atop each other. An analogous construction is used to generate appropriate layering within the subsurface.

3.2.3.2 Current atmosphere

Data on the physical properties of the current martian atmosphere were taken from the on-line resource Mars Climate Database (MCD) [141, 88] (accessed August 2005). MCD contains information on many atmospheric parameters on a 5° by 5° longitude-latitude grid of the surface of Mars, and is available for free use (http://johnson.lmd.jussieu.fr:8080/las/servlets/dataset). The Mars Climate Database was created by numerical simulation of Mars' atmosphere using a General Circulation Model (GCM), as employed for weather forecasting and climate studies on Earth. This database has been extensively validated using available observational data, and is claimed to be superior to so-called "engineering models" such as MarsGRAM that simply interpolate between the sparse data points. Thus an accurate representation of the atmospheric column can be imported into this Geant4 model for any location on the surface, local time and any day of the martian year.

The data that was extracted from MCD represents noon on a Summer day within Arabia Terra. MCD defines 12 seasons, based on the solar longitude (L_s). Each season covers 30° of solar longitude and is typically 50-60 days long (variation exists due to the obliquity of the martian orbit). The database was queried for midday during summer in the southern hemisphere (L_s = 270 – 300; season 9 – 10, with each season 47 Mars solar days long), which is the perihelion of the elliptical orbit and thus the annual peak for atmospheric density. The location was selected as 30°E and 10°N as it lies at the reference altitude with a surface pressure of 600 Pa, and is the region within which backscatter neutron spectrometry suggests has the highest incidence of near sub-surface water ice at low latitudes [157]. Figure 3.1 displays the surface pressure and temperature data calculated by MCD for this location and time.

The Mars Pathfinder lander discovered variations in the surface atmospheric pressure at its landing site in Ares Vallis over both diurnal and seasonal cycles [199], but these do not exceed ±5% from the mean and so are negligible in terms of particle propagation modeling.

MCD outputs data on the vertical dependency of atmospheric density and temperature as a function of sigma, the ratio of pressure to surface pressure, which produces a linear plot of sigma vs. density or temperature. These values were converted to altitude, as described on the "Level Documentation" page of the MCD website:

$$z = -H.ln(sigma) \tag{3.1}$$

where z is the calculated altitude in km and H is the scale height of the martian atmosphere (given to be 10 km).

MCD gives atmospheric data for 32 sigma levels: up to an altitude of 150 km. For the purposes of this radiation transport model, however, only the first 20 levels were taken because at this

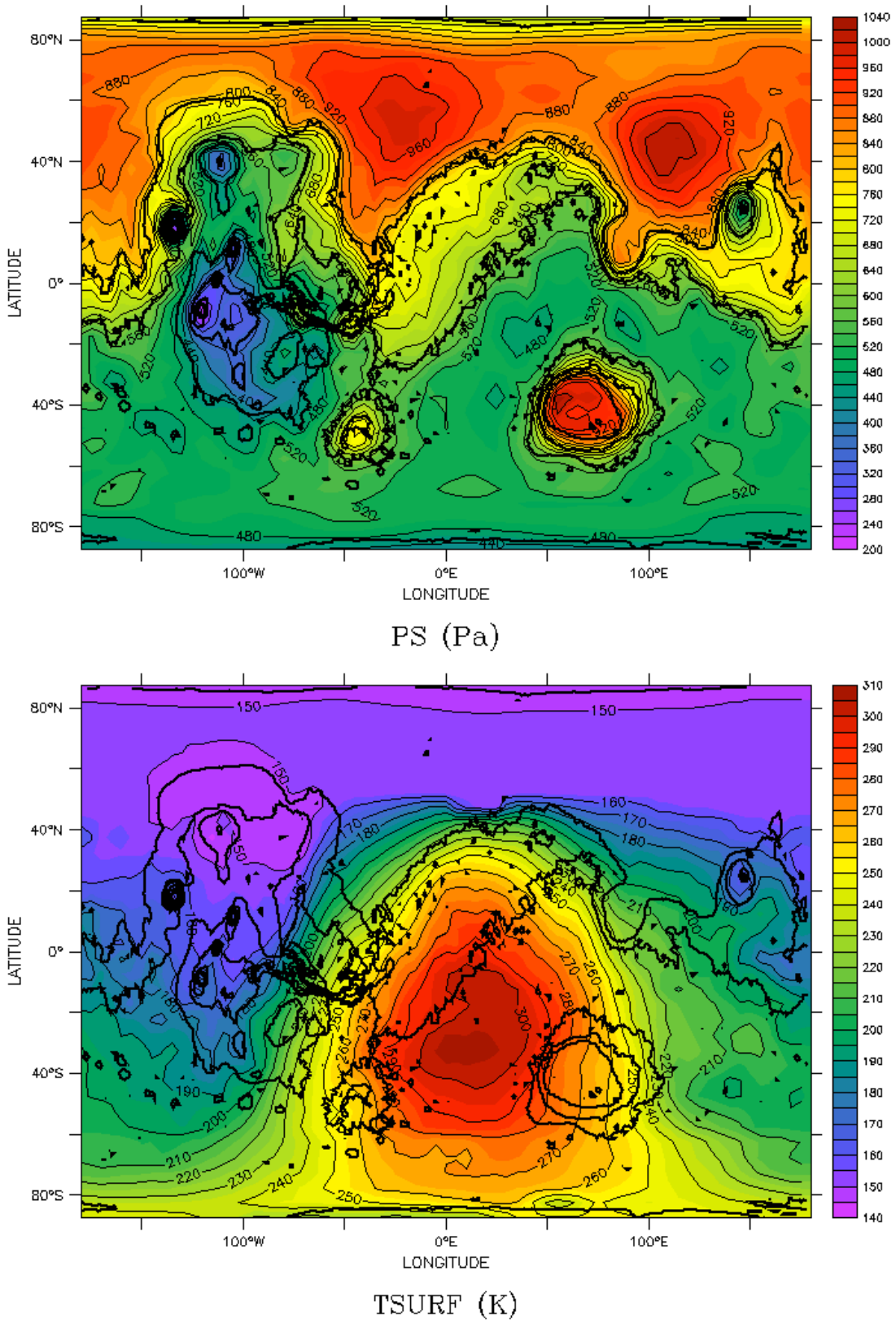

Figure 3.1: Environmental data extracted from the Mars Climate Database [141, 88]: the surface atmospheric pressure (top) and surface temperature (bottom) at noon on a Summer day ($L_s = 270 - 300$) for the location 30°E and 10°N within Arabia Terra.

maximum altitude of 65.8 km MCD reports the atmospheric density to be less than 0.2% that of the surface, and thus treating any further atmospheric column will not have a significant effect on shielding and the surface radiation field. Figure 3.2 plots the altitude profiles for martian atmospheric pressure, density and temperature, as extracted from MCD and imported into the Geant4 Mars radiation model.

The atmospheric pressure, temperature and density data could be interpolated between these 20 points to produce a finer layering of the atmospheric column within the model, but this was not considered to be necessary. As explained below in Section 3.2.3.4, increasing the number of boundaries that propagating particles must pass through can dramatically slow processing of the model, and no significant benefit was expected from treating the atmosphere with finer layers. Density decreases exponentially with altitude and so layers nearer the surface are created thinner, with the top atmospheric slab nearly 7 km thick and the bottom layer only 12.5 m thick.

The geometrical attributes of each of the 20 atmospheric layers were stored in data arrays, *atmosLayerAlts[20]* and *atmosLayerHalfThick[20]*, respectively, and were extracted in turn by the Geant4 construction loop. The pertinent physical properties of each layer were held in further arrays, *tempStore[20]*, *densStore[20]* and *pressStore[20]*, and attributed to the G4Material as each new layer was generated.

3.2.3.3 Altitude variation and paleo-atmospheres

Mars exhibits the greatest topographic extremes of any body in the solar system, with roughly a 34 km difference between the bottom of the Hellas impact basin and the peak of Olympus Mons (Mars Orbiter Laser Altimeter data, ftp://public.sos.noaa.gov/astronomy/mars_mola). Geographical location can therefore have a significant effect on the surface radiation environment due to variation in atmospheric shielding depth. The atmospheric profile at these locations was modelled using the same method as that for primordial scenarios, as follows.

The cosmic radiation reaching the martian surface would have increased over geological time as the atmospheric shielding diminished, and so calculations of the subsurface dose profile under different atmospheric pressures are important for estimating long-term biomarker persistence. One previous study has modeled the martian surface radiation environment beneath a substantially denser primordial atmosphere [159] and found the presence or absence of a global dipole magnetic field, of a similar strength to the current terrestrial field, to exert minimal influence on the surface radiation field due to the dominant shielding effect of a thick atmospheric shield.

Although both the primordial atmospheric pressure possessed by Mars and the time course of its erosion are difficult to constrain [119], the shielding effects of different atmospheric columns can be calculated, even if the absolute time they correspond to is dependent on the particular atmospheric history model. Equation 3.2, a reformulation of the sigma function used by MCD [141, 88], was used to model primordial atmospheres:

$$P = P_0.e^{-z/z_1} \tag{3.2}$$

where P = pressure at the given altitude, P_0 = the surface pressure, z = altitude, and z_1 is the scale height of the martian atmosphere, calculated using:

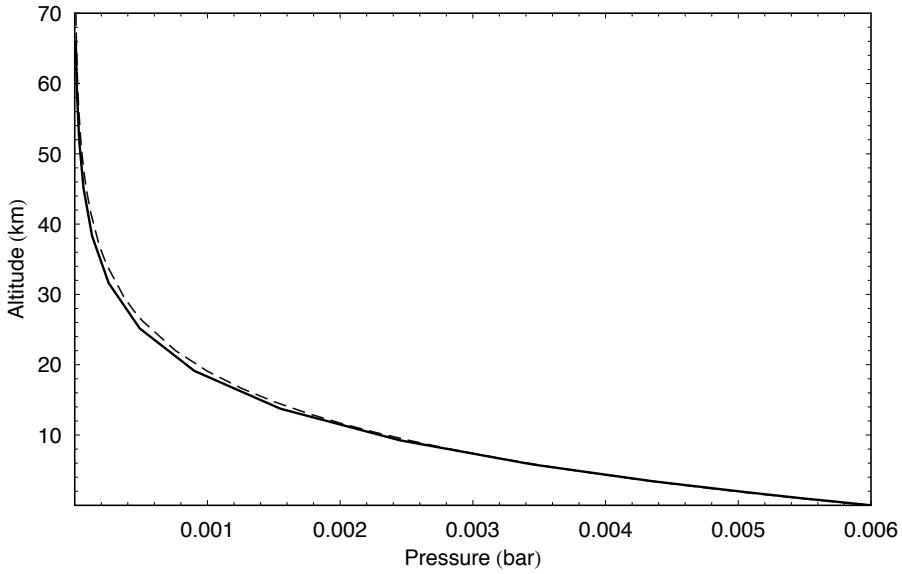

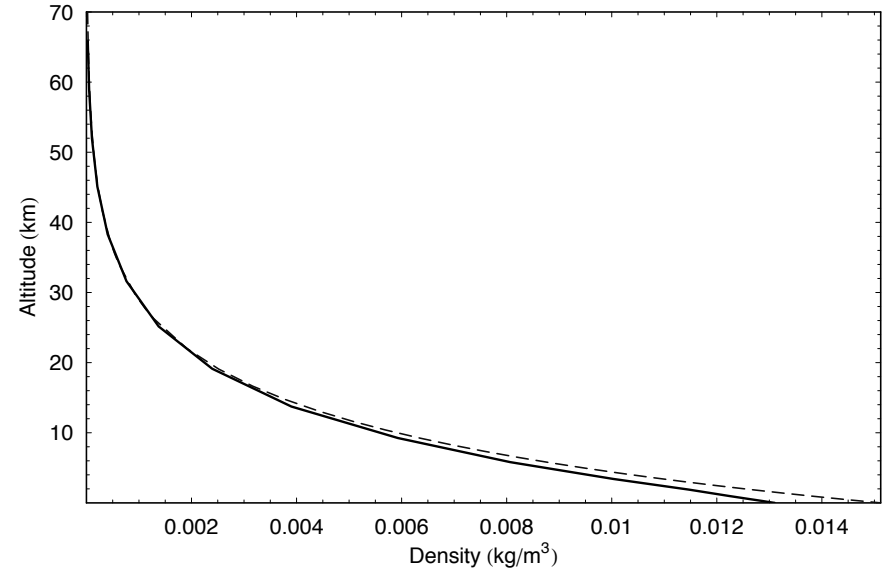

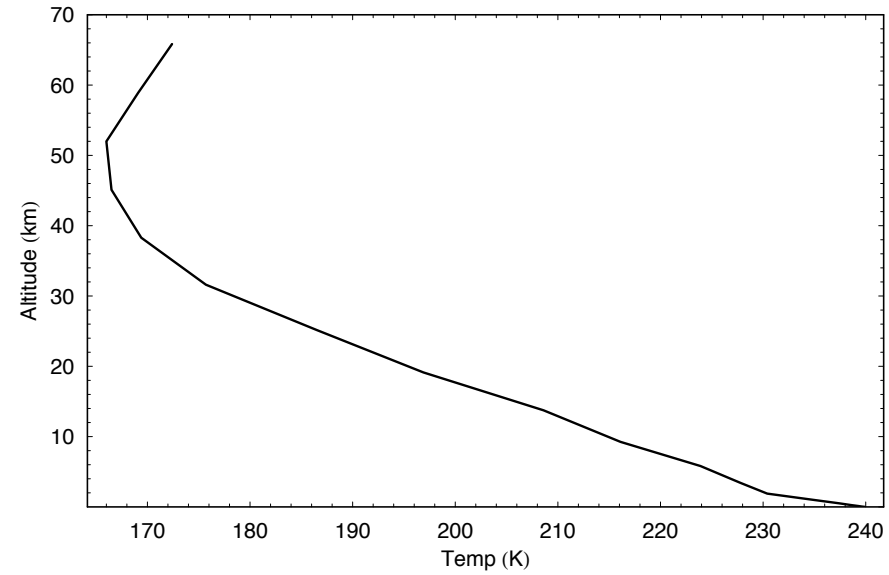

Figure 3.2: Altitude profiles for martian atmospheric pressure, density and temperature, as extracted from Mars Climate Database [141, 88] (parameters explained in the text) and imported into the Geant4 radiation model. The dashed lines in the pressure and density plots are those calculated by the atmospheric model described in Section 3.2.3.3 to demonstrate its validity.

$$z_1 = k.T/g.M \tag{3.3}$$

where k = the Boltzmann constant, T = the characteristic temperature of the martian atmosphere (calculated from the MCD data to be currently 210 K, and agreeing well with the value of ∼212 K cited in Allen's Astrophysical Quantities (2001) [60]), g = the gravitational field strength of Mars, and M = average molecular mass of the atmosphere (taken here to be pure CO_2). This calculation finds a scale height of 10.7 km, agreeing well with the figure of 11 km cited in Allen's Astrophysical Quantities (2001) [60].

The Ideal Gas Equation can then be used to calculate the density profile as a function of the above pressure profile and characteristic temperature. Even though the temperature is not constant through the atmosphere, these exponential functions still provide a good atmospheric approximation. The validity of this atmospheric model is demonstrated in the pressure plot in Figure 3.2, where it is compared against the data provided by MCD.

In any case, in terms of modelling radiation propagation the exact density and pressure profiles are much less important than the overall shielding thickness. Figure 3.3 plots the density profiles calculated using the above method for primordial scenarios with surface pressures of 0.01 bar (27 g/cm^2), 0.1 bar (268 g/cm^2) and 0.385 bar (1033 g/cm^2). This 0.385 bar scenario was chosen as it produces an atmosphere with a shielding depth of 1033 g/cm^2, equivalent to the current terrestrial atmosphere [168].

A denser atmosphere would produce a higher temperature through improved efficiency of the greenhouse effect, but to what extent is very poorly constrained as the greenhouse mechanisms that operated throughout martian history are unknown [89, 102]. Assuming an additional warming of 10 K for a 0.385 bar atmosphere, the calculated density profile is plotted in Figure 3.3, along with the profiles produced by ±20 K limits. The scale height is recalculated in each case, but does not change substantially as it varies only linearly with temperature.

As can be seen, the density profile is not overly sensitive to changes in characteristic temperature. Furthermore, the shielding depth (the integral under the density curve) of these ±20 K atmospheres differs by less than 0.1% from the calculated 1033 g/cm^2 at 220 K. Thus, in terms of attenuating impingent cosmic radiation, the atmosphere models used here are robust to changes in parameters.

3.2.3.4 Surface

The operational requirement for the first configuration of the martian model was to output the energy spectra of secondary particles as well as the radiation dose deposited at regular depths in the subsurface. The original design solution was to create thin water layers (1 μm) sandwiched between rock layers (10 cm), each with a nm-scale gap of vacuum in between to avoid the afore-mentioned issue of volume overlap leading to segmentation faults and simulation crash. The advantage of such a set-up is that it is very easy to recreate the subsurface profiles of the regolith. The commands to create a regolith layer logical volume, which is then positioned at the appropriate depth as a physical volume, are placed in a *for* loop with parameters such as subsurface regolith density, temperature, water content, or elemental composition set to be simple functions of the incrementing depth. Thus, an arbitrarily complex scenario,

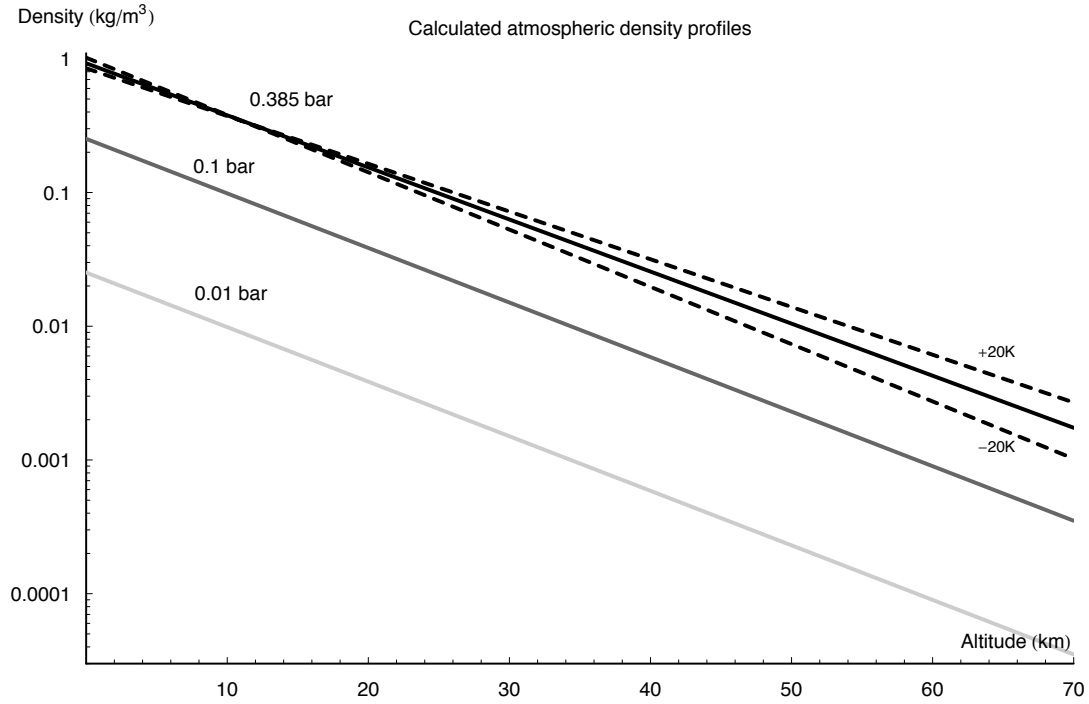

Figure 3.3: Altitude-density profiles of the calculated primordial atmosphere scenarios. Temperature sensitivity (±20 K limits) also shown for the 0.385 bar surface pressure case.

such as modeling the martian surface with a depth of wind-blown dust (dry, low density, soil elemental composition) atop a permafrost-laden regolith (higher density, increasing water content with depth, bulk rock elemental composition), is no more difficult to define within the DetectorConstructor than a basic uniform block of regolith.

The problem discovered with such a model set-up, however, is that it introduces an enormous number of layer surfaces within the 20 m of subsurface. With the design set to micron-thick water films buried between 10 cm regolith layers the number of top and bottom boundaries for all of the 200 water and rock slices totals 800, with roughly 200 surfaces subdividing the surface region with greatest particle flux within the secondary cascades. As explained in Section 2.4.3 on page 41, the propagation methods within Geant4 require that a particle must terminate a step just before a volume boundary and initiate a new step on the other side of the boundary. Thus the number of steps taken by propagating particles is forced much higher by this model design. This is especially true of the uncharged secondaries, such as neutrons and gammas, which could otherwise be allowed longer step lengths as they do not interact with the Coulomb field and only rarely interact with a target nucleus, but instead were being forced to take a much greater number of smaller steps. Looking ahead to Figure 6.4 on page 115, it can be seen that neutron and gamma flux in the near subsurface out-numbers other secondaries by more than an order of magnitude.

This excessive subdivision of the martian subsurface greatly increased the processing time required, with no commensurate benefit in data produced. The solution was to remove the numerous regolith layers, and instead embed the thin water layers as daughter volumes within the regolith container volume. This design was found to produce a marked increase in processing efficiency, and is a perfectly adequate solution for the uniform regolith scenarios; dry homogeneous and pure ice. For the more advanced regolith scenario of wet heterogeneous, whereby a layer of dry dust is created atop a denser permafrost-bearing regolith block, three

regolith layers were created, with individual layer thickness, density and composition, and the water layers embedded within these.

For the second application of the martian model, designed to calculate the energy deposited in the subsurface itself, the water layers were removed and only a single surface volume was considered for dry homogenous and pure ice models, with three layers for wet heterogeneous, in order to increase the running efficiency.

3.3 Visualisation

The capability for visualisation of the model geometry and particle tracks was added very early in the development process, as being able to see the computer's representation of the geometry is a very powerful tool in bug-checking. The Heprep visualisation option was found to be very slow in rendering particle tracks, and could only present the model geometry as a wire-frame, not as solid volumes with appropriate shading. The capability for displaying through OpenGL was therefore coded into the model, with the macro file OGLVis.mac written to provide the necessary specifications to Geant4.

The visualisation attributes of the World volume, and atmosphere and regolith daughter volumes were set to transparent. The regolith layers were set to appear red, and the atmosphere layers as blue. Within the *for* loop constructing and positioning the atmosphere layers, the saturation of the visualisation colour was specified as a linear function of the position altitude, so that higher layers are specified as darker colours. The effect of this is that the atmosphere is rendered as a smooth graduation from light blue at the surface to black at the top of the column. This can be seen clearly in the visualisation image in Figure 3.4.

Particle tracks within the secondary cascades are rendered with the default Geant4 settings, colour-coded to particle charge as explained in Section 2.8 on page 47. No action for visualising particle interaction events within the sensitive detectors was coded into the model, considering the enormous number of such events within the secondary cascades and the number of sensitive detectors embedded in the subsurface column. Figure 3.4 also displays the visualisation of the model geometry and particle tracks of the subsurface particle cascade initiated by an energetic primary.

3.4 Physics models

No default physics list is provided by Geant4, so it is a requirement of the application developer to register relevant processes to particles. Deciding on relevant processes and models to include and appropriate energy ranges requires an in-depth understanding of high energy particle physics, and was not feasible for the author. Therefore, pre-formed physics lists were sought. The Geant4 collaboration hosted a website that claimed to provide such approporate formulations, including one labelled Cosmic Ray Showers which would have been ideal. The website links were dead, however, and on enquiry to the named software developers it was revealed that such a project had fallen to the way-side. Another researcher, Laurent Desorgher, was able to provide the required physics lists, which he had created for his freeware Geant4 package ATMOCOSMICS [72]. ATMOCOSMICS had been designed for simulating cosmic ray particle showers

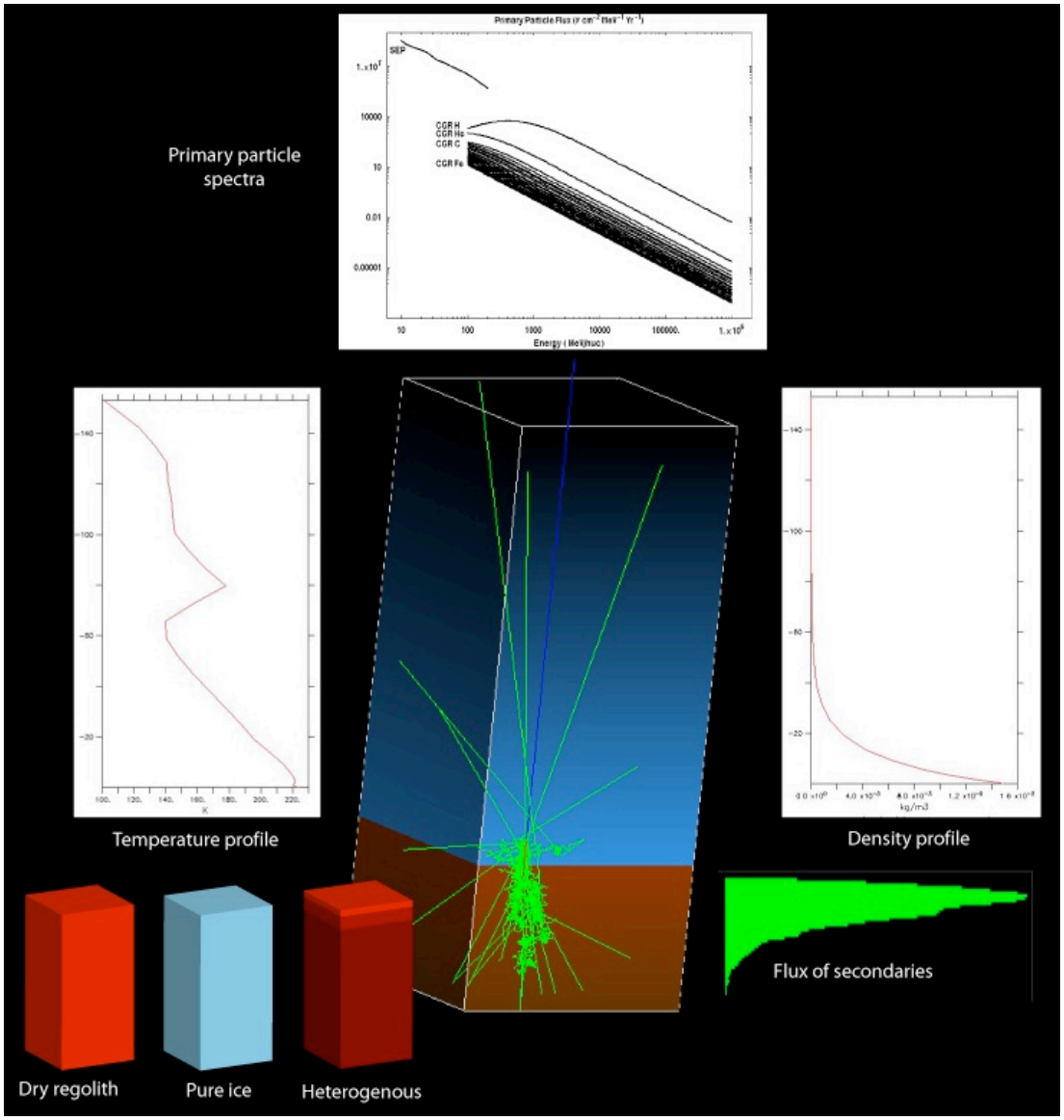

Figure 3.4: Schematic of the Mars radiation model design. The central visualisation is produced by the model and shows the geometry of atmosphere and subsurface columns (here scaled arbitrarily), and the blue particle track of an energetic ion penetrating the thin martian atmosphere to generate a great cascade of secondaries within the subsurface (colour-coded to particle charge: neutral, green; positive, blue; negative, red). Inputs to the model, such as the energy spectra for SEP and GCR primaries (top) and physical parameters of the atmosphere (left and right) are also shown. Three surface scenarios were constructed, dry regolith, pure ice, and a spatially heterogenous layered permafrost model. Data produced by the model is depicted by the green histogram of secondary flux as a function of depth.

in the terrestrial atmosphere, and so contained physics descriptions appropriate to the martian model, already validated against experimental data [72]. Desorgher had since merged ATMOCOSMICS with another of his models, MAGNETOCOSMICS for simulating particle transport in the geomagnetic field, to produce the more complete package PLANETOCOSMICS [71].

Although this physics list was obtained from a collaborator, it was necessary to completely understand its workings in order to integrate the class structure into the existing model. In fact, an error in the provided ATMOCOSMICS physics lists was identified by the author and corrected, as described below in Section 3.4.4.

3.4.1 Class structure

The complete ATMOCOSMICS physics lists are divided into six separate source files:

- ATMOCOSPhysicsList.cc
- ATMOCOSGeneralPhysics.cc
- ATMOCOSElectroMagneticPhysics.cc
- ATMOCOSMuonPhysics.cc
- ATMOCOSHadronicPhysics.cc
- ATMOCOSIonHadronicPhysics.cc

ATMOCOSPhysicsList.cc is the master class, called by the Geant4 run manager to invoke the registration of relevant physics models for all particle types. ATMOCOSGeneralPhysics.cc adds decay processes to the defined list of particles, and the applicability of the other four classes is self-explanatory from their name.

The physics models used by the martian radiation model are the ATMOCOSMICS defaults, as follows: electromagnetic physics is set as "STANDARD"; hadronic physics as "QGSP_BIC_HP" and light ion hadronic physics as "BIC". Thus, the model uses the standard electromagnetic models and does not implement the low energy extensions, such as treatment of Rayleigh scattering and fluorescence of excited atoms. These low energy physics extensions are valid down to about 250 eV and make direct use of electron shell cross-section data (whereas the standard functions which are optimized for higher energies rely on parameterisations of these data) [228], but are not worth the processing cost for the simulation of energetic secondary cascades. The QGSP_BIC_HP hadronic physics combination implements available models as follows [70].

3.4.2 Hadronic physics

The reactions of energetic (E $>$ 15 GeV) pions, kaons and nucleons are simulated using theory-driven models. A quark gluon string (QGS) model is employed to model the "punch-through" interactions of an energetic projectile with the target nucleus. After this interaction, the decay of the excited nucleus back to equilibrium is modeled with an extensive evaporation phase (using G4Evaporation, G4FermiBreakUp and G4StatMF multiple fragmentation classes). For

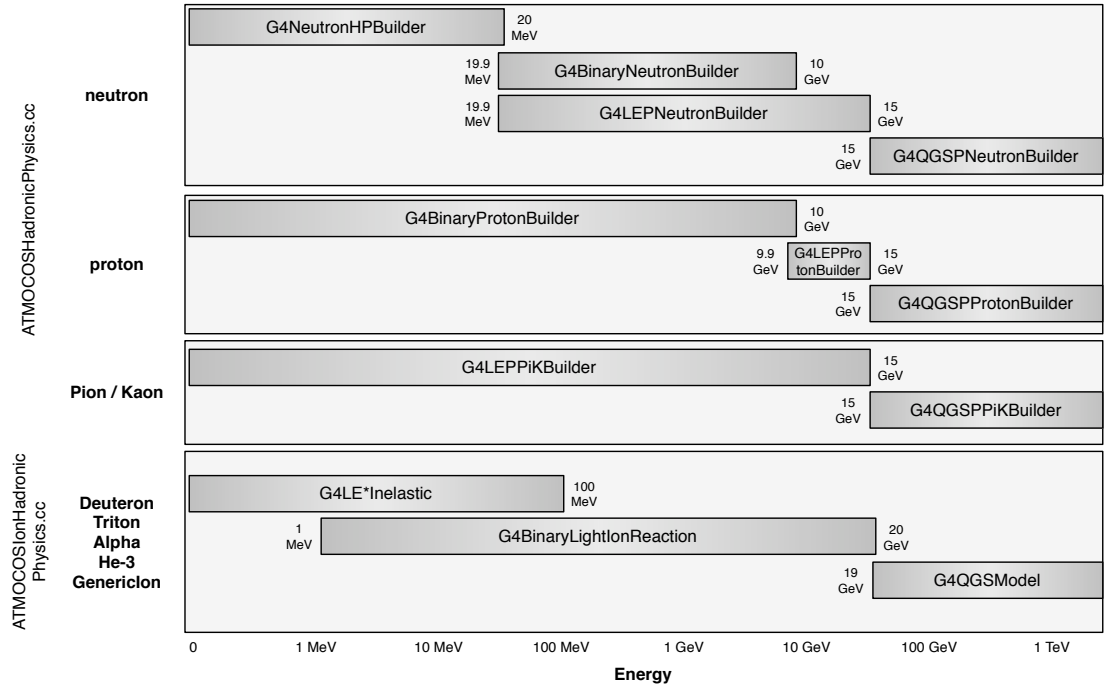

Figure 3.5: Diagram showing the Geant4 classes, and energy ranges, used to model hadron and nuclear interactions in the ATMOCOSMICS physics lists adopted in this model. Diagram constructed by the author.

lower energy inelastic interactions and elastic scattering of these particles, the Geant4 low energy LEP and high energy HEP parameterised models are employed. Inelastic scattering of protons, neutrons, pions and kaons below 10-15 GeV is calculated with the appropriate binary intranuclear cascade (BIC) models [70].

An extension to the BIC model is used to treat the hadronic interaction of light ions with a target nucleus. The PLANETOCOSMICS manual [70] states that the validity of this model is only up to Z=6 (carbon ion projectiles) with an energy limit of 5 GeV/nuc. In conversation with the creator [Desorgher, personal communication], however, it was discussed that pushing the light ion BIC model up to energies of 10 GeV/nuc, or possibly even slightly higher, still produced reasonable results, and is probably not greatly incorrect for Fe ions [personal communications]. Unfortunately, the standard distribution of Geant4 provides no capability for simulating heavy or very energetic ions beyond the validity of the BIC model. Despite these Z and E limitations for simulating heavy ions, however, the Geant4 physics descriptions can still handle 87% of the complete GCR spectra, as calculated by energy integration of the CREME-96 primary model (Z=1-6 and E<10GeV/nuc).

Elastic and inelastic scattering of neutrons with energy < 20 MeV uses the Geant4 HPNeutron model based on the ENDF (Evaluated Nuclear Data File, a database of cross-sections, angular distributions, and so on) (http://www.nndc.bnl.gov/exfor7/endf00.htm). No electromagnetic nuclear physics is considered.

A summary of the Geant4 physics model classes employed by these physics lists in simulation of hadronic and ion hadronic interactions, and the energy ranges over which they are registered to be active, is provided in Figure 3.5. Muon and electromagnetic electromagnetic physics lists are not shown in this chart as these define no energy dependency on the models invoked.

In order to simulate primary ions up to the energy ceiling of 10 GeV/nuc, the maximum energy for the range of application of the Binary Cascade physics model for light ions was pushed to 20 GeV/nuc. This is necessary to prevent crashing of the model if any nuclear fragments are produced with an energy per nucleon higher than the primary, and is beyond the stated maximum of applicability of the BC model. The vast majority of secondary ions remain below the 10 GeV/nuc maximum, however, and the BC model is not expected to produce greatly inaccurate results above the energy limit [Desorgher, personal communication].

3.4.3 Cut in range

The cut in range assigned to the electromagnetic particles (gamma, electron and positron) with the *SetCuts()* function (see Section 2.4.4 on page 43) was chosen to be 1 cm, as follows. If an electromagnetic particle is created at a distance greater than the range cut from a sensitive detector it is only allowed to continue its propagation if it has an energy greater than the calculated cut for the material, as it may contribute to the data gathered. Thus, the cut in range should be selected to be small enough so that the lowest energy data collection bin of interest is not neglected, and yet large enough so that low energy particles are terminated and processing time conserved. Table 3.1 shows the cuts in energy calculated by Geant4 for a 1 cm range cut within the main materials in the martian model. The lowest energy bin for the secondary spectra is 1 MeV, and therefore this choice of CutValue is not problematic.

Table 3.1: The electromagnetic particle energy cuts calculated by Geant4 for a 1 cm cut in range within the three main materials in the model: the surface-level atmosphere (1.31×10^{-5} g/cm^3), dry topsoil (2.81 g/cm^3), water (1 g/cm^3)

	gamma	e^-	e^+
Atmosphere	990 eV	990 eV	990 eV
Dry topsoil	23.32 keV	4.838 MeV	4.605 MeV
Water	7.764 keV	2.147 MeV	2.044 MeV

In addition to the Geant4 cut in range method for saving processor time, a user action was written to kill unnecessary particles. *An if* logical statement was coded into the G4StackingAction class to detect newly created tracks of the particle type "lepton" with charge 0. These conditions define neutrinos, which are created by nuclear reactions but do not themselves interact with the material of the martian atmosphere and regolith. Tracking their trajectory through the model only wastes processor time and so these tracks are removed from the stacking manager as soon as they are created.

3.4.4 Resolution of physics bug

A problem was isolated and solved within the ATMOCOSMICS physics lists provided by Desorgher. During model testing a curiously anomalous result was noticed: the penetration of heavy ions exceeded that of all other secondaries, with the flux profile also not following the expected exponential decay curve, as seen in Figure 3.6.

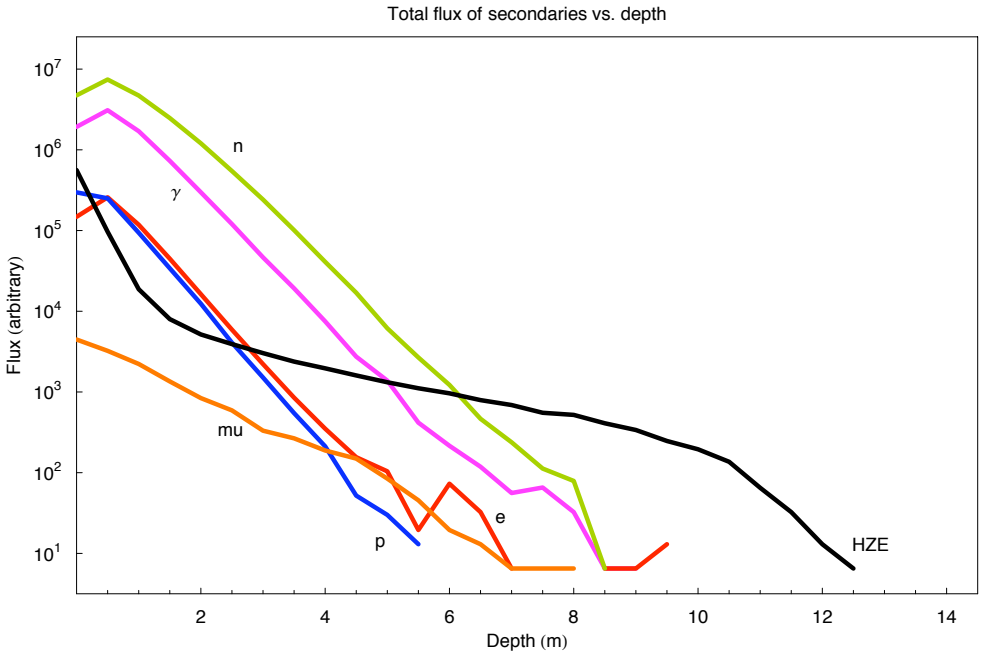

Figure 3.6: The flux-depth profiles of particles in the secondary cascades created by C-12 ion primaries (non-normalised, arbitrary units of flux). The error in the physics lists is manifested in the anomalous behaviour of HZE particles (black line); such particles are penetrating much deeper into the martian regolith than any other secondaries, and are not following the expected profile of exponential decline.

Certain ions were propagating much further than they ought to, indicating an error somewhere within the physics model code. Two possibilities for the root of the problem include the data processing routines incorrectly attributing other secondaries as heavy ions (deemed to be a very unlikely possibility) or that certain heavy ions were escaping treatment by the physics lists and so could propagate through ∼10 m of solid rock without triggering an interaction.

This error was originally thought to be due to primary ions generated with more energy than was permitted by the Geant4 physics list. The light ion binary cascade physics model ought not be used for ions with energy greater than 10 GeV/nuc (see above), and so any ions for which this holds true may fall outside the energy ranges defined for physical interactions. They would thus evade physical interaction and propagate unhindered through metres of matter. However, even primary ions permitted by this limit, such as 100 GeV C-12 ions (8.33 GeV/nuc), were still seen to produce anomalous secondary ion cascades. It was reasoned, therefore, that even though the primary ions fell within this limit (e.g. a 100 GeV C-12 primary), break-up of the primary could result in nuclear fragments exceeding the energy limit.

To test this hypothesis, the model was set-up with a monoenergetic source of 100 GeV C-12 primaries (8.33 GeV/nuc), and the user class G4StackingAction commanded to report to an external text file every time a secondary ion exceeds an energy threshold of 8.5 GeV/nuc (i.e. greater than the primary particle). The results from a total test sample of 545 100 GeV C-12 primaries are given in Table 3.2.

All of these energetic secondary particles were found to be lighter than Z=3 (He-4, He-3, He-2, triton and deuteron). The test revealed that although it was indeed possible through projectile fragmentation to produce lighter ions with a kinetic energy per nucleon greater than the primary,

Table 3.2: Results of a test run of 545 100 GeV C-12 primaries (8.33 GeV/nuc), counting the number of secondary ions produced exceeding the stated energy limits.

Energy limit	# secondary ions exceeding limit
E > 8.5 GeV/nuc	301
E > 9.0 GeV/nuc	6
E > 9.5 GeV/nuc	0
E > 10.0 GeV/nuc	0

none of these exceeded the 10 GeV/nuc limit. This energy limit hypothesis could not, therefore, account for the anomalous results and was rejected.

A second test model set-up was programmed to provide additional output to help track-down where the physics error lay. The data stream sent to external text file now included greater information on any secondaries exceeding 6 GeV/nuc, including the position of the particle within the model, as well as the full profiles of energy deposition and secondary energy spectra, to provide information to help spot any pattern in the occurrence of this hadronic anomaly. The energy of the primary was stepped down over the course of several model runs to attempt to isolate at what energy the hadronic physics problem first appears. C-12 primaries were run at 80 GeV, 70 GeV, 60 GeV, 50 GeV, and 20 GeV, as well as 20 GeV alpha primaries. The problem was seen to occur down to 50 GeV C-12 primaries and 20 GeV alphas, but not for 20 GeV C-12. This suggested that there may have been an energy-dependence to the occurrence of the anomaly, but was not limited to the higher energy primaries.

A third test model was constructed, this time outputting data on every single nucleus detecting crossing a sensitive detector boundary, to enable searching for any pattern in the occurrence of the hadronic fault. Only a single primary was simulated in each model run and results in which the anomaly occurred were separated from normal runs to aid trouble-shooting. It was noticed in the problematic runs that a He-3 nucleus propagated across many consecutive sensitive detectors, registering in successively deeper sensitive detectors with a diminishing kinetic energy, but still often propagating up to 8 m through the regolith material. In each case the trackID of the penetrating particle was identical in all the sensitive detectors, confirming that it was indeed the same He-3 nucleus propagating unhindered. Apparently, therefore, a He-3 ion, once created by nuclear fragmentation, does not seem to undergo proper physical interaction irrespective of its kinetic energy (ranging from around 20 GeV down to less than 0.1 GeV).

In light of this discovery, the ATMOCOSMICS physics lists imported into this martian model were scrutinized for potential subtle bugs, focussing on the specifications for He-3 ions in the hadronic physics list. It was thus discovered that although He-3 ions have an Elastic process defined, no physics models were registered to He-3 for inelastic interactions. The anomalously deep penetration of the hadronic cascade is therefore explained by errant He-3 ions that do not interact inelastically, but steadily lose kinetic energy through elastic collisions with target nuclei until they are at rest and removed from the Geant4 tracking manager. This error was corrected, and the model re-run to confirm that the hadronic physics was indeed now behaving as expected.

3.5 Particle Source

3.5.1 SEP and GCR primary spectra models

Several recent models exist to describe the GCR environment, in terms of particle energy spectra, at different locations within the solar system and as modulation by the sun's magnetic field varies. These are, in summary [164]:

- Nymmik's Model, or the Moscow State University Model [171, 170]
- CREME-96 (Cosmic Ray Effects on MicroElectronics) model, an update of CREME-85, based on Nymmik's Model of GCR [221]
- CHIME Model [45]
- Badhwar and O'Neill Model, or the Johnson Space Center Model [24, 25, 176]

The alternative models differ from each other mainly in their selection of the unmodified local interstellar spectrum and the solar activity parameter used to calculate modulation of the primary spectrum by the heliospheric magnetic field [164]. Uncertainties in the GCR spectra are reported to be around 15%, whilst uncertainties in the modeled SEP spectra may be much larger [164].

In the first instance, this research used the GCR and SEP spectra provided by ESA's SPENVIS (SPace ENVironment Information System) on-line database (http://www.spenvis.oma.be). This database is used widely by the space community and can be accessed through a user-friendly website. Spectra can be requested of both GCR (implementing the CREME-85 model [3]) and mean SEP (using the King [131] or JPL [85] models of solar proton events) for any period in the solar activity cycle and any interplanetary radial distance from the Sun (relative to the mean Earth-Sun distance, the astronomical unit, AU), and so were ideal for the modelling of cosmic rays at Mars. SPENVIS 4.2 was accessed in November 2005 for cosmic ray spectra at 1.5 AU (mean martian orbit): the JPL-91 model [85] solar energetic proton spectrum averaged over the 11-year solar activity cycle and GCR spectra [3] at solar minimum and maximum for ions H – Fe. A power-law tail was extrapolated from each of the GCR spectra to extend beyond the SPENVIS energy limit of 20 GeV/nuc to 1 TeV/nuc.

For the purposes of simulating the primary GCR spectra in the model, this great range in primary energy was subdivided into four sections covering one order of magnitude in energy each: 100 MeV/nuc – 1 GeV/nuc; 1 GeV/nuc – 10 GeV/nuc; 10 GeV/nuc – 100 GeV/nuc; 100 GeV/nuc – 1 TeV/nuc. Each of these sections was then simulated in turn so as to ensure that sufficient particles from all energy levels were sampled and the primary spectrum reproduced as faithfully as possible. These energy subdivisions are shown in the primary spectra plotted in Figure 1.4 on page 23.

It was discovered late in the development and utilisation of the martian radiation model, however, that the GCR spectra produced by the SPENVIS database are erroneous. This issue, and its resolution, is discussed in depth at the beginning of Chapter 5. More reliable GCR energy spectra were therefore sought, and the CREME-96 model [221] was accessed directly from the

National Research Laboratory (NRL) dedicated website (https://creme96.nrl.navy.mil). GCR near-Earth interplanetary fluxes were obtained for ions H – Fe, covering the energy range 1 MeV/nuc – 100 GeV/nuc, at solar minimum and maximum. No attempt was made to re-weight these energy spectra produced for near-Earth interplanetary space (1 AU from the Sun) to the 1.5 AU mean martian orbit because although the GCR intensity increases when moving radially outward towards the boundary of the heliosphere, the gradient in the inner solar system is small and can be justifiably neglected [164]. Figure 3.7, below, reproduces the plot of GCR flux (130 – 220 MeV protons) as a function of radial heliocentric distance in astronomical units (AU) from McDonald *et al.* (2003) [150]. It can be seen that there is very little change between terrestrial (1 AU) and martian (1.5 AU) orbits at either solar activity minimum or maximum, although Fujii and McDonald (1997) [94] report that the radial intensity gradients are greater at solar maximum. The GCR flux at the orbit of Mars is expected to be no more than ∼5% greater than that at 1 AU [164]. Re-weighting of solar particle event proton fluence from measurements in near-Earth space to martian orbit should, however, be conducted using an inverse square law [164].

The primary spectra used in generating the results reported here (annual mean SEP spectrum from SPENVIS and GCR spectra for H – Fe ions from CREME-96) are plotted in Figure 1.4 on page 23.

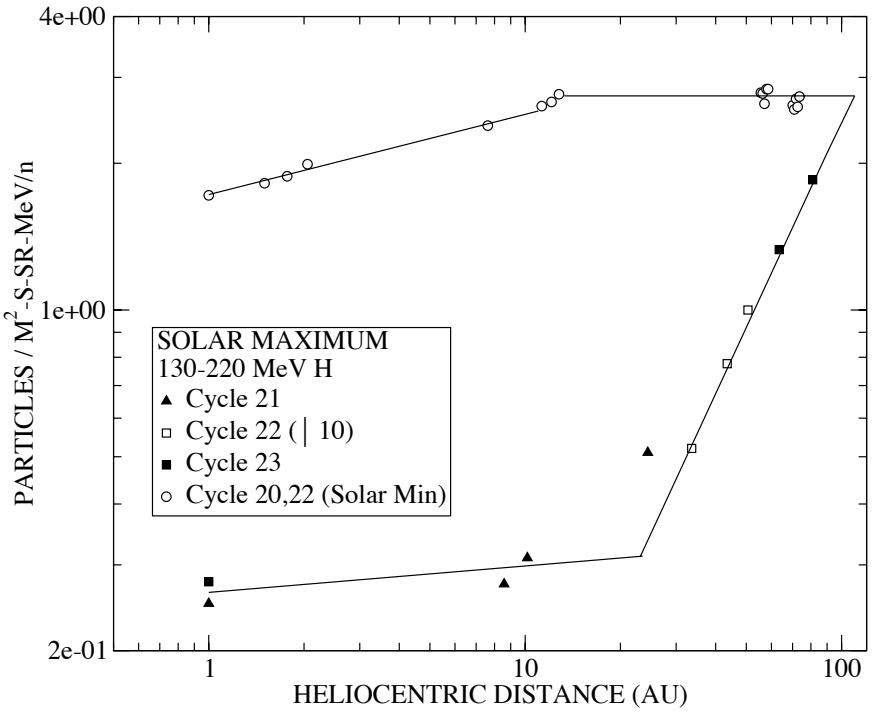

Figure 3.7: The GCR flux (130 – 220 MeV protons) as a function of radial heliocentric distance for both solar activity maximum and minimum conditions reported by Fujii and McDonald (1997) [94], showing that the radial intensity gradient is very low in the inner solar system and the difference in GCR flux between Earth orbit (1 AU) and martian orbit (1.5 AU) can be neglected.

3.5.2 Primary source geometry

The isotropic cosmic radiation incident on the martian surface from a hemispherical source surface (the sky) is reproduced in the model using a geometric transformation [202, 126]. A

point source emitting primary particles with a cosine-law angular distribution incident on a perpendicular planar surface recreates the spread of incoming particles, with most incident perpendicularly onto the martian surface and a diminishing flux at larger incident angles, with the limit of no flux striking the surface horizontally.

Within the Geant4 model, General Particle Source (see Section 2.5.1 on page 45) is used to position the point source at 75 km altitude, above the center of the atmosphere-surface column, and generate primaries within a cone ($-\pi/2 \leq \theta \leq \pi/2$) with momentum distribution $cos(\theta)$. The energy of each generated primary is drawn from a histogram describing the desired primary spectrum. Although surface and subsurface particle fluence is normalised to that incident on a cm^2 unit area, the x and y dimensions of the model column are actually arbitrarily large in order to capture the full angular distribution of primaries. The values selected, $x = y =$ 5,000 km, ensure that no primaries or secondaries exit the world volume through the side faces and so are captured by the sensitive detectors.

Normalisation of the data generated by simulated primaries to the actual incident cosmic ray spectra (both SEP and GCR) is as follows.

3.5.3 Fluence normalisation

The incident fluence of isotropic cosmic ray primaries onto a unit area planar surface is given as $\varphi(E, \theta)$, a function of both primary energy and angle of incidence and so takes units of $cm^{-2}MeV^{-1}Sr^{-1}$. The angular distribution of primaries incident onto a planar surface can be simulated with a perpendicular cone of particles emanating from a point source with a cosine-law angular distribution [126]. This simulated integral flux, known as current, is given as:

$$j(E, \theta) = \varphi(E, \theta).cos\theta \ , \quad 0 \leq \theta \leq \pi/2 \tag{3.4}$$

where the $cos\theta$ factor determines the cosine-law angular dependence: most flux is incident perpendicularly onto the target surface, diminishing with larger θ and with the limit of no flux entering horizontally ($cos\frac{\pi}{2} = 0$).

The total incident current, integrated over both the entire energy range considered and the $0 \leq \theta \leq \pi/2$ angular distribution of the particle cone is thus:

$$J = 2\pi \int_{E_{min}}^{E_{max}} \int_{0}^{\pi/2} j(E, \theta) \ sin\theta \ d\theta \ dE \tag{3.5}$$

with the factor 2π derived from an initial integration around the azimuthal angle Substituting in the identity of the simulated fluence given in Equation 3.4 yields:

$$J = 2\pi \int_{E_{min}}^{E_{max}} \int_{0}^{\pi/2} \varphi(E, \theta) \ cos\theta \ sin\theta \ d\theta \ dE \tag{3.6}$$

$$J = \frac{1}{2} \ 2\pi \int_{E_{min}}^{E_{max}} \varphi(E) \ dE \tag{3.7}$$

$$J = \pi \int_{E_{min}}^{E_{max}} \varphi(E)\, dE \tag{3.8}$$

The factor of π is thus used to normalise the fluence of the simulated spectra to that of the actual cosmic ray spectra with units $cm^{-2}MeV^{-1}$. The segments of the simulated spectrum are fitted to this target primary spectrum as explained in Section 3.10 on page 79.

3.6 Event detection and data capture

Two distinct modes of data acquisition were developed for the martian model. Firstly, data was required on the fluence and energy spectra of important secondary particles, as well as the radiation dose, both physical and biologically-weighted, delivered to microbial populations as a function of depth in the subsurface. Secondly, a simplified data acquisition structure was used to register only the energy delivered to the subsurface material as a function of depth, thus greatly improving processing time.

3.6.1 First configuration

As outlined in Section 3.2, the first application of the model involved burying micron-thick layers of water every 10 cm within the martian subsurface. The water component added by the embedded cell layers is negligible, as they contribute less than 0.001% water by mass (1 micron-layer per 10 cm thickness of regolith). These were designated as sensitive detectors (SD), and thus triggered a hit for every event satisfying the selective criteria defined in the SD class. The criteria used were: for every fifth sensitive detector layer report on the energy and type of every particle traversing the top surface, and also report on the particle type and energy deposited in every energy deposition event in all SD water layers. The deposited energies were also weighted by a factor related to biological effect, a function of the depositing particle type, energy and linear energy transfer, as explained in Section 3.6.3.

The desired information from these events was stored in data arrays during processing, and output to an external file at regular intervals. The energy deposition storage array was thus a matrix of 13 columns, consisting of the most important particle types (gamma, e^-/e^+, muon, pion, neutron, proton, deuteron/triton, He-3/alpha, Z3-11, Z11-18, Z19-36, other) and one total tally, and 200 rows (data acquired for every 10 cm, over 20 m depth). The weighted energy deposition matrix was of identical dimensions.

Information on particle energy spectra was stored by filling-up a 14,400-element three-dimensional data array: 40 depths (every 0.5 m for 20 m) by 6 particle types (gamma, e^-/e^+, muon, neutron, proton, HZE) by 60 energy bins. The energy bins were distributed evenly through logarithmic space between 1 MeV and 1 TeV, with 10 bins assigned to each order of magnitude of energy.

Furthermore, an energy histogram of simulated primaries that have contributed to the data was stored to enable collation of data from separate runs to recreate the complete cosmic radiation spectra. Also recorded were tallies on the total number of primaries processed, the lowest energy and the highest energy primary.

3.6.2 Second configuration

After processing, analysis, and publication of results of the first application, the martian model was redesigned to produce data on the energy deposited in the surface material itself, rather than thin layers of water. The removal of the 200 water slices and intervening rock layers greatly increased the processing efficiency of the model, as explained in Section 3.2.3.4. With only a single sensitive detector in the subsurface (or three in the case of the subdivided wet heterogeneous model), it was no longer possible to use the repeated layers to extract information on the depth of any energy deposition event. The solution was to use "virtual layering".

The user defines the number of depth bins to be used in calculating the dose-depth profile during processing, equating to the number of virtual layers inside the subsurface. Virtual layer boundaries thus occur every $^{total\,depth}/_{number\,of\,layers}$ m in the subsurface. The subsurface sensitive detectors are only triggered by energy deposition events, and capture information on the pre-step and post-step point of the propagating particle over which the energy is deposited. The virtual layer that this step corresponds to is calculated, and the deposited energy binned accordingly. If the energy deposition step is calculated to have traversed a boundary between two virtual layers, the energy deposited over that step is attributed to the two layers in accordance with the proportion of the step length in each.

3.6.3 Biologically-weighted doses

The International Commission on Radiological Protection (ICRP) provides information, recommendations and guidance on many aspects of ionising radiation. Several of its reports [113, 114, for example] contain guidelines on the method for weighting physically absorbed radiation doses to account for the differing radiological potential of, for example, heavy ions compared to gamma rays, appropriate to this study. These weighting factors have been used previously in astrobiology research on the effects of ionising radiation on microbial survival [181]. The product of the absorbed dose, D, and the corresponding radiation weighting factor, w_R, is termed the equivalent dose, H_T. The weighting factors are dependent on the particle type and energy. The weighting factor for x- and gamma-ray photons of any energy is specified as 1, and the factor for other radiations is based on observational data of their relative biological effectiveness, RBE (see Radiobiology Section 1.3 on page 25). The 1990 Recommendations of the ICRP [114] are used here as specified below in Table 3.3. Neutrons are not listed here as they are not directly ionising, and their radiological effect is mediated by recoil nuclei, fragments, or protons.

Table 3.3: Radiation weighting factors. Taken from Table 1, p.6 of ICRP 1990 [114].

Particle type and energy range	Radiation weighting factor, w_R
Photons, all energies	1
Electrons, all energies	1
Muons, all energies	1
Protons, energy $>$ 2 MeV	5
Alpha particles, fission fragments, heavy nuclei	20

The weighting factor for radiation types not listed in Table 3.3, such as slow protons, is calculated from the LET-dependent quality factor, Q(L), as given in Table 3.4.

Table 3.4: Specified Q-L relationships. Taken from Table A-1, Annex A, p.81 of ICRP 1990 [114]

Linear Energy Transfer, L, in water (keV/μm)	Quality Factor, Q(L)
< 10	1
10 – 100	0.32L - 2.2
> 100	$300/\sqrt{L}$

The sum of the products of each energy deposition event and the particle-type-dependent weighting factor yields a biologically-weighted dose. Cellular survival after exposure to such a calculated dose can be estimated using experimentally-derived data on the surviving fraction of an original cell population after a known dose of a reference radiation (i.e. gamma or X-rays). The surviving fraction taken here to represent complete inactivation (sterilisation) of a microbial population in a soil sample is 10^{-6}. This threshold level is consistent with that used in previous studies [154, 181] and is also a functionally-meaningful cut-off, as will be discussed in Section 8.1 on page 144.

The survival curves of representative organisms were extracted from the literature, with the 10^{-6} limit extrapolated to be 1 kGy and 15 kGy for *E. coli* and *D. radiodurans* respectively [30], and 8.4 kGy for *B. subtilis* spores [33] .

3.7 Magnetic field

Some applications of the Geant4 toolkit can be satisfied with a simple uniform magnetic field attached to a daughter volume: modeling the emission of bremsstrahlung photons by an energetic electron deflecting by the Lorentz force within a synchrotron, for example. Simulating the influence of the martian crustal anomalies on incident cosmic radiation particles, however, requires a far more sophisticated approach. Crucially, the localised fields of the martian crustal anomalies are complex in both distribution and geometry, and so the magnetic field vectors must be explicitly defined at a lattice of points within a given volume.

The capability to read-in a 3D vector field from an external data file is presented in the advanced training example "*purging_magnet*", distributed with the Geant4 package. The magnetic field is described within a numerical matrix specifying the local field line vector (i.e. both field strength and direction) at a series of (x,y,z) coordinates. The coordinate granularity of this field grid can be refined for the specific scenario. Setting a shorter distance between data points allows for the accurate specification of a more spatially intricate field; fewer data points allows the optimisation of usage of computer memory as the vector field is stored by the programme. Linear interpolation is used to define field vectors between the explicitly specified coordinates.

Within the martian radiation model, a dedicated class, TabulatedField3D.cc, imports the vector field from the external file and stores it within arrays for later interrogation. This complex magnetic field is then attached to the atmosphere logical volume so that it is inherited by all daughter volumes, namely the layered atmospheric physical volumes. Whilst transporting charged particles through a region with attached magnetic field, Geant4 takes into account the associated Lorentz force and and solves the equation of motion to simulate the particle

deflection (see Section 2.4.5 on page 43). When queried, the TabulatedField3D class returns the x,y and z components of the local magnetic field at a specified point, and Geant4 uses this to calculate the deflection away from a linear trajectory during the stepping of the particle.

Extracting data on the fluence of charged particles onto the martian surface beneath a crustal anomaly is achieved by modifying the Hit class (see Section 2.6 on page 46) to register every particle traversing the top surface of the regolith block, and export the (x,y) coordinate of this strike to an external data file. After termination of the simulation, this data file is imported into a Mathematica programme (see Section 3.10 on page 79) written to display the spatial distribution of particle strikes onto the plane. Further post-processing is performed to generate a particle fluence map, with the individual hits summed into a grid of spatial bins (of user-defined dimensions), which can also be shaded to a fluence scale to produce a colour-coded surface fluence map.

The functionality of this code was tested by designing an artificial vector field with radially-symmetrical geometry similar to that of an isolated martian crustal anomaly (see Figure 1.3 on page 18). The magnetic vector at any point within a cuboidal volume of dimensions $100\times100\times50$ is defined as $(x/r,\ y/r,\ 2cos(r)/100.pi)$, where r is the radial distance from the origin, $r = \sqrt{x^2 + y^2}$, and with each vector component additionally scaled-down linearly as a function of altitude, z. A tabulated data file was constructed describing this vector field, and imported into the Geant4 model to test particle transport.

The success of this is displayed in Figure 3.8, with physics modeling turned off and subsurface particle propagation and and energy deposition ignored to alleviate processing demands.

Thus the deflection of primary particles propagating through the crustal anomalies, as well as back-scatter particles escaping upwards from the martian surface, can be handled simultaneously to the modelling of interactions within secondary cascades in the atmosphere.

Appropriate 3D data files describing the actual martian anomalies could not be located, however, and attempts to extract the C++ classes from PLANETOCOSMICS performing field transformations of the Cain 90 degree spherical harmonic model [42] were also unsuccessful. So although full functionality for simulating particle propagation through the crustal anomalies was developed in the martian model, the raw data could not be acquired and this feature of the model has not yet been utilised. Calculations were performed, however, on the gyroradii of charged particles of different type and energy to determine whether deflection of primaries by the crustal anomalies was likely to be a major influence on the surface radiation environment.

3.7.1 Calculation of gyroradii

A charged particle moving through a magnetic field experiences a Lorentz force, acting perpendicular to the velocity vector to cause the particle trajectory to curve into a circle (see Section 2.4.5 on page 43). The radius of this circle, the *gyroradius* or *cyclotron radius*, is calculated as follows.

The vector of the Lorentz force, $\mathbf{F}$, is given by the component of the charged particle velocity, $\mathbf{v}$, perpendicular to the magnetic field vector, $\mathbf{B}$ [132]:

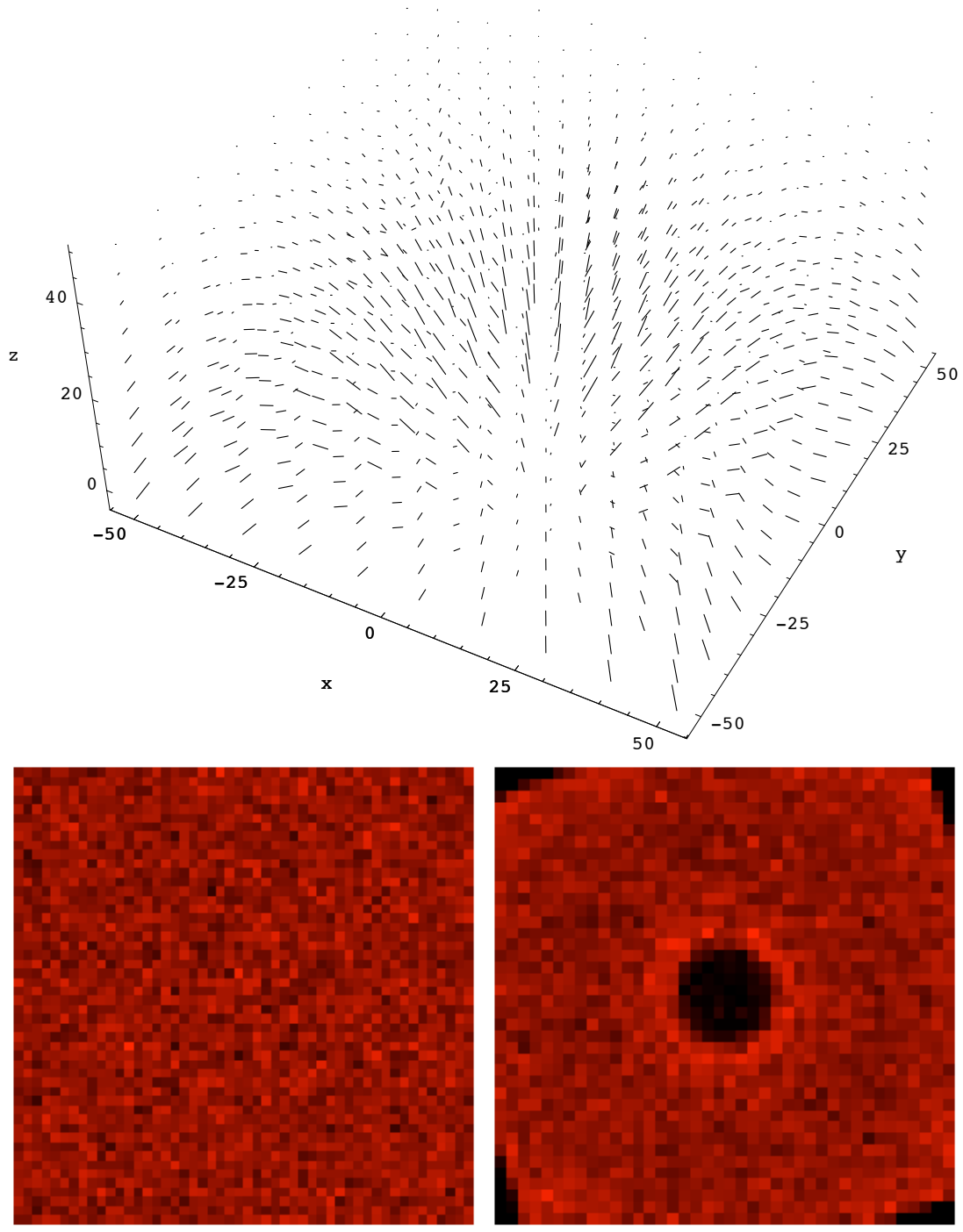

Figure 3.8: Tracking charged particle propagation through arbitrarily-complex magnetic fields. Top: the radially-symmetric vector field designed to test correct functionality of the model. Bottom: proton fluence maps (perpendicular incidence) on the martian surface with no magnetic field (left) and beneath the simulated crustal magnetic anomaly (right). All distances, field strengths and proton energies arbitrary for the sake of code validation.

$$\mathbf{F} = q(\mathbf{v} \times \mathbf{B}) \tag{3.9}$$

$$F = qv_{\perp}B \tag{3.10}$$

where $v_{\perp}$ is the velocity component perpendicular to the field direction, and B is the magnetic field strength.

The acceleration experienced by a particle following a circular path with constant speed (where the velocity vector is always perpendicular to the circle radius) is:

$$\mathbf{a} = \mathbf{v^2}/r \tag{3.11}$$

Substituting Equations 3.10 and 3.11 into Newton's Second Law of Motion ($\mathbf{F}$=m$\mathbf{a}$) yields:

$$qv_{\perp}B = m(v_{\perp}^2/r) \tag{3.12}$$

which rearranged to make the gyroradius, r, the subject becomes:

$$r = \frac{mv_{\perp}}{qB} \tag{3.13}$$

or the ratio of particle momentum to the product of charge and field strength.

For relativistic particles, the gyroradius is given as the ratio of the particle's relativistic momentum to its charge and the magnetic field strength perpendicular to the velocity vector. The *rigidity* of a charged particle is the ratio of its momentum to charge, and thus the gyroradius is ultimately a function of the particle energy and charge, and the field strength, as follows.

Relativistic momentum, P, is given by:

$$P = \sqrt{{E_{total}}^2 - {E_0}^2} \tag{3.14}$$

where E_{total} (MeV) is the sum of $E_{kinetic}$ and E_0, the rest mass energy. The proton rest mass is 938 MeV, and for electrons is 0.511 MeV [78]. Rigidity, R, is then:

$$R = P/Z \tag{3.15}$$

with Z in electron units. A unit change yields the rigidity in MKS (meter, kilogram, second) SI units:

$$R_{MKS} = R.10^6/c \tag{3.16}$$

where c is the speed of light, 2.9979×10^8 m/s. The gyroradius, ρ, in meters, is given as the ratio of rigidity to perpendicular field strength, B, in Tesla.

$$\rho = R_{MKS}/B \tag{3.17}$$

These calculations were coded and implemented in an Excel spreadsheet to output the gyroradius of a charged particle moving perpendicularly to the magnetic field direction, with the relevant parameters user-defined.

3.8 Randomisation

A randomisation class needs to be included in the model set-up, else each run would be identical. Randomisation within the model was implemented with HepRandom, because, as detailed in Section 2.10.3 on page 49, the internal state of the engine can be stored simply as two *long* variables and used to re-run a simulation of interest. HepRandom was implemented by utilising computer code contained within the Geant4 advanced example "*cosmicray_charging*". The randomisation seeds are regenerated every run from the computer's system clock, thus ensuring that each simulation run is properly randomised and unique.

3.9 Distributed computing

The running of Geant4 simulations of particle physics can be very processor-intensive, particularly for more energetic primaries. Attempting to generate sufficient data running the model solely on the author's laptop was quickly found to be totally impractical, and so the greater computing resources of the departmental computer network of G4 and G5 iMac machines were employed.

The Geant4 code must be compiled for both G4 and G5 processors, and so a compilation script was written to compile the model first as a G5 executable and secondly as a G4 executable, with the compiled program automatically sent through the local network to the appropriate machines. After compilation, another script is used to cycle through each machine in turn to instruct it to process a particular segment of the primary spectrum. The G5 computers can process several times faster than the older G4 machines, thus the most efficient system for farming out processing jobs to the iMac network was to send the lower energy primaries to G4 machines, and the higher energies to G5.

For reasons unknown, computers would occasionally hang whilst processing the martian model, and so another script was written to interrogate each of the computers on the network in turn, retrieving information on how many primary particles each has processed, whether any user is currently logged-on, and the time-stamp of the most recent saved data file. Thus, if a particular computer has hung and not recently saved a data file it can be instructed through the network to abort the current simulation and restart afresh. The most current saved file is recovered so that no data is lost.

When sufficient primaries have been processed, another script is executed to instruct each computer to abort the current model and retrieve the most recent saved data file. These raw data files are uniquely labelled, and then processed to produce the required information, as described below.

3.10 Post-processing

Geant4 provides no native data processing or plotting capability, but is designed to output data into a number of optional packages. Utilization of several external data processing packages, recommended by the Geant4 documentation [232], was attempted. Anaphe had been discontinued in its support by the developers ("dead-ended"), and no installation for MacOSX could be found. JAIDA and AIDAJNI require Geant4 to be compiled with OpenGL visualisation disabled, and so were discounted due to this incompatibility. OpenScientist requires the prior installation of OpenMotif and additional libraries added, which was all dutifully followed, but OpenScientist could not be successfully installed. The decision was therefore made to create bespoke data capture, pre-processing and storage code within the Geant4 martian model. The data capture and pre-processing routines are described in Section 3.6 on page 72, with the details of data output and post-processing described below.

A series of Mathematica programmes (Mathematica ver.5.2, Macintosh, © Wolfram Research, Inc., www.wolfram.co.uk) were written to automate the process of combining data produced by separate runs of the model, weight them accordingly to recreate the complete primary spectra, and plot desired results. The sequential process described below is summarised diagrammatically in Figure 3.9.

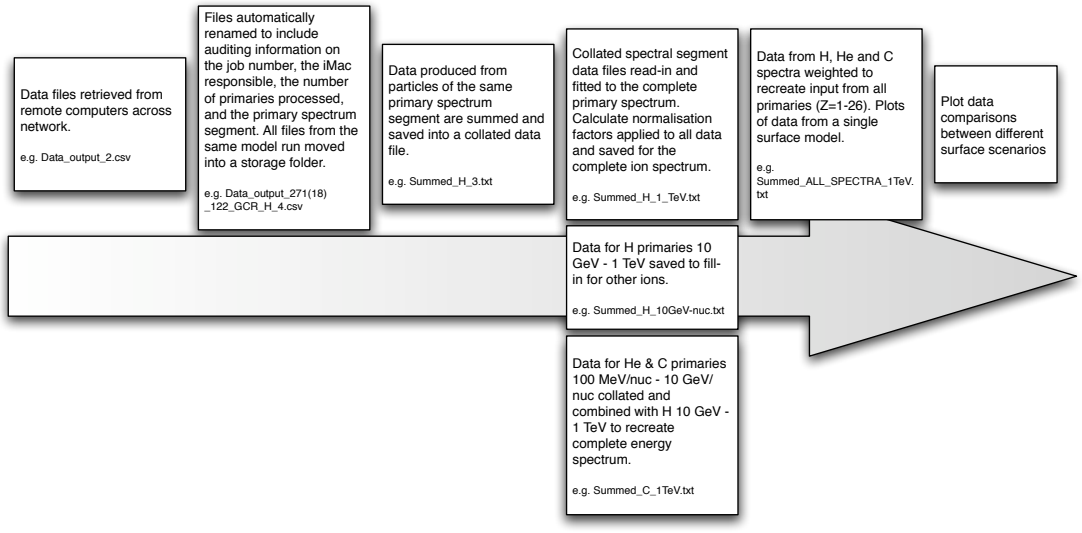

Figure 3.9: Schematic illustrating the post-processing and recombination of model data

Firstly, a programme is run to access the file names of the recently-completed processing jobs, and relabel them with pertinent information. Thus, the example filename "Data_output_271(18) _122_GCR_H_4.csv" includes the job number; the iMac responsible; the number of primaries processed; and the primary spectrum segment. All data files from the same model run are stored in the same folder.

Data produced from particles of the same primary spectrum segment - proton primaries between 1 GeV and 10 GeV, for example - are read in to another Mathematica programme, one data file at a time, and summed. This collated data is saved in a new file, such as: "Summed_H_1.txt". The programme collates each primary spectrum segment in turn, and for all primary particle types (GCR H, He and C, and SEP), in a nested loop structure.

The collated data files for each spectral segment are read in to another Mathematica programme and fitted to the target primary spectrum. This is accomplished by integrating beneath the primary spectrum to find the total energy contained within each of the four energy bands, and finding the ratio of this value to the energy contained within the processed primary segments. Multiplying the primary fluence data of each segment by its calculated factor thus recreates the target spectrum, as shown in Figure 3.10.

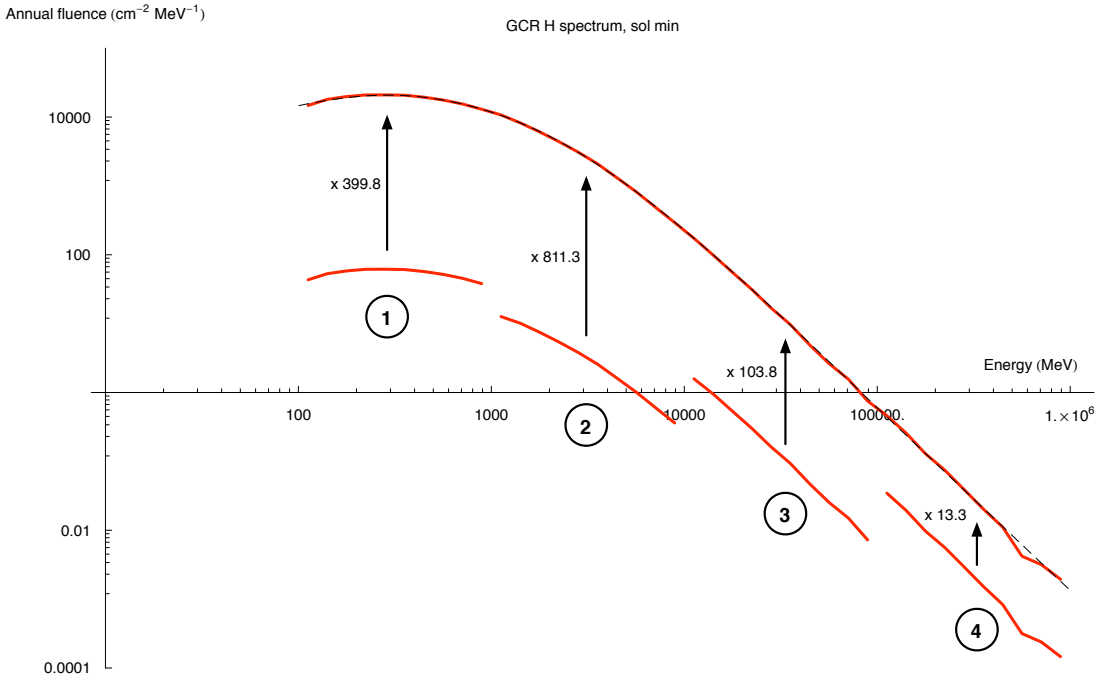

Figure 3.10: Recreating the complete GCR proton spectrum (dotted line) by weighting the data from primaries simulated in the four energy bands (red lines).

These calculated multiplication factors are then applied to all of the data generated by the appropriate spectral segment, and the data generated by the four contiguous energy segments collated together. This data set, representing the results from the complete primary spectrum (100 MeV/nuc – 1 TeV/nuc) for a complete year of fluence for a single primary ion, is now saved in a data file such as "Summed_H_1_TeV.txt". The data generated by the higher energy GCR proton primaries (10 GeV – 1 TeV) is resaved in another storage file, e.g. "Summed_H_10GeV-nuc.txt", in order to be used to fill-in for the other simulated primary ions, He and C, for the energy range beyond that which can be simulated by Geant4.

Data from the three explicitly-modeled primary ions, H, He and C, are multiplied by calculated weighting factors to account for the input of all GCR ion primaries (Z=1–26). Helium data is used to fill-in for ions Z=2–4 and carbon data is used to fill-in for ions Z=5–26 for energies up to 10 Gev/nuc. Beyond this energy limit, imposed by the limitations of Geant4 light ion physics models, proton data is used, as shown in Figure 3.11.

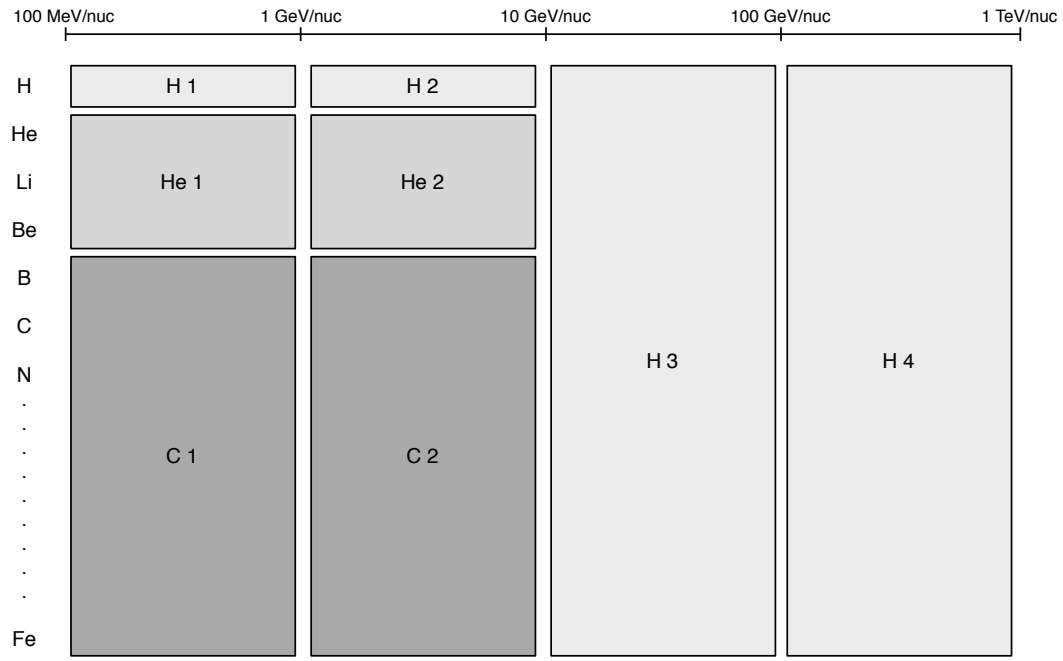

Figure 3.11: Approximation of the complete GCR spectra with modelled H, He and C primaries, and the use of proton data to fill-in the GCR spectrum beyond the ion and energy limits of Geant4 physics models.

The weighting factors are calculated as the ratio of the sum of integrations of all primary ions being filled-in for within the appropriate energy limits to the energy integration of the modeled primary spectrum. At the end of this process, the generated data, which now represents the modelled results from the annual complete GCR spectra (Z=1–26, E=100 MeV – 1 TeV), is saved to a data file called "Summed_ALL_SPECTRA_1TeV.txt".

The final step of data analysis, once complete data for each of the different surface scenarios has been generated and processed, is to load all the results into a single Mathematica programme coded with display functions, and plot the data to allow comparisons between the different set-ups.

Thus, the design of this post-processing and data handling system is much like a pipe-line, with the raw data steadily being refined and combined by a series of independent programmes with clearly-defined functions in the sequential process. Processed data is stored in unique files at the end of each stage, safe for further use or access by other programmes to handle the data in different ways. If more data is generated, or an alteration made to the required presentation of the results, the relevant data file is updated and the processing chain down-stream of that point run in sequence again. The complete data for a whole model run can be processed in minutes, almost entirely automatically. Such a system also makes importing of different data sets and drawing comparison plots very simple.

3.10.1 Proton-only approximation

If data is not required on spectra or fluence of secondaries, or deposited doses weighted by particle type, a reasonable approximation can be used to accelerate processing. The entire

GCR spectra, Z=1–26, E=100 MeV – 1 TeV, can be treated by simulating proton primaries only, and weighting data to account for the heavier ions, accordingly. Energy integrating the CREME-96 model shows that during solar minimum, protons account for 72.8% of the total energy delivered by GCR (70.4% at solar maximum), with 18.9% due to alpha particles (20.5% at solar maximum) and all heavier ions combined contributing only 8.2% (9.0%) of the total energy.

The appropriate weighting factor is calculated by finding the ratio of the energy integral beneath the proton primary spectra to the sum of the integrals for all heavier ions (helium to iron primaries). Integrating the CREME-96 model between 100 MeV/nuc and 1 TeV/nuc, the factor is found to be 1.37282 at solar minimum, and 1.41959 at solar maximum.

The proton-only approximation is used in the second application of the martian model. Validation of the results produced by this approximation is given in Section 5.5 on page 110.

3.11 Chapter summary

- The martian cosmic radiation model is columnar in design, with a layered atmospheric volume (simulations run of both the current situation and over planetary history) atop 20 m depth of subsurface (with several representative scenarios devised), as can be visualised by the code.
- Two configurations of the subsurface geometry and data extraction method were developed within the martian model, allowing the determination of particle energy spectra and biologically-relevant radiation doses as a function of depth, and doses deposited in the regolith itself, respectively.
- Primary cosmic radiation particles are projected down through the model, recreating the energy spectra of both SEP and GCR, and routines capable of simulating particle deflection by the crustal magnetic anomalies were also developed and tested.
- Appropriate physics models handle the high energy interactions within the secondary cascades, and during development of the martian radiation model an important bug in the adopted physics lists was identified and resolved.
- Distributed computing is employed to handle the onerous processing demanded by this sophisticated radiation simulation, and an extensive post-processing routine was developed to collate and normalise the modeled data and output desired data.

Chapter 4

Experimental method

Within this multidisciplinary study into the astrobiological implications of the martian radiation environment it is necessary to conduct ionising irradiation microbial survival experiments appropriate to martian conditions alongside the computer modeling of cosmic rays in the subsurface. The microbiological work conducted here involves firstly culturing novel cold-tolerant bacterial isolates from the Antarctic Dry Valleys, a terrestrial environment analogous to the martian surface, and characterising their phylogenetic diversity through molecular biology techniques. Several of these novel strains, and two model bacteria, were selected for gamma-ray exposures, with the experimental set-up designed to determine their survival in the ionising radiation environment of the martian subsurface permafrost and so linked to the dose rate predictions made by the martian radiation model.

4.1 Sterilization conditions

Unless otherwise stated, all culture media, buffers, reagents, glassware, and durable labware were sterilized by autoclaving for 20 minutes at 121°C. The polyethylene (PE) plastic caps used with the glass vials for irradiation are not thermostable, and so were sterilized by five hours' exposure to 254 nm UV lamps.

4.2 Sampling of Antarctic soils

The Antarctic soil sample utilised in this study was collected from the Miers Valley, within the McMurdo Dry Valleys region of the Antarctic continent, during the Antarctic summer of 2000. The sampling was performed by Don Cowan, and the particular soil sample used was collected

from GPS coordinates S 78° 05.868' E 163° 47.903' on 22^{nd} January 2000. The sample was noted as being a surface sediment from a shallow (2-5 cm deep) glacial run-off stream, located 300 m from the Western end of L Miers.

Collection was performed aseptically into autoclaved polypropylene tubes. During the field-work expedition, samples were stored underground to ensure their temperature did not rise above 0°C. Once the samples had been transported to Scott base they were stored at -20°C, and were transported back to the UK on dry ice [Don Cowan, personal communication]. Since delivery to the microbiology laboratory at UCL, the samples have been stored for the majority of the time at -80°C, with a few months at 4°C and a more recent period at -20°C.

4.3 Solutions and Media

All the solutions and media were prepared using reverse osmosis (RO) water and sterilised by autoclaving, as above.

4.3.1 X-gal (5-bromo-4-chloro-3-indoyl-βD-galactopyranoside)

X-gal (Sigma) was dissolved in dimethylformamide (Sigma) to give a 40 mg/ml stock solution. The stock solution was added post-autoclaving to molten media (55°C) to a final concentration of 40 μg/ml.

4.3.2 Ampicillin

Ampicillin (Sigma) was dissolved in sterile deionised water to give a 10 mg/ml solution, filter sterilised (0.22 μm pore size filter, Whatmann) and stored at -20°C as a stock solution. The stock solution was added to molten media (55°C) to a final concentration of 50 μg/ml.

4.3.3 Phosphate Buffer Solution (PBS)

Dulbecco's Phosphate Buffer Solution (Sigma), without calcium chloride or magnesium chloride, was used from the bottle.

4.3.4 Culture media

A total of five different growth media were used throughout this research: Luria Bertani (LB), Nutrient Broth (NB), Czapek-Dox (CZD), R2A, and Starch Minimal Media (SMM). Both liquid cultures and solid plates were used. Agar (Difco) was added at a concentration of 2% (w/v) and sterilised molten media poured into 9 cm petri dishes. Quarter strength preparations of CZD, NB, and R2A media were also used for culturing as the samples were isolated from an environment observed to contain minimum organic matter.

4.3.4.1 Luria Bertani (LB)

Luria Bertani broth (Miller) was made to manufacturers instructions: 25.0 g/l of de-ionised water.

4.3.4.2 Nutrient Broth (NB)

Nutrient Broth CM0001 (Oxoid) was made to manufacturers instructions: 13.0 g/l of de-ionised water.

4.3.4.3 Czapek-Dox (CZD)

Czapek-Dox broth (Difco) was made to manufacturers instructions: 35.0 g/l of de-ionised water.

4.3.4.4 R2A

R2A broth (Difco) was made to manufacturers instructions: 18.2 g/l of de-ionised water.

4.3.4.5 Starch Minimal Media (SMM)

Potato starch (Sigma) was used at concentration 5 g/l of de-ionised water, added to make up to 90% of the total volume, and autoclaved. After allowing the broth to cool, the following autoclaved reagents were added: 1/10 volume of M9 salts and 1/100 volume of calcium/magnesium salts.

4.4 Cultivation of microbes from Antarctic samples

The exterior of the sample tube was sterilized with an ethanol wipe and, under sterile conditions, several grams of frozen surface material were removed from the collection tube into a sterile universal tube.

This sub-sample was allowed to thaw slowly over night to emulate the natural warming of Antarctic surface as summer approaches so as to minimise the thermal stress imposed upon the microbes. Ten milliliters of sterile PBS was added to the sample, and vortexed briefly to dislodge cells from the grains and hold them in suspension. PBS was used for this extraction rather than de-ionised water so as to minimise the osmotic shock to the microbes. Unless otherwise stated, PBS was also used for all other cell dilution procedures.

The abundance of culturable bacteria within the soil sample was not known (although Gilichinksy (2002) [98] reports 5.2×10^2 – 6.4×10^4 cells/g for viable aerobes in the Dry Valleys) so a 100-fold dilution series of the buffer was performed. Fifty microlitre volumes of each dilution were pipetted and spread evenly around the surface of a different agar plate with a sterile glass spreader until dry. Five dilution levels (neat, 10^{-2}, 10^{-4}, 10^{-6}, 10^{-8}) were plated on to five

different media (1/4NB, 1/4R2A, 1/4CZD, CZD, and SMM), yielding a total combinatorial set of 25 experimental growth replicates. An extra sterile plate of each medium type was designated as a control and stored with the spread plates to assess contamination. The plates were incubated at 4°C for 15 days.

Plates were examined for colonies after incubation. Individual colonies were picked off and replated onto the same nutrient agar they had been isolated from. Colonies were selected according to size, texture and colour such that the range of morphologies, and thus hopefully phylogenetic diversity, was fully represented. This process of colony picking and replating was repeated until it was certain all isolates were pure cultures, usually requiring two or three iterations. The agar plates were then harvested by flooding with 5 ml of the corresponding broth, scraping colonies from the surface and pipetting into an eppendorf tube. Samples were vortexed to break-up the colonies and stored in 20% glycerol solution (final concentration) at -20°C to serve as stocks for further work.

Twenty-nine separate pure-culture isolates were stored in glycerol. Of these, the isolates which produced the largest colonies at 4°C were identified as fast-growers and these 17 selected for further work, with the majority of attention focussed on the 12 strains which were isolated on 1/4NB, 1/4CZD and CZD media: isolate numbers MV.1, MV.3, MV.4, MV.5, MV.7, MV.8, MV.10, MV.23, MV.24, MV.25, MV.26 and MV.27.

Deinococcus radiodurans, obtained from Renos Savva of Birkbeck College, University of London, was grown on the same variety of nutrient media to determine the best for future work. SMM, 1/2NBA, 1/4NBA. 1/4R2A, CZD, and 1/4CZD were all tested. Although *D. radiodurans* was found to grow on all media except for SMM, growth was fastest on 1/4NBA (larger colonies even than on the more concentrated 1/2NBA) and so this medium was chosen for further work.

4.5 Identification of isolated strains

The 12 strains of most interest, those that formed the fastest growing colonies on NB and CZD media (isolate numbers MV.1, MV.3, MV.4, MV.5, MV.7, MV.8, MV.10, MV.23, MV.24, MV.25, MV.26 and MV.27), were identified by 16S sequencing using molecular methods detailed in this section.

4.5.1 DNA extraction

One hundred microlitres of the pure culture glycerol stocks were used to inoculate 5 ml broths of the appropriate nutrient medium in 10 ml universal tubes. They were incubated at 4°C for 16 days with constant agitation until the liquid cultures were turbid with high cell numbers. Samples of each (1.5 ml) were extracted, and centrifuged (9000 × g, 5 min) to pellet bacterial cells. The "CTAB Chromosomal DNA Preparation" protocol [27] was followed to extract genomic DNA from each of these cell pellets.

The bacterial pellet was lysed with 500 μl of lysis buffer (20 μg/ml proteinase K, 0.5% w/v SDS). Prewarmed (65°C) CTAB solution (80 μl; 0.7 M NaCl, 10% Hexadecyl trimethyl ammonium bromide) and NaCl (100 μl, 5 M) were added after a 30 min incubation at 55°C. Samples were

further incubated for 10 min at 65°C. Isoamyl alcohol:chloroform (1:24, 680 μl) was added and the sample shaken vigorously to form an emulsion. The organic and aqueous phases were separated by centrifugation (9000 × g, 5 min) and the aqueous phase collected. DNA was precipitated by the addition of isopropanol (0.6 volumes), mixing and incubation at room temperature for 10 min. Further centrifugation (9000 × g, 5 min) pelleted the DNA, which was subsequently washed with 70% cold ethanol (v/v) and resuspended in molecular grade water.

To confirm that DNA had in fact been isolated from each of the 12 microbial strains, a sample of each was run through a 0.8% agarose elctrophoresis gel for 1 hour, as described below.

4.5.2 Agarose gel electrophoresis

During this procedure, DNA fragments were regularly separated by electrophoresis on a horizontal gel apparatus (Bio-Rad Sub-Cell).

Gels were made in the laboratory with electrophoresis grade agarose at 0.8% w/v (used for separating whole-genome extracts) or 1.0% w/v (for PCR products) dissolved in 1 x Tris borate EDTA buffer (TBE). The 1 x TBE was also used as the running buffer in the gel tank. Ethidium bromide (0.01 μg/ml, 0.05 μl) is added to the gels before setting in order to visualise DNA. Loading buffer (0.4% w/v bromophenol blue, 0.4% w/v xylene crystal, 50% v/v glycerol) was diluted five-fold and mixed with samples in a 1:1 ratio. Quantification and estimation of size of DNA fragments was achieved using Hyperladder I (Bioline). Gels were run at 80 V for 45-60 mins, until the strands have been adequately separated as indicated by the loading dye. DNA bands within the gel are then visualised and photographed fluorescing under UV light using a Gene Genius Bio Imaging system (Syngene) and PC (Dell).

4.5.3 PCR amplification of 16S gene

From the whole-genome DNA extracts, polymerase chain reaction (PCR) was used to selectively amplify the 16S rRNA gene. PCR employs the Taq polymerase enzyme and thermocycling to copy sections of the template DNA between the provided oligonucleotide primers. Thus, the template DNA in this case is the Antarctic microbe genome extract, and the primers 27 F [227] and Un1492R [67] were selected to amplify the bacterial 16S rRNA gene as they are considered universal for eubacteria. The complete 16S rRNA gene is around 1,550 bases long, dependent on bacterial strain (1541 for *E. coli* complete sequence*;* NCBI sequence ref. J01859). Table 4.1 gives the sequences of this oligonucleotide primer pair. It can be seen that these selected primers amplify a DNA fragment of approximately 1,500 bases; the vast majority of the 16S rRNA gene.

Table 4.1: Primer pair used in PCR amplification of bacterial 16S rRNA gene.
[a] *E. coli* numbering of 16S rRNA gene

Primer	Sequence 5' – 3'	Position[a]	Reference
27 F	`AGTTTGATCCTGGCTCAG`	7 – 27	Weisburg *et al.* (1991) [227]
Un1492R	`GGTACCTTGTTACGACTT`	1492 – 1510	DeLong (1992) [67]

PCR amplification was performed using a Techne TC-512 thermal cycler machine. All reactions were carried out in a 50 μl total volume, comprised as follows: 1 μl template DNA; 5 μl Taq

buffer; 0.5 μl Taq (5 U/μl); 0.5 μl deoxynucleotide triphosphates (dNTPs, 25 mM of each); 0.5 μl 27 F primer (100 pmol/μl); 0.5 μl Un1492R primer (100 pmol/μl); 42 μl molecular grade water.

In addition to the 12 Antarctic microbial samples, a positive control (of known bacterial DNA) and a negative control (pure water) are run to confirm that the PCR reaction has operated properly and without DNA contamination, respectively.

The PCR conditions used were an initial denaturation step of 95°C for 4 mins, followed by 25 cycles of 94°C for 30s, 55°C for 30s and 72°C for 1 min. A final elongation step of 72°C for 5 mins was used.

After PCR, the products were run on an electrophoresis gel (Section 4.5.2) to confirm that the 12 Antarctic samples had indeed been amplified to yield DNA fragments of appropriate length, and that the negative control showed no DNA present (indicating no contamination).

4.5.4 PCR product cleaning and extraction

The PCR products were then cleaned, by running each on another electrophoresis gel. The DNA bands corresponding to the PCR product were excised from the gel under UV illumination and precisely weighed and stored in sterile eppendorfs.

The DNA was extracted from these gel slices using the "QIAquick Gel Extraction Kit Protocol" (QIAGEN) by following the manufacturers instructions. The volume of buffer required was calculated from the weights of the gel slices. The DNA was eluted out of the extraction columns and stored at -20°C, with a sample of each run on an electrophoresis gel to confirm that DNA had been extracted correctly from each gel slice by the procedure.

4.5.5 DNA ligation

The purified PCR products of the 16S rRNA genes were now ligated into the pGEM-T®easy plasmid vector (Promega).

A total volume of 10 μl was prepared for each of the 12 DNA samples, along with one +ve control (provided control DNA rather than PCR product) and one negative control (water instead of DNA): 0.5 μl pGEM-T easy plasmid; 5.0 μl ligation buffer; 1.0 μl T4 DNA ligase enzyme; 2.0 μl PCR product; 1.5 μl d H_2O.

Ligations were incubated over-night at 4°C.

4.5.6 Transformation

Competent cells of *E. coli* Top10F' were prepared for transformation by treatment of a mid-log population with 75 mM calcium chloride, and stored for future use at -80°C [161]. The ligation product (2 μl) was mixed with 50 μl competent cells in a sterile eppendorf and incubated on ice for 20 min. The cells were then heat-shocked at 42°C in a water bath for 45 seconds, before

being returned quickly to ice for 2 minutes. LB culture medium (450 μl) was added, and the cells incubated for 1.5 hours at 37°C, with constant shaking at 150 rpm. The samples of recombinant cells were then plated out in duplicate (100 μl and 50 μl) onto selective media: LB agar plates with 50 μg/ml of ampicillin antibiotic. For the blue/white screening of recombinants, X-gal and IPTG were also added to the cooling agar before pouring at a final concentration of 80 μg/ml and 0.5 mM, respectively. The nature of this selection and screening methodology is that only cells that have taken-up the pGEM-T plasmid (which contains a gene conferring ampicillin resistance) can survive on the selective medium plates, and of these growing colonies, only those which have the desired DNA fragment (the 16S rRNA gene in this case) correctly inserted into the LacZ gene do not metabolise X-Gal into a blue pigment.

Thus, after over-night incubation at 37°C, white recombinant *E. coli* colonies were selected and picked-off by sterile loop to inoculate 5 ml nutrient broth containing ampicillin (50 μg/ml) to maintain the selective conditions. After over-night incubation at 37°C, 1 ml volumes of each of these liquid cultures were stored with 30% glycerol (final concentration) at -20°C.

4.5.7 Purification of Transformed plasmids

A further 1 ml sample of the recombinant *E. coli* cultures were used to extract purified plasmid from the overnight growth. A "QIAprep Spin Miniprep Kit" (QIAGEN) was used, following the manufacturers instructions.

In order to verify that the recovered plasmids all contained an insert of similar length, a 5 μl volume of each of the 12 samples was restriction digested and run on an electrophoresis gel. The composition for the 10 μl digest was: 1 μl *Eco*R1 buffer (NEB); 0.5 μl *Eco*R1 restriction enzyme (NEB); 5 μl plasmid; 3.5 μl water.

These samples were incubated at 37°C in a Thermomixer (Eppendorf) for 2 hours, and then the fragmented plasmids run on a gel with a marker ladder (HyperLadder 1, Bioline).

4.5.8 DNA sequencing

Before being sent for sequencing the amount of DNA contained in each sample of purified plasmid was determined by a Nanodrop ND-1000 spectrophotometer and diluted with diH_2O to give 9-16 fmol/μl in 12 μl. Sequencing of plasmids containing the rRNA gene inserts was performed by Scientific Support Services, Wolfson Institute for Biomedical Research (University College London). The vector-specific primers used were M13F and M13R [183], each producing an end-sequence of the gene.

4.5.9 Analysis of Sequence Data

Editing of the DNA sequences was performed with the freeware software 4Peaks (Version 1.7.2), created by A. Griekspoor and Tom Groothuis (mekentosj.com) and run on a Mac OS X 10.4 machine. The returned sequences were edited to remove vector sequence and any degraded sequence where the signal is too low or ambiguous. Only about 400 bases of good gene sequence

was produced from each of the ends, however, and so the sequencing did not produce overlap within the gene. Consequently, the complete 16S rRNA gene sequence cannot be recovered and the forward and reverse sequences are thus treated individually.

Identification of each isolate based on its 16S rRNA gene sequence was confirmed using both the Ribosomal Database Project, RDP, (http://rdp.cme.msu.edu/) and BLASTn (NCBI) sequence search utility (www.ncbi.nlm.nih.gov/BLAST), performed in December 2007. RDP reports the identity of an entered 16S rRNA gene sequence to the genus level, and BLASTn can be used to search for the closest relatives of a sequence, which can give identification to the genus, and occasionally species, level. Identification was performed using both RDP and BLASTn on all 12 novel Antarctic isolates, using the sequences obtained from both the forward and reverse sequencing primers. Thus each isolate is identified four times.

After genus-level classification of each isolate, close examination of all BLASTn search results (both forward and reverse sequences) was performed to collate close-relatives that have been previously identified from similar low-temperature environments, such as other Antarctic or Arctic locations, deep sea sediments, and mountainous glaciers, permafrosts or soils. The RDP and BLASTn databases were also accessed for the 16S rRNA gene sequences of representative species from the other major bacterial clades. The GenBank (http://www.ncbi.nlm.nih.gov/Genbank/) accession number is a unique code identifying a sequence stored on databases such as RDP and BLASTn, and provides additional information such as the sampling location and conditions and relevant papers published.

RDP was then used to plot phylogenetic trees showing sequence relationships between the novel Antarctic isolates, closely-related strains from similar environments and the representative species of major bacterial clades. RDP plots phylogenetic trees using the Weighbor weighted neighbor-joining tree building algorithm (http://rdp.cme.msu.edu/treebuilder). An appropriate outgroup sequence, whereby the sequences in the group being plotted are more closely related to each other than to the outgroup, was selected in each case to improve the tree topology.

The amplified isolate 16S gene could have been ligated into the plasmid in either direction prior to sequencing, and so only the sequences corresponding to the forward sequencing of the beginning of the 16S gene (either M13-40 or M13rev sequencing primers, indicated in Table 7.3 on page 132) were selected for tree-plotting. Correspondingly, only the environmental strain sequences returned by a BLASTn search of these novel isolate sequence were included.

4.6 Irradiation experiments

4.6.1 Irradiation vessels

All irradiation samples, and control samples, were stored in 2.0 ml borosilicate clear glass vials (2-CV, Chromacol, purchased through Fisher Scientific) sterilised by autoclaving. Aluminium crimp lids are not recommended for irradiations as they scatter gamma rays, and so can alter the radiation dose a sample is exposed to. Thus, 11 mm polyethylene snap caps were used to seal the vials (11-PEC1, Chromacol, purchased through Fisher Scientific). These polyethylene plastic caps were not thermostable, and so were sterilised by a 5 hour exposure to 254 nm UV lamp, with both the inside and outside exposed, rather than autoclaving.

4.6.2 Preparation of cell samples

Cell populations were prepared for the irradiation experiment. Sterile conical flasks, with fluting to improve aeration, were filled with 200 ml of the appropriate nutrient medium and stirred continuously with a magnetic stirrer during growth at room temperature. Five millilitre samples from a starter culture were used to inoculate the broth. One millilitre samples were taken regularly from the culture, and the optical density measured to allow the growth to be followed.

The extent of radioresistance depends on physiological conditions, such as the growth/irradiation medium, and age of the culture [155]. Thus, growth of liquid cultures was followed by regular testing of the optical density (OD) at 600 nm using a spectrophotometer, and a 100 ml sample drawn by pipette from the culturing vessel during the mid-late-log phase of the growth curve. Regular OD measurements were continued on the liquid culture after extraction of the sample, so as to confirm that the sampling had indeed occurred during the mid-late-log-phase. When the culture reached the stationary phase and the growth leveled off, the experiment was terminated and the culture sterilized by autoclave.

One millilitre volumes of this sample were pipetted into 30 autoclave-sterilised glass vials. These were stoppered with the polyethylene caps, arranged widely-spaced in a plastic holder, and frozen rapidly in a -80°C freezer. This procedure was designed to emulate the change in environmental conditions of martian subsurface aquifer water being disgorged onto the exposed surface and freezing.

Only between 13 and 22 of the vials were actually required by the irradiation experimental designs explained in Sections 4.6.3.3 and 4.6.3.4. The rest of the 30 vials were saved to serve as unirradiated controls and for emergency use (in case, for example, some of the designated experimental vials broke during transportation). This foresight in redundancy in the experimental design became crucial in the running of the *D. radiodurans* exposure, as explained in Section 4.6.3.4.

Cell counts of the same culture used for the frozen samples were also plated immediately after extraction. These represent the population numbers before freezing and irradiation, and so are vital for calculation of freeze-thaw survival rates. To ensure accuracy of these crucial data, two replicate dilution series were conducted, and 100 μl samples from these were also plated and counted in duplicate.

4.6.3 Irradiation procedure

4.6.3.1 General details of exposure set-up

The two most common sources of gamma rays used in industry or other sectors for bacterial inactivation, in food preservation or medical sterilisation, for example, are the radionuclides cobalt-60 and cesium-137 [100, 204, 77]. Cranfield University offers access to a cobalt-60 radionuclide gamma-ray source in Shrivenham. The lay-out of the exposure facility is shown in Figure 4.1.

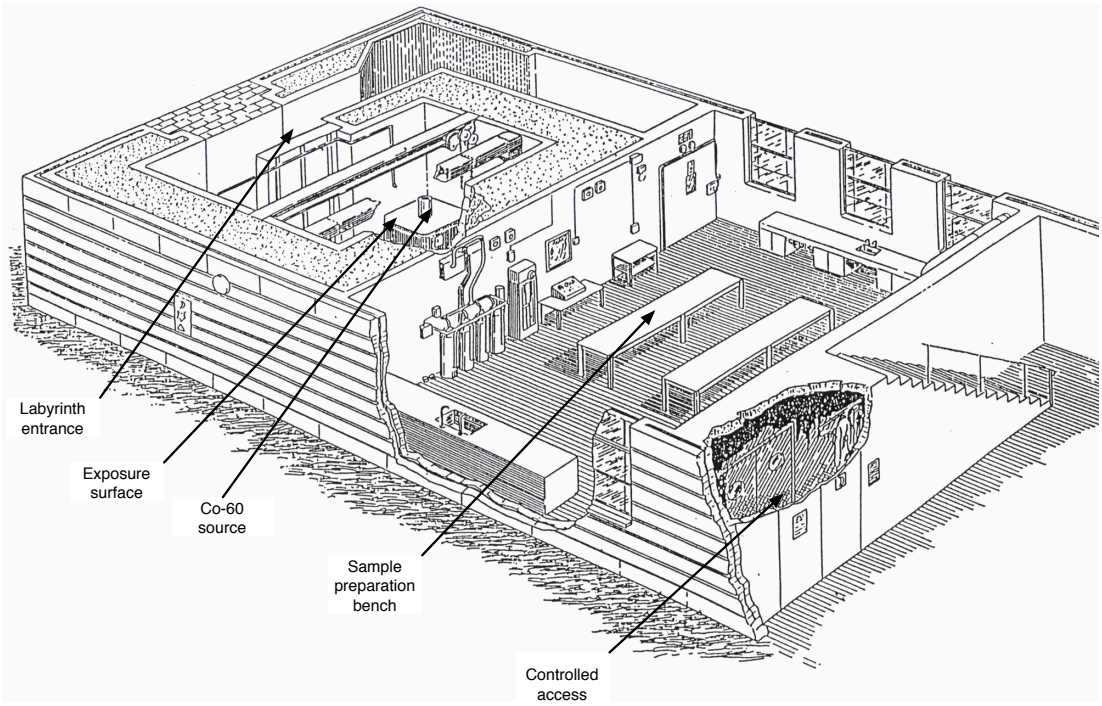

Figure 4.1: Lay-out of Cranfield University cobalt-60 gamma irradiation facility, Shrivenham. Diagram provided by Cranfield University and annotated by the author.

The Co-60 rods are set in a cylindrical arrangement, and housed within a 1 m cube of shielding. The source can be extended up out of the cube to expose samples placed on the table-top surface of the shielding. Different dose rates can be achieved from the equipment by positioning samples at varying distances from the source. The contours of equal dose-rate are circles centered on the cylindrical source. The dose-distance relationship is not a strict inverse square law as the gamma-rays do not emanate from a point-source, but a cylindrical shell of encased cobalt rods, and the exponent of the function is nearer -1.95. Dose rate measurements around the geometry of the source have been conducted for experimental design, and the dosimetry is repeated immediately before exposure to ensure accuracy. The accuracy of the doses delivered to samples is stated to be $\pm 5\%$ [Keith Lovell, personal communication], which includes error in the timing of the exposure, positioning of the sample and dosimetry.

The microbial culture samples, frozen in glass vials at -80°C as explained in the previous section, needed to be kept frozen on dry-ice (-79°) throughout an exposure of several hours. Thin-walled polystyrene boxes were chosen for their balance of thermal insulation characteristics and minimal shielding to gamma-rays (due to their very low density). Cardboard templates were constructed as bottom linings for each polystyrene box, with a deep groove following the curve of a circle with the desired radius from the source. This not only securely gripped the vials to prevent them moving during irradiation, but also enable them to be quickly arranged along the required precise curve from the source. On arrival at the exposure facility, the glass vials were carefully set-up in sequence inside the polystyrene boxes and packed with dry ice. Within the boxes, the sample vials were arranged in a clockwise sequence so that they could be removed as quickly and accurately as possible. The cobalt source was exposed for a period of 60 minutes at a time, before certain samples were removed from the irradiation boxes and stored back on dry-ice. Thus the final samples to be removed received the greatest dose.

The boxes themselves need to be positioned very accurately around the source, both to ensure

that the vials inside are at the correct radial distance and that the boxes do not shield each other when tightly packed into the designed arrangement. A scale diagram of the exposure area was constructed, with the desired dose-rate contours marked, and placed around the source. The boxes had alignment marks to allow precise positioning on these contour lines, and so were set-up as per the designs shown in Figure 4.2 and 4.4.

The control samples were also removed from the -80°C freezer, packaged and transported with the experimental vials to the irradiation facility, and throughout the experiment remained on dry ice at -79°C on the lab bench outside the gamma-exposure room in identical environmental conditions to the experimental vials.

After each hour of exposure, the source was retracted into the shielding, and the appropriate vials removed from the exposure boxes and placed in the storage box in the adjoining laboratory, also refrigerated with dry ice. The dry ice in the exposure boxes was replenished as necessary during sample retrieval every hour. An inventory of all vials and their exposure time was checked off as samples were removed from the exposure room.

Due to limited space around the cylindrical cobalt source, there is a compromise that must be struck in the experimental design. Placing samples, within their bulky refrigeration boxes, close to the source delivers very high doses over the course of the exposure, but shields samples placed further out. Positioning the boxes around a circular locus further back from the source allows room for more samples, but provides a lower dose rate. Depending on the aims of each irradiation, as specified in Sections 4.6.3.3 and 4.6.3.4, the experimental design was optimized for different objectives.

Selection of the range of gamma exposure doses for the different bacterial strains in the experimental design was informed by previously-reported survival characteristics in the literature [30, for example] and linked to the martian subsurface dose rates calculated by the modeling work already described.

As will be explained below, the dose rates used in the irradiation exposures range between 0.3 kGy/hr and 1.69 kGy/hr. The results of the first configuration of the computer model, which will be provided in great detail in Chapter 6, indicate that the physically absorbed dose deposition rate (i.e. not biologically-weighted) on the martian surface from SEP and GCR totals 0.16 Gy/year. The maximum dose rate produced by the irradiation design described here thus represents a delivery rate almost 10^8 times faster: every second of irradiation at the 1.69 kGy/hr set-up recreates almost three years of exposure on the martian surface. A more faithful comparison between the experimental set-up (gamma-ray exposure in ice at -79°C) and the martian subsurface is considering organisms buried 3 m deep in pure water ice, whereby the contribution from high-LET particles (such as protons and HZE) has been substantially reduced and the radiation environment is well-approximated by a gamma-ray source. Under these conditions, the model predicts an unweighted dose rate of 0.05 Gy/year, and thus every second of irradiation at the maximum dose delivery rate of this experimental design recreates ∼10 years exposure at 3 m depth in ice on Mars.

4.6.3.2 Post-irradiation procedure

After the radiation exposure, frozen but not irradiated control samples were thawed slowly within their glass vial at room temperature. As explained above, these control samples were

exposed to identical procedures to the experimental samples, all except for exposure in the gamma-ray room. Cells within these samples thus represent the data for survival under freeze-thaw but not irradiation, and so provide the initial population number from which irradiation-induced cell death is calculated. To ensure the highest degree of accuracy in determining these population numbers, three control vials for each bacterial strain were thawed and underwent a dilution series independently, with agar plating and colony counting also conducted in triplicate.

Once this freeze-thaw survival rate was known for the strains, the survival under different radiation doses could be determined. Starting with the lowest dose exposures, and steadily progressing to higher doses (to aid estimation of the appropriate sample dilutions when plating), sample vials were thawed, diluted, plated, incubated and cell counts determined from triplicate plates as above.

For the Antarctic isolates and *D. radiodurans*, initial freeze-thaw population numbers were of the order 10^7 - 10^8 cells/ml, and so dilutions of 10^{-5} were typically used. As the dose increased, fewer cells survived, and so a lower dilution factor was used to ensure there was always roughly $20 - 200$ colonies on the plate to count. Occasional miscalculations of the appropriate dilution meant that a few data points were lost as either there were too few colonies to count with statistical significance, or too many grew to form a near-confluent bacterial mat. The control sample cell counts for *E. coli* were also subsequently found to be inconsistent with the lowest exposure irradiated samples (roughly a factor of ten lower, almost certainly due to a calibration problem with the pipette used for the dilution series), and so the initial count was recovered by back-extrapolation from the experimental data. The *E. coli* freeze-thaw survival was confirmed by repeat experiment.

For the very highest doses, and corresponding death rates, it was necessary to concentrate the vial contents even more than the neat sample. The 1 ml sample was pipetted from the glass irradiation vial into a sterile eppendorf tube, and centrifuged at 9,000 $\times$ g for 2 minutes. The supernatant was discarded and the cell pellet resuspended by vortex in 100 μl of fresh broth, thus yielding a ten-fold concentration of the cell sample (an effective 10^{+1} dilution). In this case, the cell count could only be accomplished in duplicate, with 50 μl of the sample pipetted and spread onto each agar plate.

4.6.3.3 Specifics of Irradiation Experiment 1

The aims of the first irradiation were two-fold. Firstly, to assess microbial survival over a wide range of radiation doses, extending to as high a dose as permissible whilst still providing good data coverage at lower doses where a shoulder may exist in the survival curve. Secondly, it was assumed that for metabolically-inactive cells (i.e. frozen at -79°C) radiation survival is a function of total dose received, and independent of dose rate. Demonstrating that this assumption does indeed hold true is crucial if data collected from cells exposed at different distances from the source are to be collated.

Two representative bacterial strains were selected as negative and positive controls, and were expected to show very little radioresistance and greatest resistance, respectively. Thus *E. coli* strain C600 was chosen as the negative control, and *D. radiodurans* as the positive. The bacterial strains isolated from the Antarctic Dry Valleys can be expected to exhibit a radiation resistance intermediate between these two extremes: less than *D. radiodurans* but greater than

E. coli because they are environmental microbes exposed to regular freezing and desiccation. As outlined in Section 1.3 on page 25, there is believed to be a strong causative link between adaptation for desiccation survival and radiation resistance. The novel Antarctic isolate MV.27 was also selected for the initial irradiation experiment as it is fast-growing at 4°C and so might be expected to be particularly well-adapted for survival in the cold, desiccating environment of the Dry Valleys, and thus also exhibit radiation resistance.

As explained in Section 4.6.3.1, the conflicting experimental demands of achieving high doses as well as producing many data points across the dose range require a carefully-balanced compromise. *D. radiodurans* was expected to show a much greater radioresistance than other microbes and so required very high doses. *E. coli*, on the other hand, was expected to suffer a steep kill-curve at low doses and so required good dose-level-resolution at low doses, whereas the radioresistance of MV.27 was unknown. These requirements presented a challenge to accommodate in the experimental design.

The gamma-ray facility at Cranfield University was able to offer a 6-hour exposure, which is a major determinant in the total doses achieved from different experimental set-ups. As an optimal compromise between the conflicting requirements of generating meaningful data that provided both a good dose-resolution and high maximum dose, an experimental design with three tiers of dose rate was developed. The majority of samples are placed along an intermediate dose-rate contour of 0.5 kGy/hr (11 cm from the source), with a large set placed further back at 0.3 kGy/hr (16 cm range) to probe survival at low doses with a good dose-resolution, and a third tier placed very close to the source on the 1.5 kGy/hr contour (4 cm) to expose *D. radiodurans* to the highest doses. To demonstrate that survival of frozen cells is independent of dose rate, the dose ranges covered by samples set at different distances from the source were designed to over-lap to allow comparison of data sets.

The experimental design uses 21 sample vials of *E. coli*, 22 of MV.27 and 20 of *D. radiodurans*. Split between the different dose rate tiers, and allowing for repetition of data points, the samples were allotted as shown in Table 4.2.

Table 4.2: Radiation doses for sample exposure, kGy, divided between three dose rate contours (0.3, 0.5, 1.5 kGy/hr) and with replicates shown.

E. coli		**MV.27**		***D. radiodurans***	
Total dose (kGy)		**Total dose (kGy)**		**Total dose (kGy)**	
0.3 kGy/hr	**0.5 kGy/hr**	**0.3 kGy/hr**	**0.5 kGy/hr**	**0.5 kGy/hr**	**1.5 kGy/hr**
0.3 x2		0.3 x2		0.5 x2	
	0.5 x2		0.5 x2	1.0 x2	
0.6		0.6 x2		1.5 x2	1.5
0.9		0.9		2.0 x2	
	1.0 x2		1.0 x2	2.5 x2	
1.2		1.2		3.0 x3	3.0
1.5	1.5 x2	1.5	1.5 x2		4.5
1.8 x2		1.8 x2			6.0
	2.0 x2		2.0 x2		7.5
	2.5 x2		2.5 x2		9.0 x2
	3.0 x3		3.0 x3		
Total: 21		Total: 22		Total: 20	

Figure 4.2 displays a scale diagram of the experimental design, showing the three concentric dose-rate contours used, the arrangement of the refrigeration boxes and the vials positioned

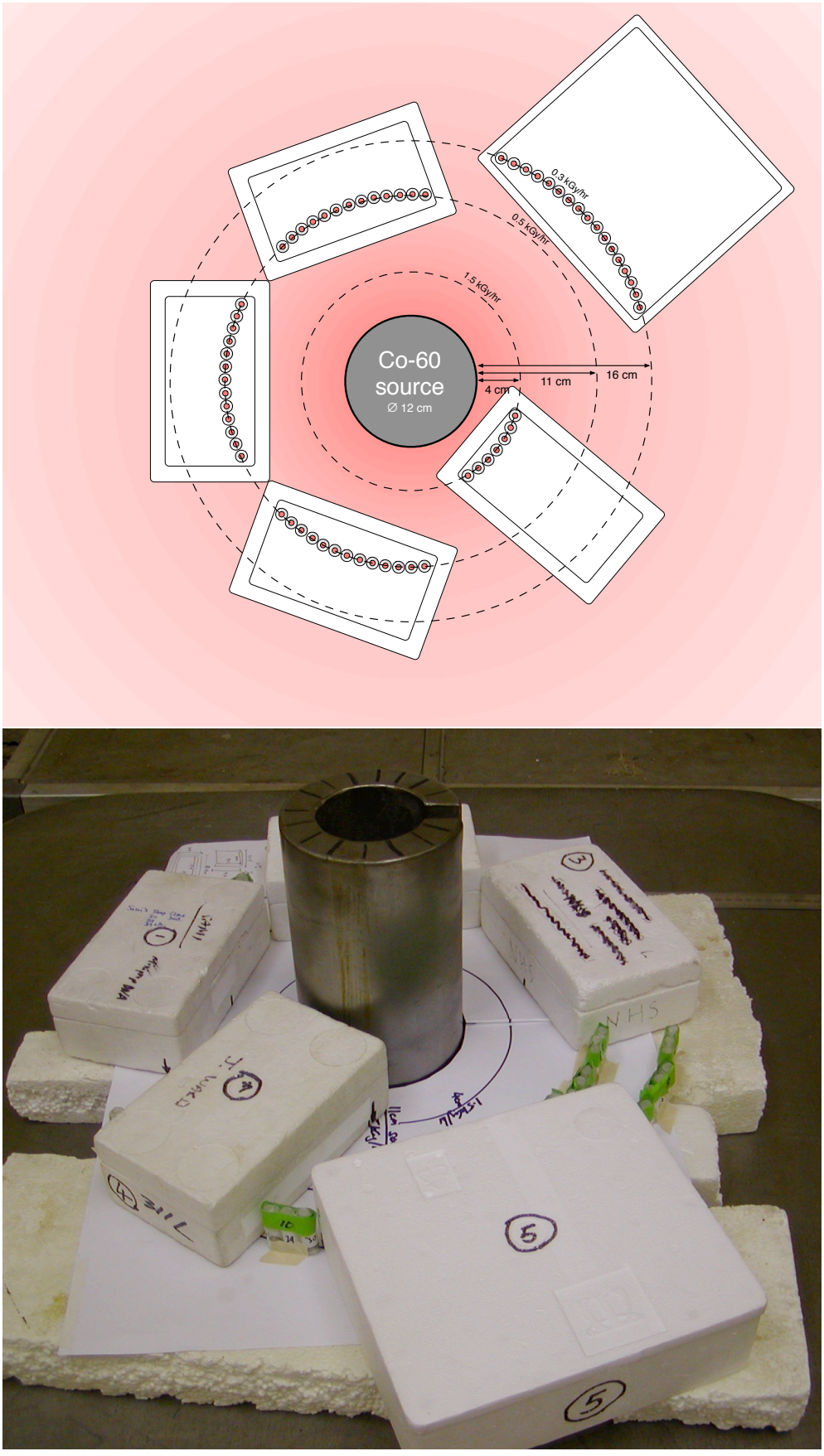

Figure 4.2: Top: scale diagram of experimental set-up for first gamma-irradiation exposure, showing the three concentric dose-rate contours, and sample vials positioned along them within the refrigeration boxes. Bottom: photograph of exposure set-up.

along precise circular curves within them. Also shown is a photograph of the refrigeration boxes precisely arranged on the scale diagram prior to irradiation.

Despite the inventory system used for checking the correct samples were removed at each time-point, a mistake was made and one *D. radiodurans* was not removed after the 3^{rd} hour. It was decided to leave this exposed until the end of the 6^{th} hour to yield an additional data point at the maximum dose.

4.6.3.4 Specifics of Irradiation Experiment 2

When the opportunity for a second irradiation session became available, the results so far were considered and two requirements for additional data were identified. Firstly, more of the novel isolates need to be irradiated to assess their survival characteristics, and potentially identify one with an unusually-high resistance. Secondly, the irradiation of *D. radiodurans* needs to be extended to much higher doses since no significant decrease in survival had yet been observed.

The isolated strains MV.7 and MV.10 were selected as their colonies are morphologically distinct from the MV.27 strain previously irradiated (as shown in Table 7.2 on page 129), and so were likely to represent diverse species. Starter cultures of MV.7, MV.10 and *D. radiodurans* were used to inoculate separate stirred 200 ml broth flasks, as described in Section 4.6.2. The *D. radiodurans* culture did not increase in OD over 24 hours, however. The broth was therefore inoculated with a second 5 ml starter culture to try to get the growth culture going. After a further 34 hours of incubation the *D. radiodurans* culture was still not growing. Time had run-out before the scheduled irradiation slot, and so it was decided to abandon the liquid culture and instead use the remaining seven *D. radiodurans* samples from the first gamma exposure. The irradiation experimental design was modified accordingly, to use fewer replicates of *D. radiodurans* vials without sacrificing the range of doses covered, and leave enough samples remaining to act as controls.

To ensure the validity of this approach, one of the frozen *D. radiodurans* vials was designated as the control and the surviving cell count determined immediately after the irradiation procedure. The surviving population as determined from this set of cell counts was compared to the first set of cell counts ascertained for the two initial *D. radiodurans* controls 3 months earlier, as shown in the box and whisker plot in Figure 4.3.

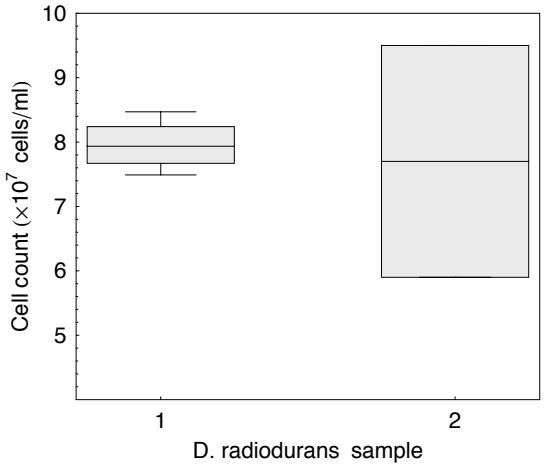

Figure 4.3: Box and whisker plot of the two sets of cell counts performed on the *D. radiodurans* control samples immediately after irradiation experiment 1 and 2. Data given in Table 4.3.

A two-tailed Welch's approximate t-test was also performed on the two sets, with the null hypothesis that there is no difference between the means, as shown in Table 4.3. The test failed to reject this null hypothesis at a significance level of 0.05 (p=0.829), meaning that there is no statistically-significant difference between the mean cell counts of the two sets. This verifies that the greater length of time spend frozen at -80°C had not significantly affected the survival of the *D. radiodurans* cells before irradiation, and that the data sets from the two irradiation experiments could be reliably combined.

Table 4.3: Comparison between the first set of control *D. radiodurans* cell counts, and the second set conducted before irradiation experiment 2. The individual plate counts are shown, along with the mean calculated for each set and the result of a two-tailed Welch's approximate t-test that the population means are the same. The calculated p-value is 0.829, thus failing to reject the null hypothesis at significance level = 0.05. There is no statistically-significant difference between the mean cell counts of the two sets and they can be treated as the same.

	Cell counts ($\times 10^7$ cells/ml)			Mean
Set 1	7.49	7.98	7.67	
	8.24	8.47	7.89	7.96
Set 2	9.50	7.70	5.90	7.70
Two-tailed Welch's approximate t-test p-value = 0.829				

A longer exposure time of 9 hours was granted by Cranfield University for this irradiation proposal. The design requirements for the irradiation were to place the *D. radiodurans* as physically close to the source as possible and provide space further out to irradiate two sets of microbial samples at a lower dose rate. The minimum distance a vial can be placed from the source, with the intervening bulk of the polystyrene refrigeration box, is 3 cm, which corresponds to a dose rate of 1.69 kGy/hr. 13 sample vials each of MV.7 and MV.10 were positioned along the 0.5 kGy/hr contour (11 cm from source), and 4 each on the 1.69 kGy/hr contour. Thus, the samples were arranged as shown in Figure 4.4, and given the exposures listed in Table 4.4.

The results of the laboratory work described here, on both the cultivation and identification of novel strains of psychrotolerant bacteria from the Antarctic dry valleys, a martian analogue location, and the determination of the gamma ray radiation resistance of these strains at a temperature characteristic of the martian surface, will be discussed in Chapter 6. The following two chapters will deal with the results generated by the martian radiation model, firstly in validating the model predictions against previously-published studies, and secondly discussing all the new results produced.

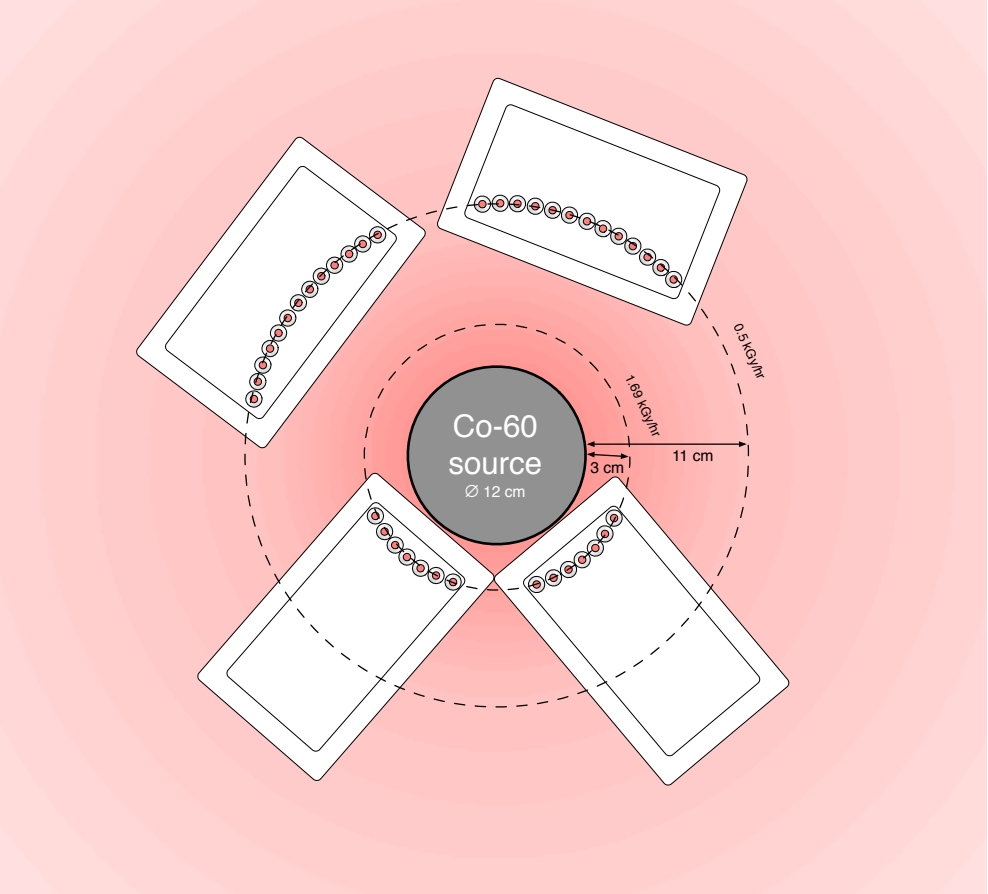

Figure 4.4: Scale diagram of experimental set-up for second gamma-irradiation exposure

Table 4.4: Radiation doses for sample exposure, kGy, divided between two dose rate contours (0.5 and 1.69 kGy/hr) and with replicates shown.

MV.7 & MV.10		***D. radiodurans***
Total Dose (kGy)		**Total Dose (kGy)**
0.5 kGy/hr	**1.69 kGy/hr**	**1.69 kGy/hr**
0.5 x2		6.76
1.0 x2		8.45
1.5		10.14
2.0		11.83
2.5		13.52
3.0		15.21
	3.38	
3.5		
4.0 x2		
4.5 x2		
	5.07	
	6.76	
	8.45	
Total: 17 each		Total: 6

4.7 Chapter summary

- Novel bacterial isolates were cultured from the Miers Valley of Antarctica, an analogue site of the martian surface, and characterised in terms of colony morphology and growth behaviour.
- Molecular biology work was conducted on twelve strains identified as fast-growers at 4°C, including whole genome DNA extraction, PCR amplification of the 16S rRNA gene, and subsequent cloning and sequencing of the gene. These sequences were compared to the on-line 16S rRNA gene sequence database RDP and also run through BLASTn searches to identify the novel strains to genus level.
- Cell populations of three of the novel isolates, MV.7, MV.10 and MV.27, and two model organisms, *E. coli* and *D. radiodurans*, were grown in liquid culture and frozen at -79°C (194 K) for gamma-irradiation, a temperature characteristic of the mid-latitude martian surface and suspending cellular metabolism and DNA repair.
- Gamma irradiation experiments were carefully designed so as to optimise dose-range covered and dose resolution and for five microbes expected to exhibit very different radiation survival behaviour. Exposure doses were linked to the results of the computer modeling, and the outcome of the first irradiation experiment aided design-improvement for the second. Post-irradiation cell populations were determined and thus the survival fraction as a function of gamma-ray dose.

Chapter 5

Results: Model validation

Chapter 3 has detailed how the martian radiation model was developed, with the code checked at regular stages for correct functionality in terms of the geometry, particle propagation through magnetic fields, event detection and data gathering, and so on. This first results chapter explains how once completed, the correct integration of all the separate parts of the code, and the post-processing and normalisation routines, were all extensively tested and validated against previously-published studies. The following chapter will present all of the novel results unique to this modeling approach.

Also presented here are the results of validation tests run to confirm the correct refitting of generated data to the CREME-96 primary spectra model after an error was discovered in the SPENVIS database, and that the proton-only approximation employed by the second configuration of the model is justified for dose-depth results.

5.1 Resolution of primary spectrum error

It was realised late in the process of simulating the first model application that the primary GCR spectrum being used, provided by SPENVIS, was probably not in fact correct. The nature of the error is believed partly to be the use of incorrect units for data given on the database (energies stated as MeV not MeV/nuc), but correction for this still produced highly suspect spectra.

Figure 5.1, produced by Laurent Desorgher, plots the SPENVIS spectra for Z=1, 2, 26 (H, He, and Fe ions) primaries extracted for January 2000 against that of other GCR models and experimental data. Shown are the CREME-96 model [221] and the latest Badhwar and O'Neill

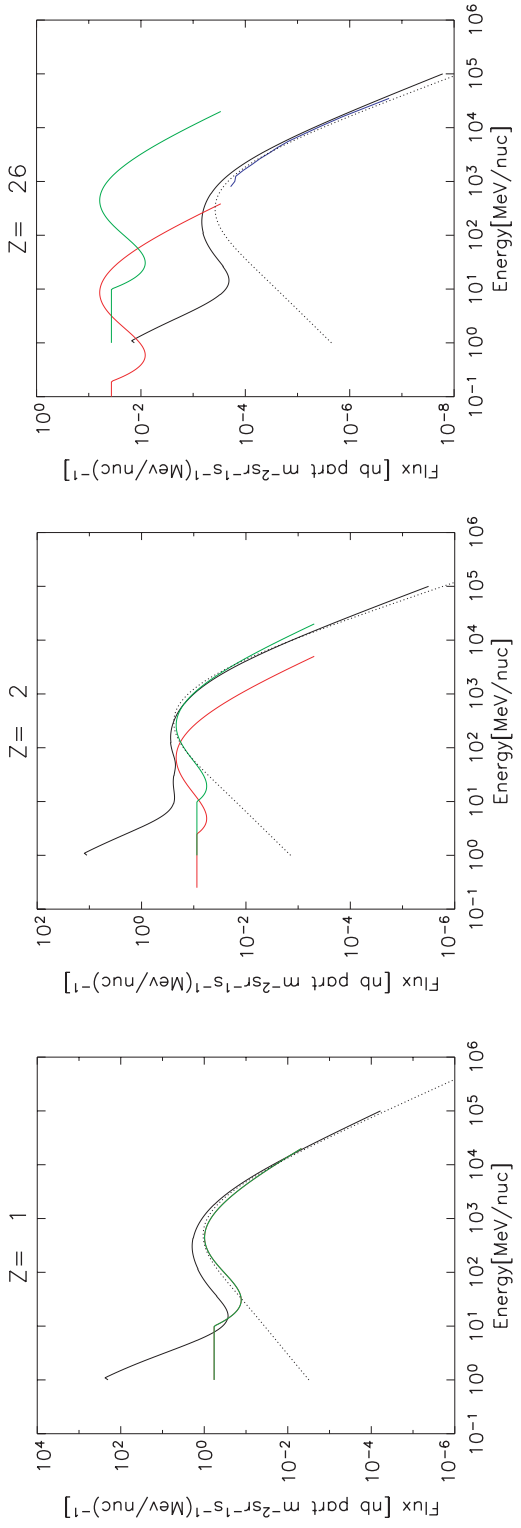

Figure 5.1: Comparison of GCR primary spectra models and measurements for hydrogen (Z=1), helium (Z=2) and iron nuclei (Z=26). SPENVIS assuming energies given in MeV (red); SPENVIS assuming energies given in MeV/nuc (green); CREME-96 model (black solid) [221]; the most recent Badhwar and O'Neill model (black dashed) [176]; Engelmann *et al.* (1990) experimental data for Z>3 (blue) [80]. Plots prepared by Laurent Desorgher.

model [176] for January 2000, and the data from the cosmic ray experiment aboard the HEAO-3 satellite reported by Engelmann *et al.* (1990) [80].

It can be seen in Figure 5.1 that even if the SPENVIS database is assumed to have stated the incorrect units for energy, namely MeV rather than MeV/nuc, the given spectra differ greatly from other models and experimental data, especially for heavier ions. CREME-96 and the Badhwar and O'Neill models agree well above about 1 GeV/nuc, and also show a close correspondence with the measurements presented by Engelmann *et al.* (1990) [80].

This issue was not found to be easily resolvable [personal communication: Laurent Desorgher (PLANETOCOSMICS), Bart Quaghebeur (SPENVIS), Hugh Evans (ESA)] and so the SPENVIS database was abandoned for the CREME-96 model. The extensive amount of data already generated by the model processing was refitted to the new CREME-96 primary spectra (using the post-processing pipeline described in 3.10 on page 79). This refitting process precisely recreates the total energy delivered by the primary GCR spectra, but produces artifactual discontinuities in the output particle spectra due to the nature of the histogram input of primary particles during simulation. Figure 5.2 plots the comparison between the primary proton spectra given by SPENVIS and CREME-96, and the modeled spectrum refitted from SPENVIS to CREME-96.

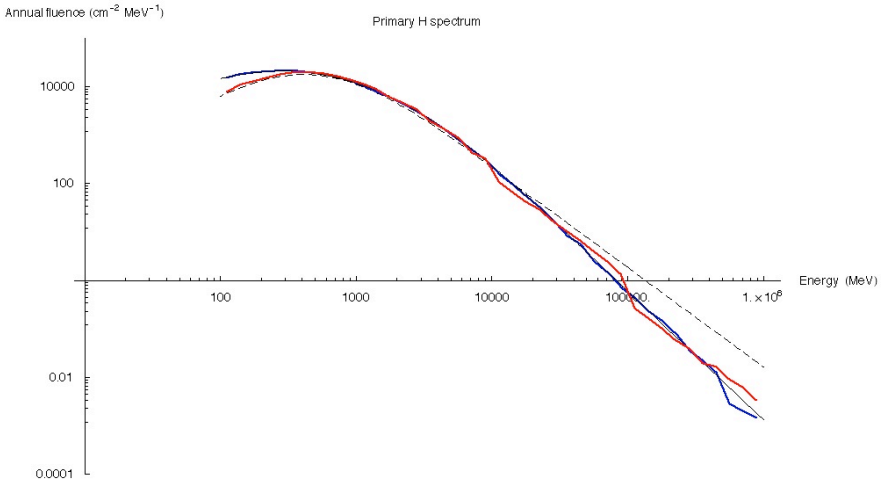

Figure 5.2: Comparison of the primary proton spectrum given by SPENVIS (dashed black line) and CREME-96 (solid black line). Also displayed is the modeled spectrum refitted from SPENVIS to CREME-96 (red line), showing artifactual discontinuities at 10 GeV and 100 GeV, and the fit produced by rerunning the model using CREME-96 from the outset (blue line).

A validity check was run to ensure that this primary spectrum refitting did not affect the generated data. Figure 5.3 shows the accumulation rate of physically-absorbed dose (Gy/year) as a function of depth underground in the 1 g/cm^3 dry homogenous surface model from GCR primary protons, calculated by the second configuration of the model. There can be seen to be no discernible discrepancy between the data generated from the SPENVIS spectrum and subsequently refitted to CREME-96, and test data generated from the CREME-96 primary spectrum originally. The only results to show any evidence of this necessary refitting are the proton energy spectra in the top layers of the subsurface (for example, see Figure 6.1 on page 113).

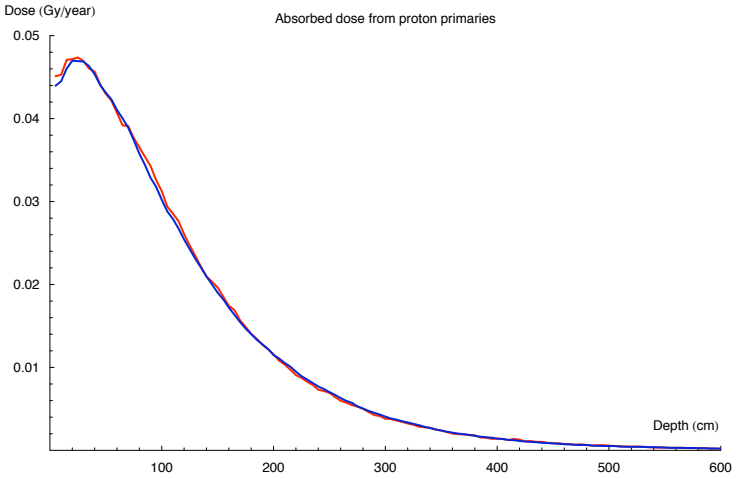

Figure 5.3: Comparison of physically-absorbed dose as a function of depth in the martian 1 g/cm^3 dry homogenous subsurface from GCR primary protons, providing validation that the necessary refitting of data generated with the SPENVIS primary spectra (red) does not differ from that generated *de novo* from the CREME-96 spectra (blue).

5.2 Charged particle propagation within crustal fields

As described in the Section 3.7 on page 74, the functionality to model particle deflection by the crustal fields was attempted. Although the capability for reproducing arbitrarily-complex magnetic fields within the atmosphere and registering surface particle strikes to produce fluence maps were both accomplished, no suitable data matrix file of the 3D field vectors of the martian anomalies could be sourced. The surface flux maps presented in Figure 5.4 and published in Dartnell *et al.* (2007b) [65] were therefore produced by a collaborator, Laurent Desorgher, using PLANETOCOSMICS and the CAIN90 spherical harmonic model of the crustal magnetic fields [42]. One million 10 MeV electrons and protons were propagated through the most intense crustal magnetic fields over Terra Sirenum, centred on −47.8°N 174°E (see Figure 1.3 on page 18).

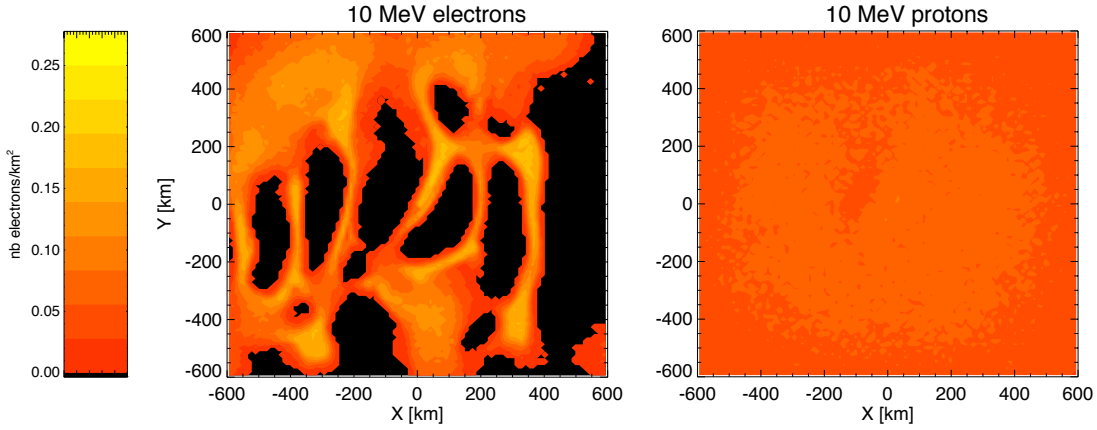

Figure 5.4: Surface fluence maps of 10^6 modelled 10 MeV electrons and protons propagating through the most intense magnetic anomalies over Terra Sirenum, centred on −47.8°N 174°E (see Figure 1.3 on page 18). Plot created by Laurent Desorgher, published in collaboration with the author [65]

Such low energy electrons can be seen to experience significant deflection by the anomalies,

producing a protective umbrella effect of particle shadows where no flux strikes the surface surrounded by pile-up regions of focused flux. Protons of the same energy, however, experience minimal deflection in such a field due to their higher rigidity.

The maximum horizontal field vector in the Terra Sirenum region below 200 km altitude is on the order of 1 μT [42]. Using the formulae described in Section 3.7.1 on page 75, the gyroradius of a perpendicularly-incident 10 MeV electron is calculated to be 35 km, and so it is effectively deflected by the crustal anomaly as it spirals along the field lines. Protons of equal energy have a much larger gyroradius of 460 km and are only minimally deflected. These simulations were performed without modeling particle attenuation by the atmosphere, however, and none of these primaries would in fact reach the surface. Primaries able to significantly penetrate into the martian subsurface, with an energy of around 1 GeV, corresponding to the peak GCR proton flux, have gyroradii in these field strengths of nearly 6000 km, and so experience negligible deflection. Primary particles with enough energy to penetrate the atmosphere and deposit dose within the subsurface are not appreciably deflected by the magnetic anomalies.

Charged secondaries may be created within the atmosphere with an energy low enough to experience significant deflection, but with a total current martian atmospheric shielding density of 16 g/cm^2 (above the reference altitude; atmospheric density is less above the strongest magnetic anomalies as they occur in the southern highlands) this is a minimal source of particles propagating towards the surface. Figure 6.5 on page 116 shows the surface flux of secondary electrons produced within the atmosphere with energy less than 10 MeV to be more than three orders of magnitude less than primary protons at the same energy. It is also important to note that most of these low-energy secondaries would have been produced close to the surface as the atmospheric density rises (there is not currently the capability to output this information from the model, but it can be included in future work) and so have less opportunity for being deflected by the crustal anomalies. The martian atmosphere is thus a net absorber of particles with energy low enough to be significantly deflected by the crustal magnetic fields, and these anomalies can be ignored in subsequent modeling of the subsurface radiation environment on Mars.

Although PLANETOCOSMICS was well-suited for this investigation into particle deflection by the crustal magnetic anomalies, and plotting surface fluence maps, it was not suitable for the rest of the modeling required by this astrobiology study as it was not capable of treating the subsurface radiation environment.

5.3 Comparison of surface particle energy spectra

5.3.1 PLANETOCOSMICS

The proper implementation of the provided physics lists (from an older version of ATMOCOSMICS package, as described in Section 3.4 on page 62) and the data capture and post-processing routines was tested by verifying data produced by this model against that published for the PLANETOCOSMICS package [101]. Figure 5.5 displays the comparison between the spectral data generated by this model against PLANETOCOSMICS, for protons, neutrons, gamma, and electrons, on the martian surface from GCR protons, 100 MeV $\leq$ E $\leq$ 100 GeV, during solar minimum. The proton plot also shows the primary GCR H spectrum (in black).

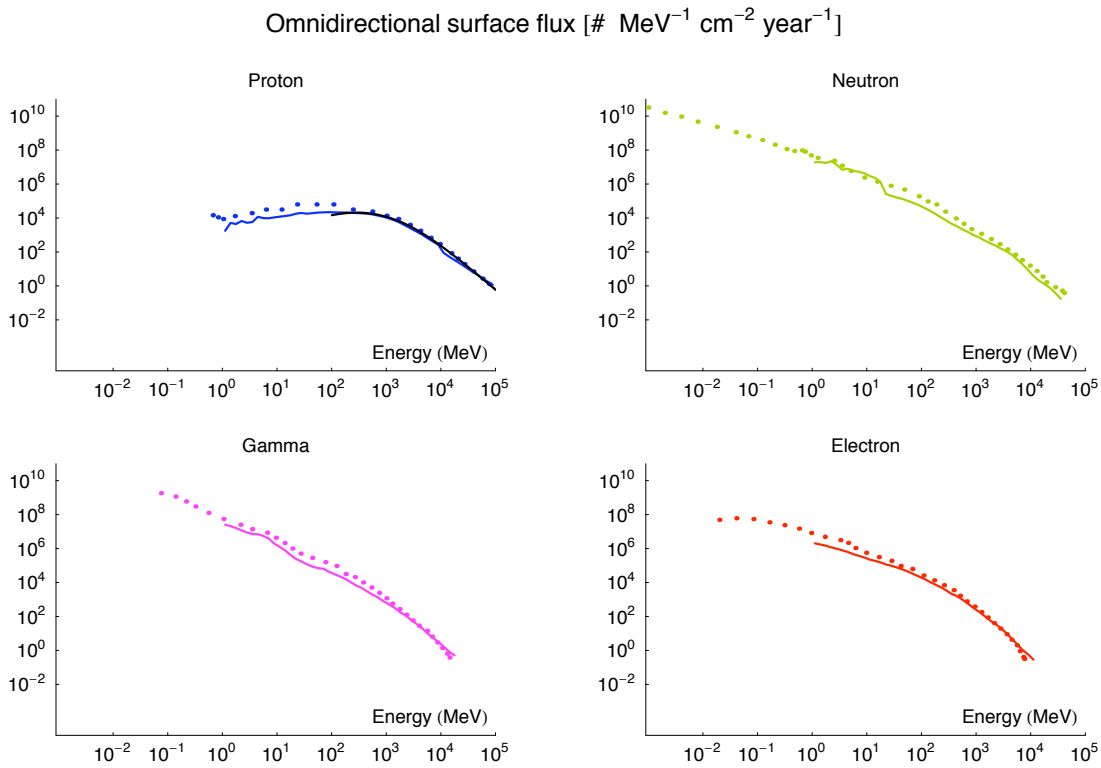

Figure 5.5: Comparison of omnidirectional flux energy spectra for major particle types on the martian surface from GCR primary protons (100 MeV $\leq$ E $\leq$ 100 GeV, solar minimum spectrum) calculated by this model (solid line) and published results from PLANETOCOSMICS package [101] (dotted). The primary GCR proton spectrum used in this modeling (CREME-96) plotted in black.

There can be seen to be an excellent correspondence between all the model results across the entire energy range. The data for proton energies above ~500 MeV are in especially good agreement. The surface neutron spectrum produced by this model is discussed in greater detail in Section 5.3.3.

5.3.2 MarsGRAM

Another model, MarsGRAM, has been developed using Geant4, but is independent of either PLANETOCOSMICS or this model in terms of the programme architecture and physics modeling employed, and so is a valid second verification for this model. Keating *et al.* (2005) [126] report on the results of simulations carried out with 10^5 protons drawn from the solar minimum CREME-96 GCR proton spectrum. These data are plotted against those produced here in Figure 5.6.

The gradient of the two curves can be seen to correspond very closely across the entire energy range, with a particularly good agreement in the calculated electron spectrum. The MarsGRAM proton, neutron and gamma spectra, however, appear to be of uniformly higher flux by a factor of ~3. In particular, the MarsGRAM proton spectrum shows greater flux than that reported from the PLANETOCOSMICS package [101], and even higher than the GCR primary spectrum used in this research. This confirms that the discrepancy is not due to a difference in the physics modeling, but that Keating *et al.* (2005) [126] have used a primary proton spectrum slightly harder than that used here.

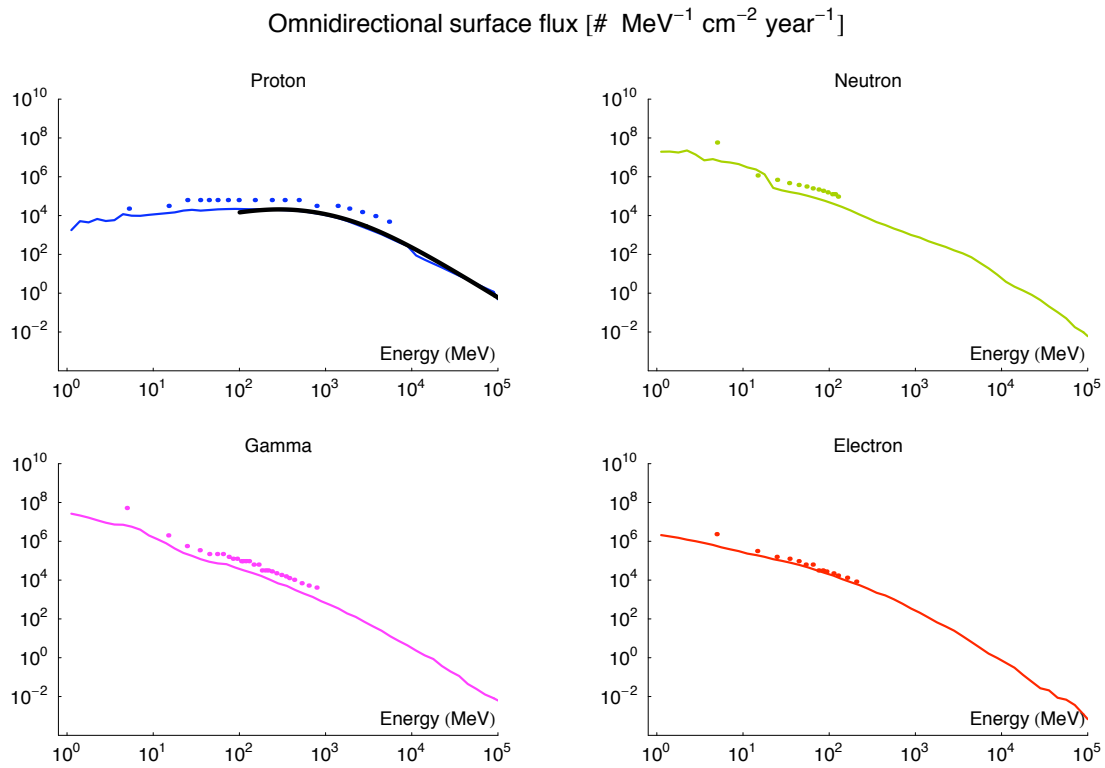

Figure 5.6: Comparison of omnidirectional flux energy spectra for major particle types on the martian surface from GCR primary protons (CREME-96, solar minimum spectrum) calculated by this model (solid line) and published results from MarsGRAM [126] (dotted). The primary GCR proton spectrum used in this modeling (CREME-96) plotted in black.

5.3.3 Surface neutron environment

Clowdsley *et al.* (2000) [52] report on HZETRN simulations of the martian surface neutron environment from the annual fluence of GCR ions. Figure 5.7 displays the comparison of this published data against this model predictions, using the Dry Homogenous surface model, for both forward propagating and back-scattering neutrons.

Clowdsley *et al.* (2000) [52] find the forward-propagating component of neutron flux on the surface to be relatively low below ∼20 MeV. This is because neutrons are not present in the primary GCR spectrum and must be produced as secondary particles in nuclear interactions within the minimal shielding provided by the atmosphere. Below ∼20 MeV the albedo flux becomes dominant as neutrons produced underground backscatter up through the surface. The model reported here finds the energy threshold for the dominance of backscattering neutrons to be higher, at ∼100 MeV.

Across the comparable energy range, there can be seen to be an excellent correspondence between the two models in the calculated spectra of forward-propagating neutrons, but the omnidirectional flux (forward + backscatter) calculated by this model shows a steep rise below 23 MeV. Below this energy threshold, the total neutron flux calculated by this model is elevated by a factor of roughly 5.6. The forward-propagating neutron spectrum shows no such feature, so this must be due to the contribution from backscattering neutrons.

It seems likely that this spectral feature is in error within this model, as the three other models discussed here (PLANETOCOSMICS, MarsGRAM, and that of Clowdsley *et al.* (2000)) show

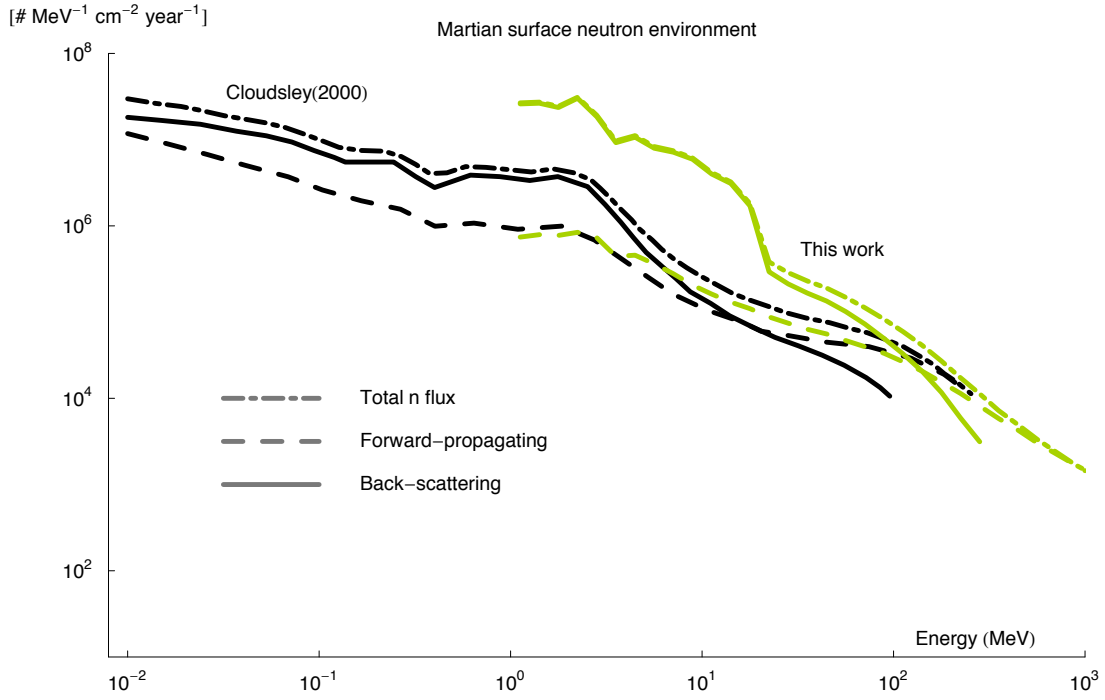

Figure 5.7: The martian surface neutron environment from GCR ions, as calculated by Clowdsley *et al.* (2000) [52] (black lines) and this Dry Homogenous surface model (green), subdivided as follows: forward-propagating neutrons (dashed line); back-scattering neutrons (solid line); total omnidirectional flux (dot-dash line).

no such effect. The discrepancy is not due to an error in the data capture or post-processing streams, as it affects only a very select energy range of a single secondary particle type, and so must lie within neutron treatment by the Geant4 physics lists used here. However, this discrepancy is not anticipated to be problematic, as it affects only neutrons below ∼20 MeV in energy and does not cause discrepancies in the spectra of any other secondary particles. An acute problem in neutron modeling would be expected to also affect protons of a similar energy due to elastic collisions with hydrogen nucleii, but no such anomaly is observed in the proton spectrum. Thus, although the root cause of this anomaly remains unknown, despite extensive testing of the model programming, it is not a systemic problem and has no adverse effect on the correct functionality of the model as a whole.

5.3.4 Mars Odyssey

De-excitation of the hydrogen nucleus following neutron-capture produces a distinctive gamma ray of 2,223 keV (2.2 MeV), and has been used to infer the abundance of water ice in the near subsurface of Mars [40] as described in Section 1.1.1 on page 16. This feature can be seen clearly in the gamma emission spectrum produced by the model. Figure 5.8 displays the calculated gamma spectrum between 1,122 keV and 3,548 keV for the Dry Homogenous and Pure Ice surface models. The spectrum recorded by the gamma ray spectrometer (GRS) aboard Mars Odyssey, accumulated over the south polar region, is also shown, demonstrating the sharp spike in flux at 2,223 keV [40]. The data output from the model is an omnidirectional surface flux per unit area, whereas the Odyssey data is detector counts from the GRS in orbit and so for comparison in Figure 5.8 both data sets are normalised to arbitrary units of fluence.

The fact that the model accurately reproduces observational data on the gamma spectrum

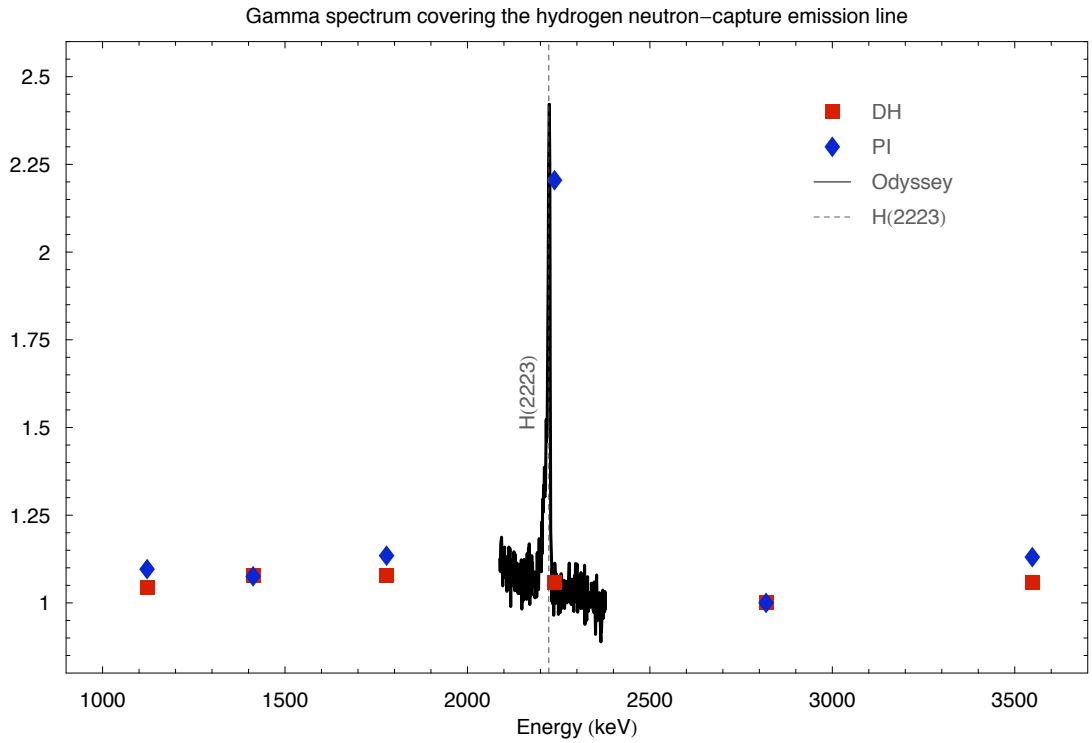

Figure 5.8: Modeled gamma spectrum data for the Dry Homogenous (DH) and Pure Ice (PI) surface models overlaid on the gamma emission spectrum measured by Mars Odyssey over the south polar region (Boynton *et al.* 2002 [40]). Also marked is the hydrogen neutron-capture gamma emission energy of 2,223 keV. Both sets of data have been normalised to arbitrary units of fluence.

corroborates that not only the physics lists, but also the data collection and post-processing routines, are all functioning as designed.

5.4 Comparison of particle fluence

5.4.1 Particle traversal per unit area

The total particle flux, i.e. the integration of the energy spectrum for a particle type at a particular depth, can also be compared against previously-published work to confirm the validity of the physics models and normalization used here.

Cucinotta *et al.* (2002) [63] calculate the probable number of particle-hits per human cell (taken to be 100 μm^2 cross-sectional area) at the martian surface under solar minimum conditions. These data are presented alongside the corresponding figures for annual particle flux per 100 μm^2 calculated by this model in Table 5.5.

Table 5.1: Calculated number of particle hits per human cell (100 μm^2) per year near solar minimum on the martian surface

	Proton	HZE (Z=2-28)
Cucinotta *et al.* (2002) [63]	88.4	2.9
This model	33.15	3.3

There can be seen to be a very close agreement on the surface HZE flux, with a discrepancy on proton fluence of only a factor of 2.5 between the two models, most likely due to a small difference in the primary proton spectra at low energy used in these two studies.

5.5 Proton-weighting approximation

Here it is demonstrated that for dose-depth data, when information on specific particle types is not required, the complete GCR spectra can be justifiably approximated with suitably-weighted proton-only data (the superposition model [133]), as was utilised in the second configuration of the model. The dose-depth profile was simulated with the GCR spectra modeled firstly using only weighted proton data and secondly using appropriately-energy-weighted data from proton, helium and carbon primaries (CREME-96 solar minimum GCR flux, 16 g/cm^2 atmosphere, 3 g/cm^3 dry regolith surface). Comparison of the results so obtained is shown in Figure 5.9. It should be stressed that the Geant4 particle modeling here does not neglect nucleus-nucleus interactions, and recoil nuclei and nuclear fragments in the target are treated fully within the Z and E constraints of the available physics descriptions, but only proton primaries are used to emulate the full incoming GCR particle spectra.

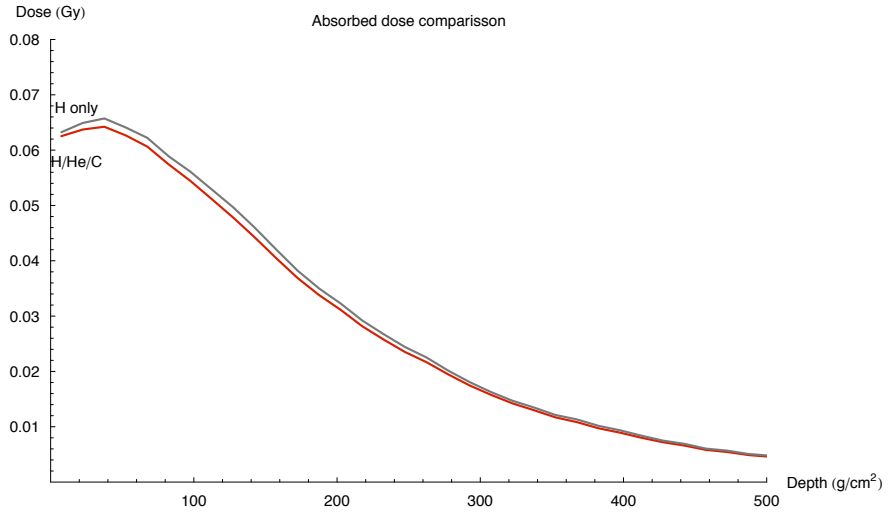

Figure 5.9: Comparison of dose-depth profiles in the martian subsurface (3 g/cm^3 dry regolith) from solar minimum GCR flux, calculated using the weighted proton-only approximation (second configuration of the model) and the more computationally-demanding simulation using recombined data from hydrogen, helium and carbon ion primaries (first configuration).

The two plots can be seen to differ only marginally, with the proton-only calculation yielding a dose differing by no more than 3% in the top 500 g/cm^2 from the much more computationally-expensive model incorporating data from hydrogen, helium and carbon ion primaries. This difference is negligible considering the greater sources of variation inherent in such radiation modeling, such as differing GCR primary spectra models and particle interaction models. Furthermore, it should be noted that the scaling approximation would become increasingly accurate at deeper depths because the primary ions will have undergone extensive hadronic interactions and the flux transformed from highly-ionizing ions (with large Z^2 values, see Section 1.2 on page 22) into unbound nucleons.

The finding that the proton-only model calculates a slightly higher total dose deposited in the regolith is thought to be a real effect and not an artifact of the weighting of data from several primary ions. One possible explanation is that the more extensive nuclear reactions triggered by the relatively small flux of heavier ions produces more albedo particles, with slightly more of the incoming energy thus "leaking" back out of the regolith.

5.6 Chapter summary

- The model described here was developed to address for the first time certain features of the martian radiation environment, principally the particle energy spectra and doses deposited in the subsurface. The model was designed, however, to also produce output that repeated the work of earlier studies, so as to validate the correct functionality and predictions of this model, before moving on to the novel work. Numerous tests of the model predictions have been presented, of both particle energy spectra and surface fluence, all of which confirm the correct general functionality of the model.
- The influence of charged particle deflection by the crustal magnetic anomalies has been treated, through both surface fluence mapping and gyroradius calculations, but can be ignored when considering the subsurface radiation environment because particles with enough energy to penetrate the atmosphere and deposit dose in the subsurface are not deflected appreciably by these weak magnetic fields.
- A problem with erroneous primary spectra provided by the SPENVIS database was overcome by refitting the extensive data already generated to the CREME-96 model, and the validity of this approach confirmed.
- The validity of the proton-only approximation used in the second configuration of the model for treating the full GCR ion spectra when only dose-depth data are required, and not information on specific particle types, was confirmed through test runs.

Chapter 6

Modelling Results

As detailed in Chapter 3, the model was run in two fundamentally different modes. Firstly, with a succession of micron-thick water layers embedded at regular depths in the regolith to approximate bacteria, outputting biologically-weighted radiation doses and particle energy spectra and fluxes. Secondly, the regolith block was "virtually sub-divided" into layers, allowing much improved processing efficiency, and outputting data only on the physically absorbed dose. The results from these applications are treated in turn here.

6.1 Particle energy spectra and fluences

Figure 6.1 displays the particle energy spectra across six orders of magnitude (1 MeV to 1 TeV) at the martian surface, as determined by the first configuration of the radiation model. The six most important particle species are shown: protons, HZE, neutrons, gamma, electrons/positrons and muons, although it should again be noted that the Monte Carlo methodology employed here generates and tracks all secondary particles in both the hadronic and electromagnetic cascades. The discontinuities in the proton spectrum at 10 GeV and 100 GeV are due to the refitting of the primary spectrum, forced by the discovery of errors in the SPENVIS database, as reported in Section 5.1. Artifacts created by simulating the entire HZE primary spectra (H – Fe ions) by using helium and carbon primaries up to 10 GeV/nuc (limited by the Geant4 physics models) are also visible in the HZE spectrum at high energies. The feature in the proton spectrum at around 100 MeV is due to the low energy cut-off of the SEP spectrum given by SPENVIS.

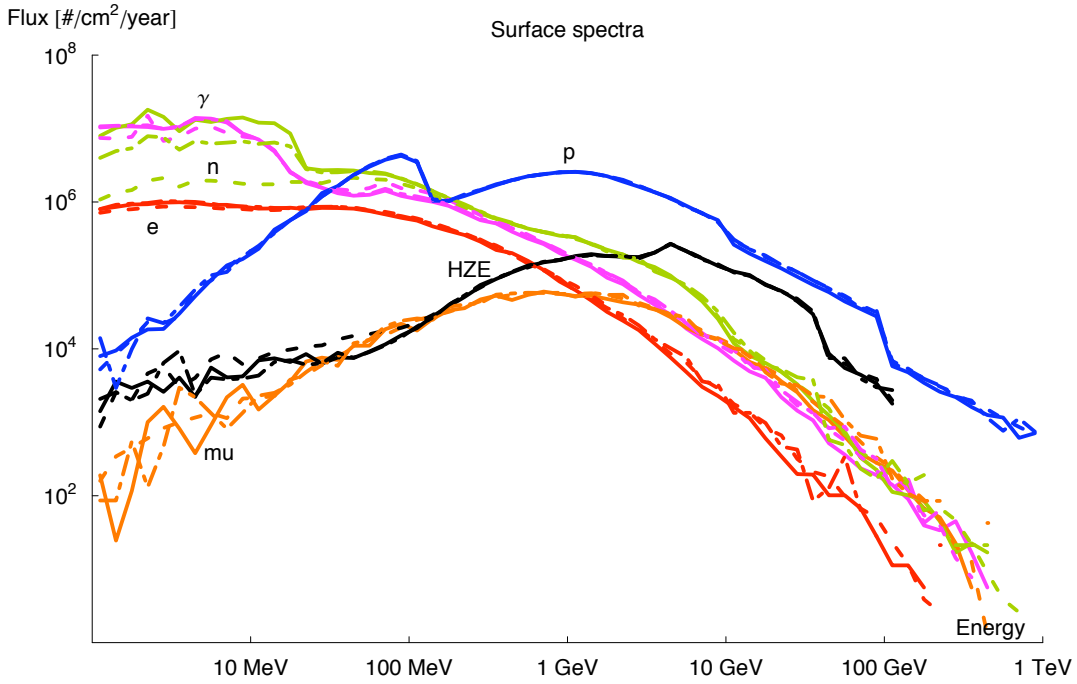

Figure 6.1: Energy spectra of the six most important particles at the martian surface from SEP and GCR (solar minimum). Colour-coding of particle types: HZE (black), proton (blue), neutron (green), muon (orange), gamma (purple), electron/positron (red). Surface model indicated as follows: Dry Homogenous (solid), Pure Ice (dashed), and Wet Heterogeneous (dot-dash).

The surface flux of protons, HZE and muons can be seen to be invariant on the ground model, as expected since this hard component of the cascade does not backscatter and so differences in regolith composition have no effect on surface flux. At high energies, proton and HZE flux dominates the surface radiation environment, but below ∼45–25 MeV the secondary particles, gamma-rays, neutrons and electrons/positrons have the greatest flux. The enhanced neutron fluence at low energies from surface backscatter is also clear, as is also reported by Clowdsley *et al.* (2000) [52] and was discussed in detail in Section 5.3.3 on page 107

Figure 6.2 shows the energy spectra of proton and HZE particles as a function of depth in both the dry homogenous (DH) regolith and the pure ice (PI) surface model, every 0.5 m to a maximum of 2 m for DH and 5 m for PI, from SEP and GCR (solar minimum) primaries. The enhancement in low energy protons (below ∼100 MeV) on the martian surface from solar energetic particle events can be seen to be rapidly attenuated within the top 0.5 m of both ice and rock shielding. The peak proton flux due to GCR can be seen to be energy-shifted from ∼1 GeV to ∼300 MeV between the surface and 2 m depth in the regolith.

Despite the noise inherent in this modeled data, especially at the extremes of energy and at greater depth, the high energy HZE can be seen to be modified most by the rock or ice shielding. This is due both to ionisation losses to the target causing an energy down-shift in the spectrum, and nuclear interactions leading to fragmentation of the primary HZE into protons and neutrons. It is also evident in both graphs that the HZE flux at all energies is attenuated more rapidly than protons. This is due to the higher charge of HZE ions, which are therefore are more highly ionising and so lose their energy more rapidly to the shielding material (see the explanation of the Bethe-Bloch formula in Section 1.2 on page 22). The lower energy HZE and protons show least reduction from the primary spectrum because these particles are regenerated by nuclear fragmentation within the hadronic cascade. The HZE spectra in the pure ice surface show a

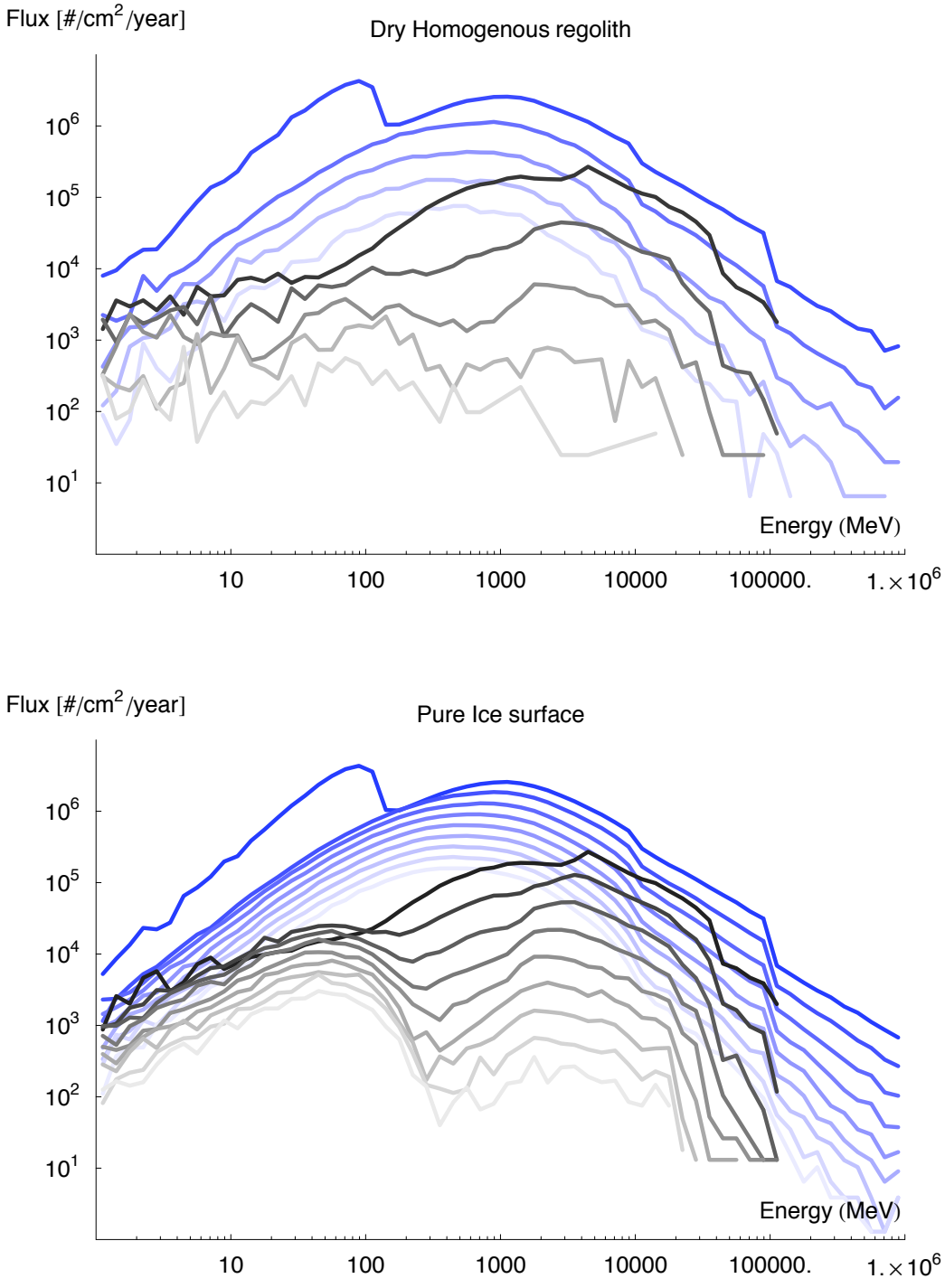

Figure 6.2: Modification of the proton (blue) and HZE (black) spectra as a function of depth in the dry homgoenous regolith (top) and pure ice (bottom) surface models, from SEP and GCR (solar minimum). Spectra are shown at depths every 0.5 m (coded by colour intensity in the plot) from the martian surface to a maximum depth of 2 m in the dry homogenous surface and 5 m in pure ice.

clear development into a bimodal distribution of particle energies by around 1.5 m depth, with local peaks at approximately 50 MeV and 2.5 GeV. The dry homogenous HZE spectra also show the higher-energy peak (∼2.5 GeV) at 0.5 m depth, but not the lower-energy spectral feature. This difference may be due to the fact that targets with low atomic mass, such as the hydrogen-rich ice, have a larger nuclear interaction cross-section and so more effectively fragment the projectile HZE ions [74]. By 5 m depth in ice, the higher-energy peak in the HZE spectrum has diminished, leaving only a broad hump at lower energies.

Figure 6.3 shows the calculated spectra of protons, HZE, neutrons, gamma, electrons/positrons and muons at 1 m depth. The lower energy neutron spectra can be seen to be strongly dependent on the regolith model. This is due to the efficient moderation and capture of neutrons by the high hydrogen content of water. These energy spectra are not specific to microbial targets and so can also be used to calculate the dose absorbed by astronauts within habitats protected by regolith-derived shielding.

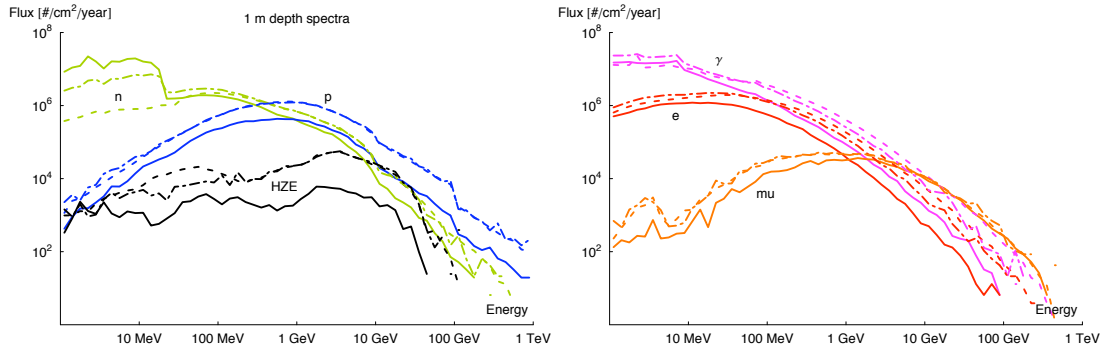

Figure 6.3: Energy spectra of the six most important particles at 1 m depth from GCR at solar minimum. Colour-coding of particle types: HZE (black), proton (blue), neutron (green), muon (orange), gamma (purple), electron/positron (red). Surface model indicated as follows: DH (solid), PI (dashed), and WH (dot-dash).

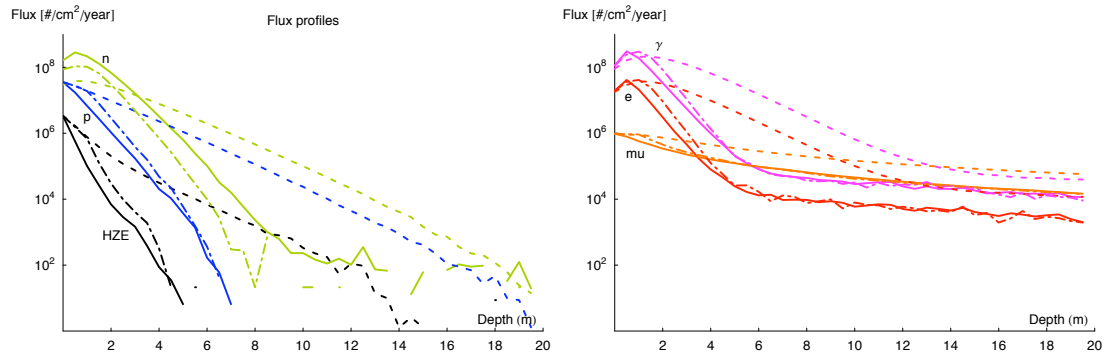

Figure 6.4: Attenuation with depth for (top) hadronic core, and (bottom) muons and electromagnetic cascade. Surface model indicated as follows: DH (solid), PI (dashed), and WH (dot-dash).

Figure 6.4 shows the flux of proton, HZE, neutron, muon, gamma and e^-/e^+ secondaries as a function of depth. Both hadronic and electromagnetic cascades can be seen to be attenuated least by the pure ice model, due to the lower shielding density of the ice target. Neutron flux, however, is attenuated quickest within the wet heterogeneous regolith as this shielding material is both hydrogenous and dense. Pfotzer maxima are observed within the gamma and electron

depth-profiles of all three regolith models, occurring 1 m deeper in pure ice than the more dense dry homogenous target. In all regolith scenarios the gamma flux declines until it meets the muon profile, with these weakly-interacting secondaries penetrating at appreciable levels to the full 20 m depth modelled. The electron flux follows at a factor of five lower as they are produced by muon decay and gamma pair-production. On average, a microbial cell (taken to have cross-sectional area of 10^{-12} m^2) on the surface is traversed by an HZE (Z≥2) every 30 years, and every 145 years 1 m deep in the wet heterogeneous surface.

Figure 6.5 compares the different contributions to the surface radiation environment (dry homogenous subsurface model). The spectra of primary protons and HZE ions are shown (simulated with physical interactions in both the atmosphere and subsurface columns turned off), the radiation modulation by the atmosphere only (backscatter neglected by turning off physical interactions in the subsurface material), and the complete radiation environment on the surface (influences of both atmosphere and backscatter from subsurface considered). Artifacts of primary spectra reconstruction can be seen in the proton spectrum at 10 GeV and 100 GeV, and in the HZE spectrum where helium and carbon ion primaries were used to fill-in for the entire HZE flux as far as possible within the constraints imposed by Geant4 physics models.

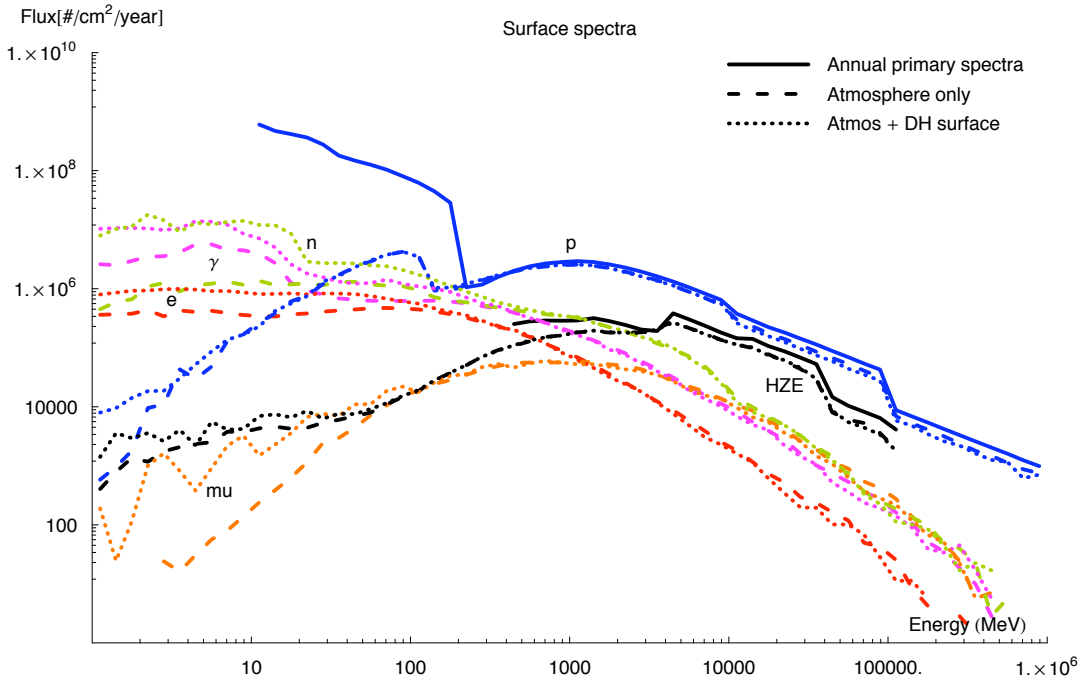

Figure 6.5: Components of the particle energy spectra on the martian surface from different sources. Shown are the annual primary spectra (SEP and GCR protons and HZE only; solid lines), the spectra produced beneath the martian atmosphere (with backscatter from the subsurface neglected; dashed lines) and the complete surface spectra (both atmospheric and Dry Homogenous surface shielding considered; dotted lines). Fluence enhancement due to backscattering (albedo) particles is evident where the dotted line is elevated above the dashed. Colour-coding of particle types: HZE (black), proton (blue), neutron (green), muon (orange), gamma (purple), electron/positron (red).

A slight decrease in high energy proton flux from atmospheric shielding is demonstrated and significant attenuation of proton fluence seen below ~200 MeV, which is of primary importance to the surface radiation environment during a solar energetic particle event. At intermediate proton energies, of a few hundred MeV to a few GeV, there can be seen to be no net atmospheric effect; particle attenuation at these energies is balanced by secondary proton production within the atmospheric column.

The enhanced neutron fluence below 500 MeV due to surface backscatter is also clear, and matches the energy threshold reported by Clowdsley *et al.* (2000) [52], as was discussed in detail in Section 5.3.3 on page 107. Both gamma-ray and electron flux show an enhancement of roughly 2× from albedo fluence below 200–300 MeV, and calculated muon fluence, although noisy at low energies, is clearly increasingly enhanced below 100 MeV due to backscattering particles from the subsurface.

6.2 Microbial survival

Figure 6.6 plots the annual accumulation of physically-absorbed dose and biologically-weighted dose as a function of depth for all three surface models. The surface weighted dose is almost 0.85 Gy/year for all three models, of which in DH 20% is mediated by backscattering particles and 35% contributed from SEP.

A single flare can deliver several percent of the average annual fluence in a matter of hours. The proton spectrum recorded from the very hard January 20th 2005 event [153] was corrected for martian orbit by inverse-square distance scaling and run through the model. The calculated surface dose rate approaches $1\text{x}10^{-3}$ Gy/hr. Although present at a high flux, SEP are not particularly energetic and only deposit significant dose in the top 10 cm of the two rocky surfaces and top 20 cm in the PI model.

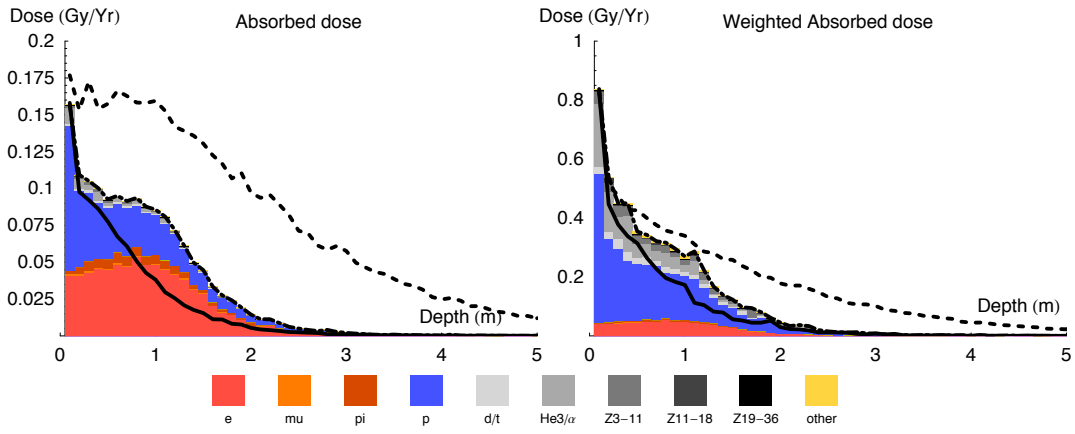

Figure 6.6: The decline in absorbed dose (left) and biologically-weighted dose (right) with depth. Shown for all three surface models: DH (solid), PI (dashed), and WH (dot-dash). Energy deposition within WH model colour-coded by particle-type.

A segmented bar chart showing the dose contributions from different particles has been overlain the curve for the Wet Heterogeneous (WH) model. Energy deposition by all particles is included, but HZE, protons, muons and e^-/e^+ dominate. The absorbed dose graph shows the surface spike from SEP flux, with the proton influence steadily diminishing with depth, and muon and e^-/e^+ deposition becoming increasingly dominant in the radiation field. Averaged over the top meter of WH regolith, HZE particles contribute only 7% of the absorbed dose, but due to their disproportionately deleterious effect at the cellular level make up 31% of the weighted absorbed dose. Using the annual accumulation of weighted dose it is possible to determine the population survival times (defined in Section 3.6.3 on page 73 as a million-fold decrease in viable cell number) for each of the three model organisms as a function of depth within each of the surface scenarios, as shown in Table 6.1.

Table 6.1: Summary of calculated biologically-weighted doses and microbial survival times as a function of depth in the martian subsurface, from SEP and GCR (solar minimum).
[a] DH, dry homogenous; PI, pure ice; WH, wet heterogeneous.
[b] Not including radionuclide contribution. Values shown for depths >2 m are averaged over ±0.5 m.
[c] 10^6 population reduction. EC: *E. coli*; BS: *B. subtillis*; DR: *D. radiodurans.*

Depth (m)	**Surface model[a]**	**Absorbed Dose (Gy/year)[b]**	**Weighted Dose (Gy/year)[b]**	**Survival Time (years)[c]**		
				EC	**BS**	**DR**
0	DH	0.16	0.83	1,200	10,100	18,100
	PI	0.18	0.83	1,200	10,100	18,100
	WH	0.16	0.84	1,200	10,000	17,900
0.5	DH	0.07	0.27	3,800	31,700	56,600
	PI	0.16	0.4	2,500	21,000	37,500
	WH	0.10	0.34	2,900	24,500	43,800
1.0	DH	0.03	0.11	8,900	75,000	134,000
	PI	0.15	0.31	3,200	27,000	48,000
	WH	0.08	0.29	3,500	29,000	52,000
2.0	DH	4.7×10^{-3}	0.02	43,000	370,000	650,000
	PI	9.4×10^{-2}	0.17	5,900	50,000	90,000
	WH	1.1×10^{-2}	0.03	30,000	250,000	450,000
5.0	DH	1.3×10^{-4}	6.5×10^{-4}	1.5×10^{6}	1.3×10^{7}	2.3×10^{7}
	PI	1.2×10^{-2}	2.5×10^{-2}	4.1×10^{4}	3.4×10^{5}	6.1×10^{5}
	WH	9.5×10^{-5}	2.0×10^{-4}	5.1×10^{6}	4.3×10^{7}	7.6×10^{7}
10.0	DH	2.3×10^{-5}	2.3×10^{-5}	4.3×10^{7}	3.6×10^{8}	6.5×10^{8}
	PI	3.5×10^{-4}	6.0×10^{-4}	1.7×10^{6}	1.4×10^{7}	2.5×10^{7}
	WH	2.8×10^{-5}	3.4×10^{-5}	3.0×10^{7}	2.5×10^{8}	4.5×10^{8}
20.0	DH	6.7×10^{-6}	6.7×10^{-6}	1.5×10^{8}	1.3×10^{9}	2.2×10^{9}
	PI	4.1×10^{-5}	4.8×10^{-5}	2.1×10^{7}	1.7×10^{8}	3.1×10^{8}
	WH	5.6×10^{-6}	6.8×10^{-6}	1.5×10^{8}	1.2×10^{9}	2.2×10^{9}

The results for microbial survival calculated here are consistent with those of previous studies. Taking the Dry Homogenous surface scenario (density of 2.81 g/cm^3), and considering the contribution from GCR only, this model predicts that a population of *D. radiodurans* on the martian surface (0 g/cm^2 shielding depth) will suffer a 10^6 reduction within 153,000 years. This value is bracketed by the comparable results of Mileikowsky *et al.* (2000) [154], which calculate a survival period of 2.8 million years before 10^6 population reduction of *D. radiodurans* on the surface, and Pavlov *et al.* (2002) [181], which calculates 10^8 inactivation within 30,000 years in the top 20 g/cm^2 of subsurface. At 500 g/cm^2 depth, this model calculates a *D. radiodurans* population persistence of 1.8 million years, whereas Mileikowsky *et al.* (2000) [154] find a longer survival period of 14 million years. By the shielding depth at which the cosmic ray influence has been reduced to less than that expected from the natural radioactivity of the regolith (4 $\times$ 10^{-4} Gy/year [154]), calculated here to be $\sim$ 1,000 g/cm^2 ($\sim$ 3.5 m deep in 2.81 g/cm^3 dry regolith), this model calculates a *D. radiodurans* population can survive for 40 million years, matching the findings of Pavlov *et al.* (2002) [181].

6.3 Dose deposited in regolith

With the second configuration of the radiation model set-up to record only physical dose deposited in the martian subsurface, a 3 g/cm^3 dry dust model beneath a 16 g/cm^2 atmosphere and solar minimum GCR flux, the current martian surface dose is calculated to be 6.2 cGy/year, building to a peak of 6.6 cGy/year at 40 g/cm^2 shielding depth ($\sim$13 cm in this surface scenario). These figures agree well with those presented in Simonsen & Nealy (1991) [207] and McKeever *et al.* (2003) [151], but differ from two other studies into the martian subsurface radiation dose. Pavlov *et al.* (2002) [181] report values of a peak dose of 20 cGy/year at 25 g/cm^2 depth and Mileikosky *et al.* (2000) [154] find a surface dose of 19.4 cGy/year, building to a peak of 24.9 cGy/year at 30 g/cm^2 depth. The probable reasons for this discrepancy in calculated subsurface dose between the two sets of models will be discussed at length in Section 8.3 on page 148.

6.3.1 Surface properties

Figure 6.7 (top) shows the dose-depth profiles calculated for four distinct surface scenarios: 1 g/cm^3 dry dust, 3 g/cm^3 dry regolith, 1 g/cm^3 water ice, and the layered permafrost model (WH). The dose peak occurs at a shallower depth in the 3 g/cm^3 dry regolith due to its greater density, but this scales to an equal shielding depth (40 g/cm^2) as the 1 g/cm^3 dry dust surface. The 1 g/cm^3 ice material creates a dose peak slightly shallower at 30 g/cm^2 depth. The top meter of loose topsoil of the wet heterogeneous permafrost model shows a dose intermediate between the dry dust and pure ice models of similar density, and a rapid decline in dose through the higher density ice-laden regolith beneath.

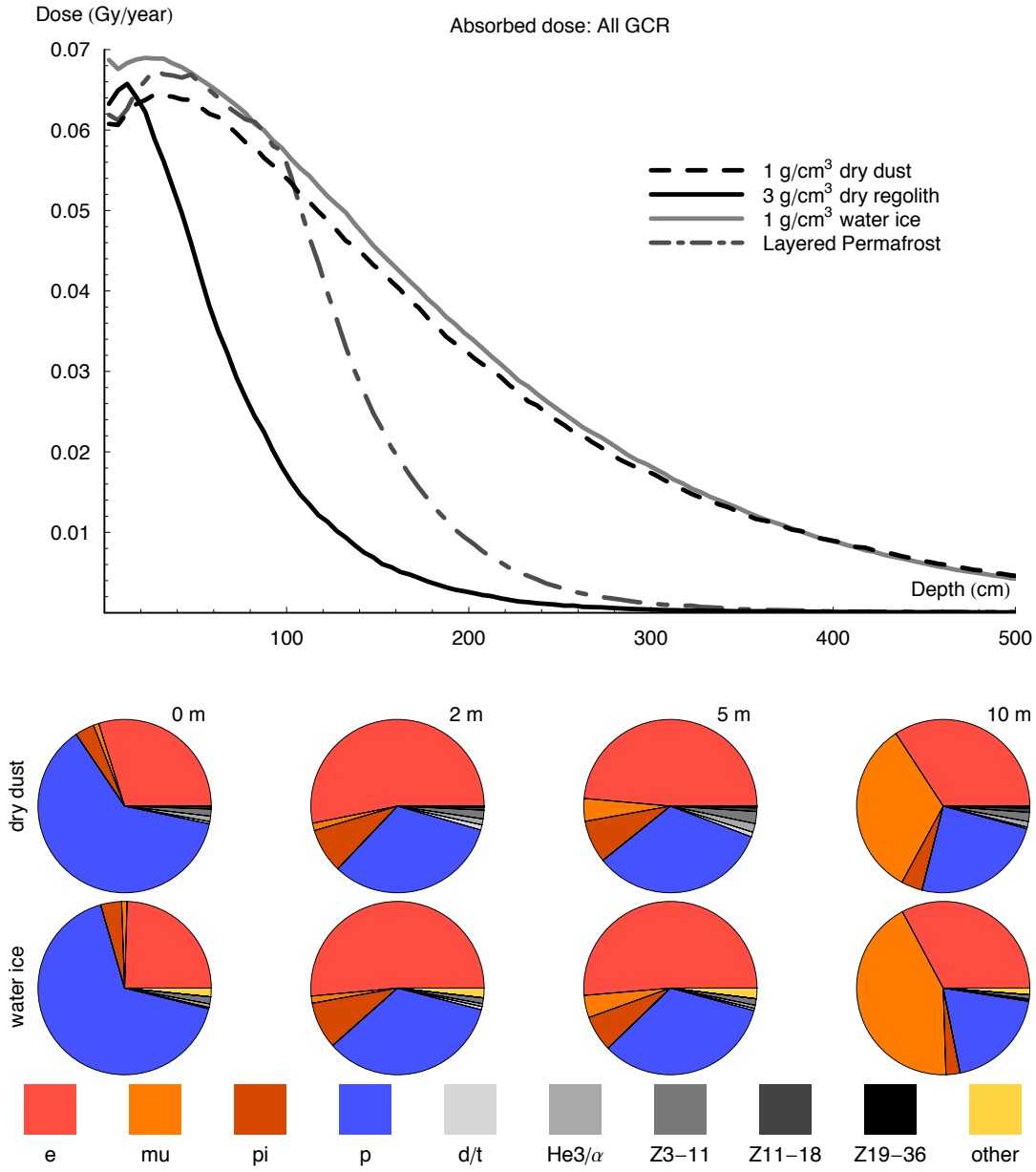

Figure 6.7: Dose profiles for different surface scenarios under solar minimum GCR irradiation. Bottom: Dose deposited by the changing composition of the ionising radiation field with depth, compared between 1 g/cm3 dry dust and water ice material.

Figure 6.7 also shows the composition of the ionising radiation field (proportion of dose deposited by different particle types) as it changes with depth. In general the hadronic cascade of HZE and protons is attenuated with depth and the more deeply penetrating (weakly interacting) particles, muons and pions, and the electrons produced in the electromagnetic cascade, become increasingly dominant in the radiation environment. At all depths, the HZE dose is lower in the ice material as it contains a much lower compositional proportion of heavy elements and so generates fewer HZE in the hadronic cascade. By 10 m (1000g/cm^2) depth the ice shielding material produces a radiation environment with a significantly greater muon contribution. Neutrons, although treated in full by the particle interactions model, are uncharged and do not directly ionise the material, but cause recoiling protons which are highly ionising. This may explain the higher proportion of proton-delivered dose at the surface of the ice: caused by moderation of back-scattering neutrons.

Integration under the dose-depth curve gives the total amount of energy deposited in the surface. The 20 m depth of dry regolith is found to absorb 73% of the total energy delivered by the GCR flux (around 0.02 J/cm^3/year), the rest being absorbed by the atmosphere (5% of the total) or escaping with back-scattering particles (mostly neutrons and gammas). The pure ice column retains 76% of the incoming energy, the slight increase presumably due to more effective capture of neutrons by its hydrogenous content (most significantly the backscattering neutrons, creating the higher dose observed on the surface).

6.3.2 Solar activity

Figure 6.8 shows the calculations when irradiating the 1 g/cm^3 dry dust model with the CREME-96 GCR spectra for either solar minimum or solar maximum conditions. The surface and peak dose during solar minimum can be seen to be about double that of solar maximum. Integrated over the entire 20 m depth, the dose deposited during solar maximum is only two-thirds that of minimum activity conditions. Furthermore, the peak dose during solar maximum, although less in magnitude, occurs 20 g/cm^2 deeper in the surface.

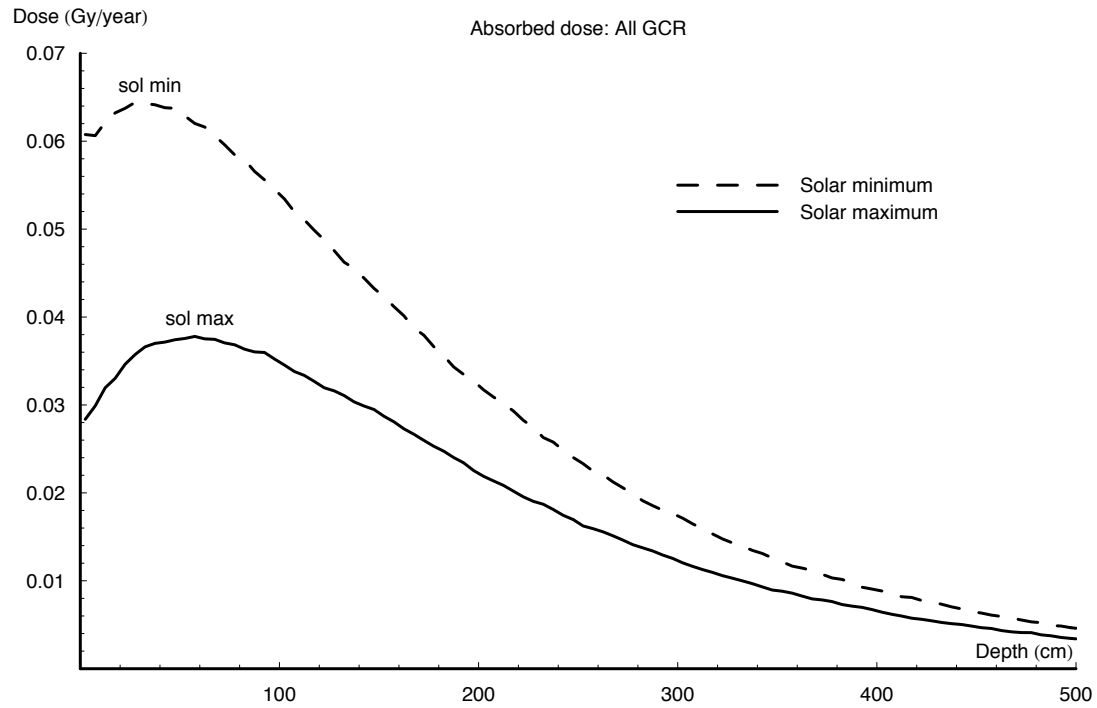

Figure 6.8: Subsurface dose profiles from GCR spectra (CREME-96) under solar activity maximum and minimum conditions (1 g/cm^3 dry dust surface model).

These are all effects of the significant heliospheric modulation of primaries less than about 10 GeV/nuc during periods of solar maximum. As seen in Figure 1.4 on page 23, there is an order of magnitude difference in flux for 100 MeV primary protons between solar minimum and maximum (CREME-96 model), and still a modulation factor of 3.6 at 1 GeV. Figure 6.9 shows the dose contribution from the different energy bands using during simulation of the GCR proton spectrum at solar minimum, with the section numbers corresponding to the ranges indicated in Figure 1.4.

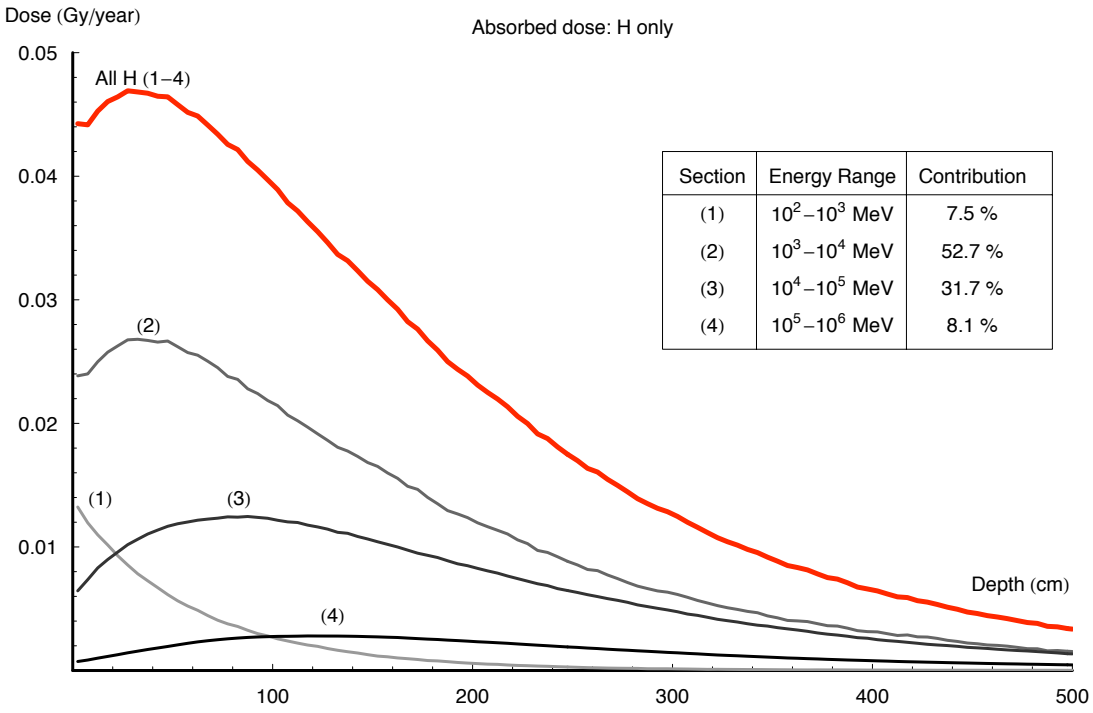

Figure 6.9: Dose contributions from different energy ranges of the primary GCR proton spectrum (CREME-96) at solar minimum (1 g/cm^3 dry dust surface model). Section numbers correspond to the energy bands used in modeling, indicated in Figure 1.4 on page 23.

Several important features are evident here. Protons <1 GeV (energy section 1) produce no dose peak; their profile is a simple exponential decay. The primaries do not carry enough kinetic energy for collisions to generate a hadronic cascade and they are quickly attenuated by the shielding matter. Each higher energy segment of the proton spectrum produces a deeper peak. Section 4 (100 GeV – 1 TeV protons) produces a gentle peak at 1.3 m depth, three times deeper than section 2 primaries (1 GeV – 10 GeV), but due to the very low flux of such high energy primaries this section does not contribute a large proportion of the total annual dose. The most important energy band of the primary spectrum is section 2 as it combines a high flux with relatively energetic particles. Shown in Figure 6.9, this energy range (1 GeV – 10 GeV) deposits over half of the total dose in the subsurface. These primaries are significantly modulated by the heliosphere between solar maximum and minimum phases (Figure 1.4 on page 23), and so the solar activity cycle is manifested in the changing subsurface dose profile (shown in Figure 6.8) principally through modulation of primary protons in the energy band 1 GeV –10 GeV (section 2 in this model).

6.3.3 Topographic elevation

Figure 6.10 plots the dose profiles in 1 g/cm^3 dry dust for three characteristic elevations on Mars: the top of Olympus Mons, bottom of Hellas impact basin, and the datum altitude, as well as a null atmosphere (vacuum). The general trend across the four scenarios of increasing atmospheric thickness is a decreasing peak dose at a shallower depth in the subsurface.

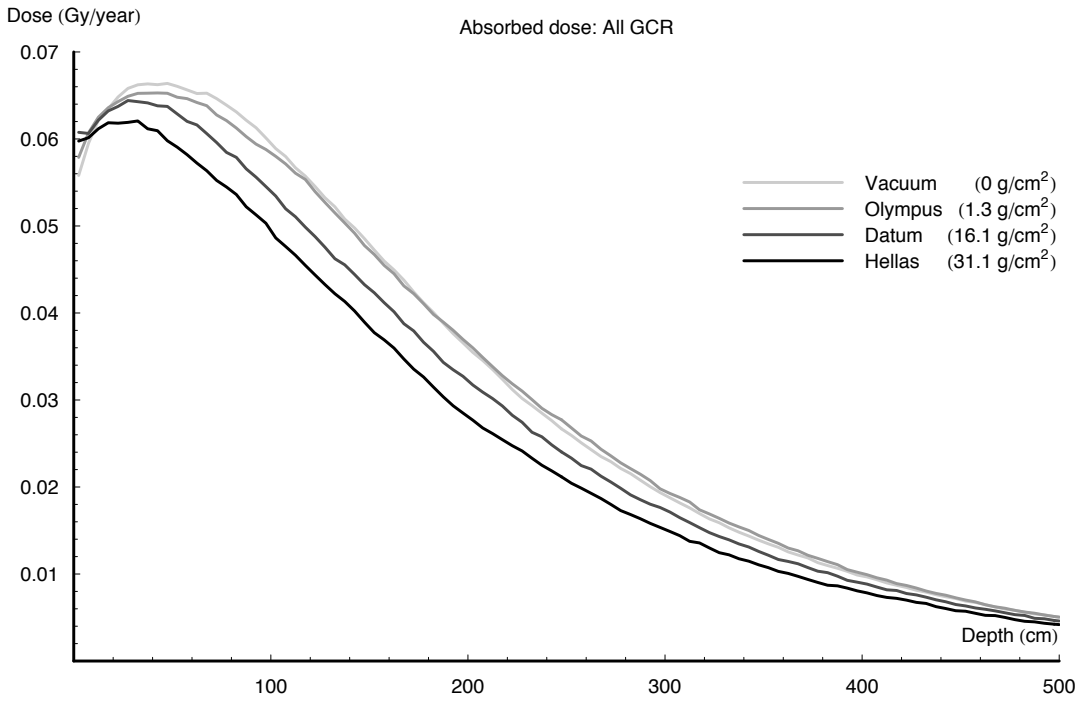

Figure 6.10: Subsurface GCR dose profiles (1 g/cm^3 dry dust surface model) for locations with different elevations on Mars during solar minimum (CREME-96 spectra); the bottom of the Hellas impact basin, the datum altutude, the top of Olympus Mons, and also a simulation with no atmospheric column included (vacuum).

Even though the martian atmosphere is comparatively thin, providing only 6 mbar surface pressure at the reference altitude, it can be seen that its radiation shielding properties should not be discounted. Comparison of the dose profile at the datum altitude against that beneath vacuum indicates that even a 16 g/cm^2 depth of atmosphere affects cosmic ray propagation. Perhaps paradoxically, the effect of this additional shielding is to actually increase the surface dose by 10% through limited initiation of secondary cascades. At the lower elevation of the Hellas basin, the surface dose is lower as the doubled atmospheric shielding thickness begins to exert an attenuation effect. Beneath about a meter's subsurface depth, the dose profiles for Olympus Mons, datum altitude and Hellas basin roughly follow each other but for a $\sim$16 g/cm^2 shift in depth, and by 5 m depth, variation in atmospheric thickness has negligible remaining effect.

6.3.4 Diminishing atmospheric pressure over geological time

Figure 6.11 plots the subsurface dose profiles under four surface pressure scenarios (0.385 bar, 1033 g/cm^2; 0.1 bar, 268 g/cm^2; 0.01 bar, 27 g/cm^2; 0.006 bar, 16 g/cm^2). This sequence of diminishing atmospheric thickness is taken to represent gaseous loss over the geological history of the planet, independent of models attempting absolute dating of these stages. The 0.385 bar scenario was selected as it represents a primordial martian atmosphere with identical shielding depth (1033 g/cm^2) to the current terrestrial atmospheric column [168].

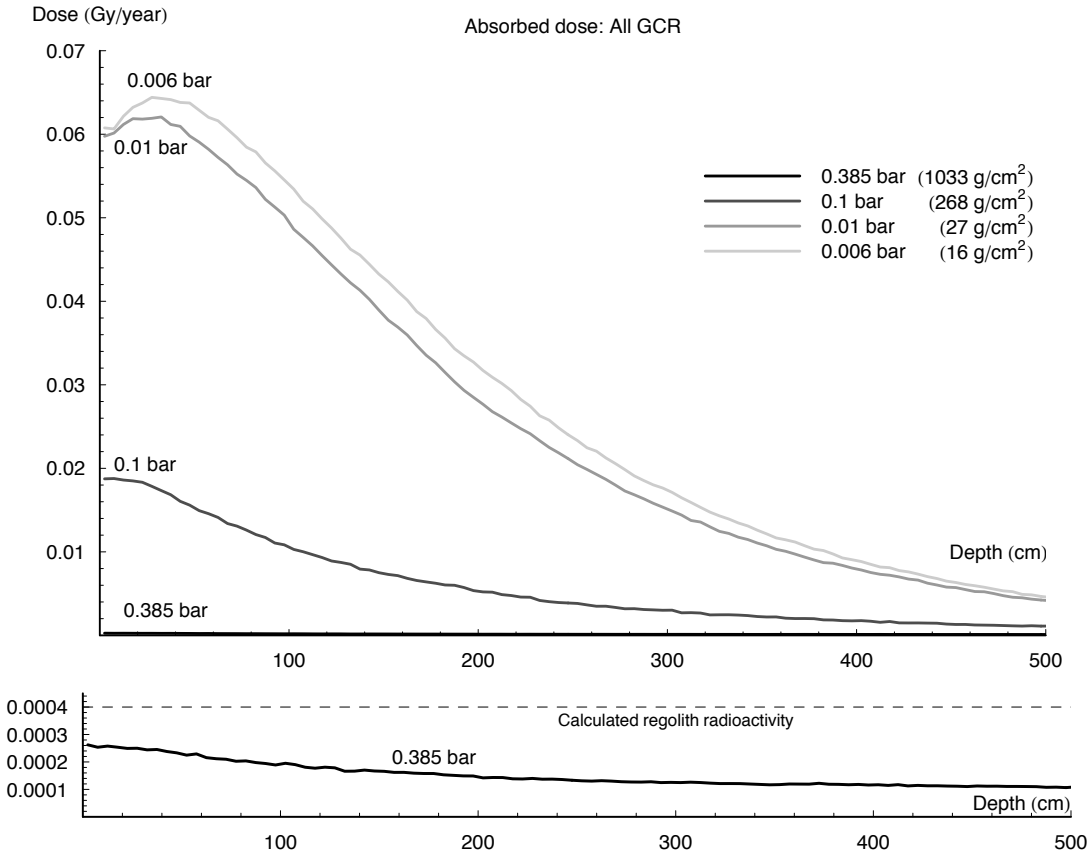

Figure 6.11: Subsurface (1 g/cm^3 dry dust surface model) solar minimum GCR (CREME-96 spectra) dose profiles under decreasing atmospheric depths, over the geological history of Mars. Rescaled plot of 0.385 bar case shown below.

Decreasing surface pressure produces a non-linear response of total atmospheric shielding thickness (integration of the density-altitude profile), and thus also of generated subsurface dose profile. Scaling with the combined shielding thickness of atmosphere and subsurface, however, the surface dose under a 0.385 bar atmosphere is roughly equivalent to that at 10 m depth with the current atmosphere, and the surface dose under a 0.1 bar atmosphere equivalent to 2.4 m depth with 0.01 bar atmosphere.

Figure 6.11 also shows a replot of the subsurface dose profile beneath a 0.385 bar atmosphere (which produces an identical shielding depth to the current 1 bar terrestrial atmosphere) on an expanded scale. The surface dose, deposited almost entirely by muons and electrons, is 2.6×10^{-4} Gy/year, less than the calculated 4×10^{-4} Gy/year contribution from natural radioactivity of the regolith [154], and so the subsurface effects of cosmic rays are not significant beneath such a dense atmosphere.

Further interpretation and discussion of these data, and integration with the results of the microbiology and experimental irradiation work, is provided in Chapter 8.

6.4 Chapter summary

- The results reported here represent the first detailed description of the spatially- and temporally-variable complex ionising radiation environment of the martian subsurface.
- The major novel results include the energy spectra for six particle types, across six orders of magnitude in energy, from both solar energetic protons and galactic cosmic rays, as a function of depth underground, and in three distinct models of the martian subsurface.
- The surface radiation environment is discussed in terms of the relative contributions from secondaries produced in the atmosphere or backscattering upwards from the subsurface, and the attenuation in particle flux at increasing depth by the shielding of the subsurface.
- The biological effects of this ionising radiation field have been treated by using the deposited dose, weighted by appropriate factors, to calculate likely microbial population survival times.
- More extensive studies on the profile of dose deposited underground have been conducted to explore the influence of many different environmental parameters. These include the subsurface composition, the primary GCR spectra (modulated by the solar activity cycle), topographic elevation upon the martian surface, and the diminishing atmospheric density over a planetary time-scale.

Chapter 7

Microbiology & irradiation results

The previous chapter presented the results of the computer modeling research; theoretical work on accurately characterising for the first time the ionising radiation environment of the martian near-subsurface. In this chapter, results are presented on the microbiology research conducted alongside to further assess the habitability of this environment. This microbiology research was conducted along two main lines of investigation.

Firstly, the culturable microbial diversity of a surface sample from the Miers Valley was investigated. The novel isolates were identified using a molecular biological technique, 16S rRNA gene sequencing, and the phylogenetic relationship between these strains and others previously detected in similar harsh low-temperature environments was established. This sampling location, one of the Dry Valleys of Antarctica, is considered to be a terrestrial analogue site of Mars, and so characterisation of microbial life here provides valuable insight into the astrobiology potential of the martian near-subsurface.

Secondly, three of the novel Antarctic isolates, and two model organisms, were selected for gamma ray irradiation survival experiments at -79°C, a temperature characteristic of the martian surface. These gamma ray exposure experiments were planned and designed with reference to the results of the computer modeling, and they address survival of a major environmental hazard of the martian near-subsurface absent in Antarctica; ionising radiation.

7.1 Culturing from Antarctic Dry Valley

As described in the Methods Section 4.4 on page 85 (Chapter 4), a soil sample collected from the Miers Valley of Antarctica was tested for culturable microbes on a variety of solid growth media. The results of colonies observed after 15 days incubation at 4°C are shown in Table 7.1.

Table 7.1: Combinatorial grid of colony growth observed on media plates after 15 days growth at 4°C

Dilut^n	$\frac{1}{4}$ NBA	$\frac{1}{4}$ R2A	CZD	$\frac{1}{4}$ CZD	SMM
neat	Good spread of isolated colonies: white, creamy, and bright yellow	Good spread of tiny white and creamy colonies	Contiguous mess of protruded yellowy cream gloopy colonies - more dense than $\frac{1}{4}$CZD. Small white colonies and smaller white ones.	Lots of very large gloopy creamy white colonies, with smaller colonies growing in the gaps.	Lots of small pearly white colonies. Probably too slow growing to be of use.
10^{-2}	Larger, gloopy cream colonies, and smaller white colonies	Gloopy, creamy and white colonies	Isolated yellowy-cream colonies and smaller white ones	Smaller yellowy-cream colonies as above, but not joined into a contiguous mat. Also smaller white colonies	As above. A few noticeably larger than the other colonies (all pearly white), but still quite small.
10^{-4}	Very few, small white colonies	Few gloopy and also watery-looking colonies	Several very small white colonies	Few small white colonies	Few tiny white colonies.
10^{-6}	–	–	–	–	–
10^{-8}	–	–	–	–	–

Although not precisely quantified, it was observed that fewest microbes could be cultured on the starch minimal medium (SMM) plates. Furthermore, no colonies were found on any medium at a dilution greater than 10^{-4}. The dominant colony morphology appeared to be the fast-growing colonies gloopy-cream in appearance.

From these mixed populations, individual colonies were repeatedly picked-off and re-plated onto the medium used to isolate them until pure cultures were produced. For ease of nomenclature each of these isolates was relabeled with a numerical code. All were cultured from the Miers Valley soil sample, and so this strain number is prefixed with "MV". Table 7.2 lists the isolates thus derived.

Of these isolates, several were identified to be particularly fast-growing at Antarctic summer temperatures (largest colonies after 14 days incubation at 4°C). Such strains are indicated in Table 7.2 with a bullet-mark (•). Of these fast-growing strains, 12 were selected for further work based on the ease with which they could be cultured on NB or CZD agar. These are MV.1, MV.3, MV.4, MV.5, MV.7, MV.8, MV.10, MV.23, MV.24, MV.25, MV.26, MV.27.

Experiments were conducted to see if the strains which were isolated on other media could also be supported on NB agar. The following strains were discovered to also grow on $\frac{1}{4}$ NB medium at 4°C: MV.13, MV.14, MV.15, MV.18, MV.22, MV.24, MV.26, and MV.27. Strains isolated on full-strength CZD agar, MV.1, MV.3, MV.4, MV.5, were discovered to also grow well on $\frac{1}{4}$CZD agar plates.

Growth experiments at room temperature revealed that many of the isolates were not strict *psychrophiles* (defined as maximum growth rates at temperatures lower than 15°C [194]), but *psychrotolerant* as the fastest growers at 4°C actually grew more rapidly to form larger colonies after 14 days at room temperature. Gilichinsky (2000) [98, Table 8.1] also reports that the number of viable aerobic bacteria cultured from Antarctic Dry Valley sands peaks at 20°C, roughly a factor of ten higher than at either 4°C or 30°C. Several of the novel strains isolated in this research were discovered to grow rapidly at room temperature: MV.1, MV.7, MV.8, MV.10, and MV.27. These strains were therefore ideal candidates for selecting for irradiation experiments, as post-exposure cell survival plates could be grown up at room temperature for colony counting within 2–4 days, rather than 14–15 days incubated at 4°C.

Furthermore, it was discovered that MV.7, MV.10 and MV.27 also grow well in nutrient broth, thus enabling them to be cultured to high population number in liquid culture for use in the irradiation experiments.

Figure 7.1 displays photographs of colony plates of the 12 fastest-growing strains isolated on NB or CZD medium, re-streaked on to either $\frac{1}{4}$NB or $\frac{1}{4}$CZD agar accordingly. These images are taken with light transmitted through the plates from a lightbox, and so larger colonies appear darker. Photographs were taken of all strains growing on quarter-strength media so as to keep light transmission uniform. Colony appearances are reported in Table 7.2. Close familiarity with the colony morphologies and colours of the three environmental strains selected for the irradiation experiments, MV.7, MV.10, and MV.27, aids in identifying and excluding contaminants during growth experiments or survival cell counts.

Table 7.2: List of microbial strains isolated from the Miers Valley surface sample. The fastest-growing strains (largest colonies after 14 days incubation at 4°C) are also indicated in the table with a bullet mark (•).

Growth medium	Medium isolate #	Description	Isolate code	Fast Growth
CZD	1	Large, creamy coloured, gloopy colonies	MV.1	•
	2	Quite small colonies, white, feathery-appearance	MV.2	
	6	Large, gloopy, creamy	MV.3	•
	7	Large, gloopy, creamy	MV.4	•
	9	Large, gloopy, creamy (MV.1, 3,4,5 all look very similar)	MV.5	•
$\frac{1}{4}$**NBA**	1	Small white colonies	MV.6	
	2	Mid-sized, bright yellow colonies, shiny, often with clear boundaries	MV.7	•
	3	Mid-sized, bright yellow colonies	MV.8	•
	4	Small, milky-white colonies	MV.9	
	5	Large, gloopy-milky colonies	MV.10	•
	6	Small, white colonies	MV.11	
	7	Small, creamy colonies	MV.12	
$\frac{1}{4}$**R2A**	1	Large, gloopy white colonies	MV.13	•
	2	Large, gloopy white colonies	MV.14	•
	3	Large, gloopy white colonies	MV.15	•
	4	Tiny, clear colonies	MV.16	
	5	Large with dark-yellow center and pale border ("fried egg" look)	MV.17	
	6	Large, clear white gloopy colonies	MV.18	•
	7	Small, gloopy white colonies	MV.19	
	8	Small, gloopy white colonies	MV.20	
	9	Small, gloopy white colonies	MV.21	
	10	Large, gloopy, clear white colonies	MV.22	•
$\frac{1}{4}$**CZD**	1	Large, gloopy, creamy-white colonies	MV.23	•
	3	Mid-sized, bright white colonies	MV.24	•
	4	Large, creamy gloopy colonies	MV.25	•
	5	Large, creamy gloopy colonies	MV.26	•
	6	Large, cream-coloured, less gloopy - more distinct colonies	MV.27	•
	8	Large, less gloopy, white colonies	MV.28	
	9	Small colonies, clear-white gloop	MV.29	

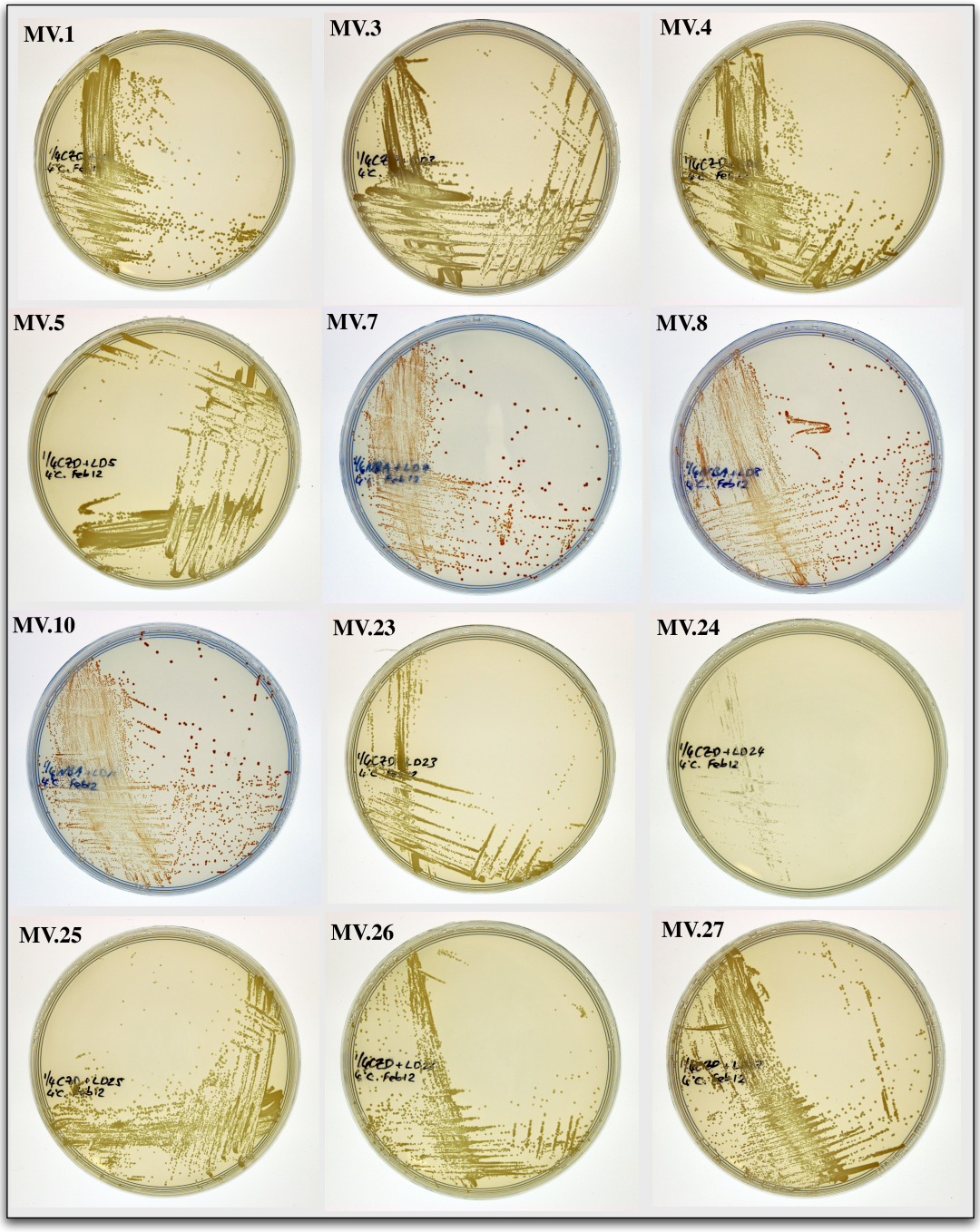

Figure 7.1: Photographs of the 12 fastest-growing novel Antarctic isolate colonies isolated on NB or CZD agar, taken with light transmitted through plate from a lightbox. All strains grown on quarter-strength agar of the medium from which they were isolated, listed in Table 7.2. From left to right, top to botom: MV.1, MV.3, MV.4, MV.5, MV.7, MV.8, MV.10, MV.23, MV.24, MV.25, MV.26, MV.27.

7.2 Growth of *D. radiodurans*

D. radiodurans was discovered to produce easily-countable brightly-coloured colonies on $\frac{1}{4}$NB agar after four days at room temperature. Figure 7.2 shows the distinctive pink-coloured colonies of *D. radiodurans* (grown here on $\frac{1}{4}$NB agar).

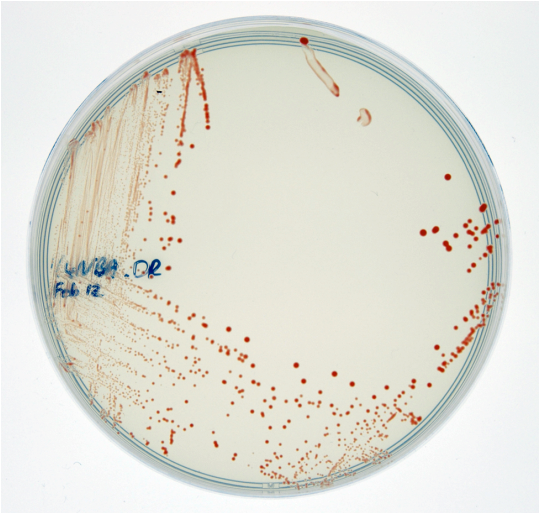

Figure 7.2: Photograph of the pink-coloured colonies of the radiation resistant bacterium *Deinococcus radiodurans*.

7.3 Identification of isolated strains

As explained in Methods Section 4.5 on page 86, 12 of the strains which grew fastest at 4°C were selected for molecular biology work to determine their identity. For each isolate, the 16S rRNA gene was amplified, cloned, sequenced, and compared against on-line databases of previously cloned sequences. Table 7.3 lists the Ribosomal Database Project (RDP) genus level identification and BLASTn closest match for each of the Antarctic strains and both the sequencing primers used. As explained in Section 4.5.3 on page 87, the selected PCR primers amplify a DNA fragment of approximately 1,500 base pairs, representing the vast majority of the 16S rRNA gene. This sequence is then cloned and end-sequenced. Only about 400 bases of good gene sequence is produced from each of the ends, however, and so the sequencing does not produce overlap within the gene. Consequently, the complete 16S rRNA gene sequence has not been recovered and the forward and reverse sequences are thus treated individually. Appendix I contains the gene sequences thus obtained.

The isolates can be seen to belong to four distinct bacterial genera: *Pseudomonas* (MV.1, MV.3, MV.4, MV.5, MV.23, MV.25, MV.26, MV.27), *Brevundimonas* (MV.7), *Arthrobacter* (MV.8 and MV.24) and *Rhodococcus* (MV.10). These correspond to two bacteria phyla; Proteobacteria (*Pseudomonas* and *Brevundimonas*) and Actinobacteria (*Arthrobacter* and *Rhodococcus*). These classifications can be considered to be robust, as they are confirmed by the sequences obtained from both ends of the 16S rRNA gene, and by both RDP identification and BLASTn nearest relative search.

Table 7.4 displays close relatives of these novel Antarctic isolates from similar low-temperature environments, such as other Antarctic sampling locations, mountainous permafrost or deep-sea

Table 7.3: 16S rRNA gene identification of the 12 Antarctic isolates. The sequence length recovered from both sequencing primers is shown, with the corresponding genus-level Ribosomal Database Project (RDP) identification and BLASTn nearest releative identity. Sequences shown in bold were identified as the forward sequence and used to plot the phylogenetic trees shown in Figures 7.3 and 7.4.

Isolate	**Sequence**		**RDP**	**BLASTn nearest relative**			
	Direction	**Length**	**Genus**	**Genus**	**Max score**	**Query Coverage**	**E value**
MV.1	**M13-40**	**417**	*Pseudomonas*	*Pseudomonas*	760	100%	0.0
	M13rev	420	*Pseudomonas*	*Pseudomonas*	776	100%	0.0
MV.3	**M13-40**	**417**	*Pseudomonas*	*Pseudomonas*	765	99%	0.0
	M13rev	417	*Pseudomonas*	*Pseudomonas*	765	100%	0.0
MV.4	M13-40	418	*Pseudomonas*	*Pseudomonas*	773	100%	0.0
	M13rev	**417**	*Pseudomonas*	*Pseudomonas*	765	100%	0.0
MV.5	**M13-40**	**416**	*Pseudomonas*	*Pseudomonas*	769	100%	0.0
	M13rev	462	*Pseudomonas*	*Pseudomonas*	854	100%	0.0
MV.7	**M13-40**	**402**	*Brevundimonas*	*Brevundimonas*	736	99%	0.0
	M13rev	440	*Brevundimonas*	*Brevundimonas*	809	99%	0.0
MV.8	M13-40	368	*Arthrobacter*	*Arthrobacter*	676	99%	0.0
	M13rev	**368**	*Arthrobacter*	*Arthrobacter*	680	100%	0.0
MV.10	M13-40	464	*Rhodococcus*	*Rhodococcus*	852	99%	0.0
	M13rev	**412**	*Rhodococcus*	*Rhodococcus*	761	100%	0.0
MV.23	**M13-40**	**397**	*Pseudomonas*	*Pseudomonas*	728	100%	0.0
	M13rev	410	*Pseudomonas*	*Pseudomonas*	758	100%	0.0
MV.24	**M13-40**	**384**	*Arthrobacter*	*Arthrobacter*	710	100%	0.0
	M13rev	169	*Arthrobacter*	*Arthrobacter*	211	100%	0.0
MV.25	**M13-40**	**416**	*Pseudomonas*	*Pseudomonas*	761	100%	0.0
	M13rev	394	*Pseudomonas*	*Pseudomonas*	728	100%	0.0
MV.26	M13-40	475	*Pseudomonas*	*Pseudomonas*	878	100%	0.0
	M13rev	**416**	*Pseudomonas*	*Pseudomonas*	767	100%	0.0
MV.27	**M13-40**	**418**	*Pseudomonas*	*Pseudomonas*	771	99%	0.0
	M13rev	477	*Pseudomonas*	*Pseudomonas*	881	100%	0.0

sediments, as identified by BLASTn search of both forward and reverse sequences. Also listed is the sequence similarity between each related strain and the underlined isolate from this work. These selected isolates were those used in the gamma ray irradiation experiments described in Methods Section 4.6 on page 90. Not all of the related strains shown Table 7.4 were successfully cultured as pure isolates by the researchers: many were identified directly from metagenomic environmental samples by PCR and 16S ribosomal gene sequencing.

It can be seen that the close relatives of the strains isolated in this work inhabit, or at least have been identified from, a broad range of locations from deep-sea sediments to mountain permafrosts. They also appear to be globally distributed, having been identified at latitudes between the Arctic and Antarctic. Of particular interest within the context of astrobiology is the discovery that *Brevundiomonas* sp. MV.7 shares a 99% sequence similarity with an uncultured bacterium identified within a spacecraft assembly clean room at Kennedy Space Center. The implications of this will be explored in the next chapter.

Phylogenetic trees were plotted to further elucidate the taxonomy and show the degree of relatedness of the novel isolates to each other, the strains from similar environments, and species representative of major bacterial clades. Figure 7.3 was plotted using the Ribosome Database Project (RDP) and shows the relationship between the 12 novel Antarctic isolates (forward sequences only), and representative species from other major bacterial clades (mostly complete gene sequences). These representative species were chosen to populate the phylogenetic tree, so as to place the novel isolates within the context of other major clades within the eubacterial domain of life. The outgroup strain used to improve tree topology was *D. radiodurans*. Bacterial strains selected for the gamma-ray irradiation experiments are indicated with an asterisk (*). In general, the calculated phylogeny tree can be seen to be well defined and correctly structured.

Figure 7.4 shows phylogenetic trees plotted for just the pseudomonas, actinobacteria and brevundimonas bacterial clades, illustrating the relationship between the novel isolates, type strains representative of the group, and the selected organisms from similar low-temperature environments shown in Table 7.4 (forward sequence matches only).

The eight novel pseudomonas isolates can be seen to cluster closely together on the 16S rRNA phylogenetic tree shown in Figure 7.4 (top). The *arthrobacter* strains MV.8 and MV.24 are shown by the middle tree in Figure 7.4 to be very closely related to each other. Comparing the aligned 16S rRNA gene sequences from these two isolates reveals that they share an identical sequence for all 368 bases that sequence is available for both. On the basis of this information, it is likely that the novel *arthrobacter* isolates MV.8 and MV.24 are in fact two representatives of the same bacterial strain isolated independently from agar cultures of the Miers Valley environmental sample.

7.4 Gamma irradiation

Three of the novel strains isolated from Antarctica were irradiated: *Brevundimonas* sp. MV.7, *Rhodococcus* sp. MV.10 and *Pseudomonas* sp. MV.27. Two control organisms were also exposed: *E. coli* strain C600, expected to show minimal radiation resistance, and *D. radiodurans*, an environmental bacterium which exhibits an extraordinary resistance to ionising radiation [155].

Table 7.4: Sequences of high 16S rRNA gene similarity to the novel isolates from similar low-temperature environments, identified by BLASTn search of 16S rRNA gene sequence from both forward and reverse sequences. Sequence similarity given for the underlined isolate, and isolates selected for irradiation survival experimentation indicated with an asterisk (*).

Genus	**Isolates from this study**	**Psychrotolerant relatives**		
		Sequence similarity	Sampling description	GenBank Accession #
Pseudomonas	MV.1	99%	Isolate; deep sea sediment, Prydz Bay, Antarctica	AM111061
	MV.3	99%	Uncultured; Antarctic top soil	AY267367
	MV.4	99%	Isolated psychrophile; Antarctic deep sea sediment	AJ519791
	MV.5	99%	Cold-tolerant isolate; Alpine soil	AY263470
	MV.23	99%	Isolated extremophile; deep-sea sediment	AJ551160
	MV.25	99%	Psychrotrophic isolate; Himalayas	AM746975
	MV.26	98%	Psychrotolerant isolate; Arctic soil, Finnish Lapland	DQ234520
	MV.27*			
Brevundimonas	MV.7*	100%	Uncultured; moraine lakes and glacial meltwaters, Mount Everest	DQ675501
		100%	Isolated; La Gorce Mountains soil, Antarctica	DQ351732
		99%	Uncultured; spacecraft assembly clean room, Kennedy Space Center	DQ532317
		99%	Psychrotolerant isolate; Qinghai-Tibet Plateau permafrost	DQ108394
		95%	Isolated; beneath John Evans Glacier, high Arctic, Canada	DQ628967
		95%	Isolated; microbial mat from Lake Fryxell, McMurdo Dry Valleys	AJ440993
Arthrobacter	MV.8, MV.24	99%	Cytotoxic isolate; Antarctica	EF471900
		99%	Uncultured; ancient permafrost soil	EU083797
		99%	Isolated; Chinese Great Wall Station, Antarctica	AM491456
		99%	Psychrotolerant isolate; Qinghai-Tibet Plateau permafrost	DQ177477
		99%	Isolated extremophile; deep-sea sediment	AJ551151
		99%	Isolated; deep-sea sediment	EU181231
Rhodococcus	MV.10*	99%	Uncultured; beneath John Evans Glacier, high Arctic, Canada	DQ228410
		99%	Isolated; Kafni Glacier soil, Himalayas	EF459533
		99%	Isolated extremophile; deep-sea sediment	AJ551145
		97%	Psychrotolerant isolate; Arctic soil, Finnish Lapland	DQ234488

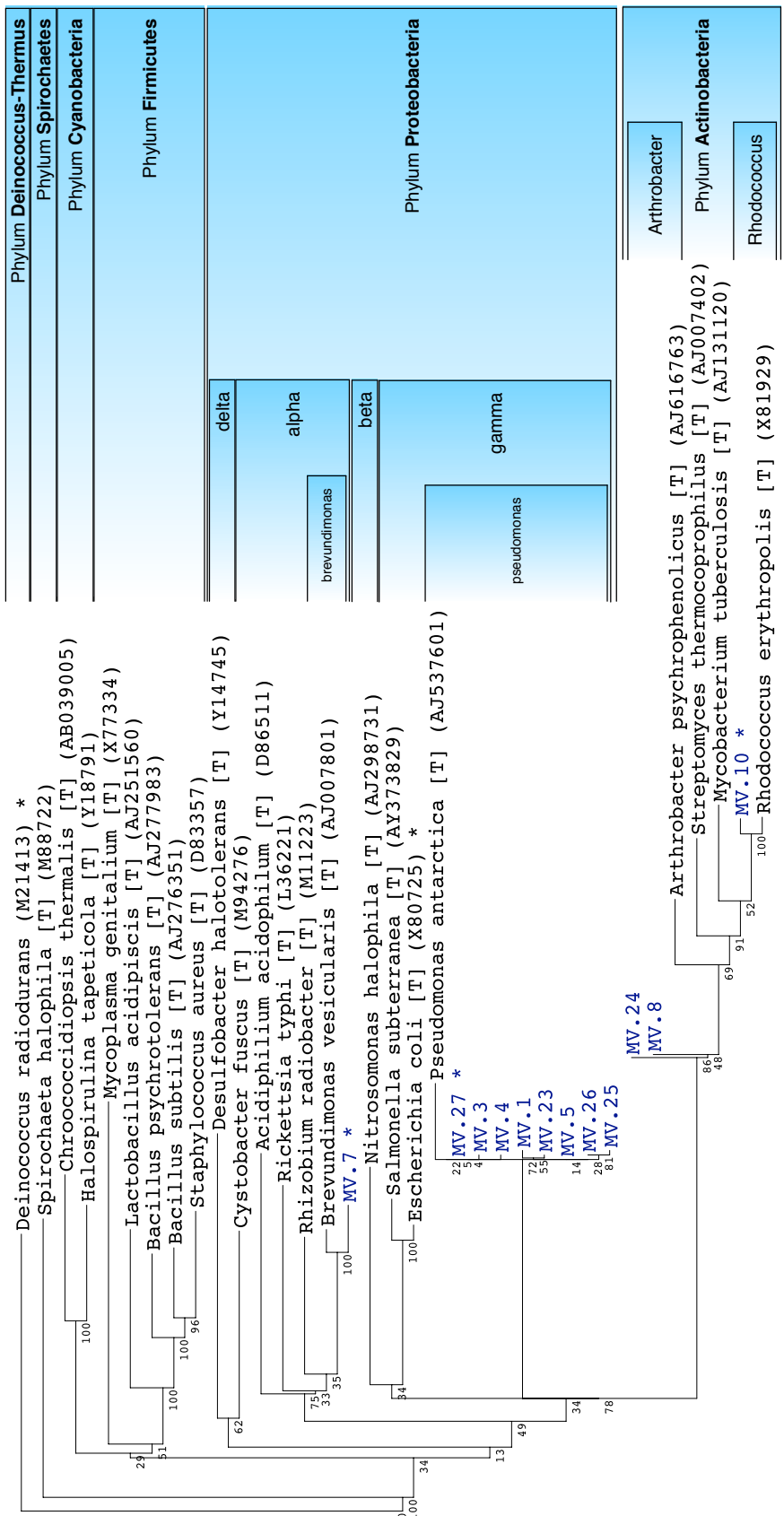

Figure 7.3: Phylogenetic tree of all 12 novel Antarctic isolates (highlighted in blue) and representative species of major bactieral clades, plotted using the Ribosomal Database Project. The GenBank accession numbers of strains are given, type strains are indicated with [T], and strains selected for the irradiation survival experimentation are indicated with an asterisk (*). The outgroup strain used to improve tree topology was *D. radiodurans*.

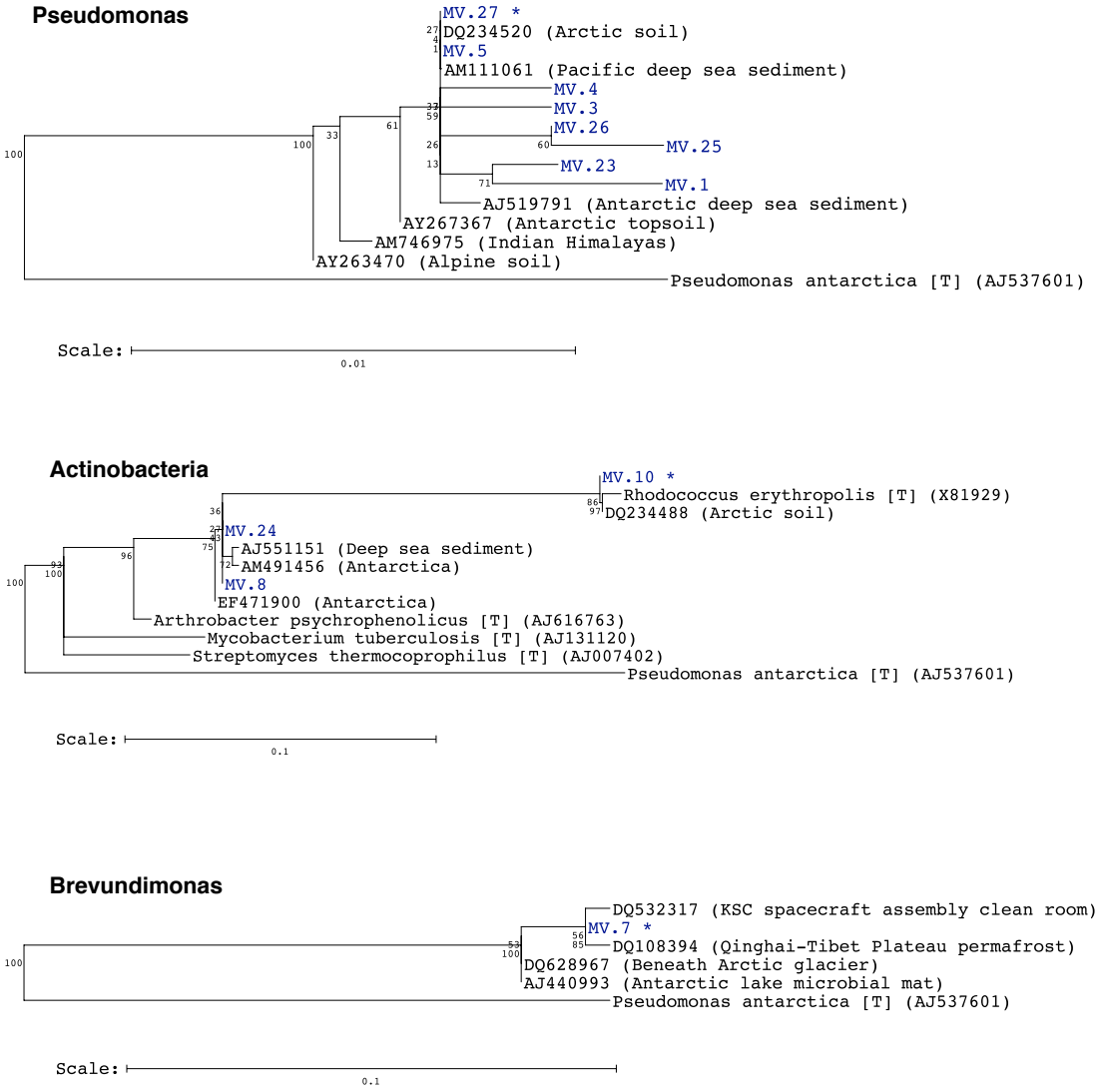

Figure 7.4: Replotted phylogenetic trees of just the *pseudomonas* (top), actinobacteria (middle) and *brevundimonas* (bottom) groups, constructed using the Ribosomal Database Project. Shown are the novel Antarctic isolates highlighted in blue, closely-related strains discovered in similar low-temperature environments, and representative type strains. The GenBank accession numbers of strains are given, type strains are indicated with [T], and strains selected for the irradiation survival experimentation are indicated with an asterisk (*). The outgroup strain used to improve tree topology in all three cases was *P. antarctica* [T].

Table 7.5: Cell counts of bacterial cultures prepared for irradiation. The population density in the liquid cultures before freezing to -80°C; the thawed-sample post-freeze cell count constituting the control sample for no radiation dose, from which irradiation survival fractions are calculated; and the calculated population survival over this freeze-thaw process.

Bacterium	Pre-freeze population count (cells/ml)	Post-thaw population count (cells/ml)	Freeze-thaw survival
E. coli	3.95×10^8	7.75×10^6	1.96 %
D. radiodurans	6.89×10^7	7.87×10^7	114 %
Brevundimonas sp. MV.7	3.00×10^8	2.54×10^8	84.7 %
Rhodococcus sp. MV.10	6.03×10^7	5.89×10^7	97.7 %
Pseudomonas sp. MV.27	7.57×10^8	2.55×10^8	33.7 %

The cell counts for the pre-freeze liquid growth culture and the freeze-thaw control population are given below in Table 7.5. The raw data for these and all irradiation survival experiments, listing the exposure dose, replicate cell counts and mean, and calculated survival fraction are given for each of these five organisms in Appendix 1.

It can be seen that the Antarctic isolates *Brevundimonas* sp. MV.7 and *Rhodococcus* sp. MV.10 both exhibit excellent survival of the freeze-thaw process, with *Pseudomonas* sp. MV.27 still showing a one-in-three survival of the procedure. This behaviour can of course be expected of bacteria isolated from the Dry Valleys environment, where freeze-thaw is a regular occurrence over the summer diurnal cycle. The value calculated for *D. radiodurans*, indicating a greater population *after* freezing than before, is certainly due to slight experimental error in sample dilution or preparing and counting the colony plates, and the important result remains that this strain of environmental organism displays near-total survival of the freeze-thaw process inherent to the irradiation experiment set-up. *E. coli*, on the other hand, experiences only one-in-fifty survival during freezing. This also was to be expected, as *E. coli* is an enterobacteria normally resident in the human intestinal tract, and so would have no requirement for adaptation to freeze-thaw survival in its natural habitat. The third column of Table 7.5, the post-thaw count of the control samples, is the population number from which all irradiation survival fractions are calculated, as explained in Section 4.6.3.2 on page 93.

Figures 7.5 – 7.10 display the plotted survival data from these irradiations. The logarithmic survival scale on the y-axis shows the ratio of viable population number (in colony-forming units per millilitre) after exposure to a particular dose of gamma-rays to the unirradiated control, and runs from 1 (100% survival) to 10^{-8} (one in ten million survival). Each datum point represents an arithmetic mean of the cell counts obtained from plating out in triplicate, except where a plate had become contaminated to the extent it was necessary to discount it. The data points are colour-coded depending on the dose-rate (i.e. distance from the cobalt-60 source) that the sample was irradiated at. Error bars are displayed as the maximum and minimum count obtained, and in general are so small as to be obscured by the datum point itself. *D. radiodurans* samples were irradiated at three of these four dose-rates, other cells at a subset of only two. Also calculated and plotted for each data set is an exponential line of best-fit, fixed to the initial point (1,0), of the form: $y = e^{-\gamma . x}$

The first crucial result evident in these plots is that for every bacterial strain irradiated all data points lie along the same dose response line, regardless of the dose rate used. The colour-coding represents the dose rate at which the samples were exposed and this observation indicates

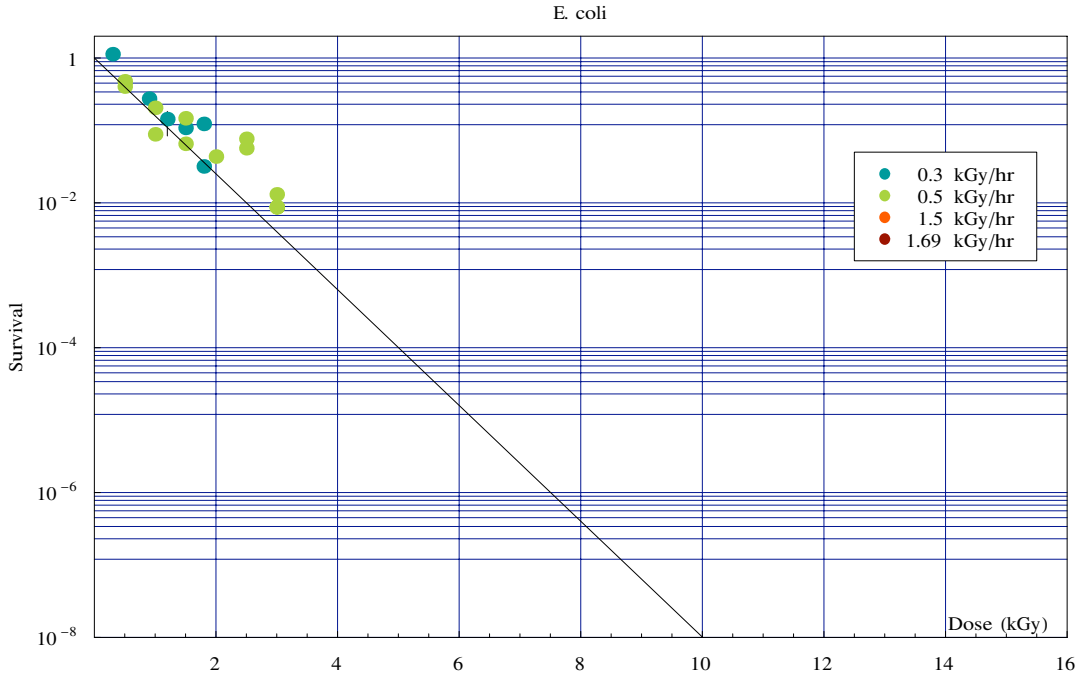

Figure 7.5: Gamma ray irradiation survival curve of the model species *E. coli*, expected to show radiosensitivity. Error bars and exponential lines of best-fit shown.

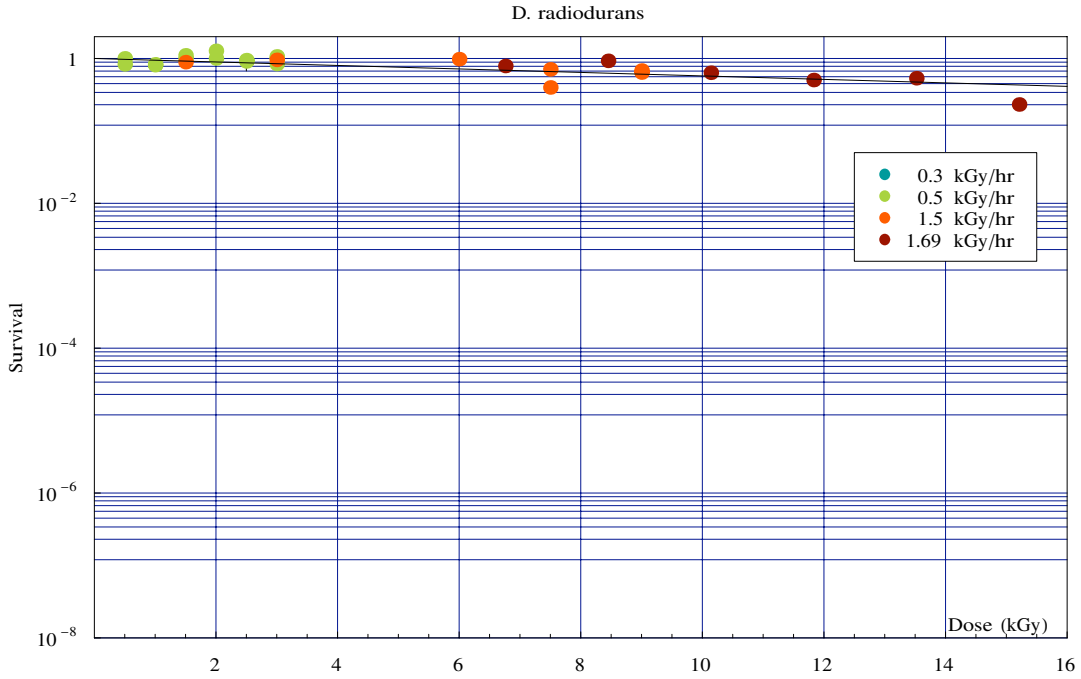

Figure 7.6: Gamma ray irradiation survival curve of the model species *D. radiodurans*, expected to show radioresistance. Error bars and exponential lines of best-fit shown.

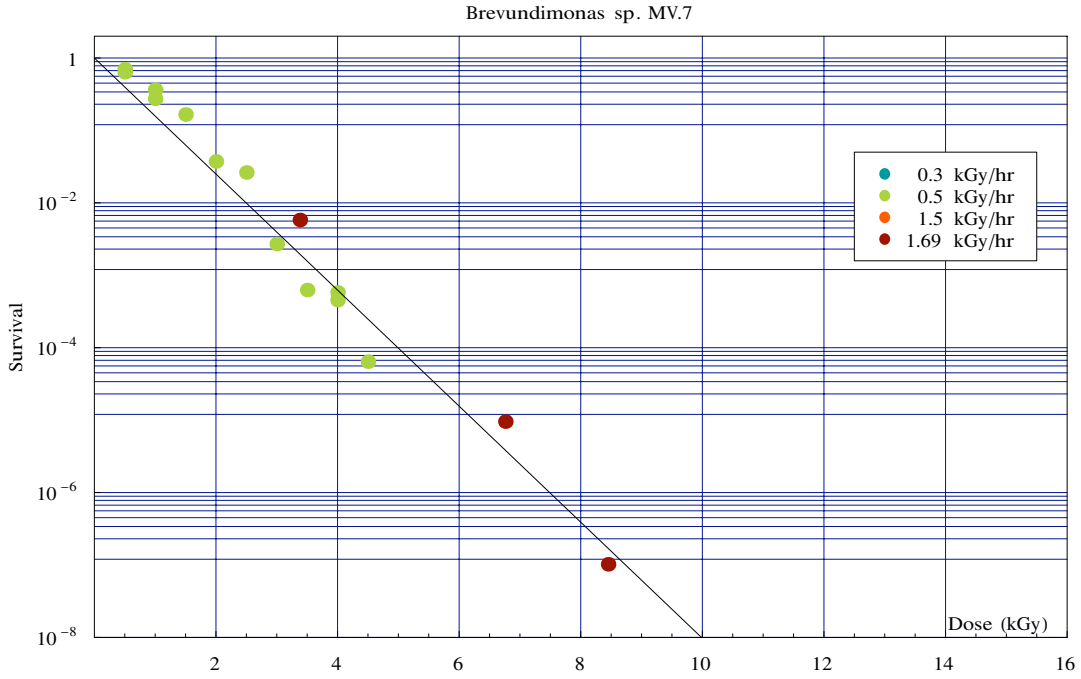

Figure 7.7: Gamma ray irradiation survival curve of the novel Antarctic isolate *Brevundimonas* sp. MV.7. Error bars and exponential lines of best-fit shown.

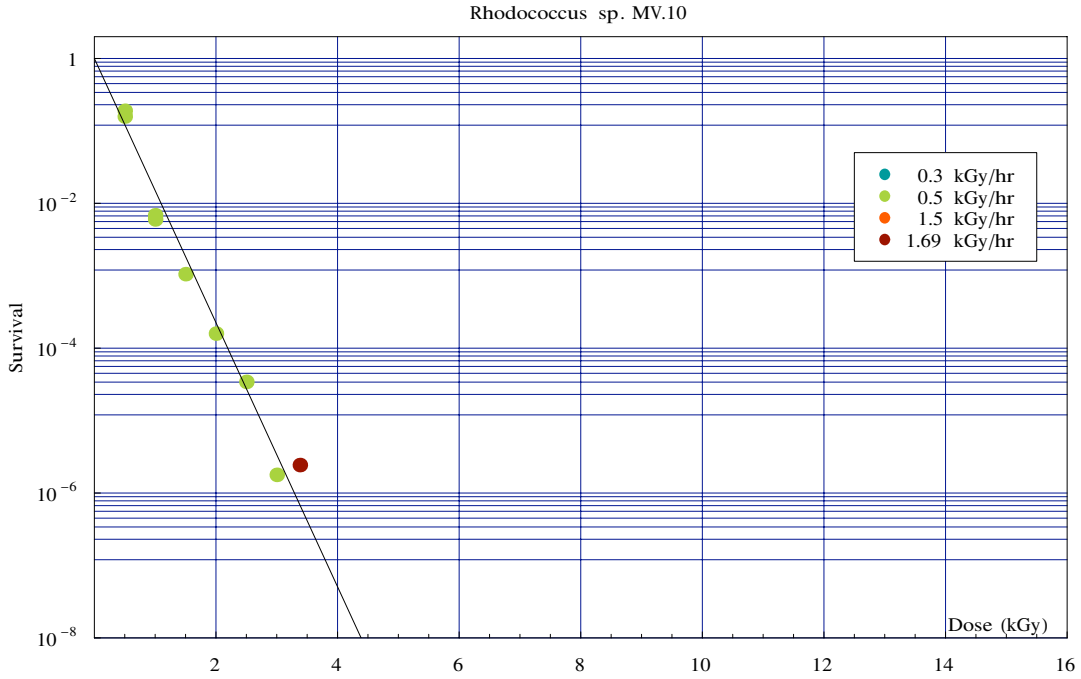

Figure 7.8: Gamma ray irradiation survival curve of the novel Antarctic isolate *Rhodococcus* sp. MV.10. Error bars and exponential lines of best-fit shown.

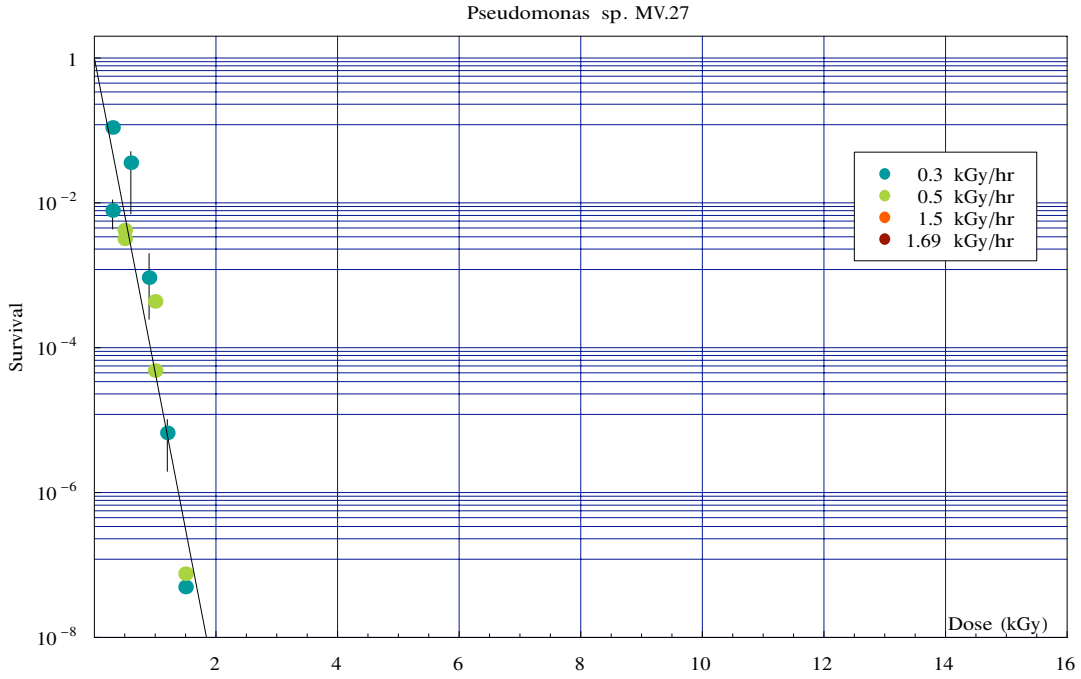

Figure 7.9: Gamma ray irradiation survival curve of the novel Antarctic isolate *Pseudomonas* sp. MV.27. Error bars and exponential lines of best-fit shown.

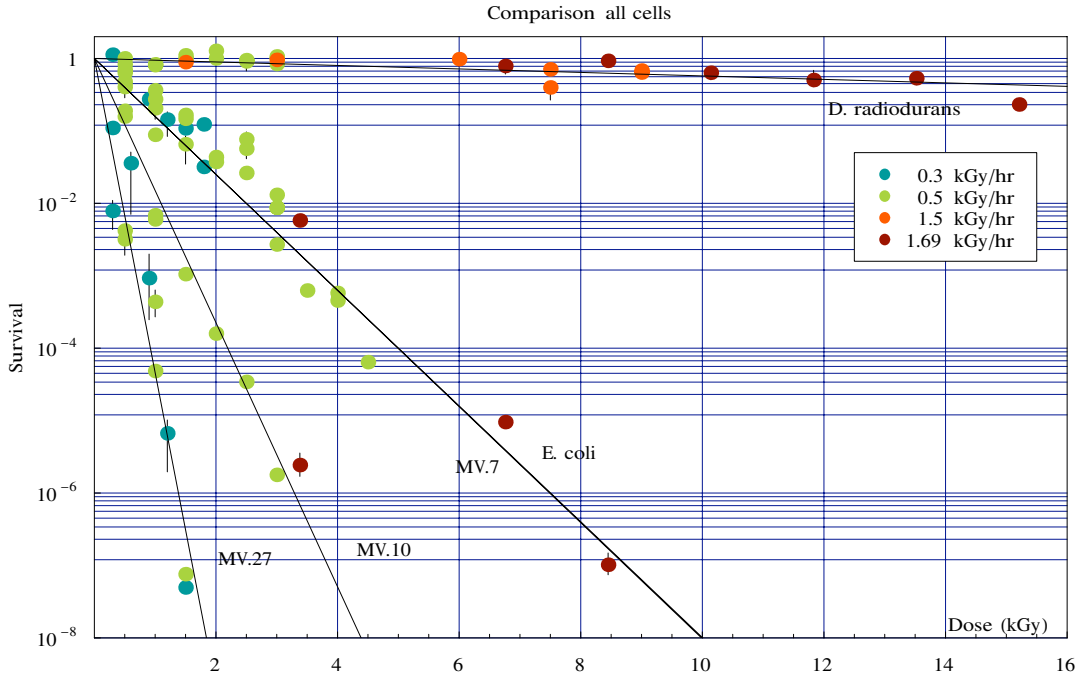

Figure 7.10: Comparison of gamma ray irradiation survival characteristics of all five irradiated strains. Error bars and exponential lines of best-fit shown.

there is no systematic effect of dose rate on cellular survival after irradiation at -79°C. This is especially clear in the *D. radiodurans* data, with results collected over a wide range of dose rates (0.5 kGy/hr – 1.69 kGy/hr) all clustering very tightly along the same line. As out-lined in Methods Section 4.6.3.3 on page 94, demonstrating to be true the assumption that dose-rate is not an important factor for frozen samples was one of the prime aims of the irradiation experiments. Cells which are rendered metabolically-inactive by freezing cannot repair radiation damage during the course of the experiment, and so the rate at which this dose is delivered is inconsequential to subsequent survival. Thus, it has been justified that results on irradiation survival collected at different dose rates can indeed be collated into a single data-set for each microorganism for analysis.

Table 7.6 shows the fitted parameter, γ, of the exponential dose-effect survival function ($y = e^{-\gamma.x}$) for each bacterial strain irradiated here. This parameter corresponds to the gradient of the best-fit line in log-linear space, and is also known as the sensitivity or inactivation constant of the cell-type under irradiation [187]. The inverse of this fitted exponent, γ^{-1}, is defined as D_{37} or D_0 and corresponds to the radiation dose required to produce an e^{-1} (36.8%) reduction in cell population. At this dose, each cell has on average experienced one lethal event, and those that survive must have been balanced by other cells taking two or more lethal events [61]. The D_0 is a standard metric of radioresistance and allows comparison between different bacterial strains or irradiation conditions [33]. Also shown in Table 7.6 is the dose required to produce a 10^6 reduction in viable population number, the threshold taken in the modelling work as complete population inactivation of an environmental sample. It should be noted that for the *E. coli* sample this calculated dose yielding 10^{-6} survival represents an extrapolation of roughly four orders of magnitude from the final data point, and so may not be as robust as the values determined for the other microbial strains by interpolation.

Table 7.6: Gamma ray survival characteristics determined for each of the five bacterial strains: γ, the fitted exponent of the irradiation survival response, of the form $e^{-\gamma.x}$; D_0, the dose necessary for a 37% viable cell number reduction; and the dose necessary to produce a million-fold population reduction.

Strain	Survival exponent, γ	D_0 (kGy)	10^{-6} survival (kGy)
E. coli	1.841	0.543	7.50
D. radiodurans	0.055	18.18	251
Brevundimonas sp. MV.7	1.845	0.542	7.49
Rhodococcus sp. MV.10	4.199	0.238	3.29
Pseudomonas sp. MV.27	9.990	0.100	1.38

As expected, *D. radiodurans* is by far the most radiation resistant of the five strains tested here, and can withstand a gamma ray dose over thirty times greater than *E. coli* before suffering a 37% reduction in viable population number (D_0). More puzzling, however, is the observation that *E. coli*, the model microorganism selected as a negative control for these exposure experiments owing to its lack of radiation resistance, survived the gamma ray exposures better than any of the Antarctic isolates. Possible reasons for this will be explored in the next chapter.

Both *D. radiodurans* and *E. coli* exhibit a far greater degree of radioresistance when exposed at -79°C than when simply chilled on ice during irradiation (e.g. [30]), the significance of which will be discussed in the following chapter. After receiving a dose of 10 kGy, *D. radiodurans* still exhibits near-total population survival, whereas the most radiation resistant Antarctic strain

irradiated here, *Brevundimonas* sp. MV.7, suffers a 10^8 reduction in cell survival. *E. coli* and *Brevundimonas* sp. MV.7 exhibit an equivalent degree of radiation resistance, and the novel Antarctic isolate exhibiting the lowest radioresitance was found to be *Pseudomonas* sp. MV.27. Comparing the inactivation constants, γ, determined here finds that *Brevundimonas* sp. MV.7 is more than 5.4 times more resistant to gamma ray radiation than *Pseudomonas* sp. MV.27.

The implications of these results covering the identity and phylogenetic relationships of the novel strains isolated here from the Antarctic dry valleys, and the radiation resistance of these strains and *E. coli* and *D. radiodurans* irradiated at a temperature characteristic of the martian surface, will be discussed within the context of the martian radiation modeling in the next chapter.

7.5 Chapter summary

- A total of 29 bacterial strains were successfully isolated from a sediment sample of the Miers Valley, Antarctica, an analogue site of the martian surface.
- 12 of the isolates exhibiting fastest growth at 4°C were selected for further work, including characterisation of colony appearance and growth characteristics, and identified by 16S rRNA gene sequencing as representatives of *Pseudomonas*, *Brevundimonas*, *Arthrobacter* and *Rhodococcus* genera.
- Phylogenetic trees were constructed for these novel isolates to investigate their relationship to each other, previously-identified strains from similar harsh environments, and type strains within the genera. These closely-related strains appear to be globally-distributed in cold environments from the Arctic to Antarctic. *Brevundimonas* sp. MV.7 shares a 99% sequence similarity with a strain identified from a spacecraft assembly clean room at Kennedy Space Center.
- *Brevundimonas* sp. MV.7, *Rhodococcus* sp. MV.10 and *D. radiodurans* were all discovered to exhibit near-total survival of freeze-thaw. *E. coli* exhibited only ∼2% survival.
- Gamma ray irradiation survival experiments were conducted on three of the novel strains, *Brevundimonas* sp. MV.7, *Rhodococcus* sp. MV.10 and *Pseudomonas* sp. MV.27, and model species *E. coli* and *D. radiodurans* at -79°C, a temperature characteristic of the martian surface. *D. radiodurans* was confirmed to show the highest degree of radiation resistance. *Brevundimonas* sp. MV.7 showed the greatest irradiation survival of the novel isolates tested, and *Pseudomonas* sp. MV.27 the worst, with a radiation sensitivity, γ, 5.4 times higher. Unexpectedly, *E. coli* was discovered to exhibit radiation resistance equivalent to *Brevundimonas* sp. MV.7 under these conditions.

Chapter 8

Discussion

Previous chapters have detailed the results generated by both the computer modeling and experimental research threads, and here they are discussed within the context of previous studies and the novel findings of this work. The major research topics are treated in turn: the survival of microbial life in the subsurface ionising radiation environment, the preservation of organic biosignatures, and results pertinent to the application of optically stimulated luminescence dating of martian sediments. The radiation dose deposition rates determined here are also compared against previous publications, and explanations sought for discrepancies between studies.

The radiation exposure experiments produced two major findings. Firstly, the microbe selected for its expected radiation sensitivity, *E. coli*, was found to survive the gamma radiation better than any of the novel Antarctic isolates, and possible reasons for this are discussed. Secondly, both model microorganisms survived exposure to gamma rays at -79°C much better than previous studies found at warmer temperatures, and the implications for this on microbial survival at martian permafrost temperatures are explored.

The last section interprets the results from both modeling and experimental efforts in the light shed by each other, and draws conclusions on the likely survival times of microbial life in the martian near subsurface. One particularly interesting discovery is the phylogenetic-proximity between one of the novel Antarctic isolates selected for irradiation and bacteria identified in two NASA clean rooms used for spacecraft assembly. The implications of this in terms of preventing the contamination of Mars with terrestrial biota are examined. Finally, modeling and experimental lines for future work are proposed, continuing and expanding upon this productive research programme.

8.1 Modeled microbial survival

The first configuration of the radiation model developed here, containing micron-thick water layers at regular depth intervals in the ground to model microorganism survival, has provided some crucial insights into the possibility of finding viable microbial life in the martian near-subsurface.

This research has discovered that the peak biologically-weighted dose rate at the martian surface is ∼0.85 Gy/year, and so at no point is the ionizing cosmic radiation environment on or beneath the martian surface lethal to even radiosensitive terrestrial bacteria. For comparison, the most intense natural radiation environment on Earth is reported to be the monazite sand deposits along certain beaches in Brazil with a dose rate of 0.4 Gy/year [33], corresponding to a depth of about 20 cm in the wet heterogeneous (WH) regolith model. Terrestrial species such as *D. radiodurans* can recover from doses four-orders of magnitude greater than this annual level with no detectable loss in viability [30]. Extreme radioresistance of terrestrial bacteria is therefore not thought to have evolved as an adaptation to the natural radiation environment *per se*, but as a side-effect of desiccation resistance [30], and there is no reason martian microbes might not have evolved even greater radioresistance.

Only metabolically active cells, however, are able to repair radiation damage and reproduce. The current freezing conditions in the near subsurface imply that any extant life will be held dormant and it is the dose accumulated over long time periods that will be crucial in determining cell survival. The results of computer modeling conducted to assess microbial population survival times, defined here as a million-fold reduction in viable cell number, were reported in Section 6.2 on page 117. In terms of planetary protection, Table 6.1 on page 118 shows that a contaminant population of terrestrial cells or spores deposited onto the martian surface by a lander probe need only be blown under a thin layer of dust for protection from rapid deactivation by UV and they will survive the SEP and GCR flux for millennia. Over geological time-scales, though, even the most radioresistant populations are inactivated. At 2 m depth, for example, the proposed ExoMars drill length [222], a *D. radiodurans* population dormant in regolith permafrost is calculated to suffer a million-fold decrease in cell number within 450,000 years. For the prospects of finding viable martian microbes then, these modeling results indicate that cells must either have been brought to the surface only recently, by outflow of deeper meltwater or exposure by impact excavation, for example, or else be able to periodically revive to repair radiation damage and reproduce, and so reset the inactivation clock.

Episodic local geothermal events may melt pockets of near-surface permafrost to allow transient bursts of metabolism and replication. Intriguingly, the dynamic gullies and seeps seen at high latitude suggest the recent transient presence of liquid water [144, 145]. Furthermore, calculations show that the near-surface temperature of high latitude ice may be high enough to allow liquid water and thus metabolism during periods of high obliquity of the martian spin axis [118]. However, liquid water is predicted during these times only in the top meter of ice, and at this depth Table 6.1 on page 118 shows that populations of even radioresistant bacteria are inactivated on the order of tens of thousands of years, far short of the calculated obliquity shift frequency on the order of tens of millions of years [138].

One site of particular astrobiological interest is a region upon the plains of Elysium, labelled (b) in the map in Figure 1.1 on page 17. This is argued to contain a frozen sea, believed to

have been disgorged by the Cerberus Fossae only 5 million years ago [162], rapidly freezing in the current climate, and presents a possible opportunity for our landers to sample water from much greater depths than they could otherwise access. Assuming cellular dormancy since soon after this discharge event, the pure ice model predicts a bore hole of around 7.5 m depth would be needed for any hope of retrieving culturable *D. radiodurans*-like bacteria from within this ice.

Ionizing radiation is also produced by radionuclide decay, and it has been calculated that the intrinsic radioactivity of martian regolith produces a dose of 4×10^{-4} Gy/year [154]. Within the WH regolith model this corresponds to a depth of ∼4.5 m at which the background activity begins to dominate over the GCR cascade. Thus, beneath this depth dormant cells receive no further shielding benefit, and *D. radiodurans* can be inactivated by radioactivity of the regolith alone in under 40 million years. The near-zero radionuclide content of pure ice implies that frozen crater lakes or the polar caps are the most favourable environments for finding viable cells after long periods of dormancy.

All of these estimated population survival times are based on the accumulated dose producing a 10^6 reduction in viable cell number, taken from published irradiation survival data (see 3.6.3 on page 73). This is not an arbitrary threshold, but, as discussed below, a functionally-meaningful threshold for population survival in the martian near-subsurface.

Compared to temperate soils, permafrost sediments support very low microbial populations [224]. Gilichinsky (2007) [97] reports a total cell count (using epifluorescent microscopy) of only 10^3 – 10^4 cells/g dry weight (d.w.) from the surface layer of the Antarctic Dry Valleys, increasing to 10^5 – 10^6 cells/g d.w. in the underlying permafrost 1.5 – 3.6 m deep, of which ≤0.1% could be successfully cultured. Vorobyova *et al.* (1997) [224] collate information from a number of studies (some in Russian) that report total counts of 10^7 – 10^8 cells/g d.w. from Antarctic permafrost sediments and 10^7 – 10^9 cells/g d.w. from Arctic permafrost sediments (>300 m depth), again finding a very low percentage of viable culturable cells. Cowan *et al.* (2002) [59] find total population numbers in the Dry Valleys consistent with this using a bioluminescent ATP method: $5 \times 10^7 - 4 \times 10^8$ cells/g wet weight (w.w.) in the surface mineral soil of Miers Valley, decreasing to $5 \times 10^5 - 8 \times 10^6$ cells/g w.w. 25 cm deep in permafrost in Taylor Valley. The total cell count has been observed to be several orders of magnitude higher in Arctic than Antarctic permafrost, but the Antarctic Dry Valleys environment is considered to be a better analogue of the martian surface due to the lower temperatures [97].

Although unambiguous detection of extinct martian microbes would be profound, even more significant would be the opportunity to characterise living cells, either *in situ* or from a sample return mission. Indeed, the Viking landers relied upon culturing metabolically-active cells for the Gas Exchange (GEX) [178] and Labelled Release (LR) [140] experiments of their Life Detection package. Assuming an estimate for viable culturable microorganisms of the order of 10^3 cells/g, the population survival threshold of 10^{-6} selected above corresponds to a single surviving cell per kilogram of topsoil or regolith rock. Considering the constraints on life detection instruments (the Viking GEX and LR experiments used a soil sample of only a few grams [178, 140]) or sample return capabilities (a future Mars Sample Return mission is currently envisioned to deliver only between 0.5 kg and a few kg of martian surface material [230, 175, 149]), this population survival threshold represents a meaningful cut-off between the potential detection or non-detection of metabolically-active cells. The estimates for population survival presented here can be improved upon by additionally taking into account the temperature-dependency of radiation resistance, as discussed in depth in Section 8.5.2 on page 158.

8.2 Modeled dose deposition in regolith

The second configuration of the model, whereby dose deposited in the subsurface was registered using virtual layering, was designed specifically to address the additional issues of how long organic molecule biomarkers might persist in the martian near-subsurface ionising radiation environment, and also to provide calibration data for use of the optically stimulated luminescence dating technique.

8.2.1 Preservation of astrobiological markers

Exposure of biological macromolecules, such as carbohydrates, nucleic acids and proteins, to ionising radiation is known to cause both fragmentation and aggregation [112]. Such radiolytic degradation of biological macromolecules is of crucial significance to the potential detectability of biosignatures in the martian subsurface. The general issue is that after millennia of cosmic irradiation it may be difficult to distinguish between break-down debris of large biomolecules, a valid signature of extinct or extant life, and the simple abiotic chemical species created *in situ* by prebiotic chemistry or exogenously-delivered by meteoritic or cometary in-fall.

For protein irradiation under martian conditions of low temperature frozen aqueous solutions, fragmentation through breakage of the polypeptide backbone is the major damage observed [86]. For example, Filali-Mouhim *et al.* (1997) [86] have found that 70 kGy of radiation is sufficient to shatter lysozyme into at least 11 small fragments. Whilst discovery of a polypeptide chain such as lysosyme, roughly 150 amino acids long [NCBI Protein database], may be good evidence of biological action, shorter amino acid chains can be produced abiotically [177, 22] and so are not a unique robust biosignature. The second configuration of the martian radiation model calculates that this accumulated dose corresponds to a 1.3 million year exposure beneath a meter of dry dust, indicating that such a clear biosignature of complex biomolecules like proteins may be lost on the order of only millennia.

Pavlov *et al.* (2002) [181] have attempted to calculate the likely persistence times of macromolecules in the martian subsurface using their own radiation transport model and a formula relating molecular bond breakage and absorbed dose. The molecular masses of enzymes have long been approximated by irradiation in aqueous solution or as a lyophilized (freeze-dried) powder [169]. The remaining biological activity of an irradiated sample of enzymes decreases exponentially with the absorbed dose, and assuming that the activity of each individual polypeptide is destroyed by a single hit (primary ionisation) the decay constant can been used to calculate the target molecular mass. Pavlov *et al.* (2002) [181] used a similar formula to estimate the proportion of molecular bonds broken in a macromolecule of given molecular mass as a function of the absorbed dose, and found that total degradation of macromolecules in the top meter of subsurface occurs in $10^8 - 10^9$ years. However, there is increasing evidence that protein radiolysis is dependent not on molecular mass but the solvent-accessible surface area, explaining the observation of preferential cleavage on solvent-exposed loops and that denatured proteins fragment to a much greater extent than native ones [86, 20]. Furthermore, such a calculation for complete destruction may greatly over-estimate the relevant persistence time, as a macromolecule may not need to be extensively radiolytically modified to escape detection by a biomarker detection instrument designed to identify specific molecules or compound classes.

In an attempt to gauge persistence times in the martian subsurface radiation environment of not macromolecules but the precursor monomers, Kminek and Bada (2006) [135] combine previously-published dose-depth calculations, taken from Mileikowsky *et al.* (2000) [154], with their experimental results on gamma irradiation of dry amino acids. The model developed here, however, finds significantly lower dose rates in the martian subsurface than reported by Mileikowsky *et al.* (2000) [154], yet consistent with other research reported in the literature (see discussion below in Section 8.3). Additionally, the Mileikowsky *et al.* (2000) model was designed to study small meteorites and so there are significant considerations in applying their data to the martian surface, as also discussed below in Section 8.3.

Another potential biosignature of great interest is that many organic molecules used by terrestrial life are selectively of a single enantiomer, whereas laboratory experiments into prebiotic chemistry produce no such pronounced bias [21], and most of the extraterrestrial amino acids isolated from the Murchison meteorite are racemised [79]. Many researchers therefore believe that if organics found on Mars were to show a distinct enantiomer bias this would constitute a robust biosignature. Surviving amino acids in a partially-radiolysed sample, however, have been found to show a significant degree of radioracemisation and thus removal of this chirality biomarker; this effect is comparable in both samples of polypetides and amino acid monomers ([36] and references to earlier work therein, including [37, 38]). This radioracemisation would operate in addition to racemisation over time due to thermal and chemical processes [23]. A close approximation to the martian subsurface scenario is provided by the experimental work reported in Bonner *et al.* (1985) [38], where homochiral samples of amino acids were dried into a clay substrate and gamma-irradiated. For L-leucine on bentonite clay, a total dose of 1.3×10^6 Gy produced 70% radiolyitc degradation of the original amino acid sample, and a radioracemisation of 4.5% of the surviving amino acids. Comparing this to the ionising radiation dose deposited in the subsurface calculated by the second configuration of the model, at 1 m depth (a reasonable estimate for the maximum depth of the oxidising layer [236]) in the 1 g/cm^3 dry dust surface model the dose accumulation rate is 0.055 Gy/year. The model therefore predicts that biogenic L-leucine in this subsurface environment would experience 70% destruction in just under 24 million years and the homochirality biosignature of the surviving molecules would have been partially erased. Thus, even if amino acids are isolated in the martian subsurface, survivors of oxidation and ionisation, the un-radiolysed fraction may exhibit enough radioracemisation to not be readily identifiable as biogenic.

Addressing the likely persistence times in the martian subsurface radiation field of different biosignatures, from macromolecule fragmentation to monomer destruction or racemisation, is of crucial significance to astrobiology. Previous experimental research has studied the response of different biomolecular systems as a function of radiation dose, but these results can only be applied to preservation on Mars with detailed knowledge of the subsurface radiation environment and dose deposition rates at different depths. Some researchers have attempted this coordination between experimental irradiation studies and modeling results, but the radiation transport model used [154] is not directly applicable to the martian surface. For these reasons, the second configuration of this radiation model was developed to calculate unweighted physical dose-depth profiles under a variety of different scenarios. The results that have been presented in Section 6.3 on page 119 can be directly applied to laboratory irradiation results in order to address the persistence of various biomarkers in the ionising radiation environment of the martian near-subsurface.

8.2.2 OSL dating

A second application of the dose-depth profiles calculated by the second configuration of the martian radiation model is in calibration of the optically stimulated luminescence dating technique.

The upper limit on OSL dating is determined by saturation of the luminescence signal, an effect due to the finite number of traps within the material, and generally occurs with a total dose on the order of several kGy [151]. The temporal limit for dating martian sediments will vary much more than on Earth. The high ionisation rate just beneath the surface from unshielded cosmic rays will produce rapid saturation, but due to the assumed lower incidence of radioisotopes in the martian surface, sediments rapidly buried to depths greater than several meters will experience a dose rate less than on Earth and so the maximum dating limit may be extended [73]. Jain *et al.* (2006) [117] report the measured saturation dose of different minerals to range between 2 – 30 kGy. The dose rate results from the second configuration of this radiation model indicate that these saturation doses permit a maximum dating limit of ∼30,000 – 460,000 years for rapid burial beneath 30 cm of dry dust, increasing to ∼400,000 – 6 million years at 5 m depth. This agrees well with the estimation of McKeever *et al.* (2003) [151] for the upper limit for dating martian sediments at 10^3 – 10^6 years.

Heavy charged particles, with their large LET value, create regions with high ionisation density. This produces local charge saturation effects, and consequently the OSL response for a given dose deposited by HZE is lower than that from low-LET radiation such as energetic electrons or gamma rays. Thus, the response to weakly ionising and densely ionising particles, such as gamma rays and heavy ions respectively, is opposite in organism survival and OSL of sediments. Without taking into account this LET-dependent variation in OSL efficiency, the simple dose rate will over-estimate the effective value [117]. However, the exact dependence of OSL efficiency on LET needs to be experimentally-determined for different particle species and each natural dosimeter mineral likely to be encountered on Mars. When such experimental data becomes available [117, for example], these efficiency functions can be readily incorporated into this particle transport model to produce more refined calibrations suitable for martian OSL dating.

The only other direct chronologies for Mars are based on the observed crater density, but this technique has poor temporal resolution and is inaccurate for features younger than about a million years. This lower age range is well covered by OSL dating, and thus it forms an essential complementary *in situ* technique for determining Mars' geomorphological and climatic history [151]. The dose profiles presented here can be employed in the necessary calibration of this dating technique.

8.3 Model comparison for dose deposited in regolith

Advances of this modeling effort over previous martian radiation astrobiological studies [154, 181, for example] include the treatment of slow neutron transport and meson production, and analysis of the effects of variation in martian atmospheric depth and composition of the subsurface. Most crucial is the permafrost content of the regolith; water is an effective neutron moderator, and as shown in Figure 6.6 on page 117 ground ice creates a significant dose enhancement in the near subsurface. Previous studies into the martian subsurface radiation

environment simulated particle propagation through a target material of dry regolith, and so this scenario was used for comparison and validation of the new martian radiation model here. Figure 8.1, below, presents the data generated by the second configuration of the model, that of the radiation dose deposited in the regolith itself, against five previously published studies.

Data is shown here for the subsurface dose delivered by GCR under both solar maximum and minimum conditions, as either a complete dose-depth profile or isolated data points, as available from the reported results in the literature. All stated depths have been converted into the same units of shielding depth (g/cm^2). Where the simulated surface density was not stated, for example in McKeever *et al.* (2003) [151], it was assumed to be the 1.1 g/cm^3 determined by the Viking landers for martian fines [49] and used for this model. Mileikowsky *et al.* (2000) [154] and Pavlov *et al.* (2002) [181] calculate results only for solar minimum. Pavlov *et al.* (2002) [181] report only two dose data-points (the peak dose at 25 g/cm^2 depth and that at 700 g/cm^2) but state that the dose does not deviate more than 20% in the top 100 g/cm^2, indicated in Figure 8.1 with a grey box. Simonsen & Nealy (1993) [205] report surface integrated astronaut skin doses (Tables 3 and 5 of that publication), which are directly comparable to the unweighted regolith doses here, for the Mars atmosphere low density model (16 g/cm^2 CO_2 at the surface, as used in this modeling) and high density model (22 g/cm^2 CO_2, yielding a second data point at an effective depth of 6 g/cm^2).

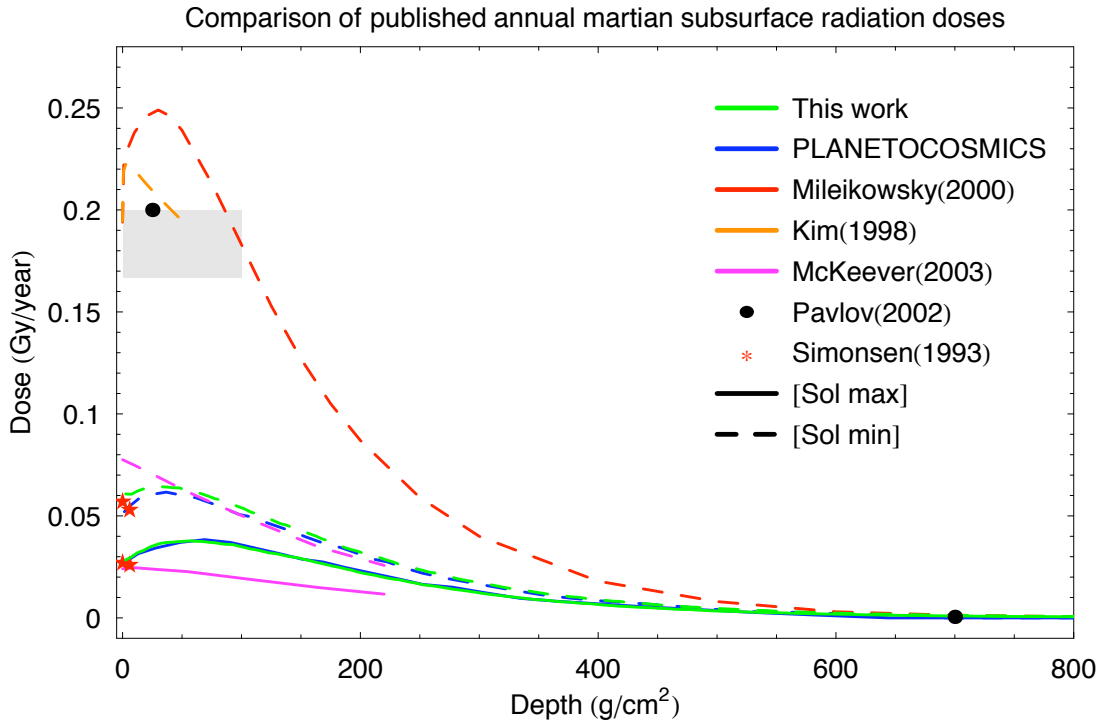

Figure 8.1: Comparison of the subsuface dose results produced by this work against other published models. Dose profiles produced by GCR under solar maximum conditions are shown in solid lines, and those modeling solar minimum as dashed lines. Both dose-depth profiles and point calculations are shown, with the models colour-coded as follows: this work (green); PLANETOCOSMICS reported in Gurtner *et al.* (2005) [101] (blue); Mileikowsky *et al.* (2000) [154] (red); Kim *et al.* (1998) [130] (orange); McKeever *et al.* (2003) [151] (purple); Pavlov *et al.* (2002) [181] (black dots); Simonsen & Nealy (1993) [205] (red stars). The dose range reported by Pavlov *et al.* (2002) [181] in the top 100 g/cm^2 is indicated with the grey box.

It can be clearly seen in Figure 8.1 that the regolith dose-depth results from the second configuration of this radiation model (green lines, as published in Dartnell *et al.* (2007) [65]) agree

exceptionally well for this dry regolith scenario with those produced by Simonsen & Nealy (1993)[205] and the PLANETOCOSMICS code reported in Gurtner *et al.* (2005) [101] for both solar minimum and maximum conditions, and agree reasonably well with those calculated by McKeever *et al.* (2003) [151]. The three other studies presented in Figure 8.1, Kim *et al.* (1998) [130], Mileikowsky *et al.* (2000) [154] and Pavlov *et al.* (2002) [181], however, report subsurface doses substantially higher than this first collection of studies. Possible explanations for this are discussed below.

Most importantly, the research reported by Mileikowsky *et al.* (2000) [154] concerned the regolith dose-depth profiles produced by GCR incident not on to the martian surface itself, but onto fragments of regolith ejected by nearby impacts into interplanetary space as meteorites, for an assessment of the theory of panspermia. The particle physics and biological approximations within such an application are identical to those required in this research, but the irradiation geometry of the scenario is significantly different. Firstly, martian meteorites are exposed to the cosmic ray environment without the protection of an atmospheric column, and so experience 16 g/cm^2 less shielding depth. Secondly, and more importantly, the fluence of primary ionising particles through a unit area of rock within a meteorite is greater than that upon the martian surface, as explained below.

Within free space, a small object, such as a meteorite or satellite, is subject to an isotropic primary fluence originating from the whole-sky spherical surface, with a solid angle of 4π steradians. A much larger celestial object, however, such as a planetary body, experiences self-shielding, and a unit area on the surface is effectively screened from fluence originating from the hemispherical surface below. Cosmic particle fluence reaches the surface of a planet only from the hemispeherical surface of the sky above, and so due to this "shadow shielding" the effective primary fluence is half that experienced by a small object in free-space [164]. A comparison of these two geometries is shown in Figure 8.2.

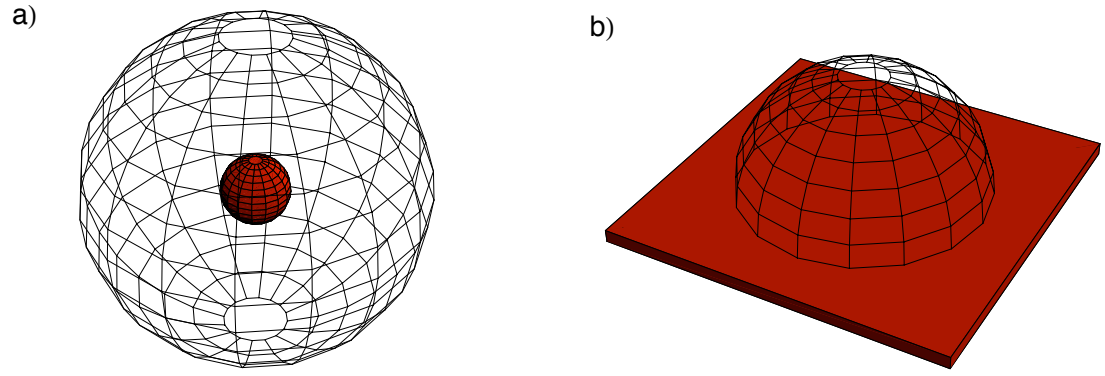

Figure 8.2: Comparison of particle flux source geometries in free space. a) a small sphere, such as a meteorite, is irradiated evenly from an enclosing spherical source surface, comprising a solid angle of 4π sr. b) the surface of a large spherical object, such as a planetary body, however, experiences self-shielding and can be treated as a planar surface irradiated only from above, comprising a solid angle of 2π sr. Diagram prepared by the author.

The dose calculations provided by Mileikowsky *et al.* (2000) [154] would therefore be *expected* to be a factor of two greater than that calculated by the other studies presented in Figure 8.1. This fluence source argument is not applicable to the higher doses reported by Kim *et al.* (1998) [130] or *Pavlov et al.* (2002) [181] (both in agreement with Mileikowsky *et al.* (2000) [154]), though, because they are attempting to model the radiation environment of the martian

subsurface and so should have normalised their primary fluence to 2π sr, just as this research has, and the other models presented in Figure 8.1 presumably have.

The greater primary flux impingent on a meteorite does not completely explain the discrepancy observed between the results of Mileikowsky *et al.* (2000) [154] and those produced by this model, however. The integration beneath the solar minimum dose-depth curve presented by Mileikowsky *et al.* (2000), yielding the total energy deposited by GCR within the top 800 g/cm^2 of regolith, is 3.09 times greater than that calculated by this research. This is significantly more than the factor of 2 expected from the whole-sky fluence normalisation argument above.

Both Mileikowsky *et al.* (2000) [154] and Kim *et al.* (1998) [130], two studies reporting a higher subsurface dose rate, used the 1977 solar minimum GCR spectra model [26], which is stated to fit a higher flux [26] than the CREME model used by this work, PLANETOCOSMICS reported in Gurtner *et al.* (2005) [101] and Simonsen & Nealy (1993) [205]. It is likely, therefore, that the elevated dose levels reported by Mileikowsky *et al.* (2000) [154] are due to a combination of the geometry of irradiation of small meteorites and use of a more energetic primary spectrum.

Figure 8.3 shows the dose profile calculated by Mileikowsky *et al.* (2000) [154] reduced by the factor of 3.09 and replotted, essentially re-normalising their data to the energy delivered by the primary spectrum used in this research. Figure 8.3 reveals that even when this dose data is re-normalised to contain the same total energy, the calculated dose-depth relationship still shows a different profile to the other models.

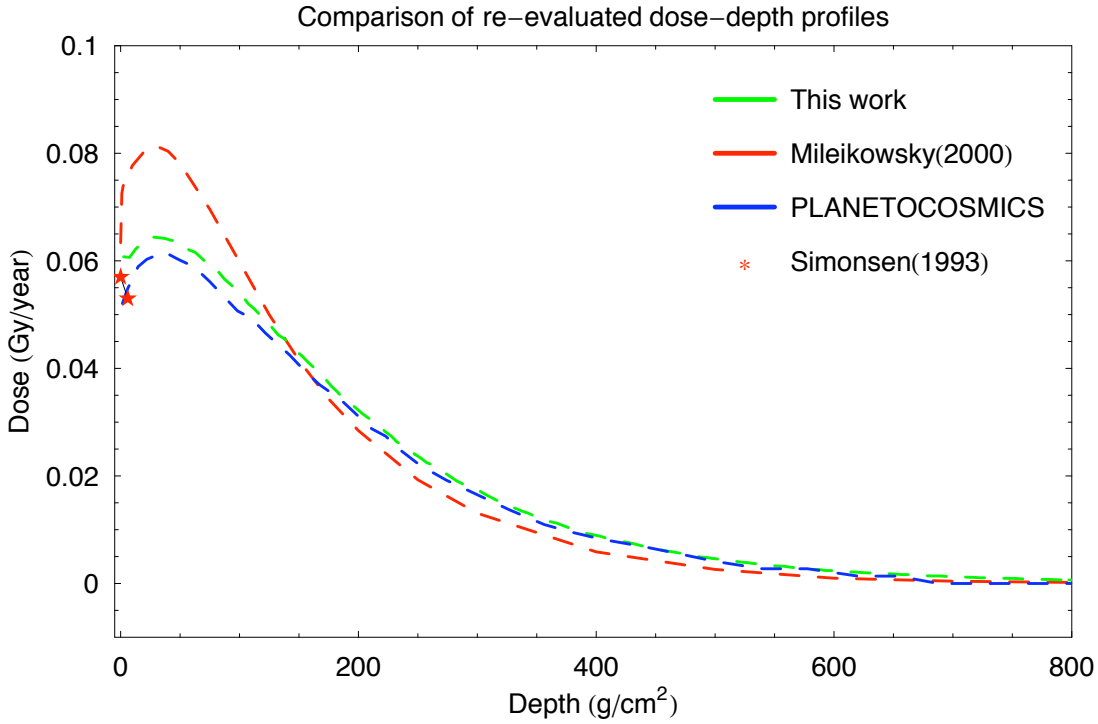

Figure 8.3: Comparison of the solar minimum subsuface dose results produced by this work against the profile reported in Mileikowsky *et al.* (2000) re-normalised by a factor of 3.09. The integrations beneath the dose-depth profile modeled here and the re-normalised Mileikowsky data now contain the same total energy delivered by GCR per annum. Models colour-coded as follows: this work (green); Mileikowsky *et al.* (2000) [154] (red); PLANETOCOSMICS reported in Gurtner *et al.* (2005) [101] (blue); Simonsen & Nealy (1993) [205] (red stars).

The Mileikowsky model produces a more pronounced peak in dose (although calculated to occur

at the same depth, ~30 g/cm^2), which then decays more sharply with increasing depth. This is almost certainly due to a difference in the physics models used. As explained in Methods Section 3.4.2 on page 64, Geant4 physics models (employed by both this research and the PLANETOCOSMICS code) are limited to the explicit modeling of ions lighter than carbon nuclei (Z=6) and ion energies less than 10 GeV/nuc, and so the contribution from other GCR HZE particles is filled-in here with proton, helium and carbon primaries data. The HZETRN code utilised by Mileikowsky *et al.* (2000) [154] incorporates many approximations of its own (see Introduction Section 1.4.1 on page 27), but is capable of simulating the propagation of HZE beyond the limits of Geant4. As formulated by the Blethe-Bloch equation, explained in Introduction Section 1.2 on page 22, the stopping power of an ion (the rate of energy loss by an ion in a target material per unit track length) is a function of Z^2. Thus, a single 10 GeV/nuc iron ion (Z=26, A=56) will deposit greater dose shallower in a target material than a fluence of 56 10 GeV protons (Z=1), despite the fact that they both deliver an equivalent energy of 560 GeV overall. The effect of accurately modeling more-highly charged HZE would therefore be to observe greater energy deposited in shallow depths and less dose deeper, once ionisation and fragmentation have reduced the average energy and Z^2, respectively, of the secondary ion fluence; as seen in the Mileikowsky *et al.* (2000) [154] results. The model developed here can be improved over time with expected advances in the applicability range of the Geant4 ion physics models.

8.4 Data comparison of both model configurations

This radiation environment model was created to address two related investigations into the subsurface ionising radiation on Mars. Firstly, what is the dose deposited in cells emplaced within the subsurface, in an attempt to gauge microbial survival, and secondly, what is the dose deposited into the bulk of the regolith itself, in order to generate data appropriate for the assessment of persistence times of organic biomarkers or calibration of optically stimulated dating techniques.

The first application was addressed by burying micron-thick water layers at regular depths within the modeled surface and recording the energy deposited within them, and the second application required a large block of surface material outputting the depth of all energy deposition events using "virtual layering". The unit of absorbed radiation dose, the Gray (Gy), is normalised to unit volume (J/cm^3), and so for targets of equal density, as the 1 g/cm^3 water layers of model one and dry dust materials of model two are, the calculated absorbed dose ought to be equivalent for the two model configurations. After cross-analysis of results from both model set-ups, however, discrepancies between the two data-sets were discovered.

Table 8.1 compares the calculated martian surface dose rate (Gy/year), both physically-absorbed dose and the biologically-weighted dose equivalent, between the two configurations of this model [66, 65], and those reported by Simonsen & Nealy (1993) [205] and Kim *et al.* (1998) [130], from GCR during both solar minimum and maximum conditions.

Table 8.1: Comparison of calculated martian surface annual accumulation rate of physical dose and biologically-weighted dose equivalent between the two model set-ups of this work [66, 65], Simonsen & Nealy (1993) [205] and Kim *et al.* (1998) [130], from GCR under both solar minimum and maximum. The final row gives the enhancement factor for dose equivalent relative to the physically-absorbed dose; the mean biological weighting applied. The models did not produce all the same data for comparison, and these cases are marked in the table with "n/a".

Dose rate (Gy/year)				
	Simonsen & Nealy (1993) [205]	Kim *et al* (1998) [130]	This work	
			Model 1 [66]	Model 2 [65]
Physical dose				
sol min	0.057	0.194	0.098	0.063
sol max	0.027	n/a	n/a	0.028
Dose equivalent				
sol min	0.132	1.201	0.537	n/a
sol max	0.067	n/a	n/a	n/a
dose equiv^t enhancement	2.3	6.2	5.5	n/a

It can be seen that the physical dose rate predictions of the second configuration of this model (the last column of Table 8.1), whereby the surface is represented as a single block with virtual layering, agree very closely to that of Simonsen & Nealy (1993) [205], disagreeing by no more than a few percent. The data generated by Kim *et al.* (1998) [130], however, are significantly higher than both this work and Simonsen & Nealy (1993) [205], as also shown in Figure 8.1. The same data generated by the first configuration of the model, whereby a micron-thick layer of water on the surface reports the energy deposited within it, is 56% higher than the second model. The data processing routines are the same in both cases, so the root of the discrepancy lies within the calculation of the absorbed dose in the first case. The dose profiles produced by the two model configurations are shown in Figure 8.4 for comparison, along with the calculated discrepancy factor, defined as the ratio of dose predicted by Model 1 : Model 2.

As noted above, dose is already normalised to unit volume, and so the thickness of the water layer sensitive detector volumes within the Geant4 model should bear no relevance. One possibility is that the micron-thickness of the water layers interferes with the modeling of the particle propagation or calculation of where energy is deposited in some manner, leading to an artifactual increase in recorded dose. However, the positioning of volume boundaries, even if relatively close as in the water layers, should have no effect on the running of the Geant4 model. As explained in Section 2.4.3 on page 41, the step length of a propagating particle is limited either by the occurrence of a discrete physical process (such as nuclear collision) or by the geometric distance to the boundary of a volume, whichever the Geant4 Tracking manager determines to be the shortest [232, Chapter 5: Tracking]. Most particle steps within the water layers will therefore be limited by the opposing volume boundary, but continuous processes, such as ionisation of the target material, occur along a particle step regardless of its length.

A second possible explanation for why a thin sensitive detector might register a different deposited dose than a thicker volume is as follows. A particle incident into a target volume has a certain probability of physical interaction, such as an HZE particle colliding with a target nucleus, and so produce secondary particles which can themselves ionise the target material and deposit energy (and thus increase the recorded dose). If a sensitive detector is thin, it

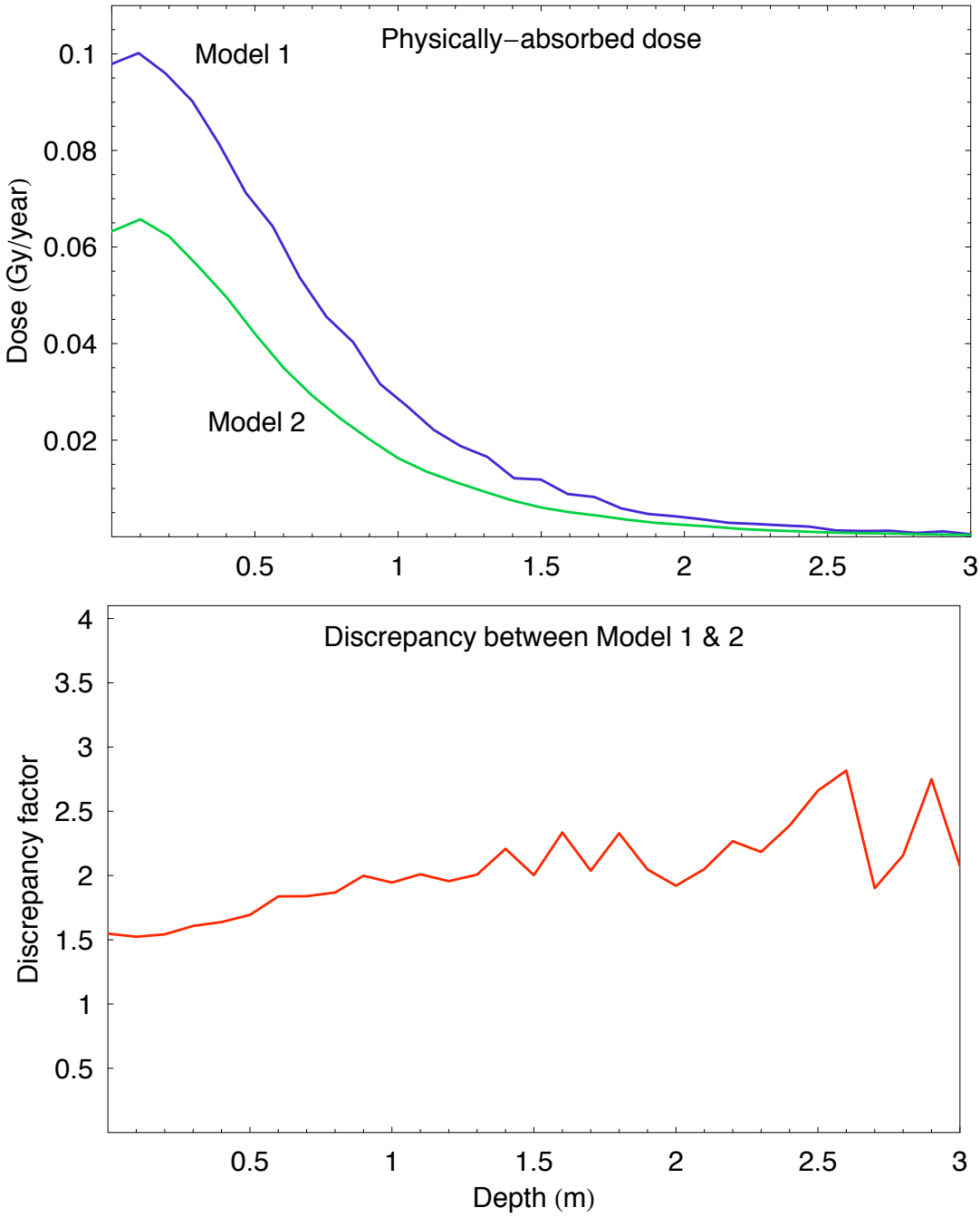

Figure 8.4: Top: the discrepancy between the physically-absorbed dose (from GCR during solar minimum) in the martian subsurface (3 g/cm^3 dry homogenous) as calculated by the first and second configurations of the model, as a function of depth. Bottom: the discrepancy factor between the two model predictions, calculated as the ratio of doses produced by Model 1 : Model 2.

may trigger a physical interaction but then not be thick enough to capture energy from the generated secondaries, such as recoiling nuclei or freed electrons. A thicker or denser target volume would capture more energy from the secondaries and so register a greater dose, an effect that may vary non-linearly with thickness (the scenario is very complex and the actual response would depend on incident particle type and energy). However, layers within a shielding mass will exist in steady-state with respect to particle flux: on average, as many secondary particles will be generated elsewhere in the shielding and enter a thin layer as the ones generated within that layer and exiting without depositing energy. Thus, only for the region immediately on the upstream surface of an irradiated volume (i.e. the very top sensitive detectors in the martian surface model) would this steady-state condition not hold true, and unbalanced secondary flux contribute to a thickness-dependence on recorded dose. However, this potential effect would create a lower recorded dose in thin surface layers, not an increase as is observed in the first configuration of the computer model. Furthermore, the discrepancy plot in Figure 8.4 shows the factor between the two model predictions to actually increase slightly from 1.5 to 2.5 over the top 2 m of martian subsurface, before the doses calculated by both models become too low and the ratio very noisy. So the steady-state hypothesis cannot explain the dose enhancement recorded by the thin water layer detectors of model one.

There is thus no reason to suspect that a sensitive detector of 1 μm thickness would experience any artifacts from particle tracking, and the discovery of the $\sim$60% discrepancy during model cross-analysis is unexpected. This effect could be further tested by a thorough and systematic investigation of calculated deposited dose as a function of sensitive detector thickness for a wide range of incident radiation types and energies, and target materials and densities. In retrospect, however, the second model set-up, which does not incorporate relatively small volumes to register the deposited dose, is probably the more robust modeling solution and therefore the preferred configuration for future development of the code described here.

Looking to the dose equivalent section of Table 8.1 on page 153, it can be seen that the discrepancy between the calculation from the first configuration of this model and the results reported by Simonsen & Nealy (1993) [205] is even greater. Simonsen & Nealy (1993) [205] calculate an annual dose equivalent of 0.132 Gy from GCR at solar minimum, whereas model 1 produces a value four times higher. This assessment of dose equivalent is calculated by weighting the physically-absorbed dose by biological-effectiveness factors dependent on the depositing particle type and energy. The final row of Table 8.1 shows the dose equivalent enhancement (the ratio of biologically-weighted dose equivalent to physically-absorbed dose): the average value by which all the dose deposition events have been biologically-weighted. In this case, the results of this model agree much more closely with that of Kim *et al.* (1998) [130] than Simonsen & Nealy (1993) [205]. The reason for this is believed to be that Simonsen & Nealy (1993) use the weighting factors advised within ICRP publication 26 [113], whereas Kim *et al.* (1998) and this work use the more recent values provided in ICRP publication 60 [114]. Thus, although the doses calculated by Kim *et al.* (1998) differ from those calculated by this model, they find a very similar mean biological-weighting of the radiation field on the martian surface.

It should also be noted that the factors used here for biologically-weighting the physically-absorbed doses, provided by ICRP publication 60 [114] and applied previously to assess microbial survival in astrobiological research [181], are representative values for the relative biological effectiveness for specified types and energies of radiation on human cells. No similar generalised set of representative values more appropriate for microbial cells is available, due in part to both greater variance in microbial response to radiation and lesser radiological interest in microbial

survival compared to human, and so use of these these data is justifiable. It is known, however, that for ionising particles with high LET this weighting factor is likely to be an over-estimate for relative biological effectiveness in bacteria [115, 218, 116], resulting in conservative values calculated for the population survival time. This over-estimate will only be relevant for the top layers of the martian subsurface, however, where HZE particles, attributed with a high relative biological effectiveness, dominate the radiation field and dose deposition.

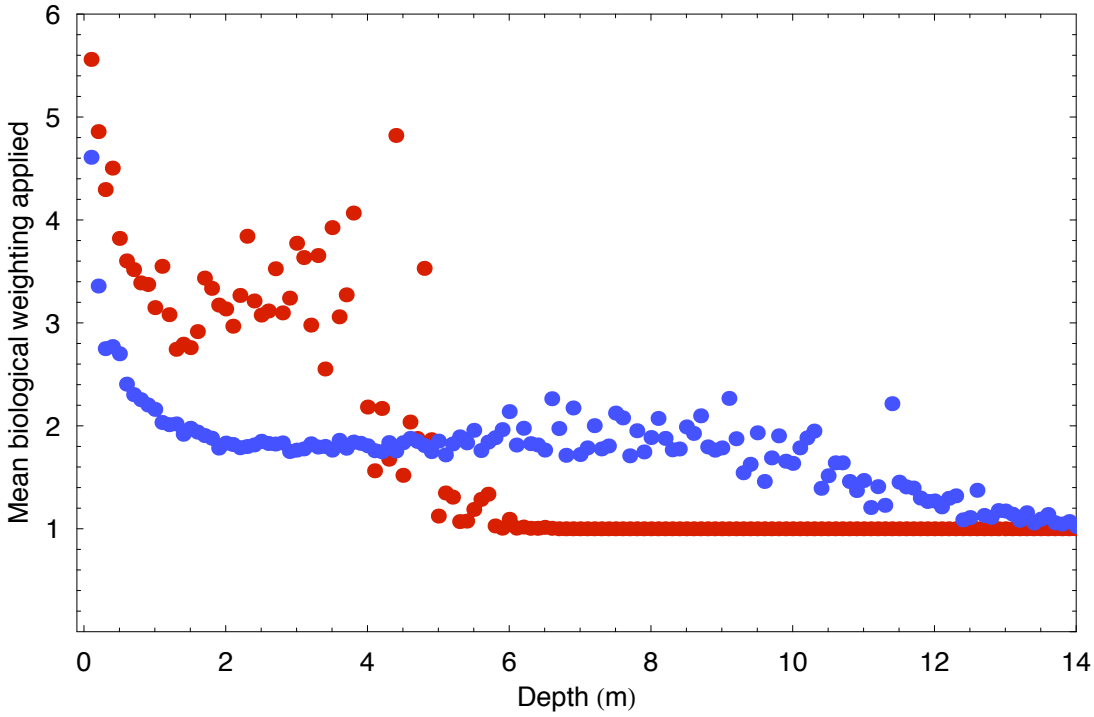

Figure 8.5: The mean biological weighting factor applied (the ratio of weighted dose to the physically-absorbed dose) as a function of depth in both the Wet Heterogenous (red) and Pure Ice (blue) models of the martian subsurface (first model configuration), from GCR during solar minimum. The mean weighting factor can be seen to approach unity at 5 m depth in the Wet Heterogenous model, and at 12 m depth in the less dense Pure Ice model.

Figure 8.5 plots the mean biological weighting factor applied as a function of depth, calculated as the ratio of the weighted dose to the physically-absorbed dose, for both the Wet Heterogeneous and Pure Ice surface models. It can be seen that in the top 4 m the ice model shows a lower mean weighting factor, due to the reduced production of recoiling heavy nuclei within the hydrogenous water shielding, but due to the lower shielding density the ice material does not absorb the propagating high-LET particles as quickly as the wet heterogeneous model and the mean biological weighting factor remains elevated for a long plateau at a factor of 2. The calculated ratio is noisy at intermediate depths due to diminishing particle flux and dose deposition. The weighting factor approaches unity within 5 m depth in the permafrost rock surface, and 10-12 m in the pure ice, where gamma rays, electrons and muons dominate the radiation field. In both surface scenarios, however, the mean weighting factor drops rapidly and the biologically weighted doses calculated using data derived from human cells are probably fair assessments for microbial survival below 1 m depth in ice and 4 m depth in permafrost rock.

In future development of the martian radiation model created here, other theoretical methods for modeling microbial response to ionsing radiation, and high-LET HZE particles in particular, can be explored. An alternative would be the track structure model of HZE propagation and cell

killing [124, 123, 121, 122, 125, covers the development of this theory], although this method still necessitates fitting of parameters to the mathematical model for any given biological endpoint in a given organism, and even so, the complex dose-survival response of *D. radiodurans* is not fully treated.

8.5 Experimental irradiation

Figures 7.5 to 7.10 on page 140 presented the irradiation survival plots of the three novel Antarctic isolates, as well as the model organisms *E. coli* and *D. radiodurans*. Two major outcomes were observed from these results. Firstly, the population of *E. coli*, expected to show the greatest degree of radiation sensitivity out of the bacterial strains studied, in fact showed a radiation resistance second only to *D. radiodurans*. Secondly, all strains were discovered to exhibit high degrees of radiation resistance when the cell populations were frozen and irradiated at -79°C, a temperature characteristic of the martian surface. The significance of these two observations are discussed below.

8.5.1 *E. coli* survival

The first surprising result from these experiments, was that *E. coli*, selected here as a negative control due to its known radiation sensitivity [30, for example], actually survives the radiation exposure better than all the novel Antarctic isolates. The calculated D_0 value (the radiation dose required to reduce viable population number by 37%) for *E. coli* from the irradiation experiments reported here, 0.543 kGy, is higher than any other strain tested, bar *D. radiodurans*. The Antarctic isolates, cultured from a very dry environment, would be expected to exhibit irradiation survival higher than *E. coli* as radiation resistance has been associated with desiccation resistance [148].

One possible explanation for this, already mentioned in Section 7.4 on page 133, is that *E. coli* was only irradiated up to 3 kGy, and survival assessments for higher doses are based on extrapolation. *E. coli* was expected to show a high degree of radiosensitivity, and so considering the tight constraints on sample numbers for the radiation exposures, irradiation was not continued to higher doses for this cell-type. Thus, although a 10^{-6} survival fraction was achieved during the experimental irrradiations of the three Antarctic isolates, calculating the necessary dose for *E. coli* requires an extrapolation of around four orders of magnitude beyond the last data point. It is possible that the irradiation survival response of *E. coli* exhibits a steeper fall-off at some point beyond this 3 kGy experimental limit, and so the calculated D_0 is valid only for low doses and is not representative of the population survival behaviour at higher doses. However, previous irradiation studies on *E. coli* find that the survival function is a simple exponential decay (see results summarised in Figure 8.6) with no change in gradient, and so the unexpectedly-high radiation resistance exhibited by *E. coli* in this experimental set-up is not believed to be an artifact of extrapolation of the data.

A second explanation is deemed to be more plausible. Table 7.5 on page 137 lists the population numbers from the control samples, both of the liquid culture before freezing and of the viable cell count after the freeze-thaw process, the latter giving the zero dose population number from which all subsequent irradiation survival fractions are calculated. It can be seen that while

all four of the environmental strains exhibit near-total survival of freeze-thaw (and especially *D. radiodurans* and Rhodococcus sp. MV.10), the *E. coli* population has already suffered ∼98% death. *E. coli* is not an environmental bacterium, and so would not be expected to be adapted for survival of freeze-thaw. The experimental protocol may therefore include an implicit strong selection for cells that are better able to repair cellular damage caused by both the sample preparation process of freeze-thaw and the radiation. For example, in an actively-growing liquid culture the population will contain a distribution of cells at different stages of DNA synthesis or cell division. If the lethal effect of freeze-thaw kills the same sub-set of cells that woud have been particularly vulnerable to irradiation, then the sample has been selectively biased towards a greater proportion of radiation resistant cells.

Such a pre-selection effect may possibly be responsible for the unexpectedly-high radiation resistance exhibited by *E. coli* in these experiments. Attempting to discount this effect by rerunning irradiation exposures above freezing would encounter problems with the possibility of continued cellular metabolism and DNA repair during irradiation.

8.5.2 Enhanced radioresistance at -79°C

The second major result from the gamma-ray exposures performed here is that not only does the *E. coli* population survive better than all the Antarctic isolates, but that both the *E. coli* and *D. radiodurans* populations exposed at -79°C exhibit radiation resistance far in excess of that published for higher temperatures.

Figure 8.6 plots the gamma irradiation survival response of *E. coli* and *D. radiodurans* populations reported in several different publications, alongside the representative survival curves provided by Battista (1997) [30] and the experimental data described here. The gamma-irradiation survival curves reported by different researchers, even with an identical form of radiation and same species of bacterium, can be seen to vary greatly. For both *E. coli* and *D. radiodurans*, the representative survival responses provided by Battista (1997) [30] are seen to be the most conservative. The representative survival curve obtained for *D. radiodurans* cultures in an unfrozen state (but chilled on ice to minimise metabolic activity during irradiation), provided by Battista (1997) [30], is seen to possess a shoulder at around 5 kGy; below which dose no measurable cell death occurs [30]. Beyond this dose threshold, *D. radiodurans* populations follow a standard exponential cell death response, reaching 10^{-6} survival after 15 kGy, the accumulated dose level taken in the modeling work described in methods Section 3.6.3 on page 73 to represent complete inactivation of an environmental population. This survival behaviour does not follow a simple exponential decline, and the response of a *D. radiodurans* population to irradiation, with both shoulder and exponential parts, more closely fits a relationship of the form $1-(1-e^{-k.D})^n$ [187]. In the survival curve shown in Figure 8.6, the representative response of *D. radiodurans* is plotted with $k = 3/2$ and $n = 5000$.

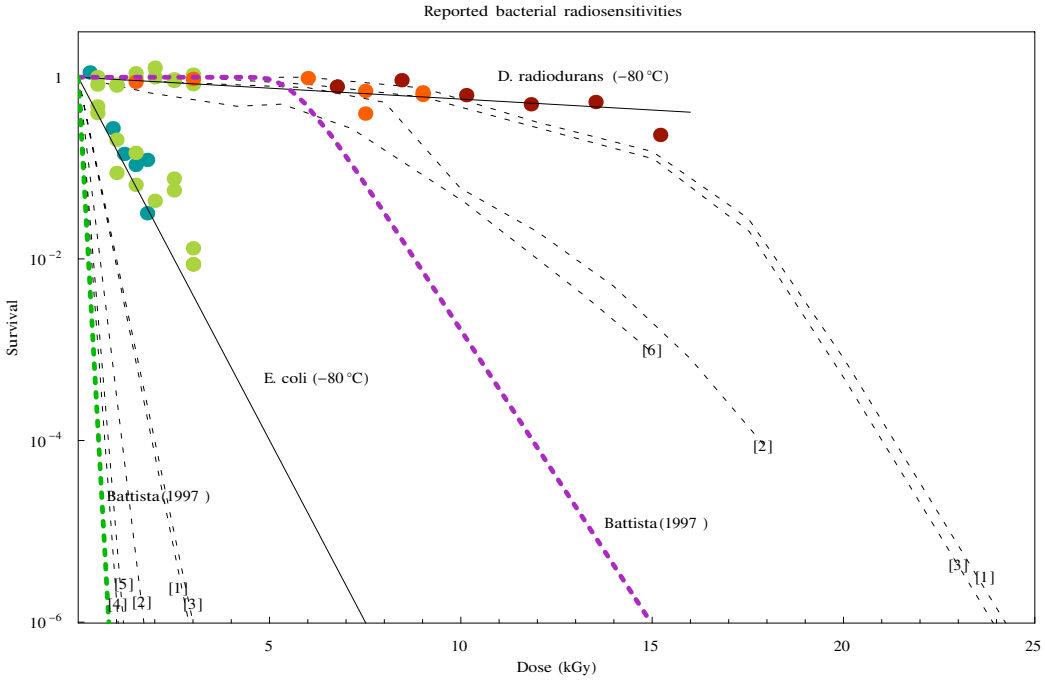

Figure 8.6: Comparison of the gamma irradiation survival of *E. coli* and *D. radiodurans* determined by this study at -79°C (data points and solid black best-fit lines), against the representative survival curves provided by Battista (1997) [30]; *E. coli*, green; *D. radiodurans*, blue; and other recent published radiation studies performed at higher temperatures (black lines: *E. coli*, dashed; *D. radiodurans*, dot-dash), numbered as follows: 1) Omelchenko *et al.* (2005) [174]; 2) Chen *et al.* (2004) [46]; 3) Daly *et al.* (2004) [64]; 4) Imamura *et al.* (1997) [115]; 5) Asgarani *et al.* (2007) [19]; 6) Ferreira *et al.* (1997) [84]

The radioresistance of the same strain is known to vary depending on both growth conditions, such as oxygen and nutrient abundance and growth phase upon irradiation [155, 223, 61], and irradiation conditions, such as abundance of oxygen, temperature, and dose rate (reviewed recently in Baumstark-Khan & Facius (2001) [33]). Many of the irradiation survival experiments reported in the literature, however, are not meticulous in stating the exact growth and exposure conditions used [115, 46, 64, 174, for example, give no details of the irradiation procedure], and so the great variance in recorded survival characteristics is difficult to account for. In particular, if a cell population is irradiated within growth medium at warm temperatures (and thus cellular metabolism and repair mechanisms potentially remaining active) at low dose rates, the observed radioresistance can be expected to be increased due to cellular repair during irradiation. For example, Ferreira *et al.* (1997) [84] state that cultures were irradiated at room temperature at a gamma dose rate of 1.34 kGy/hr, thus requiring an eleven-hour exposure for the highest dose.

The reason that the representative survival data provided by John Battista (green and blue lines in Figure 8.6) was adopted for the martian microbial survival computer modeling (see methods Section 3.6.3) is that this researcher has lead a very successful laboratory group focussing on *D. radiodurans* for many years, researching into not just the radiation response of cell populations under different conditions, but also the protection and repair mechanisms responsible for the extreme radioresistance of strains of the Deinococcus genus [148, 30, 32, 31, 61, 190, for example]. Furthermore, a great number of publications discussing astrobiology and the survival characteristics of *D. radiodurans* cite the radiation research of Battista and colleagues [191, 154, 33, 194, 181, 134, 229, 192, 182]. Battista clearly reports that cell populations are grown in aerated conditions to mid-log phase, before being irradiated on ice so as to limit

metabolic rates [30, 61]. Thus, so as to replicate this standardised experimental procedure as faithfully as possible, cell populations were here grown in aerated nutrient broth to mid-late-log phase, before being frozen and irradiated on dry ice to completely eliminate cellular metabolism and complications of dose delivery rate and also to recreate the irradiation temperatures of the martian surface.

It is also worth noting that in all of the *D. radiodurans* irradiation experiments displayed in Figure 8.6 the major difference in the observed survival characteristics is in the dose at which the viable population begins to decline: the shoulder of the survival curve. Beyond this threshold the gradients of the exponential declines are observed to be roughly equivalent, and so the dose required to produce a 10^6 viable population decrease varies between 15 kGy and 24 kGy, a factor of only 1.6. Even considering the experimental variance in measured radioresistance of *D. radiodurans* then, the input data used in the computer modeling to assess microbial survival remains robust in this respect.

Regardless of the exact details of sample preparation and irradiation conditions, however, the results obtained here for populations irradiated in a frozen state at -79°C, rather than in a chilled but un-frozen state, show an increase in radioresistance of *D. radiodurans* and *E. coli.* Reasons for this are discussed below.

Radiolysis of biomolecules occurs through both direct and indirect mechanisms: ionisation from a particle hit (dominant in dry irradiation) and attack from diffusible free radicals generated by the radiolysis of water (dominant in dilute aqueous solution, see Figure 1.6 on page 26), respectively [112]. Both direct and indirect radiolysis are of importance to microbial survival in the subsurface martian permafrost. Under gamma irradiation at room temperature, roughly 80% of DNA damage is caused indirectly by irradiation-induced diffusible reactive oxygen species [95]. These are created by radiolysis of water molecules, and within a cell diffuse a distance on the order of 3-5 nm from their generation site to attack biological molecules [112].

The generation of free radicals in an aqueous system can be studied using electron spin resonance (ESR) spectroscopy, which records the resonant absorbance of microwave energy by chemical species with unpaired electrons in a strong magnetic field [106, 209]. The technique can be used to identify radicals produced by radiolysis of water, and in simple cases, such as the irradiation of aqueous amino acids of a single kind, radicals of the substrate [106]. ESR spectroscopy studies have shown that radiolytic free radicals such as $^{\cdot}OH$ and $^{\cdot}O_2H$ are stable at 77 K (-196°C), and do not diffuse to recombine or attack substrate molecules. The diffusion of these free radicals becomes significant above 120 K. The hydrogen atom, $H^{\cdot}$, is only stabilised at 4.2 K, and retains high mobility, and consequently a short life-time, at 77 K [106]. Thus, below 77 K only $H^{\cdot}$ is free to diffuse and attack substrate molecules; above about 120 K other free radicals generated by radiolysis of the water solvent are free to diffuse and chemically attack molecules they encounter, adding to the damage inflicted by direct radiation action [83, for a recent review].

The polar nature of the DNA molecule means that it is surrounded by a shell of water of hydration. Within this hydration shell, which is several nanometers thick, the dynamics of water molecules are perturbed by charges on the DNA; ordered in an ice-like array, but retaining considerable mobility even down to -80°C, where the bulk water is completely immobilised [99]. The radiochemistry of hydration water surrounding a polarising molecule is also profoundly altered. "Dry charges" created within the shell by radiolysis of hydration water molecules,

$H_2O \rightarrow e^-_{dry} + H_2O^+_{dry}$, are transferred rapidly to the DNA molecule before solvation or the production of longer-lived molecular intermediates can occur. Ionisation within the hydration zone results in direct transfer of electrons or electron holes to the DNA without first creating diffusible free radicals. Thus, the biological end-point is the same if the DNA molecule is directly hit by ionising radiation or radiolysis occurs within the hydration shell, and the two energy transfer pathways are indistinguishable [99]. This transfer of radiolytic charges occurs even below 77 K, although subsequent radical reactions within the DNA molecule require a temperature above 77 K. DNA irradiated at 77 K is therefore a phase-separated system, with no indirect mechanism of radical diffusion and attack possible, and damage resulting only from direct hits or radiolysis within the hydration shell. Even with subsequent warming above 135 K and unlocking of diffusible radicals such as $^{\cdot}OH$, they recombine within the bulk water and do not cause chemical alterations to the DNA [99].

Thus, the direct effect of ionising radiation is not temperature-dependent, with damage occurring when both the DNA molecule itself or water molecules within the hydration shell are ionised. Additionally, above about 120 K there is an increasing component of indirect DNA damage from diffusing free radicals generated in the bulk water by radiolysis. However, although the temperature below which radical diffusion is limited has been investigated as above, the diffusion distance of different radical species as a function of ice temperature, and thus their relative importance in attacking biological molecules, is not well characterised [Ralf Kaiser, personal communication]. At the irradiation temperature used in this study, -79°C (194 K), radiolytic radical species such as $H^{\cdot}$, $^{\cdot}OH$ and $HO_2^{\cdot}$ are mobile, but still restricted in their diffusion by the low temperature. By comparison, martian midlatitude (±60°) surface temperatures during summer range between 290 K at midday and 180 K during the night, but at depths of only several centimeters into the subsurface the temperatures are steady at the diurnal mean of about 210–220 K [44]. During winter, polar temperatures drop to 150 K [44], and so cosmic ray irradiation in the near subsurface is always within the regime of free radical diffusion and indirect biological damage.

The radiation sensitivity of microbes as a function of irradiation temperature, extending to below -70°C (203 K), has been previously studied. For example, Stapleton & Edington (1956) [215] X-ray irradiated *E. coli* in oxygenated ice, and found a 20% increase in radiation resistance at -72°C compared to -12°C (assessed from the ratio of the calculated inactivation constant at the two temperatures), and a doubling of resistance by -196°C (77 K). Sommers *et al.* (2002) [211] found that *Yersinia enterocolitica*, a food-borne pathogen, exhibits an increase in gamma ray radiation resistance of almost three-fold at -76°C compared to 0°C. Powers & Tallentire (1968) [187] explored at great depth the temperature-dependency of bacterial survival due to free radical diffusion, as discussed below.

Spores of the bacterium *Bacillus megaterium* were exposed to ionising radiation (X-rays) at a range of temperatures, from 5 K to 300 K (-268°C – 27°C) [187]. At each temperature level bacterial samples were exposed to a range of radiation doses, and the resulting survival fraction plotted against dose just as in Figure 7.10 on page 140. The inactivation constant (the gradient of the exponentially declining survival, γ, as calculated for this study in Table 7.6 on page 141) was calculated for each experimental run, and plotted as a function of irradiation temperature, as reproduced in Figure 8.7. Two data sets are shown here: spores grown and irradiated in H_2O and spores grown and irradiated in heavy water, D_2O. In both cases, spores were irradiated in anoxic conditions (flushed with N_2 gas) but re-exposed to O_2 after irradiation and during colony counting. The first crucial result evident here is that the inactivation constant is not

temperature-dependent in H_2O spores below 125 K. Cell death here is due solely to the direct mechanism of radiation damage, with no contribution from radical diffusion and attack. Above 125 K, the inactivation constant, and thus radiosensitivity of the spores, increases linearly as a function of temperature due to increasing radical diffusion [187]. This interpretation of the results is corroborated by the observation that for D_2O spores radiosensitivity is always lower than for H_2O spores and becomes temperature-dependent at a higher temperature (150 K), due to the lower diffusion within heavy water.

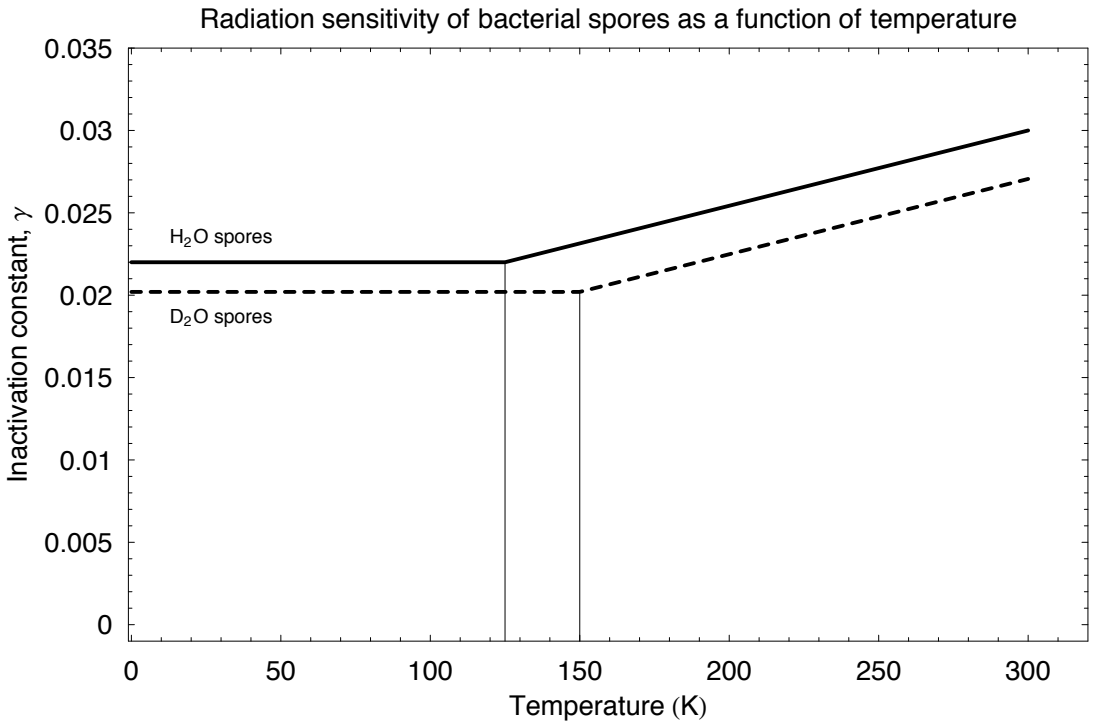

Figure 8.7: The inactivation constant (dose-survival exponential decay parameter, γ) of spores of the bacterium *Bacillus megaterium* exposed to ionising radiation (X-rays) as a function of exposure temperature. Two experimental regimes are shown; spores grown and irradiated in H_2O (solid line) and spores grown and irradiated in heavy water, D_2O (dashed line). In both cases, spores are irradiated under anoxic conditions (flushed with N_2 gas) but re-exposed to O_2 after irradiation and during colony counting. Vertical lines at 125 K and 150 K are shown as visual aids to the temperatures at which irradiation survival of H_2O spores and D_2O spores, respectively, becomes temperature dependent due to mobility of free radicals. Graph plotted by the author from experimental data provided in Powers and Tallentire (1968) [187]

The inactivation constant for H_2O spores increases by a factor of 1.36 between 125 K and 300 K (-148°C – 27°C), and at the temperature of dry ice (194 K) these results show a decrease in radiosensitivity of 16% relative to room temperature. This temperature-dependent effect on free radical diffusion and radiosensitivity explains the observation from the research reported here of improved radioresistance of *E. coli* and *D. radiodurans* when irradiated frozen on dry ice. For *E. coli*, the calculated inactivation constant at -79°C (194 K; γ=1.841) is over 2.5 times lower than the lowest reported radiosensitivity in Figure 8.6 on page 159 (line 3, γ=4.605; [64]), a much more significant temperature dependency of radiosensitvity than found with the *B. megaterium* spores [187]. This is to be expected, however, as bacterial spores are internally desiccated and so greatly reduce the generation of free radicals by radiolysis of water molecules [203].

A calculation of the temperature-dependent increase in radioresistance for *D. radiodurans* is not possible as survival data was not gathered from high enough dose exposures, and an assessment

of the final inactivation constant may be unreliable. Continuing this experiment to higher doses may reveal a shoulder in the survival response beyond 16 kGy, and thus a large increase in the calculated inactivation constant. One previous study gamma-irradiating *D. radiodurans* on dry ice finds a shoulder in the survival function at 27 kGy, and 10^{-6} population survival by 77.5 kGy [193] (a dose five times higher than that used in the modeling study).

The outcome of this discussion is that a number of studies have found radiation resistance of bacteria to be temperature-dependent above 125 K (-148°C) due to the increasing diffusion of free radicals. At the intermediate temperature used in the irradiation experimentation here, of -79°C, this restriction of radical diffusion and thus protection from radiation damage remains significant. The implications of this enhanced radioresistance at low temperatures to the modeling work already performed are significant, and are explored in the following section. Neither of the other two publications studying the astrobiological implications of ionising radiation on Mars, Mileikowsky *at al.* (2000) [154] and Pavlov *et al.* (2000) [181], included this temperature effect and it thus represents an important area for improvement of modeling efforts.

8.6 Conclusions

After the extended discussion, above, on the merits of both the modeling and experimental work performed here, and their positioning within previous studies, it remains to finally combine these two threads of research.

The irradiation experiments found only a slight decline in *D. radiodurans* survival over a wide dose range of gamma ray exposure, with the final data point collected showing 23% survival at 15.21 kGy, although without further data it is unclear whether this represents a genuine decline in survival or is due to experimental variation. Nonetheless, this is greatly above the survival response used in the modeling work to assess microbial survival within the martian subsurface. It has been shown that the temperature-dependent reduction in radiolytic free radical diffusion, and thus radiation-induced cell death, is significant at -79°C, a temperature representative of the midlatitude martian subsurface [44]. The biologically-weighted dose data calculated by the first configuration of the model calculates that within a permafrost-laden surface (the wet heterogeneous scenario) at 2 m depth, the drill length of ExoMars [222], the maximum experimental dose used here is deposited by GCR within 453,000 years. Taking the *E. coli* irradiation survival on dry ice experimentally-derived here, 10^{-6} survival of a non-radioresistant population would occur within 223,000 years at a 2 m depth in permafrost-laden rock. This calculation is 7.4 times longer than that originally estimated by the modeling, without including the temperature effect. The irradiation study found that the novel Antarctic isolate *Brevundimonas* sp. MV.7 would exhibit a near-identical survival behaviour in the ionising radiation field of the martian subsurface. This calculated survival period represents a lower bound, however. As explained in Section 8.4 on page 152, the first configuration of the model apparently produces an unexpected, and as-yet unexplained, increase in calculated deposited dose, and the biological weighting factors applied generally over-emphasise the deleterious effect of high-LET particles on microbes.

The closest correlation between the modeling and the experimental set-up is achieved by taking the doses calculated by the second configuration of the model, and thus with no potential anomalous increase in calculated dose and incorporating no biological weighting (the relative

biological effectiveness of gamma rays is by definition unity). The radiation model finds that at a depth of 12 m in 1 g/cm^3 pure water ice the predicted radiation field is dominated by low-LET ionising radiation, which is well approximated by the experimental gamma ray exposure from the cobalt-60 source. The model calculates a dose rate of 7.5×10^{-5} Gy/year from GCR at this depth. Using the lethal dose of 77.5 kGy for 10^{-6} kill of *D. radiodurans* at -79°C [193], this corresponds to population survival for a billion years, and so in terms of exogenous radiation alone a radioresistant population of martian microbes emplaced in deep ice could persist for a substantial period.

The radiation survival experimentation performed here on the novel isolate *Brevundimonas* sp. MV.7 is of particular relevance. This was the most radiation resistant of the three novel strains to be tested, and Table 7.4 on page 134 shows this bacterium from the Antarctic Dry Valleys to share 99% 16S rRNA gene sequence similarity (based on 402 nucleotide sequence) with an uncultured bacterium (Genbank accession number DQ532317.1) identified from the microbial community within a clean room used for spacecraft assembly at Kennedy Space Center (KSC) [158]. The sampling location, designated KSC-4 by the authors, was a 1 m^2 area of floor by the bay doors of a 100 K classification clean room (certified to less than 100,000 particles of size $\geq0.5\mu$m/ft^3) within the KSC Payload Hazardous and Servicing Facility (KSC-PHSF). Bacteria of the phylum alphaproteobacteria, like *Brevundimonas* sp. MV.7, were discovered to constitute over a third of the clones identified at this sampling location. *Brevundimonas* sp. MV.7 also shares 99% sequence similarity with clones detected at other locations on the floor in the same facility (samples KSC-2 and KSC-3). Furthermore, *Brevundimonas* sp. MV.7 also shares 99% sequence similarity with a clone (DQ532179.1) sampled from the geographically-distant Johnson Space Center Genesis Curation Laboratory (JSC-GCL), identified from the subfloor of a more stringent, class 10 K, assembly clean room [158]. The authors note that, in terms of desiccation and nutrient availability, the artificial maintained environments within such clean rooms are "extreme" in the context of microbial survival, and so it is not surprising that strains surviving there are similar to those isolated from the Antarctic Dry Valleys in the work reported here.

The significance is that this species of *Brevundimonas* was discovered by the research here to survive in the cold, desiccating, environment of the Miers Valley, an analogue site for the martian surface, and is also a contaminant of spacecraft construction clean rooms. There is the potential, therefore, for this organism to be inadvertently transported to the surface of Mars aboard a lander probe despite the best efforts of planetary protection protocols to prevent the forward contamination of extraterrestrial environments with terrestrial microorganisms [163]. Both the Phoenix lander and the Mars Exploration Rovers Spirit and Opportunity were assembled for final launch testing in the KSC-PHSF [Kasthuri Venkateswaran, Biotechnology and Planetary Protection Group, JPL, personal communication]. Mission failure during the landing sequence could emplace contaminant cells sufficiently far beneath the surface for protection from rapid inactivation by solar UV or even the flux of SEP, calculated here to be significant in only the top tens of cm of subsurface. Even a successfully-landed, but imperfectly sterilised, probe could shield bacteria on its underside or deposit them in a shaded enclave for them to persist for significant periods [160] or be widely redistributed and buried by dust storms The modeling studies and irradiation experiments conducted here show that under martian surface conditions of -79°C (194 K), a contaminant cell population of *Brevundimonas* sp. MV.7 could persist at a shallow depth of only 30 cm in wind-blown dust for up to 117,000 years before suffering 10^{-6} inactivation (model configuration 2, unweighted dose). Species of *Deinococcus* were also discovered in these spacecraft facilities [158], and if such radiation-resistant cells were to be

delivered to the same depth in the martian subsurface this research shows that they could persist for 1.2 million years.

Previous research on the astrobiological potential of the martian subsurface [154, 181, for example] has not included this radioprotection effect of low temperature due to restriction of radical diffusion, which is a significant aspect of the martian surface environment, and has been shown here to be non-negligible.

8.7 Further Work

The research conducted here can be extended in a number of important ways. Firstly, the computer model constructed to characterise the martian subsurface ionising radiation environment can be updated and improved. The anomalous feature in the low energy neutron spectrum has been discussed (Section 5.3.3 on page 107), and may be solved within more recent releases of the physics models and data tables of the Geant4 particle simulation toolkit (the current distribution is Geant4 9.1, this model was constructed using Geant4 7.0). Considering the crucial influence of HZE particles in the cosmic ray composition, extension of the Geant4 ion interaction models to energies beyond 10 GeV/nuc and ions heavier than Z=6 would allow a valuable refinement to the primary radiation particles simulated by this martian model.

The selection of data generated by the model can also be expanded. So far, results have been produced on the particle energy spectra and deposited doses as a function of depth underground. Many of the effects of ionising radiation, both in terms of biological endpoints (such as cell inactivation or organic molecule destrction) and the optically stimulated luminesce signal from certain minerals, are dependent on the density of ionisation produced by the local radiation field. Calculating the linear energy transfer (LET) spectrum of the martian radiation field as a function of depth would therefore also constitute a significant set of results with wide-ranging applications. LET spectrum is a useful metric that summarises the nature of an ionising radiation field more completely than simply deposited dose and is more concise than a complete description provided by the energy spectra of multiple particle types, as already calculated in this research.

The model developed here has been applied only to simulating the martian radiation field, but there are several other extraterrestrial locations with astrobiological potential where characterisation of the radiation environment would represent an important contribution. The surface ice of Jupiter's moon Europa is bathed in an intense particle flux from the trapped radiation belts of the giant planet. The clouds of Venus also represent a potential habitable zone, and like Mars has no global magnetic field to provide protection from charged particle radiation. Both of these scenarios can be addressed with a simple alteration of parameters and reprogramming of the planetary radiation model developed here.

Secondly, there are some particularly interesting aspects of the experimental irradiation work that deserve further investigation. The ionising radiation exposure experiments were conducted on three of the novel isolates from Antarctica, and a meaningful continuation would be to repeat these procedures on more of the strains. As discussed, *E. coli* was unexpectedly found to exhibit greater radiation resistance than any of the Antarctic strains, and further investigation may suggest why, and if it is indeed related to the low survival of freeze-thaw as hypothesised. In

addition, the link between radiation resistance and adaptation to dessication surival has been discussed, and it would be revealing to extend the microbiology work to test for a correlation between the desiccation resistance and radiation resistance of the novel Antarctica strains.

As already discussed at length, the martian radiation field is a complex mix of particles, but of particular significance are the highly ionising heavy ions, HZE, of the galactic cosmic rays. In general, such high-LET particles are more biologically damaging than an equivalent dose deposited by low-LET radiation. The gamma-ray exposures used in this research, therefore, can emulate only a certain part of the martian radiation environment, and a meaningful extension would be to conduct similar irradiation survival experiments using a radiation field with greater LET. Cranfield University also provides a neutron source, and so in the future a suitable exposure set-up could be designed to advance this irradiation survival work. Due to the extensive scattering of neutrons, and the high-LET recoil protons they generate, it would be necessary to optimise the experimental design using simulations with the Geant4 model, a further integration of the theoretical and experimental aspects of this interdisciplinary research programme.

8.8 Research Summary

The current martian surface environment is hostile to life, but there is extensive evidence of a warmer wetter primordial Mars during the early solar system. This realisation supports the possibility of an independent genesis of life upon Mars, or alternatively the receptivity of the planet to cross-fertilisation of microbial life from Earth through panspermia. Direct solar UV flux on the unshielded martian surface is rapidly sterilising, and is additionally thought to have generated oxidising conditions in the topsoil which would pose a severe hazard to organisms as well as the persistence of organics. Beneath this top region, the ionising radiation field generated by the penetration of both solar energetic particles and galactic cosmic rays only minimally shielded by the thin martian atmosphere and absence of a global dipolar magnetic field, will be a significant hazard to subsurface life.

This radiation field is predicted to be extremely complex, governed by the primary radiation source as well as particle interactions within the shielding material itself, with the energy spectrum and particle composition of this radiation field changing as a function of both depth and subsurface material properties. Furthermore, the biological response to ionising radiation is far from simple, dependent on both energy and particle type as well as other environmental conditions during irradiation, and must also be modeled carefully for assessment of organism survival.

This aspect of the martian environment has received attention in modeling studies of the surface radiation field with regards to the hazard it presents to human exploration. Very little research has been conducted thus far, however, on the subsurface ionising radiation environment and astrobiological implications thereof, in terms of the long-term survival of dormant native martian microbes as well as terrestrial contaminants delivered by robotic or human exploration.

The research reported here has addressed this gap in knowledge, employing an integrated programme of both computer modeling of the martian subsurface ionising radiation field as well as experimental investigation into the microbial diversity present in a martian-analogue environment, the Antarctic Dry Valleys, and the radiation survival characteristics of several representative microbial species under martian temperatures.

The computer model was developed using a particle physics toolkit, Geant4, and the physical interaction models used in the planetary radiation simulator PLANETOCOSMICS. The modeling research conducted here, however, was distinct from both PLANTOCOSMICS and all previous martian radiation studies in that it included a detailed treatment of the particle spectra as well as biologically-relevant radiation doses as a function of depth underground, for both SEP and GCR primary spectra, for a variety of appropriate subsurface property scenarios, and for a variety of locations upon the surface as well as changing atmospheric depth over geological time. In addition to generating data relevant to the assessment of survival times of microbial populations in the subsurface, this model can be applied to the persistence times of organic molecules and other biomarkers, as well as the optically-stimulated luminescence technique for dating martian sediments. The effects on the subsurface ionising radiation environment from the deflection of cosmic rays by the martian crustal anomalies was demonstrated to be negligible.

The experimental work successfully cultured a wide diversity of cold-tolerant microbes from the Miers Valley of Antarctica, identified through 16S rRNA gene sequencing. Three of these novel

isolates were selected for further study. They were discovered to demonstrate good survival to freeze-thaw as would be expected for environmental organisms from the hostile environment of an Antarctic Dry Valley, and subjected to gamma irradiation survival studies at -79°C (194 K), a temperature representative of martian midlatitude subsurface permafrost. This research found surprisingly that *E. coli,* a bacterium not expected to demonstrate a high level of radiation resistance, exhibited greater resistance to gamma rays than any of the Antarctic environmental isolates, although this is possibly due to an artifact of its poor survival to freeze-thaw. Crucially, both model organisms, *E. coli* and *D. radiodurans*, exhibited much greater radiation resistance at -79°C than that reported for higher temperatures. This is due to restriction of free radical diffusion and the indirect biological damage they mediate, and demonstrates that ambient temperature is indeed an important factor to include in assessing microbial survival on Mars. The measured radioresistance of the novel Antarctic isolate *Brevundimonas* sp. MV.7 is especially pertinent, as it was discovered to share 99% 16S rRNA gene sequence similarity with a bacterium identified in a spacecraft assembly clean room, and so is a candidate for terrestrial contamination of Mars should planetary protection protocols fail. Combination of both the computer modeling and experimental research here indicates that this organism emplaced to a shallow depth of only 30 cm in wind-blown dust could persist for up to 117,000 years before suffering 10^{-6} viable population reduction.

Bibliography

[1] M. H. Acuna, J. E. P. Connerney, N. F. Ness, R. P. Lin, D. Mitchell, C. W. Carlson, J. McFadden, K. A. Anderson, H. Reme, C. Mazelle, D. Vignes, P. Wasilewski, and P. Cloutier. Global Distribution of Crustal Magnetization Discovered by the Mars Global Surveyor MAG/ER Experiment. *Science*, 284(5415):790–793, 1999.

[2] M. H. Acuna, J. E. P Connerney, P. Wasilewski, R. P. Lin, K. A. Anderson, C. W. Carlson, J. McFadden, D. W. Curtis, D. Mitchell, H. Reme, C. Mazelle, J. A. Sauvaud, C. d'Uston, A. Cros, J. L. Medale, S. J. Bauer, P. Cloutier, M. Mayhew, D. Winterhalter, and N. F. Ness. Magnetic Field and Plasma Observations at Mars: Initial Results of the Mars Global Surveyor Mission. *Science*, 279(5357):1676–1680, 1998.

[3] J. H. Adams. Cosmic Ray Effects on MicroElectronics, Part IV. Technical report, NRL Memorandum Report 5901, 1986.

[4] S. Agostinelli, J. Allison, K. Amako, J. Apostolakis, H. Araujo, P. Arce, M. Asai, D. Axen, S. Banerjee, G. Barrand, F. Behner, L. Bellagamba, J. Boudreau, L. Broglia, A. Brunengo, H. Burkhardt, S. Chauvie, J. Chuma, R. Chytracek, G. Cooperman, G. Cosmo, P. Degtyarenko, A. Dell'Acqua, G. Depaola, D. Dietrich, R. Enami, A. Feliciello, C. Ferguson, H. Fesefeldt, G. Folger, F. Foppiano, A. Forti, S. Garelli, S. Giani, R. Giannitrapani, D. Gibin, J. J. G. Cadenas, I. Gonzalez, G. G. Abril, G. Greeniaus, W. Greiner, V. Grichine, A. Grossheim, S. Guatelli, P. Gumplinger, R. Hamatsu, K. Hashimoto, H. Hasui, A. Heikkinen, A. Howard, V. Ivanchenko, A. Johnson, F. W. Jones, J. Kallenbach, N. Kanaya, M. Kawabata, Y. Kawabata, M. Kawaguti, S. Kelner, P. Kent, A. Kimura, T. Kodama, R. Kokoulin, M. Kossov, H. Kurashige, E. Lamanna, T. Lampen, V. Lara, V. Lefebure, F. Lei, M. Liendl, W. Lockman, F. Longo, S. Magni, M. Maire, E. Medernach, K. Minamimoto, P. M. de Freitas, Y. Morita, K. Murakami, M. Nagamatu, R. Nartallo, P. Nieminen, T. Nishimura, K. Ohtsubo, M. Okamura, S. O'Neale, Y. Oohata, K. Paech, J. Perl, A. Pfeiffer, M. G. Pia, F. Ranjard, A. Rybin, S. Sadilov, E. Di Salvo, G. Santin, T. Sasaki, N. Savvas, Y. Sawada, et al. GEANT4 - A simulation toolkit. *Nuclear Instruments and Methods In Physics Research Section A - Accelerators Spectrometers Detectors And Associated Equipment*, 506(3):250–303, 2003.

[5] J. Allison, K. Amako, J. Apostolakis, H. Araujo, P. Arce Dubois, M. Asai, G. Barrand, R. Capra, S. Chauvie, R. Chytracek, G. A. P. Cirrone, G. Cooperman, G. Cosmo, G. Cuttone, G. G. Daquino, M. Donszelmann, M. Dressel, G. Folger, F. Foppiano, J. Generowicz, V. Grichine, S. Guatelli, P. Gumplinger, A. Heikkinen, I. Hrivnacova, A. Howard, S. Incerti, V. Ivanchenko, T. Johnson, F. Jones, T. Koi, R. Kokoulin, M. Kossov, H. Kurashige, V. Lara, S. Larsson, F. Lei, O. Link, F. Longo, M. Maire, A. Mantero, B. Mascialino,

I. McLaren, P. Mendez Lorenzo, K. Minamimoto, K. Murakami, P. Nieminen, L. Pandola, S. Parlati, L. Peralta, J. Perl, A. Pfeiffer, M. G. Pia, A. Ribon, P. Rodrigues, G. Russo, S. Sadilov, G. Santin, T. Sasaki, D. Smith, N. Starkov, S. Tanaka, E. Tcherniaev, B. Tome, A. Trindade, P. Truscott, L. Urban, M. Verderi, A. Walkden, J. P. Wellisch, D. C. Williams, D. Wright, and H. Yoshida. Geant4 developments and applications. *Nuclear Science, IEEE Transactions on*, 53(1):270, 2006.

[6] K. Amako. Software Reference Manual (Geant4 6.2 June 2004). Technical report, 2004.

[7] K. Amako, S. Guatelli, V. Ivanchencko, M. Maire, B. Mascialino, K. Murakami, L. Pandola, S. Parlati, M. G. Pia, and M. Piergentili. Geant4 and its validation. *Nuclear Physics B - Proceedings Supplements*, 150:44, 2006.

[8] K. Amako, S. Guatelli, V. N. Ivanchenko, M. Maire, B. Mascialino, K. Murakami, P. Nieminen, L. Pandola, S. Parlati, M. G. Pia, M. Piergentili, T. Sasaki, and L. Urban. Comparison of Geant4 Electromagnetic Physics Models Against the NIST Reference Data. *Nuclear Science, IEEE Transactions on*, 52(4):910–918, 2005.

[9] R. I. Amann, W. Ludwig, and K. H. Schleifer. Phylogenetic identification and in situ detection of individual microbial cells without cultivation. *Microbiological Reviews*, 59(1):143–169, 1995.

[10] R. M. Ambrosi, D. L. Talboys, M. R. Sims, N. P. Bannister, M. Makarewicz, T. Stevenson, I. B. Hutchinson, J. I. W. Watterson, R. C. Lanza, and L. Richter. Neutron activation analysis, gamma ray spectrometry and radiation environment monitoring instrument concept: GEORAD. *Nuclear Instruments and Methods in Physics Research Section A: Accelerators, Spectrometers, Detectors and Associated Equipment*, 539(1-2):198–216, 2005.

[11] V. Andersen, F. Ballarini, G. Battistoni, M. Campanella, M. Carboni, F. Cerutti, A. Empl, A. Fasso, A. Ferrari, and E. Gadioli. The code for space applications: recent developments. *Advances in Space Research*, 34(6):1302, 2004.

[12] G. De Angelis, M.S. Clowdsley, R. C. Singleterry, and J.W. Wilson. A new Mars radiation environment model with visualization . *Advances in Space Research*, 34:1328–1332, 2004.

[13] J. Arkani-Hamed. A 50-degree spherical harmonic model of the magnetic field of Mars. *Journal of Geophysical Research - Planets*, 106(E10):23,197–23,208, 2001.

[14] J. Arkani-Hamed. Paleomagnetic pole positions and pole reversals of Mars. *Geophysical Research Letters*, 28(17):3409–3412, 2001.

[15] J. Arkani-Hamed. An improved 50-degree spherical harmonic model of the magnetic field of Mars derived from both high-altitude and low-altitude data. *Journal of Geophysical Research-Planets*, 107(E10):art. no.–5083, 2002.

[16] J. Arkani-Hamed. A coherent model of the crustal magnetic field of Mars. *Journal of Geophysical Research-Planets*, 109(E9):art. no.–E09005, 2004.

[17] J. Arkani-Hamed and D. Boutin. Correction to "Paleomagnetic poles of Mars: Revisited". *Journal of Geophysical Research-Planets*, 109(E05007), 2004.

[18] J. Arkani-Hamed and D. Boutin. Paleomagnetic poles of Mars: Revisited. *Journal of Geophysical Research-Planets*, 109(E3):art. no.–E03011, 2004.

[19] Ezat Asgarani, Mahdiieh Shirzad, Mohammad Reza Soudi, and Hamid Reza Shahmohammadi. Study On The Effects Of Co-60 Gamma-Rays, Ultraviolet Light (UV), And Hydrogen Peroxide On Haloferax IRU. *The Internet Journal of Microbiology*, 3(1), 2007.

[20] M. Audette, X. Chen, C. Houee-Levin, M. Potier, and M. Le Maire. Protein gamma-radiolysis in frozen solutions is a macromolecular surface phenomenon: fragmentation of lysozyme, citrate synthase and alpha-lactalbumin in native or denatured states. *International Journal of Radiation Biology*, 76(5):673, 2000.

[21] J. L. Bada and S. L. Miller. Racemization and the origin of optically active organic compounds in living organisms. *Biosystems*, 20:21–26, 1987.

[22] Jeffrey L. Bada. How life began on Earth: a status report. *Earth and Planetary Science Letters*, 226(1-2):1–15, 2004.

[23] Jeffrey L. Bada and Gene D. McDonald. Amino Acid Racemization on Mars: Implications for the Preservation of Biomolecules from an Extinct Martian Biota. *Icarus*, 114(1):139, 1995.

[24] G. D. Badhwar and P. M. O'Neill. Long-term modulation of Galactic Cosmic Radiation and its model for space exploration. *Advances in Space Research*, 14(10):749–757, 1994.

[25] G. D. Badhwar and P. M. O'Neill. Galactic Cosmic Radiation Model and Its Applications. *Advances in Space Research*, 17(2):7–17, 1996.

[26] Gautam D. Badhwar, Francis A. Cucinotta, and Patrick M. O'Neill. Depth-Dose Equivalent Relationship for Cosmic Rays at Various Solar Minima. *Radiation Research*, 134(1):9–15, 1993.

[27] M. J. Bailey, A. K. Lilley, I. P. Thompson, R. B. Rainey, and R. J. Ellis. Site-directed chromosomal marking of a fluorescent pseudomonad isolated from the phytosphere of sugar beet: Stability and potential for marker gene transfer. *Molecular Ecology*, 4(6):755–763, 1995.

[28] Victor R. Baker. Water and the Martian landscape. *Nature*, 412(6843):228, 2001.

[29] A. Banin and R. L. Mancinelli. Life on Mars? I. The chemical environment. *Advances in Space Research*, 15(3):163, 1995.

[30] J. R. Battista. AGAINST ALL ODDS: The Survival Strategies of Deinococcus radiodurans. *Annual Review of Microbiology*, 51:203–224, 1997.

[31] John R. Battista. Radiation resistance: The fragments that remain. *Current Biology*, 10(5):R204, 2000.

[32] John R. Battista, Ashlee M. Earl, and Mie-Jung Park. Why is Deinococcus radiodurans so resistant to ionizing radiation? *Trends in Microbiology*, 7(9):362, 1999.

[33] Christa Baumstark-Khan and Rainer Facius. Life under conditions of ionizing radiation. In Gerda Horneck and Christa Baumstark-Khan, editors, *Astrobiology: The Quest for the Conditions of Life*. Springer, 2001.

[34] J. Beringer, G. Folger, F. Gianotti, A. Ribon, J. P. Wellisch, D. Barberis, M. Cervetto, and B. Osculati. Validation of Geant4 hadronic physics. *Nuclear Science Symposium Conference Record, 2003 IEEE*, 1:494, 2003.

[35] Jean-Loup Bertaux, Francois Leblanc, Olivier Witasse, Eric Quemerais, Jean Lilensten, S. A. Stern, B. Sandel, and Oleg Korablev. Discovery of an aurora on Mars. *Nature*, 435(7043):790, 2005.

[36] W. A. Bonner. The radiolysis and radioracemization of poly-L-leucines. *Radiation Research*, 152(1):83–87, 1999.

[37] W.F Bonner, N. E. Blair, and R. M. Lemmon. The radioracemization of amino acids by ionizing radiation: geochemical and cosmochemical implications. *Origins of life*, 9:279–290, 1979.

[38] William A. Bonner, Hillary Hall, George Chow, Yi Liang, and Richard M. Lemmon. The radiolysis and radioracemization of amino acids on clays. *Origins of Life and Evolution of Biospheres*, 15(2):103–114, 1985.

[39] Penelope J. Boston, Mikhail V. Ivanov, and Christopher P. McKay. On the possibility of chemosynthetic ecosystems in subsurface habitats on Mars. *Icarus*, 95(2):300, 1992.

[40] W. V. Boynton, W. C. Feldman, S. W. Squyres, T. H. Prettyman, J. Bruckner, L. G. Evans, R. C. Reedy, R. Starr, J. R. Arnold, D. M. Drake, P. A. J. Englert, A. E. Metzger, Igor Mitrofanov, J. I. Trombka, C. d'Uston, H. Wänke, O. Gasnault, D. K. Hamara, D. M. Janes, R. L. Marcialis, S. Maurice, I. Mikheeva, G. J. Taylor, R. Tokar, and C. Shinohara. Distribution of Hydrogen in the Near Surface of Mars: Evidence for Subsurface Ice Deposits. *Science*, 297(5578):81–85, 2002.

[41] David A. Brain and Bruce M. Jakosky. Atmospheric loss since the onset of the Martian geologic record: Combined role of impact erosion and sputtering. *Journal of Geophysical Research*, 103:22689–22694, 1998.

[42] Joseph C. Cain, Bruce B. Ferguson, and David Mozzoni. An n=90 internal potential function of the Martian crustal magnetic field. *Journal of Geophysical Research - Planets*, 108(E2):1–19, 2003.

[43] M. H. Carr. *Water on Mars*. Oxford University Press, 1996.

[44] M. H. Carr. Mars: Surface and interior. In P.R. Weissman and M.L.-A.T.V. Johnson, editors, *Encyclopedia of the Solar System*, pages 291–308. Academic Press, New York, 1999.

[45] J. Chen, D. Chenette, R. Clark, M. Garcia-Munoz, T. G. Guzik, K. R. Pyle, Y. Sang, and J. P. Wefel. A model of galactic cosmic rays for use in calculating linear energy transfer spectra. *Advances in Space Research*, 14(10):765–769, 1994.

[46] Mao-Yen Chen, Shih-Hsiung Wu, Guang-Huey Lin, Chun-Ping Lu, Yung-Ting Lin, Wen-Chang Chang, and San-San Tsay. Rubrobacter taiwanensis sp. nov., a novel thermophilic, radiation-resistant species isolated from hot springs . *International Journal of Systematic and Evolutionary Microbiology*, 54:1849–1855, 2004.

[47] B. C. Clark. Surviving the limits to life at the surface of Mars. *Journal of Geophysical Research-Planets*, 103(E12):28545–28555, 1998.

[48] B. C. Clark, A. L. Baker, A. F. Cheng, S. J. Clemett, D. McKay, H. Y. McSween, C. M. Pieters, P. Thomas, and M. Zolensky. Survival of Life on Asteroids, Comets and Other Small Bodies. *Origins of Life and Evolution of Biospheres*, 29(5):521, 1999.

[49] B. C. Clark, A. J. Castro, C. D. Rowe, A. K. Baird, P. H. Evans, Jr. Rose, H. J., III Toulmin, P., K. Keil, and W. C. Kelliher. Inorganic analyses of Martian surface samples at the Viking landing sites. *Science*, 194:1283–1288, 1976.

[50] S. M. Clifford. A model for the hydrologic and climatic behavior of water on Mars. *Journal of Geophysical Research*, 98(E6):10,973–11,016, 1993.

[51] Frank Close, John Dudeney, and Ken Pounds. Report of the Commission on the Scientific Case for Human Space Exploration. Technical report, Royal Astronomical Society, 2005.

[52] M.S. Clowdsley, J.W. Wilson, M.-H.Y. Kim, R.C. Singleterry, R.K. Tripathi, J.H. Heinbockel, F.F. Badavi, and J.L. Shinn. Neutron environments on the martian surface. In *1st International Workshop on Space Radiation Research*, pages 94–96, Arona, Italy, 2000.

[53] C. S. Cockell. The Ultraviolet Environment of Mars: Biological Implications Past, Present, and Future. *Icarus*, 146:343–359, 2000.

[54] Charles S. Cockell. The ultraviolet history of the terrestrial planets – implications for biological evolution. *Planetary and Space Science*, 48(2-3):203–214, 2000.

[55] Charles S. Cockell and John A. Raven. Zones of photosynthetic potential on Mars and the early Earth. *Icarus*, 169(2):300, 2004.

[56] J. E. P Connerney, M. H. Acuna, P. J. Wasilewski, N. F. Ness, H. Reme, C. Mazelle, D. Vignes, R. P. Lin, D. L. Mitchell, and P. A. Cloutier. Magnetic Lineations in the Ancient Crust of Mars. *Science*, 284(5415):794–798, 1999.

[57] C. Cordoba-Jabonero, M. P. Zorzano, F. Selsis, M. R. Patel, and C. S. Cockell. Radiative habitable zones in martian polar environments. *Icarus*, 175(2):360–371, 2005.

[58] G. Cosmo and G. Folger. Installation Guide for setting up Geant4 in your computing environment (Geant4 6.2 June 2004). Technical report, 2004.

[59] Don Cowan, Nick Russell, Adam Mamais, and Devon Sheppard. Antarctic Dry Valley mineral soils contain unexpectedly high levels of microbial biomass. *Extremophiles*, 6(5):431–436, 2002.

[60] Arthur N. Cox, editor. *Allen's Astrophysical Quantities*. AIP Press (Springer-Verlag), New York, 4th edition, 2001.

[61] M. M. Cox and J. R. Battista. Deinococcus radiodurans - The consummate survivor. *Nature Reviews Microbiology*, 3(11):882–892, 2005.

[62] D. H. Crider. The influence of crustal magnetism on the solar wind interaction with mars: recent observations. In *Planetary Atmospheres, Ionospheres and Plasma Interactions*, volume 33 of *Advances in Space Research*, pages 152–160. PERGAMON-ELSEVIER SCIENCE LTD, Kidlington, 2004. Times Cited: 0 Article 2 BY96F.

[63] F. A. Cucinotta, Premkumar B. Saganti, J. W. Wilson, and L. C. Simonsen. Model Predictions and Visualisation of the Particle Flux on the Surface of Mars. *Journal of Radiation Research*, 43:S35–S39, 2002.

[64] M. J. Daly, E. K. Gaidamakova, V. Y. Matrosova, A. Vasilenko, M. Zhai, A. Venkateswaran, M. Hess, M. V. Omelchenko, H. M. Kostandarithes, K. S. Makarova, L. P. Wackett, J. K. Fredrickson, and D. Ghosal. Accumulation of Mn(II) in Deinococcus radiodurans facilitates gamma-radiation resistance. *Science*, 306(5698):1025–1028, 2004.

[65] L. R. Dartnell, L. Desorgher, J. M. Ward, and A. J. Coates. Martian sub-surface ionising radiation: biosignatures and geology. *Biogeosciences*, 4:545–558, 2007.

[66] L. R. Dartnell, L. Desorgher, J. M. Ward, and A. J. Coates. Modelling the surface and subsurface Martian radiation environment: Implications for Astrobiology. *Geophysical Research Letters*, 34(2):L02207, 2007.

[67] E. F. DeLong. Archaea in coastal marine environments. *Proc.Natl.Acad.Sci. U.S.A.*, 89(12):5685–5689, 1992.

[68] E. F. DeLong and N. R. Pace. Environmental Diversity of Bacteria and Archaea. *Systematic Biology*, 50(4):470–478, 2001.

[69] G. T. Delory, C. Zeitlin, J. G. Luhmann, C. Gorguinpour, D. A. Brain, C. O. Lee, and D. Mitchell. Radiation and the Exploration of the Moon and Mars: Current Knowledge, Challenges, and Required Measurements. *AGU Fall Meeting Abstracts*, 54:03, 2004.

[70] L Desorgher. PLANETOCOSMICS Software User Manual. Technical report, Physikalisches Institut, University of Bern, 2005.

[71] L Desorgher, E. O. Fluckiger, and M. Gurtner. The planetocosmics geant4 application. In *36th COSPAR Scientific Assembly*, volume 36, 2006.

[72] L. Desorgher, E. O. Fluckiger, M. Gurtner, M. R. Moser, and R. Butikofer. Atmocosmics: A Geant 4 Code for Computing the Interaction of Cosmic Rays with the Earth's Atmosphere. *International Journal of Modern Physics A*, 20:6802–6804, 2005.

[73] P. T. Doran, S. M. Clifford, S. L. Forman, L. Nyquist, D. A. Papanastassiou, B. W. Stewart, N. C. Sturchio, T. D. Swindle, T. Cerling, J. Kargel, G. McDonald, K. Nishizumi, R. Poreda, J. W. Rice, and K. Tanaka. Mars chronology: assessing techniques for quantifying surficial processes. *Earth Science Reviews*, 67:313–337, 2004.

[74] M. Durante. Radiation protection in space. *Rivista del Nuovo Cimento*, 25(8):1–70, 2002.

[75] S. Eidelman, K. G. Hayes, K. A. Olive, M. Aguilar-Benitez, C. Amsler, D. Asner, K. S. Babu, R. M. Barnett, and J. Beringer. 24. cosmic rays. In *Review of Particle Physics* , volume 592, page 1. Physics Letters B, 2004.

[76] S. Eidelman, K. G. Hayes, K. A. Olive, M. Aguilar-Benitez, C. Amsler, D. Asner, K. S. Babu, R. M. Barnett, and J. Beringer. 27. passage of particles through matter. In *Review of Particle Physics* , volume 592, page 1. Physics Letters B, 2004.

[77] S. Eidelman, K. G. Hayes, K. A. Olive, M. Aguilar-Benitez, C. Amsler, D. Asner, K. S. Babu, R. M. Barnett, and J. Beringer. 30. commonly used radioactive sources. In *Review of Particle Physics* , volume 592, page 1. Physics Letters B, 2004.

[78] S. Eidelman, K. G. Hayes, K. A. Olive, M. Aguilar-Benitez, C. Amsler, D. Asner, K. S. Babu, R. M. Barnett, and J. Beringer. Review of Particle Physics. *Physics Letters B*, 592(1-4):1, 2004.

[79] Michael H. Engel and Bartholomew Nagy. Distribution and enantiomeric composition of amino acids in the Murchison meteorite. *Nature*, 296(5860):837, 1982.

[80] J. J. Engelmann, P. Ferrando, A. Soutoul, P. Goret, and E. Juliusson. Charge composition and energy spectra of cosmic-ray nuclei for elements from Be to NI - Results from HEAO-3-C2. *Astronomy and Astrophysics*, 233:96–111, 1990.

[81] J. C. Farman, B. G. Gardiner, and J. D. Shanklin. Large losses of total ozone in Antarctica reveal seasonal ClOx/NOx interaction. *Nature*, 315(6016):207, 1985.

[82] W. C. Feldman, W. V. Boynton, R. L. Tokar, T. H. Prettyman, O. Gasnault, S. W. Squyres, R. C. Elphic, D. J. Lawrence, S. L. Lawson, S. Maurice, G. W. McKinney, K. R. Moore, and R. C. Reedy. Global Distribution of Neutrons from Mars: Results from Mars Odyssey. *Science*, 297(5578):75–78, 2002.

[83] Christiane Ferradini and Jean-Paul Jay-Gerin. La radiolyse de l'eau et des solutions aqueuses: historique et actualite. *Can. J. Chem.*, 77:1542–1575, 1999.

[84] Ana Cristina Ferreira, M. Fernanda Nobre, Fred A. Rainey, Manuel T. Silva, Robin Wait, Jutta Burghardt, Ana Paula Chung, and Milton S. da Costa. Deinococcus geothermalis sp. nov. and Deinococcus murrayi sp. nov., two Extremely Radiation-Resistant and Slightly Thermophilic Species from Hot Springs . *International Journal Of Systematic Bacteriology*, 47(4):939–947, 1997.

[85] J. Feynman, G. Spitale, J. Wang, and S. Gabriel. Interplanetary proton fluence model - JPL 1991. *Journal of Geophysical Research*, 98(A8):13,281–13,294, 1993.

[86] A. Filali-Mouhim, M. Audette, M. St-Louis, L. Thauvette, L. Denoroy, F. Penin, X. Chen, N. Rouleau, J.-P. Le Caer, J. Rossier, M. Potier, and M. Le Maire. Lysozyme fragmentation induced by gamma-radiolysis. *International Journal of Radiation Biology*, 72(1):63, 1997.

[87] George J. Flynn. The Delivery of Organic Matter from Asteroids and Comets to the Early Surface of Mars. *Earth Moon and Planets*, 72:469–474, 1996.

[88] F. Forget, F. Hourdin, R. Fournie, C. Hourdin, O. Talagrand, M. Collins, S. R. Lewis, Peter L. Read, and J. Huot. Improved general circulation models of the Martian atmosphere from the surface to above 80 km. *Journal of Geophysical Research*, 104(E10):24,155 – 24,176, 1999.

[89] Francois Forget and Raymond T. Pierrehumbert. Warming Early Mars with Carbon Dioxide Clouds That Scatter Infrared Radiation. *Science*, 278(5341):1273–1276, 1997.

[90] Vittorio Formisano, Sushil Atreya, Therese Encrenaz, Nikolai Ignatiev, and Marco Giuranna. Detection of Methane in the Atmosphere of Mars. *Science*, 306(5702):1758–1761, 2004.

[91] G. E. Fox, E. Stackebrandt, R. B. Hespell, J. Gibson, J. Maniloff, T. A. Dyer, R. S. Wolfe, W. E. Balch, R. S. Tanner, L. J. Magrum, L. B. Zablen, R. Blakemore, R. Gupta, L. Bonen, B. J. Lewis, D. A. Stahl, K. R. Luehrsen, K. N. Chen, and C. R. Woese. The Phylogeny of Prokaryotes. *Science*, 209(4455):457, 1980.

[92] J. L. Fox. Nitrogen escape from mars. In *Martian Surface and Atmosphere Through Time*, pages 53–54, 1992.

[93] E. Imre Friedmann. Endolithic Microorganisms in the Antarctic Cold Desert. *Science*, 215(4536):1045–1053, 1982.

[94] Z. Fujii and F. B. McDonald. Radial intensity gradients of galactic cosmic rays (1972-1995) in the heliosphere. *Journal Of Geophysical Research-Space Physics*, 102(A11):24201–24208, 1997.

[95] D. Ghosal, M. V. Omelchenko, E. K. Gaidamakova, V. Y. Matrosova, A. Vasilenko, A. Venkateswaran, M. Zhai, H. M. Kostandarithes, H. Brim, K. S. Makarova, L. P. Wackett, J. K. Fredrickson, and M. J. Daly. How radiation kills cells: Survival of Deinococcus radiodurans and Shewanella oneidensis under oxidative stress. *FEMS Microbiology Reviews*, 29(2):361–375, 2005.

[96] S. Giani and G. Folger. Introduction to Geant4 (Geant4 6.2 June 2004). Technical report, 2004.

[97] D. D. A. Gilichinsky. Microbial Populations in Antarctic Permafrost: Biodiversity, State, Age, and Implication for Astrobiology. *Astrobiology*, 7(2):275–311, 2007.

[98] David A. Gilichinsky. Permafrost model of extraterrestrial habitat. In Gerda Horneck and Christa Baumstark-Khan, editors, *Astrobiology - The quest for the conditions of life*. Springer, Berlin, 2002.

[99] Silvano Gregoli, Martial Olast, and Albert Bertinchamps. Radiolytic Pathways in gamma-Irradiated DNA: Influence of Chemical and Conformational Factors. *Radiation Research*, 89(2):238–254, 1982.

[100] J. N Gregory. Isotopes in Industry. *Wool Technology and Sheep Breeding*, 5(2):55–63, 1958.

[101] M. Gurtner, L. Desorgher, E. O. Fluckiger, and M. R. Moser. Simulation of the Interaction of Space Radiation with the Martian Atmosphere and Surface. *Advances in Space Research*, 36:2176–2181, 2005.

[102] Robert M. Haberle. Early Mars Climate Models. *Journal of Geophysical Research*, 103:28467–28480, 1998.

[103] C. G.Â A. Harrison, J. E.Â P. Connerney, M. H. Acuna, P. J. Wasilewski, N. F. Ness, H. Reme, C. Mazelle, D. Vignes, R. P. Linn, D. L. Mitchell, and P. A. Cloutier. Questions About Magnetic Lineations in the Ancient Crust of Mars. *Science*, 287(5453):547a, 2000.

[104] D. M. Hassler, R. F. Wimmer-Schweingruber, R. Beaujean, S. Bottcher, S. Burmeister, F. Cucinotta, R. Muller-Mellin, A. Posner, S. Rafkin, G. Reitz, and Team The Rad. The radiation assessment detector (rad) on the mars science laboratory (msl). In *COSPAR, Plenary Meeting*, page 2720, 2006.

[105] III Head, James W., Harald Hiesinger, Mikhail A. Ivanov, Mikhail A. Kreslavsky, Stephen Pratt, and Bradley J. Thomson. Possible Ancient Oceans on Mars: Evidence from Mars Orbiter Laser Altimeter Data. *Science*, 286(5447):2134–2137, 1999.

[106] Thormod Henriksen. Radiation-Induced Free Radicals in Frozen Aqueous Solutions of Glycine. *Radiation Research*, 17(2):158–172, 1962.

[107] N. Hoffman. Modern geothermal gradients on mars and implications for subsurface liquids. In *Conference on the Geophysical Detection of Subsurface Water on Mars*, page 7044, Houston, Texas, 2001.

[108] G. Horneck, E. A. Krasavin, and S. Kozubek. Mutagenic effects of heavy-ions in bacteria. In *Life Sciences And Space Research Xxv(2)*, volume 14 of *Advances In Space Research*, pages 315–329. 1994. ISI Document Delivery No.: BA49P 10.

[109] Gerda Horneck. The microbial world and the case for Mars. *Planetary and Space Science*, 48(11):1053, 2000.

[110] N. H. Horowitz, Roy E. Cameron, and Jerry S. Hubbard. Microbiology of the Dry Valleys of Antarctica . *Science*, 176(4032):242–245, 1972.

[111] Philip Hugenholtz and Norman R. Pace. Identifying microbial diversity in the natural environment: A molecular phylogenetic approach. *Trends in Biotechnology*, 14(6):190, 1996.

[112] F. Hutchinson. Radiation Effects on Macromolecules of Biological Importance. *Annual Review of Nuclear Science*, 13:535–564, 1963.

[113] ICRP. 1987 Recommendations of the International Commission on Radiological Protection. Technical report, Pergamon Press, 1987.

[114] ICRP. 1990 Recommendations of the International Commission on Radiological Protection. Technical report, Pergamon Press, 1991.

[115] M. Imamura, T. Murata, K. Akagi, Y. Tanaka, M. Imamura, K. Inoue, N. Mizuma, Y. Kobayashi, H. Watanabe, M. Hachiya, M. Akashi, Y. Furusawa, H. Yamanaka, S. Takahashi, T. Nakano, S. Nagaoka, T. Ohnishi, Y. Obiya, and K. Harada. Relationship between LET and RBE values for Escherichia coli determined using carbon ion beams from the TIARA cyclotron and HIMAC synchrotron. *J Gen Appl Microbiol*, 43(3):175–7, 1997.

[116] M. Imamura, S. Sawada, M. Kasahara-Imamura, K. Harima, and K. Harada. Synergistic cell-killing effect of a combination of hyperthermia and heavy ion beam irradiation: in expectation of a breakthrough in the treatment of refractory cancers (review). *International Journal of Molecular Medicine*, 9(1):11 – 18, 2002.

[117] M. Jain, C. E. Andersen, L. Botter-Jensen, A. S. Murray, H. Haack, and J. C. Bridges. Luminescence dating on Mars: OSL characteristics of Martian analogue materials and GCR dosimetry. *Radiation Measurements*, 41(7-8):755–761, 2006.

[118] Bruce M. Jakosky, Kenneth H. Nealson, Corien Bakermans, Ruth E. Ley, and Michael T. Mellon. Subfreezing Activity of Microorganisms and the Potential Habitability of Mars' Polar Regions. *Astrobiology*, 3(2):343–350, 2003.

[119] Bruce M. Jakosky and Roger J. Phillips. Mars' volatile and climate history. *Nature*, 412(6843):237, 2001.

[120] R. Jaumann, E. Hauber, J. Lanz, H. Hoffmann, and G. Neukum. Geomorphological record of water-related erosion on mars. In Gerda Horneck and Christa Baumstark-Khan, editors, *Astrobiology: The Quest for the Conditions of Life*. Springer, 2001.

[121] R. Katz. Track Structure Theory in Radiobiology and in Radiation Detection. *Nuclear Track Detection*, 2(1):1–28, 1978.

[122] R. Katz. Track Structure Model of Cell Damage in Space Flight. Technical report, NASA Langley Research Center, 1992.

[123] R. Katz, B. Ackerson, B. Homayoonfar, and S. C. Sharma. Inactivation of Cells by Heavy Ion Bombardment. *Radiation Research*, 47:402–425, 1971.

[124] R. Katz and E. J. Kobetich. Particle Tracks in Emulsion. *Physical Review*, 186(2):344–350, 1969.

[125] Robert Katz, Francis A. Cucinotta, and C. X. Zhang. The calculation of radial dose from heavy ions: predictions of biological action cross sections. *Nuclear Instruments and Methods in Physics Research Section B: Beam Interactions with Materials and Atoms*, 107(1-4):287, 1996.

[126] A. Keating, A.; Mohammadzadeh, P. Nieminen, D. Maia, S. Coutinho, H. Evans, M. Pimenta, J.-P. Huot, and E. Daly. A model for Mars radiation environment characterization. *IEEE Transactions on Nuclear Science*, 52(6):2287– 2293, 2005.

[127] A. Keating, M. Pimenta, A. Mohammadzadeh, P. Nieminen, J. P. Huot, and E. Daly. The effects of atmospheric variations on the high energy radiation environment at the surface of mars. In *Second workshop on Mars atmosphere modelling and observations*, page 526, 2006.

[128] J. Kiefer, M. Brendamour, and U. Stoll. Heavy ion action on biological systems. *Nuclear Instruments and Methods In Physics Research Section B- Beam Interactions With Materials And Atoms*, 107(1-4):292–298, 1996.

[129] Jurgen Kiefer. *Biological Radiation Effects*. Springer-Verlag, Heidelberg, 1990.

[130] M.-H. Y. Kim, S. A. Thibeault, L. C. Simonsen, and J. W. Wilson. Comparison of Martian Meteorites and Martian Regolith as Shield Materials for Galactic Cosmic Rays. Technical report, Langley Research Center, Hampton, Virginia, 1998.

[131] J. H. King. Solar Proton Fluences for 1977-1983 Space Missions. *Journal of Spacecraft and Rockets*, 11:401, 1974.

[132] M. G. Kivelson and C. T. Russel, editors. *Introduction to Space Physics*. Cambridge University Press, Cambridge, 1995.

[133] H.V. Klapdor-Kleingrothaus and K. Zuber. Chapter 8: Cosmic radiation. In *Particle astrophysics*, Studies in high energy physics, cosmology, and gravitation, pages 223 – 247. Institute of Physics, Bristol, UK, 2000.

[134] Gerhard Kminek, J. L. Bada, K. Pogliano, and J. F. Ward. Radiation-dependent limit for the viability of bacterial spores in halite fluid inclusions and on Mars. *Radiation Research*, 159(6):722–729, 2003.

[135] Gerhard Kminek and Jeffrey L. Bada. The effect of ionizing radiation on the preservation of amino acids on Mars. *Earth and Planetary Science Letters*, 245(1-2):1–5, 2006.

[136] G. Kraft, M. Kramer, and M. Scholz. LET, Track Structure And Models - A Review. *Radiation And Environmental Biophysics*, 31(3):161–180, 1992.

[137] Vladimir A. Krasnopolsky. Some problems related to the origin of methane on Mars. *Icarus*, 180(2):359, 2006.

[138] J. Laskar and P. Robutel. The chaotic obliquity of the planets. *Nature*, 361(6413):608, 1993.

[139] F. Lei, P. R. Truscott, C. S. Dyer, B. Quaghebeur, D. Heynderickx, P. Nieminen, H. Evans, and E. Daly. MULASSIS: A Geant4-based multilayered shielding simulation tool. *Ieee Transactions On Nuclear Science*, 49(6):2788–2793, 2002.

[140] Gilbert V. Levin and Patricia Ann Straat. Labeled release - An experiment in radiorespirometry. *Origins of Life and Evolution of Biospheres*, 7(3):293–311, 1976.

[141] S. R. Lewis, M. Collins, P. L. Read, F. Forget, F. Hourdin, R. Fournier, C. Hourdin, O. Talagrand, and J. Huot. A climate database for Mars. *Journal of Geophysical Research*, 104(E10):24,177 – 24,194, 1999.

[142] Brad Lobitz, Byron L. Wood, Maurice M. Averner, and Christopher P. McKay. Special Feature: Use of spacecraft data to derive regions on Mars where liquid water would be stable. *PNAS*, 98(5):2132–2137, 2001.

[143] Michael C. Malin and Kenneth S. Edgett. Oceans or seas in the Martian northern lowlands: High resolution imaging tests of proposed coastlines. *Geophysical Research Letters*, 26(19):3049–3052, 1999.

[144] Michael C. Malin and Kenneth S. Edgett. Evidence for Recent Groundwater Seepage and Surface Runoff on Mars. *Science*, 288(5475):2330–2335, 2000.

[145] Michael C. Malin, Kenneth S. Edgett, Liliya V. Posiolova, Shawn M. McColley, and Eldar Z. Noe Dobrea. Present-Day Impact Cratering Rate and Contemporary Gully Activity on Mars. *Science*, 314(5805):1573–1577, 2006.

[146] Rocco L. Mancinelli. Accessing the Martian deep subsurface to search for life. *Planetary and Space Science*, 48(11):1035, 2000.

[147] Philippe Masson, Michael H. Carr, FranÃ§ois Costard, Ronald Greeley, Ernst Hauber, and Ralf Jaumann. Geomorphologic Evidence for Liquid Water. *Space Science Reviews*, 96(1-4):333–364, 2001.

[148] V. Mattimore and J. R. Battista. Radioresistance of Deinococcus radiodurans: functions necessary to survive ionizing radiation are also necessary to survive prolonged desiccation. *Journal of Bacteriology*, 178(3):633–637, 1996.

[149] R. Mattingly, R. Mattingly, S. Matousek, and F. Jordan. Continuing evolution of mars sample return continuing evolution of mars sample return. In S. Matousek, editor, *Aerospace Conference, 2004. Proceedings. 2004 IEEE*, volume 1, page 492 Vol.1, 2004.

[150] F. B. McDonald, Z. Fujii, B. Heikkila, N. Lal, and R.E. McGuire. The radial distribution of galactic cosmic rays in the heliosphere at solar minimum and solar maximum. In *28th International Cosmic Ray Conference*, pages 3965–3968, 2003.

[151] S. W. S. McKeever, D. Banerjee, M. Blair, S. M. Clifford, M. S. Clowdsley, S. S. Kim, M. Lamothe, K. Lepper, M. Leuschen, and K. J. McKeever. Concepts and approaches to in situ luminescence dating of martian sediments. *Radiation Measurements*, 37(4-5):527–534, 2003.

[152] Stephen W. S. McKeever, Regina Kalchgruber, Michael W. Blair, and Shubhada Deo. Development of methods for in situ dating of martian sediments. *Radiation Measurements*, 41(7-8):750–754, 2006.

[153] R. A. Mewaldt, C. M. S. Cohen, A. W. Labrador, R. A. Leske, G. M. Mason, M. I. Desai, M. D. Looper, J. E. Mazur, R. S. Selesnick, and D. K. Haggerty. Proton, helium, and electron spectra during the large solar particle events of October-November 2003. *Journal Of Geophysical Research-Space Physics*, 110(A9):–, 2005.

[154] C. Mileikowsky, F. A. Cucinotta, J. W. Wilson, B. Gladman, G. Horneck, L. Lindegren, J. Melosh, H. Rickman, M. Valtonen, and J. Q. Zheng. Natural transfer of viable microbes in space. 1. From Mars to Earth and Earth to Mars. *Icarus*, 145(2):391–427, 2000.

[155] K. W. Minton. DNA repair in the extremely radioresistant bacterium Deinococcus radiodurans . *Molecular Microbiology*, 13(1):9–15, 1994.

[156] I. Mitrofanov, D. Anfimov, A. Kozyrev, M. Litvak, A. Sanin, V. Tret'yakov, A. Krylov, V. Shvetsov, W. Boynton, C. Shinohara, D. Hamara, and R. S. Saunders. Maps of Subsurface Hydrogen from the High Energy Neutron Detector, Mars Odyssey. *Science*, 297(5578):78–81, 2002.

[157] I. G. Mitrofanov, M. L. Litvak, A. S. Kozyrev, A. B. Sanin, V. I. Tret'yakov, V. Yu Grin'kov, W. V. Boynton, C. Shinohara, D. Hamara, and R. S. Saunders. Soil Water Content on Mars as Estimated from Neutron Measurements by the HEND Instrument Onboard the 2001 Mars Odyssey Spacecraft. *Solar System Research*, 38:253–257, 2004.

[158] Christine Moissl, Shariff Osman, Myron T. La Duc, Anne Dekas, Eoin Brodie, Tadd DeSantis, and Kasthuri Venkateswaran. Molecular bacterial community analysis of clean rooms where spacecraft are assembled. *FEMS microbiology ecology*, 61(3):509–521, 2007.

[159] G.J. Molina-Cuberos, W. Stumptner, H. Lammer, N.I. Komle, and K. O'Brien. Cosmic Ray and UV Radiation Models on the Ancient Martian Surface. *Icarus*, 154(1):216–222(7), 2001.

[160] J. E. Moores, P. H. Smith, R. Tanner, A. C. Schuerger, and K. J. Venkateswaran. The shielding effect of small-scale martian surface geometry on ultraviolet flux. *Icarus*, 192(2):417, 2007.

[161] D. A. Morrison. Transformation in Escherichia coli: cryogenic preservation of competent cells. *Journal of Bacteriology*, 132(1):349–351, 1977.

[162] John B. Murray, Jan-Peter Muller, Gerhard Neukum, Stephanie C. Werner, Stephan van Gasselt, Ernst Hauber, Wojciech J. Markiewicz, III Head, James W., Bernard H. Foing, David Page, Karl L. Mitchell, Ganna Portyankina, and The Hrsc Co-Investigator Team. Evidence from the Mars Express High Resolution Stereo Camera for a frozen sea close to Mars' equator. *Nature*, 434(7031):352, 2005.

[163] NASA. Planetary Protection Provisions for Robotic Extraterrestrial Missions. NPR 8020.12C. Technical report, National Aeronautics and Space Administration, 2005.

[164] NCRP. NCRP Report No. 153: Information Needed to Make Radiation Protection Recommendations for Space Missions Beyond Low-Earth Orbit. Technical report, National Council on Radiation Protection and Measurements, 2006.

[165] Kenneth H. Nealson. The limits of life on Earth and searching for life on Mars. *Journal of Geophysical Research*, 102(E10):23,675–23,686, 1997.

[166] Gregory A. Nelson. Fundamental Space Radiobiology. *Gravitational and Space Biology Bulletin*, 16(2):29–36, 2003.

[167] Wayne L. Nicholson, Nobuo Munakata, Gerda Horneck, Henry J. Melosh, and Peter Setlow. Resistance of Bacillus Endospores to Extreme Terrestrial and Extraterrestrial Environments. *Microbiol. Mol. Biol. Rev.*, 64(3):548–572, 2000.

[168] United States committee on extension to the standard atmosphere NOAA. Us standard atmosphere, 1976.

[169] J. H. Nugent. Molecular-size standards for use in radiation-inactivation studies on proteins. *Biochemical Journal*, 239:459–462, 1986.

[170] R. A. Nymmik. Models describing solar cosmic ray events. *Radiation Measurements*, 26(3):417–420, 1996.

[171] R. A. Nymmik, M. I. Panasyuk, and A. A. Suslov. Galactic cosmic ray flux simulation and prediction. *Advances in Space Research*, 17(2):19–30, 1996.

[172] Keran O'Brien. Cosmic-ray propagation through the disturbed heliosphere. *Acta Astronautica*, 60(4-7):541–546, 2007.

[173] G. J. Olsen, D. J. Lane, S. J. Giovannoni, N. R. Pace, and D. A. Stahl. Microbial Ecology and Evolution: A Ribosomal RNA Approach. *Annual Review of Microbiology*, 40(1):337–365, 1986.

[174] Marina V. Omelchenko, Yuri I. Wolf, Elena K. Gaidamakova, Vera Y. Matrosova, Alexander Vasilenko, Min Zhai, Michael J. Daly, Eugene V. Koonin, and Kira S. Makarova. Comparative genomics of Thermus thermophilus and Deinococcus radiodurans: divergent routes of adaptation to thermophily and radiation resistance . *BMC Evolutionary Biology*, 5(57), 2005.

[175] William J. O'Neil and Christian Cazaux. The Mars Sample Return project. *Acta Astronautica*, 47(2-9):453–465, 2000.

[176] P. M. O'Neill. Badhwar-O'Neill galactic cosmic ray model update based on advanced composition explorer (ACE) energy spectra from 1997 to present. *Advances in Space Research*, 37:1727–1733, 2006.

[177] J. Oro and E. Stephen-Sherwood. Abiotic origin of biopolymers. *Origins of Life and Evolution of Biospheres*, 7(1):37, 1976.

[178] Vance I. Oyama. The gas exchange experiment for life detection: The Viking Mars Lander. *Icarus*, 16(1):167–184, 1972.

[179] N. R. Pace, D. A. Stahl, D. J. Lane, and G. J. Olsen. The analysis of natural microbial populations by ribosomal RNA sequences. *Advances in microbial ecology*, 9:1–55, 1986.

[180] Jean Baldus Patel. 16S rRNA gene sequencing for bacterial pathogen identification in the clinical laboratory. *Molecular Diagnosis*, 6(4):313, 2001.

[181] A. K. Pavlov, A. V. Blinov, and A. N. Konstantinov. Sterilization of Martian surface by cosmic radiation. *Planetary and Space Science*, 50(7-8):669–673, 2002.

[182] Anatoly K. Pavlov, Vitaly L. Kalinin, Alexei N. Konstantinov, Vladimir N. Shelegedin, and Alexander A. Pavlov. Was Earth Ever Infected by Martian Biota? Clues from Radioresistant Bacteria. *Astrobiology*, 6(6):911–919, 2006.

[183] D. A. Pearce, C. J. Gast, B. Lawley, and J. C. Ellis-Evans. Bacterioplankton community diversity in a maritime Antarctic lake, determined by culture-dependent and culture-independent techniques. *FEMS Microbiology Ecology*, 45(1):59–70, 2003.

[184] J. Taylor Perron, Jerry X. Mitrovica, Michael Manga, Isamu Matsuyama, and Mark A. Richards. Evidence for an ancient martian ocean in the topography of deformed shorelines. *Nature*, 447(7146):840, 2007.

[185] J. B. Pollack. Climatic change on the terrestrial planets. *Icarus*, 37:479–553, 1979.

[186] J. B. Pollack, J. F. Kasting, S. M. Richardson, and K. Poliakoff. The case for a wet, warm climate on early Mars. *Icarus*, 71(2):203, 1987.

[187] E. L. Powers and A. Tallentire. *The Role of Water in the Cellular Effects of Ioniszing Radiations*, volume 12 of *Actions Chimiques et Biologiques des Radiation*. Masson, Paris, 1968.

[188] Shubhadeep Purkayastha, Jamie R. Milligan, and William A. Bernhard. Correlation of Free Radical Yields with Strand Break Yields Produced in Plasmid DNA by the Direct Effect of Ionizing Radiation. *J Phys Chem B Condens Matter Mater Surf Interfaces Biophys.*, 109(35):16967–16973, 2005.

[189] M. Purucker, D. Ravat, H. Frey, C. Voorhies, T. Sabaka, and M. Acuna. An altitude-normalized magnetic map of Mars and its interpretation. *Geophysical Research Letters*, 27(16):2449–2452, 2000.

[190] F. A. Rainey, K. Ray, M. Ferreira, B. Z. Gatz, M. F. Nobre, D. Bagaley, B. A. Rash, M. J. Park, A. M. Earl, N. C. Shank, A. M. Small, M. C. Henk, J. R. Battista, P. Kampfer, and M. S. da Costa. Extensive diversity of ionizing-radiation-resistant bacteria recovered from Sonoran Desert soil and description of nine new species of the genus Deinococcus obtained from a single soil sample. *Applied and Environmental Microbiology*, 71(9):5225–5235, 2005.

[191] F.A. Rainey, K.E. Ray, and N. Ward-Rainey. The camels of the prokaryotic world. In C.R. Bell, M. Brylinsky, and P. Johnson-Green, editors, *Proceedings of the 8th International Symposium on Microbial Ecology*, Halifax, Canada, 1999. Atlantic Canada Society for Microbial Ecology.

[192] P. Rettberg, U. de La Vega, and G. Horneck. Deinococcus radiodurans - a model organism for life under martian conditions. In R. A. Harris and L. Ouwehand, editors, *Proceedings of the Third European Workshop on Exo-Astrobiology*, pages 59 – 62, Madrid, Spain, 2003. ESA Publications Division.

[193] R. C. Richmond, R. Sridhar, and M. J. Daly. Physicochemical survival pattern for the radiophile Deinococcus radiodurans: A polyextremophile model for life on Mars. *SPIE*, 3755:210–222, 1999.

[194] Lynn J. Rothschild and Rocco L. Mancinelli. Life in Extreme Environments. *Nature*, 409:1092–1101, 2001.

[195] Carl Sagan, O. B. Toon, and P. J. Gierasch. Climatic Change on Mars. *Science*, 181(4104):1045–1049, 1973.

[196] Premkumar B. Saganti, Francis A. Cucinotta, John W. Wilson, Lisa C. Simonsen, and Cary Zeitlin. Radiation climate map for analyzing risks to astronauts on the mars surface from galactic cosmic rays. *Space Science Reviews*, 110(1-2):143, 2004.

[197] G. Santin, P. Nieminen, H. Evans, E. Daly, F. Lei, P. R. Truscott, C. S. Dyer, B. Quaghebeur, and D. Heynderickx. New Geant4 based simulation tools for space radiation shielding and effects analysis. *Nuclear Physics B-Proceedings Supplements*, 125:69–74, 2003.

[198] Giovanni Santin, Vladimir Ivanchenko, Hugh Evans, Petteri Nieminen, and Eamonn Daly. GRAS: A General-Purpose 3-D Modular Simulation Tool for Space Environment Effects Analysis. *Ieee Transactions On Nuclear Science*, 52(6):2294 – 2299, 2005.

[199] J. T. Schofield, J. R. Barnes, D. Crisp, R. M. Haberle, S. Larsen, J. A. Magalhaes, J. R. Murphy, A. Seiff, and G. Wilson. The Mars Pathfinder Atmospheric Structure Investigation/Meteorology (ASI/MET) Experiment. *Science*, 278(5344):1752–1757, 1997.

[200] Andrew C. Schuerger, Jeff T. Richards, David A. Newcombe, and Kasthurisq Venkateswaran. Rapid inactivation of seven Bacillus spp. under simulated Mars UV irradiation. *Icarus*, 181:52–62, 2006.

[201] Dirk Schulze-Makuch, Louis N. Irwin, Jere H. Lipps, David LeMone, James M. Dohm, and Alberto G. Fairen. Scenarios for the evolution of life on Mars. *Journal of Geophysical Research (Planets)*, 110(E9):12, 2005.

[202] Stephen M. Seltzer. Electron, Electron-Bremsstrahlung and Proton Depth-Dose Data for Space-Shielding Applications. *Nuclear Science, IEEE Transactions on*, 26(6):4896, 1979.

[203] P. Setlow. Mechanisms which contribute to the long-term survival of spores of Bacillus species. *Journal of Applied Bacteriology*, 176:49S–60S, 1994.

[204] Katherine M. Shea. Technical Report: Irradiation of Food. *Pediatrics*, 106(6):1505–1510, 2000.

[205] John E. Simonsen, Lisa C. Nealy. Mars Surface Radiation Exposure for Solar Maximum Conitions and 1989 Solar Proton Events. Technical Report NASA Technical Paper 3300, NASA Technical Paper 3300, February 1992 1993.

[206] L. C. Simonsen, J. E. Nealy, L. W. Townsend, and J. W. Wilson. Radiation Exposure for Manned Mars Surface Missions. Technical Report N-90-18357;NASA-TP–2979; L–16708; NAS–1.60:2979, NASA Langley Research Center, 1990.

[207] Lisa C. Simonsen and John E. Nealy. Radiation protection for human missions to the Moon and Mars. *NASA STI/Recon Technical Report N*, 91:17999, 1991.

[208] David S. Smith, John Scalo, and J. Craig Wheeler. Transport of ionizing radiation in terrestrial-like exoplanet atmospheres. *Icarus*, 171(1):229, 2004.

[209] Douglas E. Smith. Free radicals in irradiated biological materials and systems. *Annual Review of Nuclear Science*, 12:577–603, 1962.

[210] L. A. Soderblom, R. C. Anderson, R. E. Arvidson, III Bell, J. F., N. A. Cabrol, W. Calvin, P. R. Christensen, B. C. Clark, T. Economou, B. L. Ehlmann, W. H. Farrand, D. Fike, R. Gellert, T. D. Glotch, M. P. Golombek, R. Greeley, J. P. Grotzinger, K. E. Herkenhoff, D. J. Jerolmack, J. R. Johnson, B. Jolliff, G. Klingelhofer, A. H. Knoll, Z. A. Learner, R. Li, M. C. Malin, S. M. McLennan, H. Y. McSween, D. W. Ming, R. V. Morris, Jr. Rice, J. W., L. Richter, R. Rieder, D. Rodionov, C. Schroder, F. P. Iv Seelos, J. M. Soderblom, S. W. Squyres, R. Sullivan, W. A. Watters, C. M. Weitz, M. B. Wyatt, A. Yen, and J. Zipfel. Soils of Eagle Crater and Meridiani Planum at the Opportunity Rover Landing Site. *Science*, 306(5702):1723–1726, 2004.

[211] Christopher H. Sommers, Brendan A. Niemira, Michael Tunick, and Glenn Boyd. Effect of temperature on the radiation resistance of virulent Yersinia enterocolitica. *Meat Science*, 61(3):323–328, 2002.

[212] S. W. Squyres. The History of Water on Mars. *Annual Review of Earth and Planetary Sciences*, 12(1):83–106, 1984.

[213] S. W. Squyres, J. P. Grotzinger, R. E. Arvidson, III Bell, J. F., W. Calvin, P. R. Christensen, B. C. Clark, J. A. Crisp, W. H. Farrand, K. E. Herkenhoff, J. R. Johnson, G. Klingelhofer, A. H. Knoll, S. M. McLennan, Jr. McSween, H. Y., R. V. Morris, Jr. Rice, J. W., R. Rieder, and L. A. Soderblom. In Situ Evidence for an Ancient Aqueous Environment at Meridiani Planum, Mars. *Science*, 306(5702):1709–1714, 2004.

[214] Steven W. Squyres and James F. Kasting. Early Mars: How Warm and How Wet? *Science*, 265(5173):744–749, 1994.

[215] G. E. Stapleton and C. W. Edington. Temperature Dependence of Bacterial Inactivation by X-Rays. *Radiation Research*, 5(1):39–45, 1956.

[216] Charles E. Swenberg, Gerda Horneck, and E. G. Stassinopoulos, editors. *Biological Effects and Physics of Solar and Galactic Cosmic Radiation, Part B*, volume 243B of *NATO Advanced Science Institute Series*. Plenum Press, New York, 1993.

[217] U. Szewzyk, R. Szewzyk, and T. Stenstrom. Thermophilic, Anaerobic Bacteria Isolated from a Deep Borehole in Granite in Sweden. *Proceedings of the National Academy of Sciences*, 91(5):1810–1813, 1994.

[218] R Tanaka, T Kamiya, T Sakai, M Fukuda, Y Kobayashi, A Tanaka, and H Watanabe. Recent technical progress in application of ion accelerator beams to biological studies in tiara. In *Asian Particle Accelerator Conference*, Tsukuba, Japan, 1998.

[219] Inge Loes ten Kate, James R.C. Garry, Zan Peeters, Richard Quinn, Bernard Foing, and Pascale Ehrenfreund. Amino acid photostability on the Martian surface. *Meteoritics and Planetary Science*, 40(8):1185–1193, 2005.

[220] L. W. Townsend, T. M. Miller, and Tony A. Gabriel. HETC radiation transport code development for cosmic ray shielding applications in space. *Radiation Protection Dosimetry*, 116(1-4):135–139, 2005.

[221] A. J. Tylka, J. H. Adams, P. R. Boberg, B. Brownstein, W. F. Dietrich, E. O. Flueckiger, E. L. Petersen, M. A. Shea, D. F. Smart, and E. C. Smith. CREME96: A Revision of the Cosmic Ray Effects on Micro-Electronics Code. *Ieee Transactions On Nuclear Science*, 44(6):2150–2160, 1997.

[222] Jorge Vago, Bruno Gardini, Gerhard Kminek, Pietro Baglioni, Giacinto Gianfiglio, Andrea Santovincenzo, Silvia Bayon, and Michel van Winnendael. Exomars: Searching for life on the red planet. *ESA Bulletin*, 126:17–23, 2006.

[223] Amudhan Venkateswaran, Sara C. McFarlan, Debabrota Ghosal, Kenneth W. Minton, Alexander Vasilenko, Kira Makarova, Lawrence P. Wackett, and Michael J. Daly. Physiologic Determinants of Radiation Resistance in Deinococcus radiodurans. *Applied and Environmental Microbiology*, 66(6):2620–2626, 2000.

[224] Elena Vorobyova, Vera Soina, Michael Gorlenko, Natalia Minkovskaya, Natalia Zalinova, Anzhelika Mamukelashvili, David Gilichinsky, Elizaveta Rivkina, and Tatiana Vishnivetskaya. The deep cold biosphere: facts and hypothesis. *FEMS Microbiology Reviews*, 20(3-4):277–290, 1997.

[225] H. Wänke, J. Bruckner, G. Dreibus, R. Rieder, and I. Ryabchikov. Chemical Composition of Rocks and Soils at the Pathfinder Site. *Space Science Reviews*, 96(1 - 4):317–330, 2001.

[226] Peter Weber and J. Mayo Greenberg. Can spores survive in interstellar space? *Nature*, 316(6027):403, 1985.

[227] W. G. Weisburg, S. M. Barns, D. A. Pelletier, and D. J. Lane. 16S ribosomal DNA amplification for phylogenetic study. *Journal of Bacteriology*, 173(2):697–703, 1991.

[228] J. P. Wellisch, M. Maire, and L. Urban. Physics Reference Manual. Technical report, 2004.

[229] L.E. Wells, J.C. Armstrong, and G. Gonzalez. Reseeding of early earth by impacts of returning ejecta during the late heavy bombardment. *Icarus*, 162:38–46, 2003.

[230] P. F. Wercinski. Mars sample return - A direct and minimum-risk design. *Journal of Spacecraft and Rockets*, 33(3):381–285, 1996.

[231] John W. Wilson, Francis F. Badavi, Francis A. Cucinotta, Judy L. Shinn, Gautam D. Badhwar, R. Silberberg, C. H. Tsao, Lawrence W. Townsend, and Ram K Tripathi. HZETRN: Description of a Free-Space Ion and Nucleon Transport and Shielding Computer Program. Technical Report NASA-TP-3495, 1995.

[232] D. Wright, M. Asai, J. Apostolakis, G. Cosmo, M. Maire, H. Kurashige, H. Yoshida, S. Tanaka, K. Amako, M. Dressel, T. Wenaus, W. Lockman, Y. Morita, L. Urban, J. P. Wellisch, P. Gumplinger, M. Verderi, J. Weng, J. Allison, and G. Folger. Geant4 User's Guide for Application Developers (Geant4 6.2 June 2004). Technical report, 2004.

[233] D. D. Wynn-Williams and H. G. M. Edwards. Antarctic ecosystems as models for extraterrestrial surface habitats . *Planetary and Space Science*, 48:1065–1075, 2000.

[234] A. S. Yen, S. S. Kim, M. H. Hecht, M. S. Frant, and B. Murray. Evidence That the Reactivity of the Martian Soil Is Due to Superoxide Ions. *Science*, 289(5486):1909–1912, 2000.

[235] C. Zeitlin, T. Cleghorn, F. Cucinotta, P. Saganti, V. Andersen, K. Lee, L. Pinsky, W. Atwell, R. Turner, and G. Badhwar. Overview of the Martian radiation environment experiment. *Advances in Space Research*, 33(12):2204–2210, 2004.

[236] Aaron P. Zent. On the thickness of the oxidized layer of the Martian regolith. *Journal of Geophysical Research*, 103:31491–31498, 1998.

Chapter 9

Appendices

9.1 Appendix I: Antarctic isolates 16S rRNA sequences

Here follows the 16S rRNA gene sequences determined for each of the 12 novel Antarctic isolates. The sequence obtained from the front of the gene is presented first, and then from the primer at the 3' end.

Pseudomonas sp. MV.1

AGTTTGATCC TGGCTCAGAT TGAACGCTGG CGGCAGGCCT AACACATGCA
AGTCGAGCGG CAGCACGGGT ACTTGTACCT GGTGGCGAGC GGCGGACGGG
TGAGTAATGC CTAGGAATCT GCCTGGTAGT GGGGGATAAC GCTCGGAAAC
GGACGCTAAT ACCGCATACG TCCTACGGGA GAAAGCAGGG GACCTTCGGG
CCTTGCGCTA TCAGATGAGC CTAGGTCGGA TTAGCTAGTT GGTGAGGTAA
TGGCTCACCA AGGCGACGAT CCGTAACTGG TCTGAGAGGA CGATCAGTCA
CACTGGAACT GAGACACGGT CCAGACTCCT ACGGGAGGCA GCAGTGGGGA
ATATTGGACA ATGGGCGAAA GCCTGATCCA GCCATGCCGC GTGTGTGAAG
AAGGTCTTCG GATAGTA

GGTACCTTGT TACGACTTCA CCCCAGTCAT GAATCACACC GTGGTAACCG
TCCTCCCGAA GGTTAGACTA GCTACTTCTG GTGCAACCCA CTCCCATGGT
GTGACGGGCG GTGTGTACAA GGCCCGGGAA CGTATTCACC GCGACATTCT
GATTCGCGAT TACTAGCGAT TCCGACTTCA CGCAGTCGAG TTGCAGACTG
CGATCCGGAC TACGATCGGT TTTCTGGGAT TAGCTCCACC TCGCGGCTTG
GCAACCCTCT GTACCGACCA TTGTAGCACG TGTGTAGCCC AGGCCGTAAG
GGCCATGATG ACTTGACGTC ATCCCCACCT TCCTCCGGTT TGTCACCGGC
AGTCTCCTTA GAGTGCCCAC CATTACGTGC TGGTAACTAA GGACAAGGGT
TGCGCTCGTT ACGGGACTTA

Pseudomonas sp. MV.3

AGTTTGATCC TGGCTCAGAT TGAACGCTGG CGGCAGGCCT AACACATGCA
AGTCGAGCGG CAGCACGGGT ACTTGTACCT GGTGGCGAGC GGCGGACGGG
TGAGTAATGC CTAGGAATCT GCCTGGTAGT GGGGGATAAC GCTCGGAAAC
GGACGCTAAT ACCGCATACG TCCTACGGGA GAAAGCAGGG GACCTTCGGG
CCTTGCGCTA TCAGATGAGC CTAGGTCGGA TTAGCTAGTT GGTGAGGTAA
TGGCTCACCA AGGCGACGAT CCGTAACTGG TCTGAGAGGA TGATCAGTCA
CACTGGAACT GAGACACGGT CCAGACTCCT ACGGGAGGCA GCAGTGGGGA
ATATTGGACA ATAGGCGAAA GCCTGATCCA GCCATGCCGC GTGTGTGAAG
AAGGTCTTCG GATTGTA

GGTACCTTGT TACGACTTCA CCCCAGTCAT GAATCACACC GTGGTAACCG
TCCTCCCGAA GGTTAGACTA GCTACTTCTG GTGCAACCCA CTCCCATGGT
GTGACGGGCG GTGTGTACAA GGCCCGGGAA CGTATTCACC GCGACATTCT
GATTCGCGAT TACTAGCGAT TCCGACTTCA CGCAGTCGAG TTGCAGACTG
CGATCCGGAC TACGACCGGT TTTCTGGGAT TAGCTCCACC TCGCGGCTTG
GCAACCCTCT GTACCGACCA TTGTAGCACG TGTGTAGCCC AGGCCGTAAG
GGCCATGATG ACTTGACGTC ATCCCCACCT TCCTCCGGTT TGTCACCGGC
AGTCTCCTTA GAGTGCCCAC CATTACGTGC TGGTAACTAA GGACAAGGGT
TGCGCTCGTT ACGGGAC

Pseudomonas sp. MV.4

AGTTTGATCC TGGCTCAGAT TGAACGCTGG CGGCAGGCCT AACACATGCA
AGTCGAGCGG CAGCACGGGT ACTTGTACCT GGTGGCGAGC GGCGGACGGG
TGAGTAATGC CTAGGAATCT GCCTGGTAGT GGGGGATAAC GCTCGGAAAC
GGACGCTAAT ACCGCATACG TCCTACGGGA GAAAGCAGGG GACCTCCGGG
CCTTGCGCTA TCAGATGAGC CTAGGTCGGA TTAGCTAGTT GGTGAGGTAA
TGGCTCACCA AGGCGACGAT CCGTAACTGG TCTGAGAGGA TGATCAGTCA
CACTGGAACT GAGACACGGT CCAGACTCCT ACGGGAGGCA GCAGTGGGGA
ATATTGGACA ATGGGCGAAA GCCTGATCCA GCCATGCCGC GTGTGTGAAG
AAGGTCTTCG GATTGTA

GGTACCTTGT TACGACTTCA CCCCAGTCAT GAATCACACC GTGGTAACCG
TCCTCCCGAA GGTTAGACTA GCTACTTCTG GTGCAACCCA CTCCCATGGT
GTGACGGGCG GTGTGTACAA GGCCCGGGAA CGTATTCACC GCGACATTCT
GATTCGCGAT TACTAGCGAT TCCGACTTCA CGCAGTCGAG TTGCAGACTG
CGATCCGGAC TACGATCGGT TTTCTGGGAT TAGCTCCACC TCGCGGCTTG
GCAACCCTCT GTACCGACCA TTGTAGCACG TGTGTAGCCC AGGCCGTAAG
GGCCATGATG ACTTGACGTC ATCCCCACCT TCCTCCGGTT TGTCACCGGC
AGTCTCCTTA GAGTGCCCAC CATTACGTGC TGGTAACTAA GGACAAGGGT
TGCGCTCGTT ACGGGACT

Pseudomonas sp. MV.5

AGTTTGATCC TGGCTCAGAT TGAACGCTGG CGGCAGGCCT AACACATGCA

AGTCGAGCGG CAGCACGGGT ACTTGTACCT GGTGGCGAGC GGCGGACGGG
TGAGTAATGC CTAGGAATCT GCCTGGTAGT GGGGGATAAC GCTCGGAAAC
GGACGCTAAT ACCGCATACG TCCTACGGGA GAAAGCAGGG GACCTTCGGG
CCTTGCGCTA TCAGATGAGC CTAGGTCGGA TTAGCTAGTT GGTGAGGTAA
TGGCTCACCA AGGCGACGAT CCGTAACTGG TCTGAGAGGA TGATCAGTCA
CACTGGAACT GAGACACGGT CCAGACTCCT ACGGGAGGCA GCAGTGGGGA
ATATTGGACA ATGGGCGAAA GCCTGATCCA GCCATGCCGC GTGTGTGAAG
AAGGTCTTCG GATTGT

GGTACCTTGT TACGACTTCA CCCCAGTCAT GAATCACACC GTGGTAACCG
TCCTCCCGAA GGTTAGACTA GCTACTTCTG GTGCAACCCA CTCCCATGGT
GTGACGGGCG GTGTGTACAA GGCCCGGGAA CGTATTCACC GCGACATTCT
GATTCGCGAT TACTAGCGAT TCCGACTTCA CGCAGTCGAG TTGCAGACTG
CGATCCGGAC TACGATCGGT TTTCTGGGAT TAGCTCCACC TCGCGGCTTG
GCAACCCTCT GTACCGACCA TTGTAGCACG TGTGTAGCCC AGGCCGTAAG
GGCCATGATG ACTTGACGTC ATCCCCACCT TCCTCCGGTT TGTCACCGGC
AGTCTCCTTA GAGTGCCCAC CATTACGTGC TGGTAACTAA GGACAAGGGT
TGCGCTCGTT ACGGGACTTA ACCCAACATC TCACGACACG AGCTGACGAC
AGCCATGCAG CA

Brevundimonas sp. MV.7

AGTTTGATCC TGGCTCAGAG CGAACGCTGG CGGCAGGCCT AACACATGCA
AGTCGAACGG ACCCTTCGGG GTTAGTGGCG GACGGGTGAG TAACACGTGG
GAACGTGCCT TTAGGTTCGG AATAGCTCCT GGAAACGGGT GGTAATGCCG
AATGTGCCCT TCGGGGGAAA GATTTATCGC CTTTAGAGCG GCCCGCGTCT
GATTAGCTAG TTGGTGAGGT AATGGCTCAC CAAGGCGACG ATCAGTAGCT
GGTCTGAGAG GATGACCAGC CACATTGGGA CTGAGACACG GCCCAAACTC
CTACGGGAGG CAGCAGTGGG GAATCTTGCG CAATGGGCGA AAGCCTGACG
CAGCCATGCC GCGTGAATGA TGAAGGTCTT AGGATTGTAA AATTCTTTCA
CG

GGTACCTTGT TACGACTTCA CCCCAGTCGC TGACCCTACC GTGGTCGACT
GCCTCCCTTG CGGGTTAGCG CATCGCCTTC GGGTAGAACC AACTCCCATG
GTGTGACGGG CGGTGTGTAC AAGGCCCGGG AACGTATTCA CCGCGGCATG
CTGATCCGCG ATTACTAGCG ATTCCAACTT CATGCCCTCG AGTTGCAGAG
GACAATCCGA ACTGAGACGA CTTTTAAGGA TTAACCCTCT GTAGTCGCCA
TTGTAGCACG TGTGTAGCCC ACCCTGTAAG GGCCATGAGG ACTTGACGTC
ATCCCCACCT TCCTCCGGCT TAGCACCGGC AGTCCCATTA GAGTTCCCAA
CTAAATGATG GCAACTAATG GCGAGGGTTG CGCTCGTTGC GGGACTTAAC
CCAACATCTC ACGACACGAG CTGACGACAG CCATGCAGCA

Arthrobacter sp. MV.8

AGTTTGATCC TGGCTCAGGA TGAACGCTGG CGGCGTGCTT AACACATGCA

AGTCGAACGA TGATCCCAGC TTGCTGGGGG ATTAGTGGCG AACGGGTGAG
TAACACGTGA GTAACCTGCC CTTAACTCTG GGATAAGCCT GGGAAACTGG
GTCTAATACC GGATATGACT CCTCATCGCA TGGTGGGGGG TGGAAAGCTT
TATTGTGGTT TTGGATGGAC TCGCGGCCTA TCAGCTTGTT GGTGAGGTAA
TGGCTCACCA AGGCGACGAC GGGTAGCCGG CCTGAGAGGG TGACCGGCCA
CACTGGGACT GAGACACGGC CCAGACTCCT ACGGGAGGCA GCAGTGGGGA
ATATTGCACA ATGGGCGA

GGTACCTTGT TACGACTTAG TCCCAATCGC CAGTCCCACC TTCGACAGCT
CCCTCCCACA AGGGGTTAGG CCACCGGCTT CGGGTGTTAC CAACTTTCGT
GACTTGACGG GCGGTGTGTA CAAGGCCCGG GAACGTATTC ACCGCAGCGT
TGCTGATCTG CGATTACTAG CGACTCCGAC TTCATGGGGT CGAGTTGCAG
ACCCCAATCC GAACTGAGAC CGGCTTTTTG GGATTAGCTC CACCTCACAG
TATCGCAACC CTTTGTACCG GCCATTGTAG CATGCGTGAA GCCCAAGACA
TAAGGGGCAT GATGATTTGA CGTCGTCCCC ACCTTCCTCC GAGTTGACCC
CGGCAGTCTC CTATGAGT

Rhodococcus sp. MV.10

AGTTTGATCC TGGCTCAGGA CGAACGCTGG CGGCGTGCTT AACACATGCA
AGTCGAGCGG TAAGGCCTTT CGGGGTACAC GAGCGGCGAA CGGGTGAGTA
ACACGTGGGT GATCTGCCCT GCACTTCGGG ATAAGCCTGG GAAACTGGGT
CTAATACCGG ATATGACCTC CTATCGCATG GTGGGTGGTG GAAAGATTTA
TCGGTGCAGG ATGGGCCCGC GGCCTATCAG CTTGTTGGTG GGGTAATGGC
CTACCAAGGC GACGACGGGT AGCCGACCTG AGAGGGTGAC CGGCCACACT
GGGACTGAGA CACGGCCCAG ACTCCTACGG GAGGCAGCAG TGGGGAATAT
TGCACAATGG GCGAAAGCCT GATGCAGCGA CGCCGCGTGA GGGATGACGG
CCTTCGGGTT GT

TGGTACCTTG TTACGACTTC GTCCCAATCG CCGATCCCAC CTTCGACGGC
TCCCTCCCAC AAGGGGTTAA GCCACCGGCT TCGGGTGTTA CCGACTTTCA
TGACGTGACG GGCGGTGTGT ACAAGGCCCG GGAACGTATT CACCGCAGCG
TTGCTGATCT GCGATTACTA GCGACTCCGA CTTCACGGGG TCGAGTTGCA
GACCCCGATC CGAACTGAGA CCAGCTTTAA GGGATTCGCT CCACCTCACG
GTCTCGCAGC CCTCTGTACT GGCCATTGTA GCATGTGTGA AGCCCTGGAC
ATAAGGGGCA TGATGACTTG ACGTCGTCCC CACCTTCCTC CGAGTTGACC
CCGGCAGTCT CTTACGAGTC CCCACCATAA CGTGCTGGCA ACATAAGATA
GGGGTTGCGC TCGTTGCGGG ACTTAACCCA ACATCTCACG ACACGAGCTG
ACGACAGCCA TGCA

Pseudomonas sp. MV.23

AGTTTGATCC TGGCTCAGAT TGAACGCTGG CGGCAGGCCT AACACATGCA
AGTCGAGCGG CAGCACGGGT ACTTGTACCT GGTGGCGAGC GGCGGACGGG
TGAGTAATGC CTAGGAATCT GCCTGGTAGT GGGGGATAAC GCTCGGAAAC

GGACGCTAAT ACCGCATACG TCCTACGGGA GAAAGCAGGG GACCTTCGGG
CCTTGCGCTA TCAGATGAGC CTAGGTCGGA TTAGCTAGTT GGTGAGGTAA
TGGCTCACCA AGGCGACGAT CCGTAACTGG TCTGAGAGGA TGATCAGTCA
CACTAGAACT GAGACACGGT CCAGACTCCT ACGGGAGGCA GCAGTGGGGA
ATATTGGACA ATGGGCGAAA GCCTGATCCA GCCATGCCGC GTGTGTG

GGTACCTTGT TACGACTTCA CCCCAGTCAT GAATCACACC GTGGTAACCG
TCCTCCCGAA GGTTAGACTA GCTACTTCTG GTGCAACCCA CTCCCATGGT
GTGACGGGCG GTGTGTACAA GGCCCGGGAA CGTATTCACC GCGACATTCT
GATTCGCGAT TACTAGCGAT TCCGACTTCA CGCAGTCGAG TTGCAGACTG
CGATCCGGAC TACGATCGGT TTTCTGGGAT TAGCTCCACC TCGCGGCTTG
GCAACCCTCT GTACCGACCA TTGTAGCACG TGTGTAGCCC AGGCCGTAAG
GGCCATGATG ACTTGACGTC ATCCCCACCT TCCTCCGGTT TGTCACCGGC
AGTCTCCTTA GAGTGCCCAC CATTACGTGC TGGTAACTAA GGACAAGGGT
TGCGCTCGTT

Arthrobacter sp. MV.24

AGTTTGATCC TGGCTCAGGA TGAACGCTGG CGGCGTGCTT AACACATGCA
AGTCGAACGA TGATCCCAGC TTGCTGGGGG ATTAGTGGCG AACGGGTGAG
TAACACGTGA GTAACCTGCC CTTAACTCTG GGATAAGCCT GGGAAACTGG
GTCTAATACC GGATATGACT CCTCATCGCA TGGTGGGGGG TGGAAAGCTT
TATTGTGGTT TTGGATGGAC TCGCGGCCTA TCAGCTTGTT GGTGAGGTAA
TGGCTCACCA AGGCGACGAC GGGTAGCCGG CCTGAGAGGG TGACCGGCCA
CACTGGGACT GAGACACGGC CCAGACTCCT ACGGGAGGCA GCAGTGGGGA
ATATTGCACA ATGGGCGAAA GCCTGATGCA GCGA

GGTACCTTGT TACGACTTAG TCCCAATCGC CAGTCCCACC TTCGACAGCT
CCCTCCCACA AGGGTAGGCC ACCGCTTCGG TGTACCACTT CGTGACTGAC
GGGCGTGTGT ACAGGGCCGG GACGTATCCC CGCAGCGTGC TGATCGCCAT
TACTGCGACT TCCACTCAT

Pseudomonas sp. MV.25

AGTTTGATCC TGGCTCAGAT TGAACGCTGG CGGCAGGCCT AACACATGCA
AGTCGAGCGG CAGCACTGGT ACTTGTACCT GGTGGCGAGC GGCGGACGGG
TGAGTAATGC CTAGGAATCT GCCTGGTAGT GGGGGATAAC GCTCGGAAAC
GGACGCTAAT ACCGCATACG TCCTACGGGG GAAAGCAGGG GACCTTCGGG
CCTTGCGCTA TCAGATGAGC CTAGGTCGGA TTAGCTAGTT GGTGAGGTAA
TGGCTCACCA AGGCGACGAT CCGTAACTGG TCTGAGAGGA TGATCAGTCA
CACTGGAACT GAGACACGGT CCAGACTCCT ACGGGAGGCA GCAGTGGGGA
ATATTGGACA ATGGGCGAAA GCCTGATCCA GCCATGCCGC GTGTGTGAAG
AAGGTCTTCG GATTGT

GGTACCTTGT TACGACTTCA CCCCAGTCAT GAATCACACC GTGGTAACCG

TCCTCCCGAA GGTTAGACTA GCTACTTCTG GTGCAACCCA CTCCCATGGT
GTGACGGGCG GTGTGTACAA GGCCCGGGAA CGTATTCACC GCGACATTCT
GATTCGCGAT TACTAGCGAT TCCGACTTCA CGCAGTCGAG TTGCAGACTG
CGATCCGGAC TACGATCGGT TTTCTGGGAT TAGCTCCACC TCGCGGCTTG
GCAACCCTCT GTACCGACCA TTGTAGCACG TGTGTAGCCC AGGCCGTAAG
GGCCATGATG ACTTGACGTC ATCCCCACCT TCCTCCGGTT TGTCACCGGC
AGTCTCCTTA GAGTGCCCAC CATTACGTGC TGGTAACTAA GGAC

Pseudomonas sp. MV.26

AGTTTGATCC TGGCTCAGAT TGAACGCTGG CGGCAGGCCT AACACATGCA
AGTCGAGCGG CAGCACTGGT ACTTGTACCT GGTGGCGAGC GGCGGACGGG
TGAGTAATGC CTAGGAATCT GCCTGGTAGT GGGGGATAAC GCTCGGAAAC
GGACGCTAAT ACCGCATACG TCCTACGGGA GAAAGCAGGG GACCTTCGGG
CCTTGCGCTA TCAGATGAGC CTAGGTCGGA TTAGCTAGTT GGTGAGGTAA
TGGCTCACCA AGGCGACGAT CCGTAACTGG TCTGAGAGGA TGATCAGTCA
CACTGGAACT GAGACACGGT CCAGACTCCT ACGGGAGGCA GCAGTGGGGA
ATATTGGACA ATGGGCGAAA GCCTGATCCA GCCATGCCGC GTGTGTGAAG
AAGGTCTTCG GATTGT

GGTACCTTGT TACGACTTCA CCCCAGTCAT GAATCACACC GTGGTAACCG
TCCTCCCGAA GGTTAGACTA GCTACTTCTG GTGCAACCCA CTCCCATGGT
GTGACGGGCG GTGTGTACAA GGCCCGGGAA CGTATTCACC GCGACATTCT
GATTCGCGAT TACTAGCGAT TCCGACTTCA CGCAGTCGAG TTGCAGACTG
CGATCCGGAC TACGATCGGT TTTCTGGGAT TAGCTCCACC TCGCGGCTTG
GCAACCCTCT GTACCGACCA TTGTAGCACG TGTGTAGCCC AGGCCGTAAG
GGCCATGATG ACTTGACGTC ATCCCCACCT TCCTCCGGTT TGTCACCGGC
AGTCTCCTTA GAGTGCCCAC CATTACGTGC TGGTAACTAA GGACAAGGGT
TGCGCTCGTT ACGGGACTTA ACCCAACATC TCACGACACG AGCTGACGAC
AGCCATGCAG CACCTGTCTC AATGT

Pseudomonas sp. MV.27

TAGTTTGATC CTGGCTCAGA TTGAACGCTG GCGGCAGGCC TAACACATGC
AAGTCGAGCG GCAGCACGGG TACTTGTACC TGGTGGCGAG CGGCGGACGG
GTGAGTAATG CCTAGGAATC TGCCTGGTAG TGGGGGATAA CGCTCGGAAA
CGGACGCTAA TACCGCATAC GTCCTACGGG AGAAAGCAGG GGACCTTCGG
GCCTTGCGCT ATCAGATGAG CCTAGGTCGG ATTAGCTAGT TGGTGAGGTA
ATGGCTCACC AAGGCGACGA TCCGTAACTG GTCTGAGAGG ATGATCAGTC
ACACTGGAAC TGAGACACGG TCCAGACTCC TACGGGAGGC AGCAGTGGGG
AATATTGGAC AATGGGCGAA AGCCTGATCC AGCCATGCCG CGTGTGTGAA
GAAGGTCTTC GGATTGTA

GGTACCTTGT TACGACTTCA CCCCAGTCAT GAATCACACC GTGGTAACCG
TCCTCCCGAA GGTTAGACTA GCTACTTCTG GTGCAACCCA CTCCCATGGT

GTGACGGGCG GTGTGTACAA GGCCCGGGAA CGTATTCACC GCGACATTCT
GATTCGCGAT TACTAGCGAT TCCGACTTCA CGCAGTCGAG TTGCAGACTG
CGATCCGGAC TACGATCGGT TTTCTGGGAT TAGCTCCACC TCGCGGCTTG
GCAACCCTCT GTACCGACCA TTGTAGCACG TGTGTAGCCC AGGCCGTAAG
GGCCATGATG ACTTGACGTC ATCCCCACCT TCCTCCGGTT TGTCACCGGC
AGTCTCCTTA GAGTGCCCAC CATTACGTGC TGGTAACTAA GGACAAGGGT
TGCGCTCGTT ACGGGACTTA ACCCAACATC TCACGACACG AGCTGACGAC
AGCCATGCAG CACCTGTCTC AATGTTC

9.2 Appendix II: Irradiation survival data

This Appendix contains all of the raw data gathered from the freeze-thaw survival, as summarised in Table 7.5 on page 137, and gamma-ray exposure experiments, as plotted in Figures 7.5 to 7.10 on page 140. Results are presented in turn for each of the five organisms irradiated: *E. coli* and *D. radiodurans*, and the novel Antarctic isolates *Brevundimonas* sp. MV.7, *Rhodococcus* sp. MV.10, and *Psuedomonas* sp. MV.27.

E. coli

Pre-freeze population		
Cell count (ml^{-1})		Mean
3.45×10^8	4.05×10^8	
4.22×10^8	4.06×10^8	3.95×10^8

Post-freeze control[a]
Cell count (ml^{-1})
7.75×10^6

[a] As explained in section 4.6.3.2 on page 93, the post-freeze control cell counts were erroneous and so this initial population number was recovered by back-extrapolation from the subsequent survival cell counts. The post-freeze survival was confirmed by independent experiment.

0.3 kGy/hour exposure					
Dose (kGy)	Cell count (ml^{-1})			Mean (ml^{-1})	Survival
0.3	8.45×10^6	9.60×10^6	8.19×10^6	8.75×10^6	1.13
0.9	1.88×10^6	2.44×10^6	2.06×10^6	2.13×10^6	2.74×10^{-1}
1.2	1.26×10^6	1.42×10^6	0.65×10^6	1.11×10^6	1.43×10^{-1}
1.5	0.72×10^6	0.80×10^6	1.00×10^6	8.40×10^5	1.08×10^{-1}
1.8	0.97×10^6	1.00×10^6	0.89×10^6	9.53×10^5	1.23×10^{-1}
1.8	2.14×10^5	2.80×10^5	2.46×10^5	2.47×10^5	3.18×10^{-2}

0.5 kGy/hour exposure					
Dose (kGy)	Cell count (ml^{-1})			Mean	Survival
0.5	3.40×10^{6}	3.06×10^{6}	4.63×10^{6}	3.70×10^{6}	4.77×10^{-1}
0.5	2.22×10^{6}	3.13×10^{6}	4.02×10^{6}	3.12×10^{6}	4.03×10^{-1}
1.0	1.12×10^{6}	2.09×10^{6}	1.56×10^{6}	1.59×10^{6}	2.05×10^{-1}
1.0	6.60×10^{5}	7.10×10^{5}		6.85×10^{5}	8.84×10^{-2}
1.5	5.90×10^{5}	2.70×10^{5}	6.60×10^{5}	5.07×10^{5}	6.54×10^{-2}
1.5	1.06×10^{5}	1.42×10^{5}	0.94×10^{6}	1.14×10^{6}	1.47×10^{-1}
2.0	3.31×10^{5}	3.13×10^{5}	3.69×10^{5}	3.38×10^{5}	4.36×10^{-2}
2.5	4.70×10^{5}	3.20×10^{5}	4.40×10^{5}	4.40×10^{5}	5.68×10^{-2}
2.5	5.90×10^{5}	7.50×10^{5}	4.40×10^{5}	5.93×10^{5}	7.66×10^{-2}
3.0	5.90×10^{4}	7.50×10^{4}	6.80×10^{4}	6.73×10^{4}	8.69×10^{-3}
3.0	7.00×10^{4}	7.10×10^{4}	6.20×10^{4}	6.77×10^{4}	8.73×10^{-3}
3.0	1.02×10^{5}	1.01×10^{4}		1.02×10^{5}	1.31×10^{-2}

D. radiodurans

Pre-freeze population		
Cell count (ml^{-1})		Mean
6.15×10^{7}	6.32×10^{7}	
6.90×10^{7}	8.20×10^{7}	6.89×10^{7}

Post-freeze control			
Cell count (ml^{-1})			Mean
7.49×10^{7}	7.98×10^{7}	7.67×10^{7}	
8.24×10^{7}	8.47×10^{7}	7.89×10^{7}	
9.50×10^{7}	7.70×10^{7}	5.90×10^{7}	7.87×10^{7}

0.5 kGy/hour exposure					
Dose (kGy)	Cell count (ml^{-1})			Mean	Survival
0.5	6.40×10^{7}	6.50×10^{7}	6.70×10^{7}	6.53×10^{7}	8.30×10^{-1}
0.5	7.70×10^{7}	7.10×10^{7}	8.90×10^{7}	7.90×10^{7}	1.00
1.0	6.90×10^{7}	6.40×10^{7}	6.30×10^{7}	6.53×10^{7}	8.30×10^{-1}
1.0	6.30×10^{7}	6.40×10^{7}	6.40×10^{7}	6.37×10^{7}	8.09×10^{-1}
1.5	7.70×10^{7}	7.20×10^{7}	8.20×10^{7}	7.70×10^{7}	9.78×10^{-1}
1.5	8.30×10^{7}	10.10×10^{7}	7.70×10^{7}	8.70×10^{7}	1.11
2.0	9.20×10^{7}	10.30×10^{7}	10.60×10^{7}	1.00×10^{8}	1.27
2.0	7.50×10^{7}	8.00×10^{7}	8.10×10^{7}	7.87×10^{7}	1.00
2.5	5.30×10^{7}	7.80×10^{7}	8.40×10^{7}	7.17×10^{7}	9.11×10^{-1}
2.5	7.50×10^{7}	8.20×10^{7}	6.70×10^{7}	7.47×10^{7}	9.49×10^{-1}
3.0	5.70×10^{7}	6.40×10^{7}	7.70×10^{7}	6.60×10^{7}	8.39×10^{-1}
3.0	7.00×10^{7}	7.90×10^{7}	8.80×10^{7}	7.90×10^{7}	1.00
3.0	7.60×10^{7}	8.10×10^{7}	9.50×10^{7}	8.40×10^{7}	1.07

1.5 kGy/hour exposure					
Dose (kGy)	Cell count (ml^{-1})			Mean	Survival
1.5	6.30×10^{7}	7.50×10^{7}	7.20×10^{7}	7.00×10^{7}	8.89×10^{-1}
3.0	7.20×10^{7}	7.60×10^{7}	7.80×10^{7}	7.53×10^{7}	9.57×10^{-1}
6.0	7.70×10^{7}	7.70×10^{7}	7.70×10^{7}	7.70×10^{7}	9.78×10^{-1}
7.5	2.10×10^{7}	3.70×10^{7}	3.60×10^{7}	3.13×10^{7}	3.98×10^{-1}
7.5	5.10×10^{7}	5.70×10^{7}	5.90×10^{7}	5.57×10^{7}	7.07×10^{-1}
9.0	6.30×10^{7}	4.80×10^{7}	5.00×10^{7}	5.37×10^{7}	6.82×10^{-1}
9.0	5.20×10^{7}	5.00×10^{7}	4.90×10^{7}	5.03×10^{7}	6.40×10^{-1}

1.69 kGy/hour exposure					
Dose (kGy)	Cell count (ml^{-1})			Mean	Survival
6.76	7.30×10^{7}	6.50×10^{7}	4.80×10^{7}	6.20×10^{7}	7.88×10^{-1}
8.45	8.40×10^{7}	6.20×10^{7}	7.30×10^{7}	7.30×10^{7}	9.28×10^{-1}
10.14	4.00×10^{7}	5.90×10^{7}	5.10×10^{7}	5.00×10^{7}	6.35×10^{-1}
11.83	3.20×10^{7}	3.30×10^{7}	5.40×10^{7}	3.97×10^{7}	5.04×10^{-1}
13.52	5.10×10^{7}	3.40×10^{7}	4.10×10^{7}	4.20×10^{7}	5.34×10^{-1}
15.21	1.80×10^{7}	1.90×10^{7}	1.77×10^{7}	1.82×10^{7}	2.32×10^{-1}

Brevundimonas sp. MV.7

Pre-freeze population			
Cell count (ml^{-1})			Mean
2.84×10^{8}	2.97×10^{8}	3.19×10^{8}	3.00×10^{8}

Post-freeze control			
Cell count (ml^{-1})			Mean
2.85×10^{8}	2.44×10^{8}	2.69×10^{8}	
2.35×10^{8}	2.35×10^{8}	2.54×10^{8}	2.54×10^{8}

0.5 kGy/hour exposure					
Dose (kGy)	Cell count (ml^{-1})			Mean	Survival
0.5	1.75×10^{8}	1.90×10^{8}	1.97×10^{8}	1.87×10^{8}	7.38×10^{-1}
0.5	1.79×10^{8}	1.50×10^{8}	1.84×10^{8}	1.71×10^{8}	6.73×10^{-1}
1.0	0.68×10^{8}	0.66×10^{8}	0.87×10^{8}	7.37×10^{7}	2.90×10^{-1}
1.0	1.05×10^{8}	0.97×10^{8}	0.92×10^{8}	9.80×10^{7}	3.86×10^{-1}
1.5	3.60×10^{7}	5.00×10^{7}	4.80×10^{7}	4.47×10^{7}	1.76×10^{-1}
2.0	1.02×10^{7}	1.10×10^{7}	0.89×10^{7}	1.00×10^{7}	3.95×10^{-2}
2.5	7.60×10^{6}	6.10×10^{6}	7.50×10^{6}	7.07×10^{6}	2.78×10^{-2}
3.0	7.50×10^{5}	7.50×10^{5}	6.80×10^{5}	7.27×10^{5}	2.86×10^{-3}
3.5	1.47×10^{5}	1.61×10^{5}	1.97×10^{5}	1.68×10^{5}	6.63×10^{-4}
4.0	1.53×10^{5}	1.57×10^{5}	1.57×10^{5}	1.56×10^{5}	6.13×10^{-4}
4.0	1.13×10^{5}	1.28×10^{5}	1.26×10^{5}	1.22×10^{5}	4.82×10^{-4}
4.5	1.69×10^{4}	1.87×10^{4}	1.62×10^{4}	1.73×10^{4}	6.80×10^{-5}

1.69 kGy/hour exposure					
Dose (kGy)	Cell count (ml^{-1})			Mean	Survival
3.38	1.67×10^{6}	1.59×10^{6}	1.42×10^{6}	1.56×10^{6}	6.14×10^{-3}
6.76	2.87×10^{3}	2.49×10^{3}	2.34×10^{3}	2.57×10^{3}	1.01×10^{-5}
8.45	3.00×10^{1}	4.00×10^{1}	2.00×10^{1}	2.75×10^{1}	1.08×10^{-7}

Rhodococcus sp. MV.10

Pre-freeze population			
Cell count (ml^{-1})			Mean
6.30×10^{7}	4.70×10^{7}	7.10×10^{7}	6.03×10^{7}

Post-freeze control			
Cell count (ml^{-1})			Mean
4.0×10^7	5.40×10^7	5.50×10^7	
8.70×10^7	8.50×10^7	6.00×10^7	
6.00×10^7	5.00×10^7	3.90×10^7	5.89×10^7

0.5 kGy/hour exposure					
Dose (kGy)	Cell count (ml^{-1})			Mean	Survival
0.5	0.99×10^7	1.29×10^7	1.07×10^7	1.12×10^7	1.90×10^{-1}
0.5	0.82×10^7	1.04×10^7	0.93×10^7	0.93×10^7	1.58×10^{-1}
1.0	4.50×10^5	3.50×10^5	4.10×10^5	4.03×10^5	6.85×10^{-3}
1.0	4.10×10^5	3.00×10^5	3.50×10^5	3.53×10^5	6.00×10^{-3}
1.5	6.90×10^4	6.20×10^4	5.50×10^4	6.20×10^4	1.05×10^{-3}
2.0	9.50×10^3	9.70×10^3	8.90×10^3	9.37×10^3	1.59×10^{-4}
2.5	2.19×10^3	1.97×10^3	1.89×10^3	2.02×10^3	3.42×10^{-5}
3.0	1.10×10^2	0.90×10^2	1.15×10^2	1.05×10^2	1.78×10^{-6}

1.69 kGy/hour exposure					
Dose (kGy)	Cell count (ml^{-1})			Mean	Survival
3.38	1.00×10^2	2.10×10^2	1.20×10^2	1.43×10^2	2.43×10^{-6}

Pseudomonas sp. MV.27

Pre-freeze population		
Cell count (ml^{-1})		Mean
6.77×10^8	5.88×10^8	
7.74×10^8	9.87×10^8	7.57×10^8

Post-freeze control			
Cell count (ml^{-1})			Mean
1.79×10^8	2.09×10^8	1.28×10^8	
2.07×10^8	2.42×10^8	3.65×10^8	
3.82×10^8	3.83×10^8	1.97×10^8	2.55×10^8

0.3 kGy/hour exposure					
Dose (kGy)	Cell count (ml^{-1})			Mean (ml^{-1})	Survival
0.3	1.11×10^{6}	2.80×10^{6}	2.09×10^{6}	2.00×10^{6}	7.84×10^{-3}
0.3	3.01×10^{7}	2.74×10^{7}	2.65×10^{7}	2.8×10^{7}	1.10×10^{-1}
0.6	1.26×10^{7}	0.18×10^{7}	1.30×10^{7}	9.13×10^{6}	3.58×10^{-2}
0.9	0.63×10^{5}	1.39×10^{5}	5.08×10^{5}	2.37×10^{5}	9.28×10^{-4}
1.2	0.50×10^{3}	2.00×10^{3}	2.60×10^{3}	1.7×10^{3}	6.67×10^{-6}
1.5	1.10×10^{1}	1.60×10^{1}	1.10×10^{1}	1.27×10^{1}	4.97×10^{-8}

9.3 Appendix III: Publications

Four papers have been published on the research outlined here. They are included here for reference as follows:

1. **L. R. Dartnell**, J. M. Ward, A. J. Coates (2006), Modelling Planetary Radiation Environments: Astrobiological Perspectives, *Proceedings of the European Modelling Symposium*, ISBN 0-9516509-3-9/978-0-9516509-3-6.

2. **L. R. Dartnell**, L. Desorgher, J. M. Ward, A. J. Coates (2007), Modelling the surface and subsurface Martian radiation environment: Implications for astrobiology, *Geophysical Research Letters,* 34, L02207, doi:10.1029/2006GL027494

3. P. Morthekai, M. Jain, **L. R. Dartnell**, A. S. Murray, L. Bøtter-Jensen, L. Desorgher (2007), Modelling of the dose-rate variations with depth in the Martian regolith using GEANT4, *Nuclear Instruments Methods A*, 580(1), doi:10.1016/j.nima.2007.05.118

4. **L. R. Dartnell**, L. Desorgher, J. M. Ward, A. J. Coates (2007), Martian sub-surface ionising radiation: biosignatures and geology, *Biogeosciences*, 4, 545-558